

POLARONS AND IMPURITIES IN NICKEL COBALT OXIDE

By

ROBERT REED OWINGS

A DISSERTATION PRESENTED TO THE GRADUATE SCHOOL  
OF THE UNIVERSITY OF FLORIDA IN PARTIAL FULFILLMENT  
OF THE REQUIREMENTS FOR THE DEGREE OF  
DOCTOR OF PHILOSOPHY

UNIVERSITY OF FLORIDA

2003

Copyright 2003

By

ROBERT REED OWINGS

To my lovely sweetheart, companion, and friend

## ACKNOWLEDGMENTS

Many have contributed to this work in content and by means of support and encouragement. Perhaps the greatest inspiration and motivation for the completion of this work was my wife, Sharee, whose encouragement and support was continuous and at times intense as needed. I acknowledge the patience of our two children, Parker and Londyn, who have gone at times without the attention they were entitled so that this work could be completed. Paul Holloway, my committee chair, whole-heartedly supported me in my desires to complete this program and offered timely advice and critical analysis as needed. The committee, David Norton, Rolf Hummel, Susan Sinnott, and Arthur Hebard have contributed of their time and for that I acknowledge them. Greg Exarhos was instrumental in providing experimental guidance for conducting and compiling the research. I would like to acknowledge him as my mentor, for providing perspective, guidance and insight. Chuck Windisch aided in the structural organization and proofread select sections in addition to sharing key results and data from previous studies. I acknowledge him for the significant amount of personal time he spent on reading and discussing section layouts. His patience in training me in the operation of the many lab instruments and fielding my unending questions was very much appreciated and for that I acknowledge him. Kim Ferris developed the framework for the polaron disorder model, ran the calculation, and participated in many insightful discussions on polarons, conductivity, and life as we know it. His assistance with editing in the final hours of preparation was most appreciated as were his encouraging words of perspective.

Others at the Pacific Northwest National Laboratory encouraged my progression and contributed by answering my questions and providing data and insight. Special thanks go to Mark Engelhard for XPS data and analysis, Scott Lea for AFM training, Dan Gaspar for SIMS data and analysis, Dave McCready for XRR and GIXRD data and analysis, and Tim Droubay for UPS data and VSM data all conducted at the EMSL facility. I would also like to acknowledge Mark Gross, John Johnston, Pete Martin, Dean Matson, Pete Reike, Bill Samuels, Don Stewart, Rick Williford, and others at PNNL and for their assistance with technical equipment, details, or operations. Maggie Puga-Lambers collected SIMS data at the University of Florida Microfabritech facility. Valentin Cracium performed X-ray modeling and data acquisition at the University of Florida MAIC facility. For their efforts and data provided, I thank them. I wish to extend a special thanks to Ludie Harmon, the administrative professional who, in addition to securing logistical arrangements, provided encouragement, plenty of sugar and emotional energy at both high and low times making the process more enjoyable.

Funding was provided by a fellowship from the University of Florida Alumni Association. This research was supported through the Materials Sciences and Engineering Division of the Office of Basic Energy Sciences, U.S. DOE, and the ARO through DARPA contract AO J209/00. A portion of the research in this work was performed at the W. R. Wiley Environmental Molecular Sciences Laboratory, a national scientific user facility sponsored by the U.S. Department of Energy's Office of Biological and Environmental Research and located at Pacific Northwest National Laboratory. Pacific Northwest National Laboratory is operated by Battelle Memorial Institute for DOE under Contract DE-AC06-76RLO 1830.

## TABLE OF CONTENTS

	<u>Page</u>
ACKNOWLEDGMENTS .....	IV
LIST OF TABLES .....	X
LIST OF FIGURES .....	XII
ABSTRACT .....	XVIII
CHAPTER	
1 INTRODUCTION .....	1
1.1 Introduction.....	1
1.2 Organization of the Dissertation.....	4
2 BACKGROUND OF NICKEL COBALT OXIDE.....	6
2.1 Background of Transparent Oxide Conductors .....	6
2.1.1 The Basic <i>p-n</i> Junction Diode .....	7
2.1.2 <i>N</i> -Type Transparent Conducting Oxides.....	9
2.1.3 <i>P</i> -Type Transparent Conducting Oxides .....	12
2.2 Nickel-Cobalt Oxide.....	15
2.3 Nickel-Cobalt Oxide Conduction Mechanism.....	24
2.3.1 Fundamentals of Polaron Conduction .....	24
2.3.2 Fundamentals of Free Carrier Conduction .....	26
2.3.3 Observed Properties of Free Carriers and Polarons .....	28
2.4 Nickel-Cobalt Oxide Spinel Structure .....	32
2.4.1 Spinel Sites .....	35
2.4.2 Variations of the Spinel Structure .....	38
2.4.3 Spinel and Conductivity .....	39
2.5 Summary of Literature Review .....	39
3 SPUTTERED NICKEL-COBALT OXIDE .....	41
3.1 Introduction.....	41
3.2 Film Preparation and Characterization Procedures .....	42
3.3 Characterization Results and Discussion.....	45
3.3.1 Electrical Properties.....	45
3.3.2 Optical Properties .....	54

3.3.3	Film Structural Properties.....	59
3.3.4	Post Deposition Heat Treatment.....	68
3.4	Summary and Conclusions .....	76
4	THE ROLE OF LITHIUM .....	78
4.1	Introduction.....	78
4.2	Experimental Procedure.....	80
4.2.1	Deposition.....	80
4.2.2	Characterization.....	81
4.2.3	Sample Heat Treatment .....	82
4.3	Characterization Results .....	82
4.3.1	Electrical Properties.....	82
4.3.2	Optical Properties .....	87
4.3.3	Structural Properties and Composition.....	90
4.3.4	Chemical Properties.....	94
4.4	Discussion.....	99
4.4.1	Lithium Effects.....	99
4.4.2	Effects of Heat Treatment .....	101
4.5	Conclusions.....	104
5	RHODIUM SUBSTITUTION FOR COBALT.....	106
5.1	Introduction.....	106
5.2	Experimental Procedure.....	109
5.2.1	Film Deposition .....	109
5.2.2	Post Deposition Heat Treatment.....	111
5.2.3	Characterization.....	111
5.3	Results.....	111
5.3.1	Electrical Properties.....	111
5.3.2	Optical Properties .....	114
5.3.3	Structural Properties .....	116
5.3.4	Chemical Properties.....	119
5.4	Discussion.....	122
5.5	Conclusions.....	126
6	DISORDER AND POLARON CONDUCTIVITY.....	129
6.1	Introduction.....	129
6.2	Structural Disorder.....	130
6.3	Cation Charge Disorder .....	134
6.3.1	Introduction .....	134
6.3.2	Disorder and the Polaron Hopping Activation Energy Model .....	135
6.4	Resistivity Limit .....	141
6.5	Conclusions.....	145

7	CONCLUSIONS, FUTURE WORK, AND APPLICATIONS .....	146
7.1	Conclusions.....	146
7.1.1	Sputtered Nickel-Cobalt Oxide .....	147
7.1.2	The Role of Lithium .....	148
7.1.3	Rhodium Substitution for Cobalt.....	149
7.1.4	Heat Treatment .....	151
7.1.5	Disorder and Polaron Conductivity.....	152
7.2	Future Work.....	152
7.3	Applications.....	154
APPENDIX		
A	DEPOSITION DETAILS .....	155
A.1	Sputtering.....	155
A.1.1	Definition.....	155
A.1.2	Equipment.....	156
A.1.3	Configuration/Setup.....	157
A.1.4	Target Production .....	160
A.2	Solution Deposition .....	161
B	CHARACTERIZATION METHODS AND DETAILS .....	163
B.1	Electrical Characterization.....	163
B.2.1	Hall Effect.....	163
B.2.2	van der Pauw.....	164
B.2	Optical Characterization .....	164
B.3.1	FTIR.....	164
B.3.2	UVVIS.....	165
B.4	Structural Characterization .....	165
B.4.1	Profilometry .....	165
B.4.2	XRD .....	167
B.4.3	TEM / STEM .....	169
B.5	Chemical Characterization.....	169
B.5.1	SIMS .....	169
B.5.2	UPS .....	170
B.5.3	XPS.....	170
C	CALCULATIONS, EQUATIONS, AND EFFECTS .....	172
C.1	Unit Cell Specifics .....	172
C.2	Theoretical Film Density .....	173
C.3	Heike's Rule.....	174
C.4	Absorption Coefficient Calculation.....	174
C.5	Jahn-Teller Effect.....	175
C.6	Verway Transition.....	176

C.7 Nickel-Cobalt Oxide Activation Energy Curves .....	176
C.8 Lithium in Nickel-Cobalt Oxide Activation Energy Curves .....	178
C.9 Heat Treatment Quench Model.....	179
LIST OF REFERENCES.....	180
BIOGRAPHICAL SKETCH .....	191

## LIST OF TABLES

<u>Table</u>	<u>page</u>
2-1. Choice of available <i>n</i> -type transparent conductors.....	10
2-2. Figure-of-merit, absorption coefficient and sheet resistance comparison. ....	11
2-3. Approximate minimum resistivities and plasma wavelengths for some transparent conductors. ....	12
2-4. Electrical properties of CuAlO <sub>2</sub> , CuGaO <sub>2</sub> , SrCu <sub>2</sub> O <sub>2</sub> , and NiCo <sub>2</sub> O <sub>4</sub> thin films.....	13
2-5. Comparison of nickel-cobalt oxide to nickel oxide and cobalt oxide. ....	17
2-6. Observed properties of polarons compared with free carriers.....	31
2-7. Key characteristics of small polaron hopping for nickel-cobalt oxide.....	32
3-1. Film deposition parameter and sputtering setup matrix for Ni <sub>x</sub> Co <sub>3-x</sub> O <sub>4</sub> .....	44
3-2. Values of index of refraction for films and substrates are shown individually with calculated transmission losses due to interfaces alone assuming no absorption.....	57
3-3. Extrapolated band gap values lines in Figure 3-13.....	59
3-4. Increase in activation energies of Ni <sub>x</sub> Co <sub>3-x</sub> O <sub>4</sub> from the temperature regions in Figure 3-23 graphed in Figure 3-27.....	74
4-1. Numerical data from Figure 4-10 are listed in columns. ....	92
4-2. Lattice parameter of Ni <sub>0.75</sub> Co <sub>2.25-z</sub> Li <sub>z</sub> O <sub>4</sub> as a function of lithium fraction ( <i>z</i> ) before and after rapid cooling from a 10 minute 375°C heat treatment.....	94
5-1. Composition recipe of NiCo <sub>2-v</sub> Rh <sub>v</sub> O <sub>4</sub> used for solution deposited samples. ....	110
6-1. Spinel sites and occupation for polaron density calculation.....	142
6-2. Theoretical value of conductivity assuming a polaron density given by the number of hopping polarons in a unit cell with a constant mobility. ....	143
B-1. Powder diffraction file number 73-1702 used as the standard of comparison for nickel cobalt oxide thin films and powders.....	167

B-2. X-ray reflectivity (XRR) experimental system setup parameters.....	168
B-3. Grazing-incidence x-ray diffraction (GIXRD) experimental summary system setup parameters.. .....	168
C-1. Unit cell sites and weights for density calculation.....	172
C-2. Activation energies of $\text{Ni}_x\text{Co}_{3-x}\text{O}_4$ films from Figure C-4.....	177
C-3. Activation energies of $\text{NiCo}_{2-z}\text{Li}_z\text{O}_4$ films from solution deposition. ....	178
C-4. Activation energies of $\text{Ni}_{0.75}\text{Co}_{2.25-z}\text{Li}_z\text{O}_4$ films from solution deposition. ....	178

## LIST OF FIGURES

<u>Figure</u>	<u>page</u>
1-1. A basic light emitting thin film stack consists of <i>p-n</i> junction and transparent electrode. ....	1
1-2. A basic light detecting thin film stack device consists of a <i>p-n</i> junction and a transparent electrode. ....	2
2-1. A simple <i>p-n</i> junction diode and accompanying energy band structure illustrates the locations of charge carriers and direction of charge flow. ....	8
2-2. Basic optoelectronic devices. ....	9
2-3. Visible transmission spectra of nickel-cobalt oxide from solution deposited and sputtered samples. ....	18
2-4. FTIR transmission spectrum of solution deposited nickel-cobalt oxide thin film. ....	19
2-5. Seebeck data from nickel-cobalt oxide. ....	20
2-6. The oxygen 1s binding energy region from XPS shows a peak at 531.2 eV that scales with conductivity. ....	21
2-7. Comparison of TCO transparency regions with conductivity displayed as a function of transmission wavelength. ....	22
2-8. Effects of deposition techniques on the resistivity of nickel-cobalt oxide show that sputtered films of similar compositions to solution deposited films have lower resistivities. ....	23
2-9. A bound carrier in a two-dimensional lattice is the enlarged blue atom. ....	25
2-10. The <i>particle in a box</i> plot of a particle in a one dimensional lattice bound by an infinite energy barrier. ....	27
2-11. A polaron consists of the molecules involved and the local charge region. ....	29
2-12. green tetrahedral cations (A), yellow octahedral cations (B), and black oxygen anions (O) form the spinel unit cell with a chemical formula of AB <sub>2</sub> O <sub>4</sub> ....	33

2-13. A calculated diffraction pattern for NiCo <sub>2</sub> O <sub>4</sub> annotated with peak positions, planes, and relative intensities. ....	34
2-14. Spinel unit cell layers stack with interlocking tetrahedral sites.....	36
2-15. Tetrahedral site atom (green) bonded to four surrounding oxygen (black).....	37
2-16. The octahedral site atom (yellow) bonds with six surrounding oxygen (black) anions to form a six fold orientation. ....	37
3-1. Combinatorial sputtering uses a dual cathode setup with targets of different material composition. ....	43
3-2. Conductivity versus position for combinatorial runs are displayed as a function of oxygen and argon gas composition. ....	46
3-3. Position 7 from Figure 3-2 is the position with the highest conductivity.....	47
3-4. Fraction of Ni and Co detected by XPS as a function of position on a combinatorial sputtered Ni <sub>x</sub> Co <sub>3-x</sub> O <sub>4</sub> film.....	48
3-5. Combinatorial sputtered Ni <sub>x</sub> Co <sub>3-x</sub> O <sub>4</sub> film combining conductivity and position with composition with position data .....	49
3-6. A combinatorial substrate thickness profile measured by a stylus profilometer shows that the film thickness is also graded from cobalt rich on the left to nickel rich on the right .....	49
3-7. The effect of sputtering gas pressure on NiCo alloy sputtered Ni <sub>1.5</sub> Co <sub>1.5</sub> O <sub>4</sub> thin film resistivity before and after 10 minutes at 375°C heat treatment. ....	50
3-8. Target-substrate distance affects the resistivity of sputtered nickel-cobalt oxide thin films from a NiCo alloy target. ....	51
3-9. Conductivity of Ni <sub>x</sub> Co <sub>3-x</sub> O <sub>4</sub> films on PET substrate is always less than films on other substrates by a factor of 2-4x for as-deposited samples for all pressures and compositions shown. ....	52
3-10. UPS work function measurement of NiCo <sub>2</sub> O <sub>4</sub> and Ni <sub>1.5</sub> Co <sub>1.5</sub> O <sub>4</sub> films. ....	53
3-11. FTIR traces from of reactively sputtered Ni <sub>x</sub> Co <sub>3-x</sub> O <sub>4</sub> thin films. ....	55
3-12. Optical transmission through a thin film. ....	56
3-13. Target-substrate distance effects are opposite for the optical absorption coefficient and resistivity from sputtered nickel-cobalt oxide thin films from a NiCo alloy target.....	58
3-14. Tauc's plot of Ni <sub>x</sub> Co <sub>1-x</sub> O <sub>4</sub> films show a band gap between 3 and 3.75 eV. ....	59

3-15. Increasing target to substrate sputtering distance decreases film density. ....	60
3-16. An oxygen plasma shows a confined plasma region (white plume) near the target and a more dispersed plasma region (yellow-green) at longer distances. ....	60
3-17. The three zone model described by Campbell for film growth in a vacuum. ....	61
3-18. A spinel unit cell at different angles of rotation containing octahedral atoms, minimized tetrahedral atoms, and select oxygen atoms for points of reference such as the enlarged black oxygen atom. ....	62
3-19. Grazing incident x-ray diffraction from sputtered films 50 nm thick appear to be structured as spinel-type, but do not match exactly. ....	64
3-20. Sims profile of nickel-cobalt oxide thin film shows surface composition appears to differ from the bulk composition. ....	65
3-21. Cross-sectional TEM image of sputtered nickel cobalt oxide films on (100) silicon. Nickel-cobalt oxide thin film grows in multi-grained columns. ....	66
3-22. Nickel-cobalt oxide-silicon wafer interface. ....	67
3-23. An Arrhenius plot of conductivity and the reciprocal of temperature (K) shows that at high temperatures, the film conductivity is high. ....	69
3-24. TEM image and diffraction patterns at 300 K and 600 K showing no detectable structural changes for the two temperatures. ....	70
3-25. Effects of heat treatment cooling rate after heat treatment on optical properties of $\text{Ni}_x\text{Co}_{3-x}\text{O}_4$ samples from Figure 3-23. ....	72
3-26. Resistivity of $\text{Ni}_x\text{Co}_{3-x}\text{O}_4$ . ....	73
3-27. Rapidly quenched sample activation energies of $\text{Ni}_x\text{Co}_{3-x}\text{O}_4$ change after heating when they are slowly cooled. ....	74
4-1. Thin films with added of lithium deposited from solution precursors or sputtering. ....	82
4-2. Conductivity changes based on the cooling rate following heat treatment for all compositions of lithium in nickel-cobalt oxide films. ....	83
4-3. Conductivity as a function of temperature for 50 nm thick solution deposited thin films. ....	84
4-4. Rate of sample cooling after heat treatment had a dramatic effect on conductivity. ....	85
4-5. Activation energy dependence for $\text{Ni}_{0.75}\text{Co}_{2.25-z}\text{Li}_z\text{O}_4$ and $\text{NiCo}_{2-z}\text{Li}_z\text{O}_4$ from solution on lithium content. ....	86

4-6. FTIR mid IR transmission spectra of alloy-target reactive sputter-deposited $\text{Ni}_{0.95}\text{Co}_{1.95}\text{Li}_{0.15}\text{O}_4$ .	87
4-7. FTIR mid IR transmission spectra of oxide-target sputter-deposited $\text{Ni}_{1.2}\text{Co}_{1.2}\text{Li}_{0.6}\text{O}_4$ .	88
4-8. Normalized FTIR spectra at 1200 $\text{cm}^{-1}$ show the absorption region near 1400 $\text{cm}^{-1}$ assigned to carbonate on the surface when compared with a carbonate reference spectrum shown in grey.	90
4-9. Grazing incidence XRD from combinatorial sputter deposited films deposited from oxide targets. Note the weak crystalline diffraction peaks from the film.	91
4-10. Films sputter deposited from an alloy target have a smaller lattice expansion than films deposited from oxide targets.	92
4-11. XRD of sputtered films with incremental amounts of lithium (not normalized for intensity).	93
4-12. XRD spectra show no obvious changes for fast versus slow cooling for $\text{Ni}_{0.75}\text{Co}_{2.25-z}\text{Li}_z\text{O}_4$ . Fitting the curves reveals changes shown in Table 4-4.	94
4-13. XPS of the Carbon 1s region from the combinatorial sputtered film (a) at positions identified by the color code, and (b) curve fit to show composition of position 9.	95
4-14. XPS of combinatorial deposited nickel-cobalt oxide film with variable lithium concentration.	96
4-15. SIMS depth profile of a thin film sputtered from a $\text{Ni}_{1.5}\text{Co}_{1.5}\text{Li}_{0.6}\text{O}_4$ target.	97
4-16. XPS of (a) Ni 2p, (b) Co 2p, (c) O 1s, and (d) C 1s binding energy regions from solution deposited films of nickel-cobalt oxide containing lithium following slow and fast cooling after heat treatment.	98
5-1. First principles d-band density of states calculation of rhodium substituted for cobalt. Energy of 0 eV is the Fermi energy.	108
5-2. Effect of rhodium fraction (h) on conductivity for four-layer films on silicon substrates deposited from solution.	112
5-3. Sputtered nickel-rhodium oxide and nickel-cobalt oxide films deposited at 7.5 cm in 10 mTorr of 100% oxygen.	113
5-4. Resistivity of $\text{NiRh}_4\text{O}_x$ as a function of target-substrate distance. Increased distance increases resistivity	113
5-5. Solution deposited $\text{NiCo}_{2-h}\text{Rh}_h\text{O}_4$ FTIR transmission spectra were all corrected for the silicon substrate absorption peaks.	114

5-6. Resistivity and optical absorption coefficient at 3 $\mu\text{m}$ as a function of sputtering target-substrate deposition distance. ....	115
5-7. $\text{NiRh}_2\text{O}_x$ FTIR data referenced to air (lower trace) and corrected for the silicon substrate (upper trace). ....	115
5-8. FTIR spectra of two $\text{NiRh}_4\text{O}_x$ samples of different thicknesses deposited from $\text{NiRh}_4$ alloy target by DC sputtering. ....	116
5-9. FTIR of solution deposited $\text{NiCo}_{2-h}\text{Rh}_h\text{O}_4$ and sputtered $\text{NiRh}_5\text{O}_4$ thin films corrected for silicon substrate absorption. ....	117
5-10. Far IR spectra of solution deposited $\text{NiCo}_{2-h}\text{Rh}_h\text{O}_4$ from FTIR show the structure of the films. ....	118
5-11. XRD of $\text{NiRh}_4\text{O}_x$ film from DC alloy sputter deposition. ....	118
5-12. XRD of amorphous $\text{NiRh}_2\text{O}_x$ thin film from DC alloy sputter deposition. ....	119
5-13. XPS depth profile showing the surface of sputter deposited $\text{NiRh}_2\text{O}_x$ is different than the bulk concentration. ....	120
5-14. XPS depth profile of a film sputtered from a $\text{NiRh}_4$ target shows an oxygen depleted surface. ....	121
5-15. Multiplex binding energy data from XPS depth profiles. ....	122
6-1. Schematic of disorder. ....	130
6-2. The effect of composition on temperature dependant conductivity and activation energy. ....	131
6-3. $\text{NaPO}_3$ glass phase (amorphous) with a broad band covering the bond vibrational modes. ....	132
6-4. A double well potential with the associated energies that influence carrier motion between the wells. ....	135
6-5. Schematic illustration of one (a) and two-dimensional (b) spin models for polarons defined by adjacent site interactions. ....	138
6-6. Illustration of dipole-dipole interactions between adjacent sites for polaronic spin model variables in Equation 6.2. ....	139
6-7. Energy distribution function for one-dimensional polaron disorder model. ....	140
6-8. Energy distribution function for two-dimensional polaron disorder model. ....	140

A-1. A sputtering target (red) mounted on a cathode (silver) with impinging gas ions (purple) and target particles being removed (red).	155
A-2. Vacuum chambers used for sputtering deposition.	156
A-3. Three-inch sputter cathode used to deposit thin films.	157
A-4. Combinatorial sputtering setup inside of chamber with mounted substrates prior to pump-down for sputtering.	158
A-5. Single rotation setup.	159
A-6. Offset rotation setup.	159
A-7. Double planetary rotation setup.	160
A-8. Pressed target produced from nitrate solutions used for sputtering.	161
A-9. The solution deposition method involves dropping a precursor solution on a spinning substrate prior to baking to form a film.	161
B-1. Hall effect apparatus made by MMR technologies.	163
B-2. A van der Pauw resistivity probe setup and measurement schematic.	164
B-3. Nexus 570 FTIR with 3 detectors was used for high sensitivity mid IR (4000 cm <sup>-1</sup> to 650 cm <sup>-1</sup> , mid IR (4000 cm <sup>-1</sup> to 400 cm <sup>-1</sup> ), and far IR (500 cm <sup>-1</sup> to 100 cm <sup>-1</sup> ) measurements.	164
B-4. Varian CAREY 5 dual beam ultra violet-visible spectrophotometer.	165
B-5. Stylus profilometer used to measure step height of the deposited film.	166
B-6. Optical profilometer software screen capture. Instrument made by Zygo.	166
C-1. Hexagonally packed cylinders in 3-D on film and top view.	173
C-2. Cubic packed cylinders top view and in 3-D as would be seen in the film.	173
C-3. Degenerate energy level orbitals in the normal spinel state and schematic of orbital energy shift due to the Jahn-Teller effect.	176
C-4. Activation energies are the slope taken from the curve fits to the heating traces.	177
C-5. Measured conductivity as a function of temperature for NiCo <sub>2-z</sub> Li <sub>z</sub> O <sub>4</sub> films from solution.	178
C-6. Conductivity is temperature dependent for Ni <sub>0.75</sub> Co <sub>2.25-z</sub> Li <sub>z</sub> O <sub>4</sub> from solution.	179

Abstract of Dissertation Presented to the Graduate School  
of the University of Florida in Partial Fulfillment of the  
Requirements for the Degree of Doctor of Philosophy

POLARONS AND IMPURITIES IN NICKEL COBALT OXIDE

By

ROBERT REED OWINGS

DECEMBER, 2003

Chair: Paul Holloway

Major Department: Materials Science and Engineering

The optical transparency from 0.3 to  $>10\ \mu\text{m}$  and the electrical conductivity of  $\text{Ni}_x\text{Co}_{3-x-y}\text{Li}_y\text{O}_4$  and  $\text{Ni}_x\text{Co}_{3-x-y}\text{Rh}_y\text{O}_4$  films deposited by either planar magnetron sputter deposition or from nitrate solution were investigated. The films had low optical transparencies ( $\sim 15\%$ ) over the visible region ( $\sim 300\text{-}800\text{nm}$ ), but the transparency increased ( $\sim 50\text{-}80\%$ ) at infrared wavelengths from 2 to  $25\ \mu\text{m}$ . The DC electrical conductivity ranged from 10 to  $500\ \text{Scm}^{-1}$ . These unique properties result in conduction by *p*-type polarons. Despite low mobility of polarons ( $\sim 0.1\ \text{cm}^2\text{V}^{-1}\text{s}^{-1}$ ), good conductivity results from high concentrations of small polarons ( $\sim 10^{22}\ \text{cm}^{-3}$ ). For sputtered films, the conductivity was larger with a 50%  $\text{O}_2$ -50% Ar composition, at lower sputter gas pressures (2 versus 10 mTorr), and with smaller target-substrate distances (best at 5 cm). The effects of composition are due to the resulting cation oxidation states, while the effects of pressure and substrate distance were attributed to more energetic sputtered particles causing increased mobility of surface adatoms on the depositing films.

Increased adatom mobility led to smooth films which were 20% more dense, and crystalline with a spinel structure. Li additions to sputter and solution deposited films of  $\text{Ni}_x\text{Co}_{3-x-y}\text{Li}_y\text{O}_4$  were found to decrease and increase the electrical conductivity by less than a factor of two. The decreased electrical conductivity for sputter deposited  $\text{Ni}_x\text{Co}_{3-x-y}\text{Li}_y\text{O}_4$  films resulted from Li occupying interstitial sites, rather than substitutional sites in the lattice. Surface segregation and  $\text{Li}_2\text{CO}_3$  formation were found. Quenching ( $\sim 150^\circ\text{C}/\text{min}$ ) produced higher conductivities (2x), while slow cooling ( $10^\circ\text{C}/\text{min}$ ) resulted in lower conductivities after heat treatment at  $375^\circ\text{C}$  for 10 minutes in air. This was attributed to a larger concentration of polarons upon quenching. Solution and sputter deposition of  $\text{Ni}_x\text{Co}_{3-x-y}\text{Rh}_y\text{O}_4$  films were crystalline (spinel) and amorphous, respectively, and remained so with heat treatments up to  $375^\circ\text{C}$ . Electrical conductivities were  $\sim 350 \text{ Scm}^{-1}$ . Transparency from 2 to  $10 \mu\text{m}$  was  $\sim 10\%$  higher than for nickel-cobalt oxide films. A model was developed for the relationship between cation disorder and polaron formation affecting the activation energy of electrical conductivity. Also, the physical limit of polaron concentration was used to project a maximum conductivity between  $360$  and  $2400 \text{ Scm}^{-1}$ .

## CHAPTER 1 INTRODUCTION

### 1.1 Introduction

Materials possessing optical transparency *and* electrical conductivity make up a small class of specialized materials. Transparent conducting oxide (TCO) materials are basically doped\* semiconductors categorized most often by their carrier type (*n*-type or *p*-type) or by the mechanism of charge transport (free carrier or bound). Each classification of carrier type or conduction mechanism exhibits complementary optical and electrical properties.

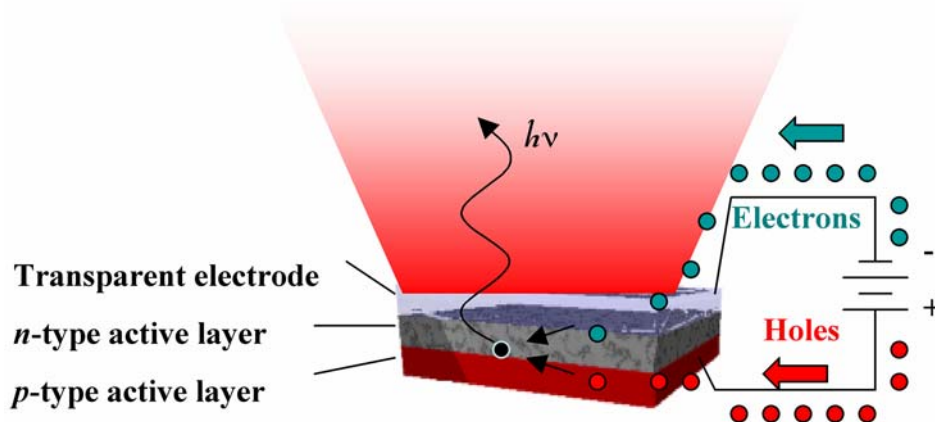


Figure 1-1. A basic light emitting thin film stack consists of *p-n* junction and transparent electrode. Injected electrons and holes combine at the *p-n* junction interface and relax to emit a photon. Note that the diagram is merely for illustrative purposes and actual thickness of films may not be proportional in scale.

Modern optoelectronics are made possible by transparent conducting oxide (TCO) electrodes. Simple devices that use TCOs are made of nanometer-thick material layers

---

\* Doping is adding trace amounts of impurities to a material.

stacked in various geometries to function as a light emitter or detector (see Figure 1-1 and Figure 1-2).

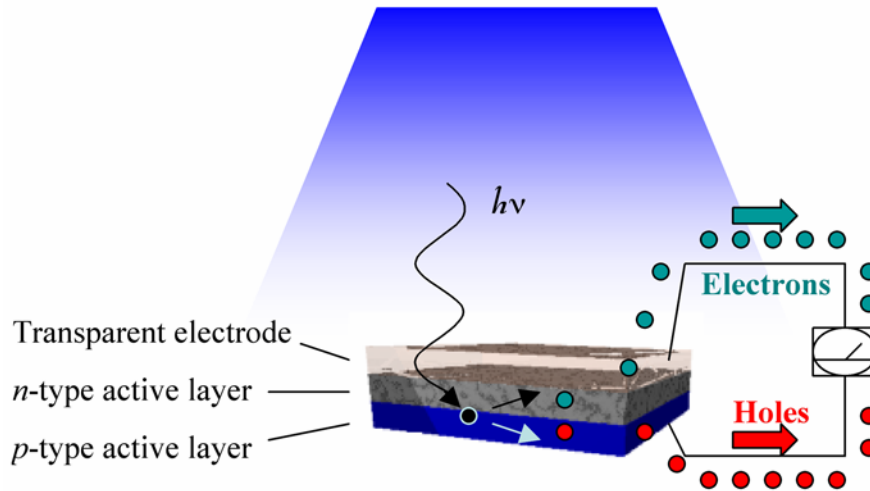


Figure 1-2. A basic light detecting thin film stack device consists of a  $p$ - $n$  junction and a transparent electrode. Impinging photons promote electrons in the valence band into the conduction band and out of the device to an ammeter or external circuit device. Note that the diagram is merely for illustrative purposes and actual thickness of films may not be proportional in scale.

A very common implementation of both devices is the remote control. The hand held unit contains the infrared emitting diode and the electronic unit to be controlled contains either a silicon diode or a photoconductor to detect the remote control's optical signal and interpret it to produce the desired result, such as changing the channel.

Novel light emitting diodes (LEDs) such as organic light emitting devices (OLEDs), polymer light emitting devices (PLEDs), and longer wavelength infrared emitting diodes (IREDs) are examples of emitting devices that require an electrode that will transmit light and conduct electricity. This demand will increase for improved solid-state lighting or flexible devices made on plastic (Bergh et al., 2001; Forrest et al., 2000). TCOs are of interest for improving optical device performance and efficiency (for items such as a solar cells and LEDs). A thorough understanding of the basic fundamentals of

how an electronic charge carrier moves in this class of materials will provide avenues for future exploitation in device development.

Electrical conduction in a solid occurs when a charged particle (referred to as a charge carrier) such as an electron moves under the influence of an applied electric field. Highly conductive materials are most often metals with large populations ( $\sim 10^{28} \text{ cm}^{-3}$ ) of unbound or free electrons residing in the conduction band. Electron conductors are *n*-type materials, while the *p*-type materials conduct by the movement of electron vacancies or *holes*. Conductivity of both types of TCOs can be controlled by doping levels to allow insulating, semiconducting, or metallic behavior (Kawazoe et al., 2000). Charge transport (electrical conduction) mechanisms in TCOs are similar to metallic free-carrier conduction or bound carrier hopping.

Oxides are transparent in the visible region when the band gap exceeds 3.1 eV (Kawazoe et al., 1997; Lewis & Paine, 2000). Most often these oxides are insulators rather than conductors due to relatively few carriers contributing to conductivity. Researchers have enhanced transparent oxides by introducing donor states just below the conduction band to produce more carriers in the band and result in conductivity increases. One trick to adding donor states requires slightly reducing the film (such as annealing in a hydrogen atmosphere) to create oxygen defect sites that act as donors (Lewis & Paine, 2000). Attempts to make transparent oxides conducting have yielded higher carrier concentrations but have also affected transmission properties. One problem with free carriers is a limited transmission region. While transparent in the optical spectrum, the onset of absorption by free carriers at the plasma frequency abruptly halts transmission. Still, other researchers have attempted to push this absorption region further out into the

IR by shifting the region of free carrier absorption to a longer wavelength. Conducting a hole instead of an electron shifts the absorption region to a longer wavelength because the hole has a larger effective mass than the electron. This *p*-type system is however in the free carrier regime and still subject to free carrier absorption, only at a longer wavelength. Larger masses also move slower than smaller masses, so conductivity of the *p*-type material is reduced. A material system conducting by a bound carrier would escape this absorption peril caused by free carriers.

A polaron is a localized carrier with an accompanying lattice strain. A polaron conducting material inherently has a low mobility as well as the absence of a plasma frequency cutoff in the infrared region. Despite a low rate of polaron hopping at room temperature, a high polaron concentration will promote a high conductivity. Recent studies have focused on increasing the density of polarons in such materials to obtain a net increase in conductivity. Polaron density can be increased by a number of ways. Disordered cation arrangement, increased oxidation state due to selective doping, or structural disorder introduced by cation size mismatch in the lattice are all ways of increasing the number of polarons in a given volume of material.

Nickel-cobalt oxide is a recently studied polaron conducting material that shows promise as an infrared-transparent conducting oxide (ITCO). NO other ITCO has been studied or reported to date. This work discusses the polaron conducting nickel-cobalt oxide system, its IR optical and electrical properties and how they are affected by key deposition parameters and the addition of impurities.

## **1.2 Organization of the Dissertation.**

Chapter 2 discusses common TCOs and details the current knowledge of their properties. Base properties of the nickel-cobalt oxide system will include the polaron

conduction mechanism and its spinel structure as reported in the literature. Chapter 3 describes efforts to enhance the nickel-cobalt oxide properties for use as an ITCO by altering the thin film deposition parameters. Chapters 4 and 5 report the effects of doping the nickel-cobalt system with lithium and rhodium, respectively. Chapter 6 discusses the conduction mechanism in the nickel-cobalt oxide system and outlines a model for understanding the effects of disorder on conductivity to explain the experimental results. A projected maximum range for conductivity is estimated as well. Conclusions from this research and recommendations for future work and applications comprise Chapter 7.

## CHAPTER 2 BACKGROUND OF NICKEL COBALT OXIDE

This chapter provides the necessary background information to understand the significance of the infrared transparent nickel-cobalt oxide system and how its properties are unique among transparent conducting oxides.

An explanation of two basic  $p$ - $n$  junction diodes is given below to illustrate the difference between  $p$ -type and  $n$ -type materials and shows how a transparent conducting layer functions as part of a light emitting or detecting device. Limitations of each type of TCO include a particular transmission window and conductivity, both of which depend on the conduction mechanism and carrier type.  $n$ -type TCOs are widely used and well developed. The  $p$ -type TCOs are limited primarily by poor conductivity and are less developed. Research has taken two different approaches to improve the conductivity of  $p$ -type TCOs. Explanations of conduction mechanisms such as free carrier movement and polaron hopping provide the background knowledge for this discussion. Nickel-cobalt oxide is the  $p$ -type material system of interest to function as an infrared transparent conducting oxide (ITCO) because of its infrared transparency, stability in oxygen, ease of preparation, phase purity, and high conductivity. Nickel-cobalt oxide exhibits these characteristics due in part to the carrier type, the conduction mechanism, and the crystal structure.

### **2.1 Background of Transparent Oxide Conductors**

Transparent conducting oxides are basically doped metal-oxide semiconductors classified as either  $n$ -type or  $p$ -type. Majority electron conductors are  $n$ -type materials,

while the  $p$ -type materials conduct by the movement of electron vacancies called *holes*. Conductivity of both types is controlled by doping to allow insulative, semiconducting, or metallic behavior (Hummel, 2001; Kawazoe et al., 2000). Currently,  $n$ -type TCOs dominate with respect to commercial use and have wide spread application because they exhibit superior conductivity and minimal photon absorption over the visible range as compared with  $p$ -type materials. However,  $p$ -type oxides exhibit some unique properties such as a majority hole carrier concentration resulting in increased infrared transparency not possessed by  $n$ -type oxides. This  $p$ -type conductivity and infrared transparency make them of interest for future development (Kawazoe et al., 2000; Kawazoe et al., 1997; Ohya et al., 1998; Windisch et al., 2001a; Windisch et al., 2001b; Windisch et al., 2002b)

### **2.1.1 The Basic $p$ - $n$ Junction Diode**

A fundamental optoelectronic device illustrates the differences between  $n$ -type and  $p$ -type materials that make up a  $p$ - $n$  junction. A diode (or rectifier) is a device that allows current to pass in one direction, but not in the reverse direction. The most basic diode consists of a  $p$ -type region next to an  $n$ -type region referred to as a  $p$ - $n$  junction. Junctions can be homojunctions, made of the same material (e.g., silicon doped with boron for  $p$ -type behavior or with phosphorus for  $n$ -type behavior (Hummel, 2001)), or heterojunctions, made from two different materials. In either case, the behavior of the diode results from the interface between the two different types of materials. A depletion region forms at the interface with an accompanying electric field (Figure 2-1), which effectively removes generated carriers or allows carrier recombination (also referred to as the *space charge region* or the *depletion layer* (Hummel, 2001)).

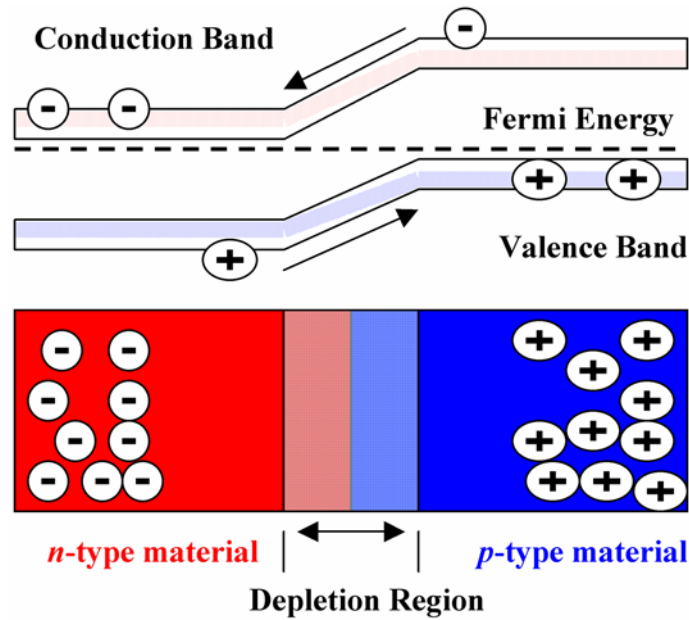


Figure 2-1. A simple  $p$ - $n$  junction diode and accompanying energy band structure illustrates the locations of charge carriers and direction of charge flow. The  $n$ -type material has electrons in the conduction band while the  $p$ -type material has holes in the valence band. When a bias is applied to the junction, the bands shift and electrons (or holes) move from left to right (or opposite) and through the rest of the circuit.

Light emission occurs as an electron and hole recombine when injected into the depletion region. The energy of the photon emitted is the difference between the energy of the electron in the conduction band and the hole in the valence band (band gap energy). Photo current is generated as photons impinge on the depletion region and excite electrons to the conduction band (over the energy gap) leaving behind holes in the valence band. Carriers are conducted away from the depletion region similar to the photo diode current diagram in Figure 2-2. Different carrier types are imperative to  $p$ - $n$  junction device behavior. Without the two different types, neither light emission nor photo-generation of carriers would occur. Figure 2-2 shows simple  $p$ - $n$  junction diodes, one as a light emitter and the other as a light detector.

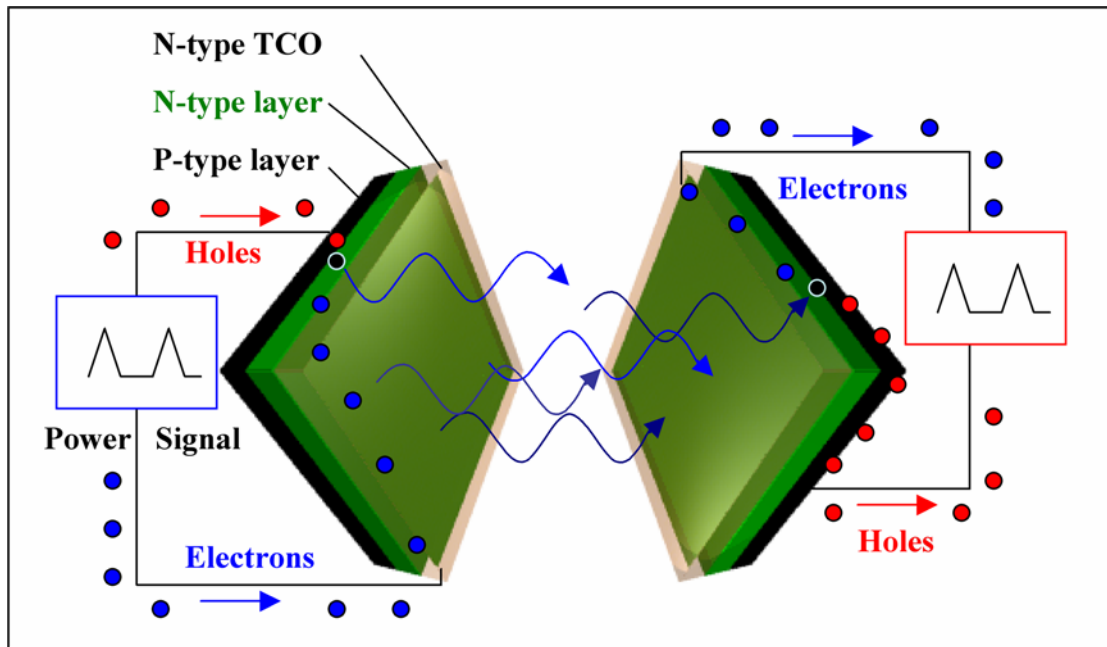


Figure 2-2. Basic optoelectronic devices. The light emitting diode (LED, on the left) incorporates *n*-type and *p*-type materials to essentially “convert” electrical current to light by combining electrons and holes and produce a photon. The photo diode (solar cell -on the right) uses light (photons from the LED) to produce electrical current by generating electron-hole pairs. Materials in these devices conduct a majority of holes or electrons and are classified as *p*-type or *n*-type respectively. TCOs are used in these devices to allow current and light to pass through to the *p-n* junction.

Key to the operation of a diode is the ability to get current in or out of the device.

Transparent conducting oxides serve a unique function in optoelectronic *p-n* junction stacks because of their conductivity and transparency. TCOs allow current to pass through to the device depletion region without significantly blocking the light that is being emitted or detected.

### 2.1.2 N-Type Transparent Conducting Oxides

Prevalent TCOs typically possess extrinsic *n*-type conduction (Chopra et al., 1983) and are more researched due to their superior conductivities. Increased research has sped development and applications of common *n*-type TCO systems such as (1) the zinc oxide system (e.g., zinc oxide doped with fluorine, boron, gallium, indium, or aluminum), (2)

cadmium stannate ( $\text{Cd}_2\text{SnO}_4$ ), (3) the tin oxide system (e.g., tin oxide and tin oxide doped with antimony [ $\text{SnO}_2:\text{Sb}$  referred to as ATO]), and (4) indium oxide doped with tin ( $\text{In}_2\text{O}_3:\text{Sn}$  referred to as indium tin oxide or ITO) (Gordon, 2000). No single TCO is suited for all applications. Table 2-1 shows that if high conductivity is important, then ITO is the best material, however if highest transparency is most important, cadmium stannate or zinc oxide may be more appropriate.

Table 2-1. Choice of available *n*-type transparent conductors.

Property	Material
Highest transparency	$\text{ZnO:F}$ , $\text{Cd}_2\text{SnO}_4$
Highest conductivity	$\text{In}_2\text{O}_3:\text{Sn}$
Lowest plasma frequency	$\text{SnO}_2:\text{F}$ , $\text{ZnO:F}$
Highest plasma frequency	$\text{In}_2\text{O}_3:\text{Sn}$
Highest work function, best contact to p-Si	$\text{SnO}_2:\text{Sb}$ , $\text{ZnSnO}_3$
Lowest work function, best contact to n-Si	$\text{ZnO:F}$
Best thermal stability	$\text{SnO}_2:\text{F}$ , $\text{Cd}_2\text{SnO}_4$
Best mechanical durability	$\text{SnO}_2:\text{F}$
Best chemical durability	$\text{SnO}_2:\text{F}$
Easiest to etch	$\text{ZnO:F}$
Best resistance to hydrogen Plasmas	$\text{ZnO:F}$
Lowest deposition temperature	$\text{SnO}_2:\text{F}$ , $\text{ZnO:B}$
Least toxic	$\text{ZnO:F}$ , $\text{SnO}_2:\text{F}$
Lowest cost	$\text{SnO}_2:\text{F}$

Reproduced from Gordon, R.G. (2000). Criteria for choosing transparent conductors. *MRS Bulletin*, 25(8), 52-57, (Table 8, p.55) by permission of *MRS Bulletin*.

Currently the most common transparent conducting material used in electronics is indium tin oxide (ITO). It transmits up to ninety percent of visible light with a resistivity near  $1 \times (10)^{-4} \Omega\text{cm}$ . High transparency, high conductivity, and chemical stability contribute to the wide use of ITO. An oxide conductor like indium tin oxide has a carrier density on the order of  $1 \times 10^{20} \text{cm}^{-3}$  to  $1 \times 10^{21} \text{cm}^{-3}$  (Minami, 2000; Minami et al., 1995; Minami et al., 2000) and a mobility typically greater than  $10 \text{cm}^2\text{V}^{-1}\text{s}^{-1}$  (Minami, 2000). Other material systems are better suited for specific applications, because each system has specific strengths and weaknesses.

Table 2-2. Figure-of-merit, absorption coefficient and sheet resistance comparison.

Material	Sheet Resistance $R_s$ ( $\Omega$ /square)	Visible Absorption Coefficient $\alpha$	Figure of Merit <sup>a</sup> $\sigma/\alpha$
ZnO:F	5	0.03	7
Cd <sub>2</sub> SnO <sub>4</sub>	7.2	0.02	7
ZnO:Al	3.8	0.05	5
In <sub>2</sub> O <sub>3</sub> :Sn	6	0.04	4
SnO <sub>2</sub> :F	8	0.04	3
ZnO:Ga	3	0.12	3
ZnO:B	8	0.06	2
SnO <sub>2</sub> :Sb	20	0.12	0.4
ZnO:In	20	0.20	0.2

Reproduced from Gordon, R.G. (2000). Criteria for choosing transparent conductors.

*MRS Bulletin*, 25(8), 52-57, (Table 2, p.53) by permission of *MRS Bulletin*.

<sup>a</sup> Figure-of-merit ( $\sigma/\alpha$ ), the calculated ratio of a material's electrical conductivity ( $\sigma$ ) to its total optical absorption coefficient ( $\alpha$ ) is one method of comparing different TCOs.  $\sigma/\alpha = -\{R_s \ln(T+R)\}^{-1}$ .  $R_s$  is the sheet resistance, T is the total visible transmittance, R is the total visible reflectance, all of which are required to calculate the figure of merit (Chopra et al., 1983). Larger figure of merit values indicate higher performing materials.  $R_s = \rho(t)/t = 1/(\sigma(t) t)$ . Resistivity, a function of thickness, when divided by film thickness is equal to sheet resistance. Conductivity is the reciprocal of resistivity (Chopra et al., 1983).

One method of comparing different TCOs on the same criteria is to devise a *figure-of-merit* number as found in Table 2-2. Sheet resistance divided by the total optical absorption coefficient gives a number to compare both electrical and optical properties simultaneously. Zinc oxide doped with fluorine and cadmium stannate have the highest figure-of-merit at 7, but due to lower conductivity and higher cost, they are not utilized as much as ITO or tin oxide. It is important to note that the figure of merit is an extremely sensitive to the wavelength of the light being transmitted.

ITO is limited in that it is essentially a *free* electron conductor. Nearly-free electrons absorb photons with energies typically less than 1.1 eV corresponding roughly to photon wavelengths longer than 1  $\mu$ m. This onset of absorption by free electrons is called the plasma frequency (Hummel, 2001). Typical values are included in Table 2-3.

While this absorption is what makes tin oxide extremely valuable to the structural

building community when used as an insulating thin film on windows, it limits the use of ITO as a transparent electrode at longer wavelengths.

Table 2-3. Approximate minimum resistivities and plasma wavelengths for some transparent conductors.

Material	Resistivity $\rho$ (m $\Omega$ cm)	Plasma $\lambda$ ( $\mu$ m)
In <sub>2</sub> O <sub>3</sub> :Sn	0.100	>1.0
Cd <sub>2</sub> SnO <sub>4</sub>	0.130	>1.3
ZnO:Al	0.150	>1.3
SnO <sub>2</sub> :F	0.200	>1.6
ZnO:F	0.400	>2.0

Reproduced from, Gordon, R.G. (2000). Criteria for choosing transparent conductors. *MRS Bulletin*, 25(8), (Table 3, p.54) by permission of *MRS Bulletin*.

Many studies have been conducted on the *n*-type oxides to develop applications, however transparent *p*-type materials are not well developed despite the need for them (Giesbers et al., 1997; He et al., 1999; Park et al., 2002).

### 2.1.3 *P*-Type Transparent Conducting Oxides

Investigations into *p*-type TCOs include two major systems (1) the nickel oxide systems, nickel oxide (Giesbers et al., 1997; Sato et al., 1993) with additions of cobalt oxide (He et al., 1999; Windisch et al., 2001a; Windisch et al., 2001b), and (2) the copper oxide systems, strontium copper oxide (Kawazoe et al., 2000), copper scandium oxide (Duan et al., 2000), copper gallium oxide (Ueda et al., 2001), lanthanum copper oxide (Ueda et al., 2000), and copper aluminum oxide (Kawazoe et al., 1997). Research conducted on *p*-type TCO material systems has yielded a few *p-n* devices, but beyond prototypes, they have not been further developed (Giesbers et al., 1997; Ohya et al., 1998).

Infrared spectra of all the listed *p*-type materials have a plasma cutoff deeper in the IR than the *n*-type TCOs except the nickel systems that do not have a published plasma

cutoff. Conducting via holes, they may be used as a *p*-type electrode next to the *p*-type layer of a *p-n* junction diode or as the *p*-type layer in the junction.

Table 2-4. Electrical properties of CuAlO<sub>2</sub>, CuGaO<sub>2</sub>, SrCu<sub>2</sub>O<sub>2</sub>, and NiCo<sub>2</sub>O<sub>4</sub> thin films.

	CuAlO <sub>2</sub> <sup>a</sup>	CuGaO <sub>2</sub> <sup>a</sup>	SrCu <sub>2</sub> O <sub>2</sub> <sup>a</sup>	NiCo <sub>2</sub> O <sub>4</sub> <sup>b</sup>
Electrical conductivity (S cm <sup>-1</sup> )	9.5x10 <sup>-1</sup>	6.3x10 <sup>-2</sup>	4.83x10 <sup>-2</sup>	333
Carrier density (cm <sup>-3</sup> )	1.3x10 <sup>17</sup>	1.7x10 <sup>18</sup>	6.1x10 <sup>17</sup>	~1x10 <sup>21</sup>
Hall mobility (cm <sup>2</sup> /V s)	10.4	0.23	0.46	< 0.1
Seebeck coefficients (μV K <sup>-1</sup> )	+183	+560	+260	~+20

<sup>a</sup>(Kawazoe et al., 2000)

<sup>b</sup>(Windisch et al., 2002b)

Limitations of *p*-type TCOs include low conductivity (near 0.1- 0.01 Scm<sup>-1</sup>) and 70%-90% transparency in the visible region. With conductivity about two orders of magnitude lower (at best) than a good *n*-type TCO such as ITO at 10000 Scm<sup>-1</sup>, *p*-type TCO electrical properties shown in Table 2-4 do not yet compare with *n*-type TCOs. Plasma absorption of free or quasi-free carriers limits transparency at longer wavelengths regardless of the conducting carrier type. Interest in *p*-type TCOs has recently renewed with new ideas on how to overcome these limitations (Kawazoe et al., 2000).

Conductivity, the major limitation for *p*-type TCOs, is a function of the number of carriers and the speed at which those carriers move through the material. Shown in equation 2.1, conductivity is a function of carrier density (*n*) multiplied by mobility (*μ*) and the charge of each carrier (*q*).

$$\sigma = \frac{1}{\rho} = n\mu q \quad (2.1)$$

Assuming this equation is suitable for all types of materials, two choices are available to increase conductivity because the charge of each carrier is constant. One choice is to increase mobility by controlling the valence band; the other option is to boost the carrier density.

**Chemical modulation of the valence band.** Kawazoe et al. suggest the limited conductivity of the *p*-type TCOs result from valence cations bonding with oxygen forming localized carriers. In contrast, high conductivity observed in *n*-type TCOs is often due to high free carrier densities even with carrier mobilities at a low  $10 \text{ cm}^2\text{V}^{-1}\text{s}^{-1}$ . Locally bound *p*-type carriers present a problem because they are less mobile than free carriers. The solution is referred to as chemical modulation of the valence band (CMVB) where cation selection in the lattice controls the valence band while maintaining quasi-free carrier movement. CMVB rids the valence band of positive holes that become deep acceptor levels by introducing covalency in the metal-oxygen bonding to form an extended valence-band structure. Transition metal oxides with unfilled  $d_{10}$  shells are not recommended for TCO applications because *d-d* transitions exhibit strong coloration in the visible. Copper oxide with select cations added was the example system (Kawazoe et al., 2000). The best conductivity reported in Table 2-4 is  $0.95 \text{ Scm}^{-1}$  for  $\text{CuAlO}_2$  indicating that this regime worked to some degree, but conductivity remains low. If mobility is at the maximum for the system, and  $e$  is constant at  $1.606 \times 10^{-19} \text{ C}$  (per electron), then the only other parameter to influence in the conductivity equation (Equation 2.1) is the number of carriers.

**Increase carrier density.** Another approach to improving conductivity is to leave the carriers localized and attempt to add more of them (Windisch et al., 2002b). Localized carriers do not exhibit the infrared absorption edge allowing transparency at longer wavelengths and are called polarons when accompanied by lattice strain. They have a very low mobility due to a hopping transport mechanism unlike free carriers. In addition, cations that have open *d* shell orbitals such as nickel and cobalt in nickel-cobalt

oxide reported by Windisch et al. have a conductivity of up to  $333.3 \text{ Scm}^{-1}$  and have exhibited transparency up to 60% at 600 nm and higher at higher wavelengths (Windisch et al., 2001a). The nickel-cobalt system is not as transparent in the visible region as the copper system, though very transparent in the infrared.

## 2.2 Nickel-Cobalt Oxide

Interest in nickel-cobalt oxide stemmed from early work on either nickel oxide or cobalt oxide. Nickel oxide studies explored electrical properties with interest in its superior transmission (near 80%) in the visible region. Attempts to exploit this in electrochromic window applications (Kitao et al., 1994), as *p*-type transparent conducting films (Sato et al., 1993), an antiferromagnetic material (Fujii et al., 1996), a functional sensor layer for chemical sensors (Kumagai et al., 1996), or as a photocathode for a solar cell (He et al., 1999), fueled interest in this system. Cubic nickel oxide has also been investigated with respect to electrical properties (Morin, 1953) and its conduction mechanism (Biju & Khadar, 2001; Parravano, 1954; Sanz et al., 1998; Snowden, 1965). Studies of nickel oxide showed experimental results, but as alluded to previously, poor conductivity of the *p*-type oxides has not encouraged interest in developing *p*-type TCOs in general for applications beyond lab experimentation.

Spinel cobalt oxide has also been studied previously as a result of its magnetic spin states (Belova et al., 1983), optical nonlinearity (Yamamoto et al., 2003), gas sensing capabilities, and solar energy reflecting properties (Cheng et al., 1998). Doping single crystals of cobalt oxide with nickel produced a significant increase in electrical conductivity (up to  $10^5$ x) while maintaining the spinel structure. Nickel cations were found to reside in octahedral sites with a valence of 2+ and 3+ (Roginskaya et al., 1997; Tareen et al., 1984) represented by the equation below.



Nickel doped cobalt oxide shows *p*-type semiconducting behavior similar to intrinsic spinel cobalt oxide (Tareen et al.). Investigators have worked to develop nickel-cobalt oxide for applications intended originally for nickel oxide or cobalt oxide (Monk & Ayub, 1997). Other interests in nickel-cobalt oxide include uses as electrodes in batteries (Liu et al., 1999; Polo Da Fonseca et al., 1999; Yoshimura et al., 1998), electrodes in solar cells (Park et al., 2002), electrodes in molten carbonate fuel cells (Kuk et al., 2001), or as a heterogeneous optical recording media, (Iida & Nishikawa, 1994). These intended uses of nickel-cobalt oxide are not paramount to this study but show other research interests in the material have been pursued in the past to develop specific applications such as using NiCo<sub>2</sub>O<sub>4</sub> as an electrocatalyst for anodic oxygen evolution (Carey et al., 1991; Haenen et al., 1986), in organic or inorganic electrosynthesis (Roginskaya et al., 1997), as a supercapacitor (Hu & Cheng, 2002), or as an infrared-transparent conducting electrode for flat panel displays, sensors, or optical limiters and switches (Goodwin-Johansson et al., 2000; Windisch et al., 2001a; Windisch et al., 2001b; Windisch et al., 2002b).

Studies of nickel-cobalt spinel have included bulk crystals (Haenen et al., 1986; Roginskaya et al., 1997; Tareen et al., 1984), powders, (Windisch, 2003) and thin films (Carey et al., 1991; Galtayries & Grimblot, 1999; Hu & Cheng, 2002; Kim et al., 2000; Marco et al., 2000; Monk & Ayub, 1997). Nickel-cobalt oxide studies have correlated the crystal structure and activity of NiCo<sub>2</sub>O<sub>4</sub> and related oxides (King & Tseung, 1974), explained the NiCo<sub>2</sub>O<sub>4</sub> spinel surface by Auger and XPS (Kim et al., 2000), and have expounded on the deposition parameters and substoichiometric structures (Carey et al., 1991). Work on the nickel-cobalt oxide system and stoichiometric deviations has

included infrared spectroscopy (Windisch et al., 2001b), laser Raman spectroscopy (Windisch et al., 2002a), Seebeck and conductivity measurements (Windisch et al., 2002b), and conductivity measurement variations correlated to film composition (Windisch et al., 2001b). Post deposition heat treatment and resulting increases in conductivity were correlated with oxygen binding energy changes (Windisch et al., 2001b; Windisch et al., 2002b; Windisch, 2003b).

Table 2-5. Comparison of nickel-cobalt oxide to nickel oxide and cobalt oxide.

	NiO	NiCo <sub>2</sub> O <sub>4</sub>	Co <sub>3</sub> O <sub>4</sub>
Breakdown temp. (°C)	1100+	400 <sup>a</sup>	895 <sup>a</sup>
Conductivity (S/cm)	2x10 <sup>-2,b</sup>	333 <sup>c</sup>	10 <sup>-6 d</sup> , 0.05 <sup>e</sup> , 0.07 <sup>f</sup>
Carrier type	<i>p</i> -type small polaron, <i>p</i> <sup>g</sup>	<i>p</i> -type small polaron <sup>h</sup>	<i>p</i> - hopping <sup>e,f,i</sup>
Carrier density (cm <sup>-3</sup> ) at room temp.	9.8x10 <sup>20 j</sup> , 10 <sup>20,k</sup> , 10 <sup>19 k</sup> 1.3x10 <sup>19 l b</sup>	5x10 <sup>21 m</sup>	2.4x10 <sup>19 e</sup>
Lattice constant (Å)	4.195 <sup>n</sup> , 4.176 <sup>o</sup>	8.114 <sup>p</sup>	8.084 <sup>q</sup> , 8.11 <sup>o</sup>
Structure	Cubic <sup>n</sup>	Spinel <sup>r</sup>	Spinel <sup>d,r</sup>
Seebeck coef.(μV/°C)	350-500 <sup>j</sup>	20 <sup>m</sup>	0 <sup>d</sup>
Band gap (eV)	4.0 <sup>s</sup> , 3.8 <sup>l</sup>	Not reported	1.5 <sup>t</sup> , 1.65 <sup>u</sup> , 2.2 <sup>v</sup> , 2.02 <sup>w</sup>

<sup>a</sup> (Haenen et al., 1986)

<sup>b</sup> (Morin, 1953)

<sup>c</sup> (Windisch et al., 2001a)

<sup>d</sup> (Tareen et al., 1984)

<sup>e</sup> (Patil et al., 1996)

<sup>f</sup> (Cheng et al., 1998)

<sup>g</sup> (Sato et al., 1993)

<sup>h</sup> (Windisch et al., 2002b)

<sup>i</sup> (Ohya et al., 1998)

<sup>j</sup> (Parravano, 1954)

<sup>k</sup> (Snowden, 1965)

<sup>l</sup> (Sato et al., 1993)

<sup>m</sup> (Windisch et al., 2002a)

<sup>n</sup> (Hotovy et al., 1998b)

<sup>o</sup> (Kennedy, 1996)

<sup>p</sup> Powder Diffraction File #73-1702 (see Appendix B for specifics)

<sup>q</sup> (Taylor & Kagle, 1963)

<sup>r</sup> (King & Tseung, 1974)

<sup>s</sup> (Lunkenheimer et al., 15)

<sup>t</sup> (Schumacher et al., 1990)

<sup>u</sup> (Varkey & Fort, 1993)

<sup>v</sup> (Pejova et al., 2001)

<sup>w</sup> (Yamamoto et al., 2003)

In Table 2-5 a comparison of nickel-cobalt oxide to nickel oxide and cobalt oxide outlines key differences in the base oxides and the mixed material. When mixed together, the breakdown temperature is 400°C (far below either binary oxide), while at the same time the carrier concentration increases by up to 10<sup>2</sup>x and the conductivity

increases by  $10^5$ x. The lattice parameter is largest for the mixture of nickel-cobalt oxide and the material exhibits the same  $p$ -type nature as both nickel oxide and cobalt oxide. Work function measurements were not available for these materials including nickel-cobalt oxide. Band gap information was also not available nor was the index of refraction

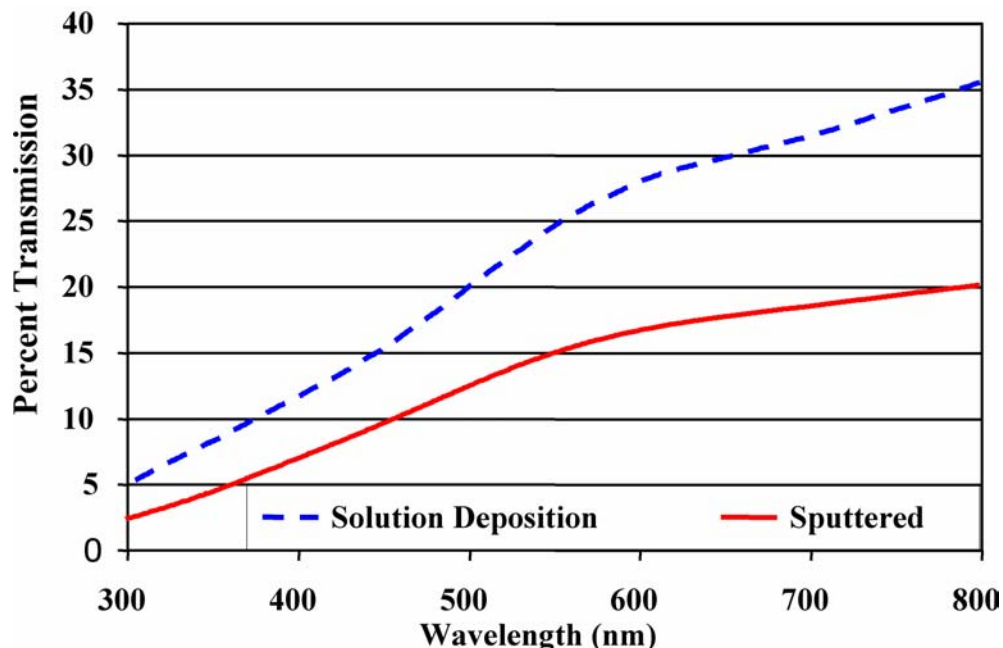


Figure 2-3. Visible transmission spectra of nickel-cobalt oxide from solution deposited and sputtered samples. Reprinted from Windisch, C.F., Exarhos, G.J., Ferris, K.F., Engelhard, M.H., & Stewart, D.C. (2001). Infrared transparent spinel films with  $p$ -type conductivity. *Thin Solid Films*, 398, 45-52 (Figure 3, p.47) with permission from Elsevier, color added.

Using the available data one might reasonably interpolate the existing reports and surmise a calculated bandgap in the neighborhood of 2.5-3.0 eV, if Vegard's law were valid for this system. However, the band gap for NiO may not be a valid number to use in this interpolation method because nickel, in  $\text{NiCo}_2\text{O}_4$ , is in the same chemical state as it would be found in  $\text{Ni}_3\text{O}_4$ . Since  $\text{Ni}_3\text{O}_4$  is not a stable phase existing at standard temperature and pressure conditions, no electrical information is available for it. Nickel

oxide and cobalt oxide individually differ in structure and electrical properties, but they both exhibit electrical properties far inferior to mixed nickel-cobalt oxide.

According to Figure 2-3, optical absorption begins near 600 nm where the transmission is nominally less than 30%. As stated previously, this is most likely due to *d-d* transitions absorbing the visible light. By TCO standards, this transparency is unacceptable for use in any practical device. Nickel-cobalt oxide transparency is acceptable at longer wavelengths as seen in Figure 2-4 below.

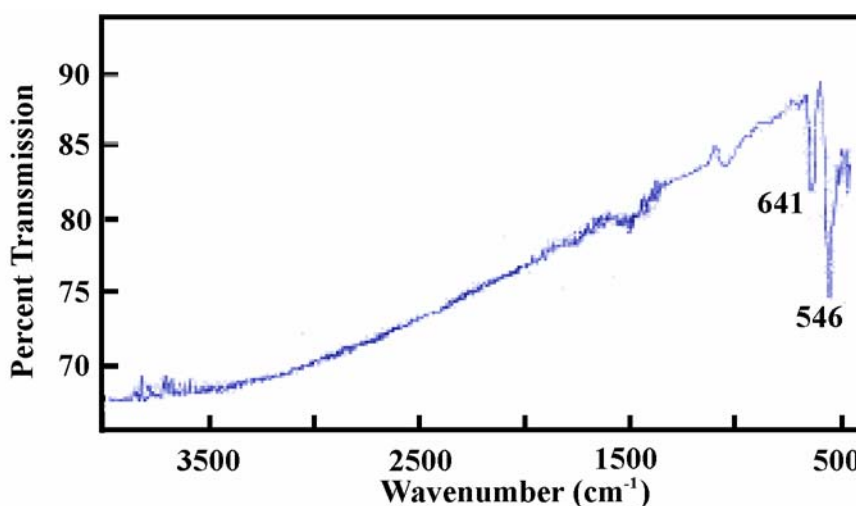


Figure 2-4. FTIR transmission spectrum of solution deposited nickel-cobalt oxide thin film. Reprinted from Windisch, C.F., Exarhos, G.J., Ferris, K.F., Engelhard, M.H., & Stewart, D.C. (2001). Infrared transparent spinel films with *p*-type conductivity. *Thin Solid Films*, 398, 45-52, (Figure 4(b), p.48) with permission from Elsevier, color added.

Separately neither nickel oxide nor cobalt oxide has the electrical properties to be of industrial interest, though they are both *p*-type with high carrier counts and low mobility. Windisch et al. determined the carrier to be *p*-type using the Seebeck coefficient (Windisch et al., 2002a; Windisch et al., 2002b). Figure 2-5 shows Seebeck data taken from a nickel-cobalt oxide thin film. They report that Ni<sup>3+</sup> also has a role in conductivity such that the mechanism of conduction is a charge transfer between resident divalent and trivalent cations suggesting it is possibly assisted by the magnetic nature of

the oxide film (Windisch et al., 2002b). The magnetic nature of the film has been blamed for difficulty in obtaining reliable results from the Hall effect measurement. Anomalous Hall effect measurements made an absolute determination of carrier concentration and carrier type difficult using the Hall effect measurement. A primary assumption of the Hall effect is that the measurement occurs in a material with *free* carriers.

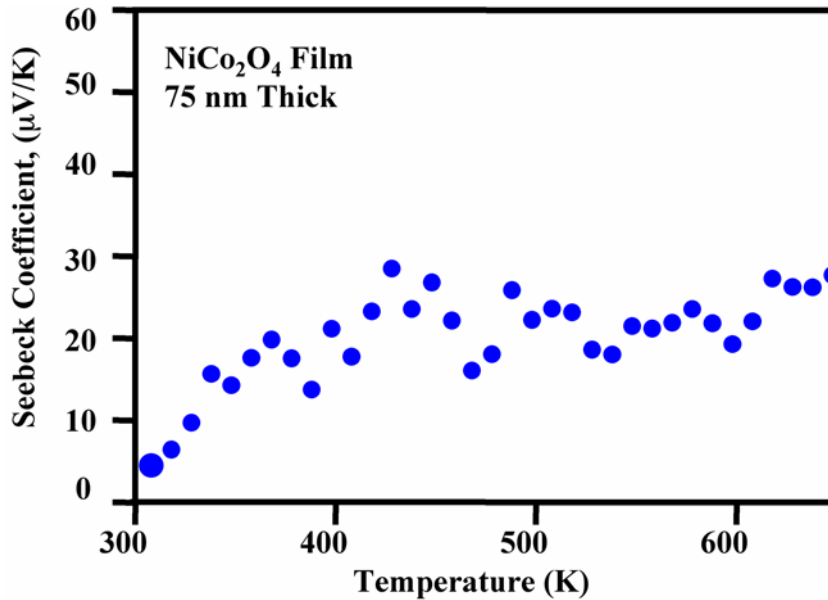


Figure 2-5. Seebeck data from nickel-cobalt oxide. Reprinted from Windisch, C.F., Ferris, K.F., Exarhos, G.J., & Sharma, S.K. (2002). Conducting spinel oxide films with infrared transparency. *Thin Solid Films*, 420, 89-99, (Figure 6(a) p.93) with permission from Elsevier, color added.

Emin addressed an anomalous Hall sign in oxide semiconductors. The sign of the Hall effect measurement depends on the nature and relative orientations of the local orbitals between which the carrier moves *and* on the local geometry. The sign of the Hall angle is not unambiguously determined by the sign of the charge carrier in the case of small-polaron hopping motion. The Hall effect depends on the local geometry and on the nature of the local electronic states. The observed anomalies of the sign of the Hall angle may be explained as simply being a manifestation of the hopping nature of the transport in phonon-assisted hopping motion (Emin, 1977). Polaron conductors and the Hall effect

have been discussed in the literature for the mentioned reasons. The Hall effect does not produce reliable reproducible values of carrier type, density, or mobility. This Hall effect anomaly is likely due to the localized nature of the carriers and the hopping conduction mechanism of nickel-cobalt oxide.

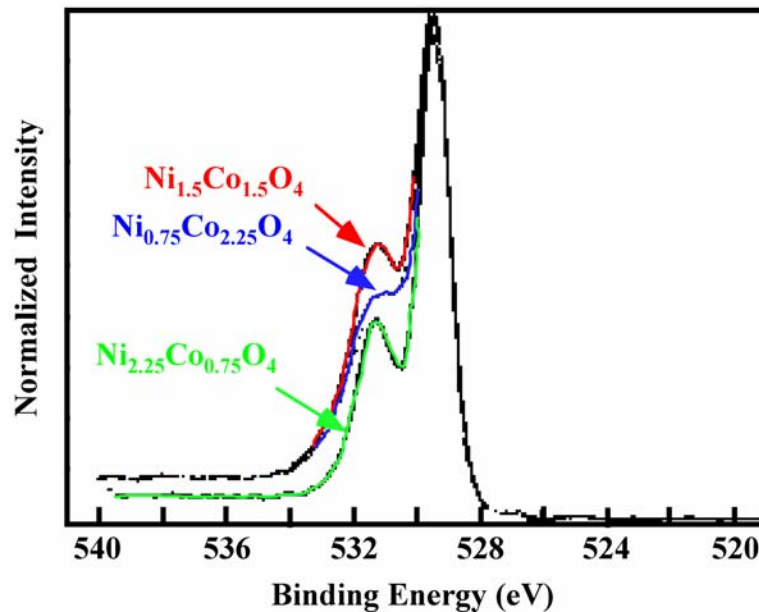


Figure 2-6. The oxygen 1s binding energy region from XPS shows a peak at 531.2 eV that scales with conductivity. Reprinted from Windisch, C.F., Exarhos, G.J., Ferris, K.F., Engelhard, M.H., & Stewart, D.C. (2001a). Infrared transparent spinel films with *p*-type conductivity. *Thin Solid Films*, 398, 45-52, (Figure 6. p.49), with permission from Elsevier, color added.

Nickel-cobalt oxide is probably a defect conductor due to adsorption of oxygen similar to nickel oxide where high oxygen partial pressure increases conductivity (Hotovy et al., 1998a). Cation vacancies produced from oxygen adsorption create holes in the valence band making the material *p*-type and it is therefore classified as an electron-defect semiconductor. (Azaroff, 1960) Additionally, the defect states of lattice oxygen monitored by XPS in the oxygen 1s region (see Figure 2-6) at a binding energy of 531.2 eV are believed to scale with conductivity and may be an indicator of polarons (Windisch et al., 2001a).

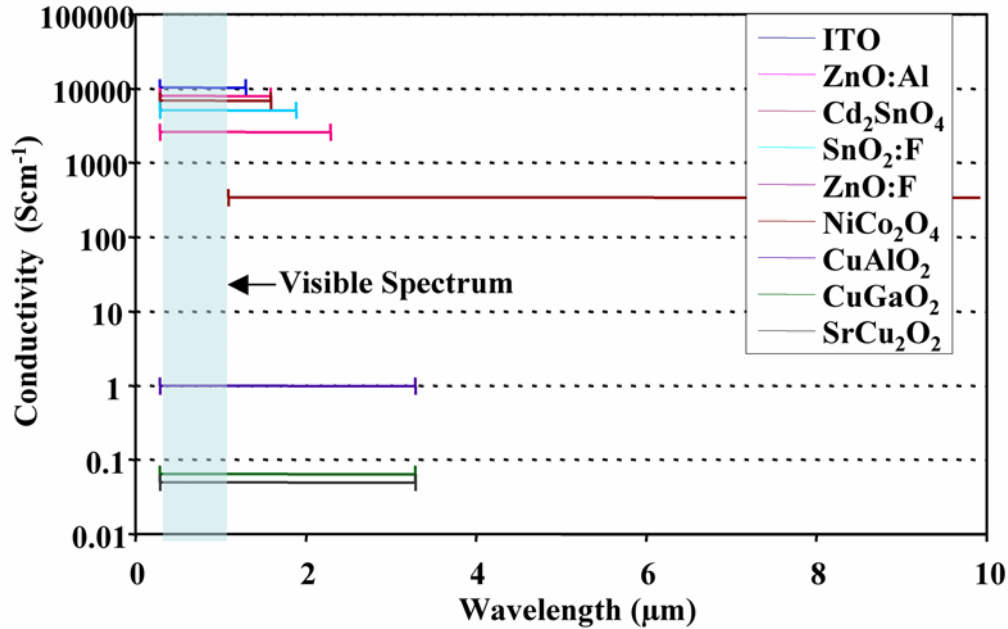


Figure 2-7. Comparison of TCO transparency regions with conductivity displayed as a function of transmission wavelength. The long line in center is nickel-cobalt oxide transparency range. It extends off the chart into the far IR with much better conductivity than the other *p*-type TCOs.\*

Windisch et al. have demonstrated the nickel-cobalt oxide system as a prospect for development with respect to conductivity and infrared transparency (shown in Figure 2-4) (Windisch et al., 2001a; Windisch et al., 2002a; Windisch et al., 2001b; Windisch et al., 2002b; Windisch, 2003b). Their work has suggested that the conductivity of the nickel-cobalt oxide system could be improved by the addition or substitution of selected cations, such as lithium, rhodium, or palladium. (Windisch et al., 2001a; Windisch et al., 2001b; Windisch et al., 2002b) Figure 2-7 shows that nickel cobalt oxide has a transparency window that extends more into the IR than typical *n*-type or other recently studied *p*-type TCOs. No other reported transparent conductor has a similar transparent region.

\* UV cutoff values of the TCOs are approximate for a qualitative comparison of the transparent regions in the IR. Plasma cutoff values for each are taken from the literature (Gordon, 2000; Windisch et al., 2001b; Windisch et al., 2002b). Plasma values for *p*-type TCOs estimated.

The nickel cobalt oxide system is unique in that it exhibits *p*-type conductivity with highly localized carriers bound to the lattice with an accompanying lattice strain, i.e. with polaron conduction. This bound carrier and lattice strain together are known as a small polaron. Carrier mobility is on the order of  $0.1 \text{ cm}^2\text{V}^{-1}\text{s}^{-1}$  due to the lattice bound localized carriers (Windisch et al., 2002b). Conduction occurs in these materials in spite of the low mobility because of a high polarons density,  $\sim 10^{21} \text{ cm}^{-3}$  (Windisch et al., 2002b). Conductivity up to  $333 \text{ Scm}^{-1}$  has been measured (Windisch et al., 2001a).

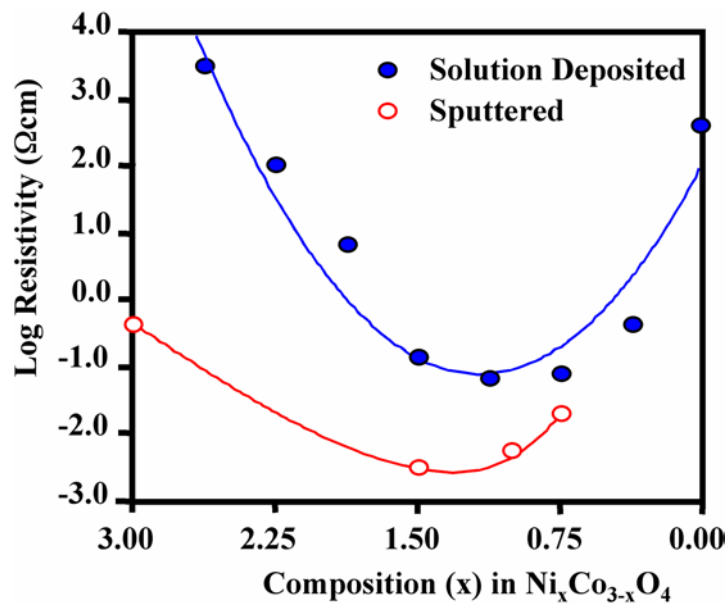


Figure 2-8. Effects of deposition techniques on the resistivity of nickel-cobalt oxide show that sputtered films of similar compositions to solution deposited films have lower resistivities. Reprinted from Windisch, C.F., Exarhos, G.J., Ferris, K.F., Engelhard, M.H., & Stewart, D.C. (2001a). Infrared transparent spinel films with *p*-type conductivity. *Thin Solid Films*, 398, 45-52. (Figure 2, p.47) with permission of Elsevier, color added.

Windisch et al. report that the best conductivity of sputtered films was found at nickel to cobalt ratio of 1:1 for sputtered films and 1:2 for solution films (Figure 2-8). Both the 1:1 sputtered and 1:2 solution deposited nickel-cobalt oxides were cubic spinel structured. Also included in Figure 2-8 was a comparison of solution and sputter deposited films showing the difference at the same composition for films deposited by

two different methods. It is believed that the difference in the film conductivity comes from lattice cation disorder accommodating polaron charge carriers (Emin & Bussac, 1994). Sputtering allowed a higher conductivity while at the same time preventing less transmission in the visible region due to strong absorption by *d-d* transitions from either the nickel or the cobalt ions. The spin state of  $\text{Co}^{3+}$  in the octahedral site may act as an acceptor and  $\text{Ni}^{2+}$  may exist in the octahedral site. Both of these cation states may enhance the conductivity (Windisch et al., 2002b).

### **2.3 Nickel-Cobalt Oxide Conduction Mechanism**

Nickel-cobalt oxide conducts electrically by a mechanism of small polaron hopping (Windisch et al., 2002b). An understanding of why polarons and free carriers are different sheds light on why the material properties are also different. Polaron conductivity gives nickel-cobalt oxide its unique properties of infrared transparency and high conductivity despite low values of mobility. Large numbers of polarons form with increased structural disorder that can be introduced by processing, selective cation addition, or cation substitution. Understanding polarons may give insight to discovering polaron-hopping conduction in other materials as well.

#### **2.3.1 Fundamentals of Polaron Conduction**

When a charge carrier such as an electron or hole distorts its neighboring lattice structure and traps itself, it is called a “polaron.” A polaron is described as an entity including both the displaced neighboring atoms (localized strain) and the trapped carrier (Cox, 1987; Emin, 1982; Austin, 1969).

Mistakenly called a polaron due to early investigations of self-trapping in polar and ionic solids, self-trapping is not restricted just to polar and ionic solids with long-range dipolar electron-lattice interactions. Polarons consist of two main types: large and small.

The two are distinguished by the severity of the localized strain area. “A small polaron is an extra electron or hole severely localized within a potential well that it creates by displacing the atoms that surround it.” (Emin, 1982, p.34). When the electronic carrier and the lattice distortion together have a linear dimension less than the lattice parameter, it is referred to as a small polaron (Kingery et al., 1975, p.870). Short-range electron-lattice interaction plays the major role allowing small polarons to occur in polar, covalent, and ionic materials and generally is comprised of interactions of the carrier with acoustic and optic vibrational modes of the lattice. Polaron motion can be described as a succession of phonon-assisted hopping steps (Emin, 1982).

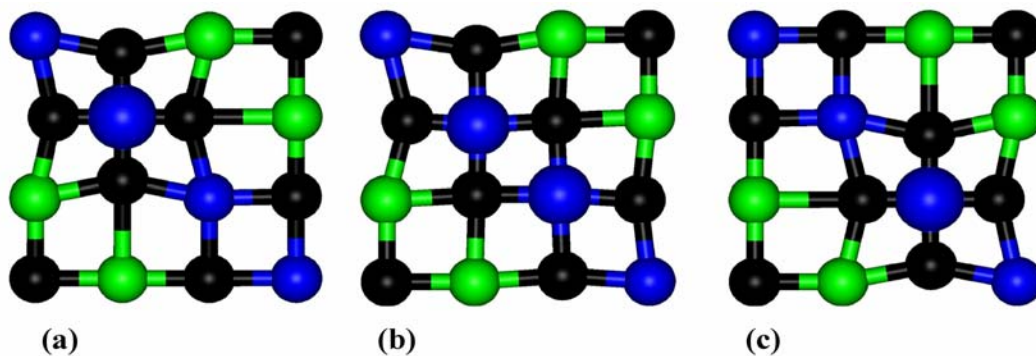


Figure 2-9. A bound carrier in a two-dimensional lattice is the enlarged blue atom. The polaron is the carrier and the accompanying strain. Schematic (a) is before the hop, (b) is the move, and (c) is the strain movement after the hop.

A hop consists of the following three steps shown in Figure 2-9 above:

1. Atoms arrange to allow multiple positions for a charge carrier.
2. The charge moves between degenerate electronic energy levels
3. Local deformation follows.

Polarons typically have a low mobility because the process of hopping as described previously takes more time than does moving a free carrier. Free carriers travel unbound with a given drift velocity ( $v_f$ ) under the influence-of-an applied electric field ( $E$ ) as seen

in Equation 2.3. In a periodic lattice, nearly-free electrons travel with a random drift velocity. With no external electric field applied, the drift velocity nets out to zero. Drift velocity is a function of the average time between scattering events ( $\tau$ ) and the mass of the carrier ( $m$ ) shown in Equation 2.3.

$$v_f = \frac{Ee\tau}{m} \quad (2.3)$$

Free carriers have small masses lending to higher velocities and therefore higher mobility given the same applied field assuming no increase in collision scattering.

$$\mu = \frac{v}{E} \quad (2.4)$$

When combined with a high carrier density, the nearly free carrier provides for a high conductivity.

$$\sigma = \frac{N_f e^2 \tau}{m} \quad (2.5)$$

Assuming that a periodic lattice moves in time with some given displacement at a frequency determined by the temperature, at any give time there is a probability that the lattice will arrange itself to allow a charge carrier to move between sites. Lattice distortion will follow. This occurrence is statistical in nature and has a finite probability at a given temperature. A bound carrier must be activated by a discrete amount of energy to *hop* from one site to another followed by the strain. Low mobility is a result of the probability of hopping combined with the energy required to hop. So, for a polaron conductor, the time between scattering events ( $\tau$ ) may well be converted to a frequency within a given time for a hop to occur. This jump rate relationship ties the motion of the carrier to the phonon motion or natural frequency of the lattice.

### 2.3.2 Fundamentals of Free Carrier Conduction

Nearly the opposite of polarons, free carriers are not locked into a specific position within the lattice. Free carriers typically have a high mobility until the carrier concentration increases to the point that they begin to interact by colliding and scattering.

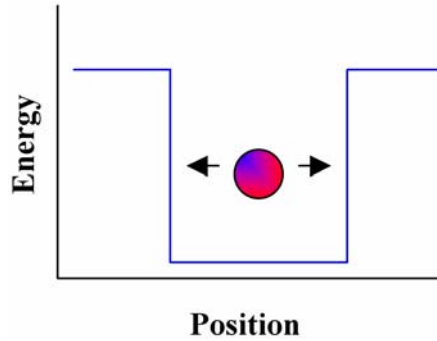


Figure 2-10. The *particle in a box* plot of a particle in a one dimensional lattice bound by an infinite energy barrier. The particle is confined to the region inside the 1-D well. The particle resides on a line and moves in a linear position (left and right) direction bounded by the energy barriers on either end.

Modeling free carriers mathematically is simple and most often done with a simple *particle in a box* model (the box term may be a misnomer when the system is one or two dimensional). The assumption for the particle in a box is a single molecule or particle in a one-dimensional position that can move linearly in two directions bounded by a potential well on each side. The graph of this energy versus position looks like a box seen in Figure 2-10, hence the name *particle in a box*. The energy for a particle in the box is described by Equation 2.3, where  $E_n$  is the allowed energy,  $n$  is the principle quantum number,  $h$  is Planck's constant,  $m$  is the mass of the particle and  $L$  is the length of the one-dimensional box.

$$E_n = \frac{n^2 h^2}{8mL^2} \quad (2.6)$$

The associated normalized wave function for the charge carrier in the well is given by Equation 2.7, where  $x$  is the position of the charge carrier in the *box*.

$$\psi_n(x) = \sqrt{\frac{2}{L}} \sin \frac{n\pi x}{L} \quad (2.7)$$

The solution to the wave function yields discrete nodes of allowed frequencies for the particle (charge carrier). These nodes correspond to discrete energies that are allowed

within the confines of the *box*. The Pauli exclusion principle\* dictates the energy levels of the quantum states of the confined electrons (or charge carriers). Each will have a unique set of quantum numbers though the energy value may be the same (degenerate). When the density of electrons is large, energy levels corresponding to quantum states are so close that the distribution is nearly continuous. This essentially continuous band of energies is referred to as a conduction or valence band for electronic conduction and is used to describe *p*-type and *n*-type materials. With free carriers, the box size is much larger than the crystal unit cell dimensions. This particular model matches classical physics based on billiard ball collisions when the dimensions of the *box* approach the centimeter scale. The picture fails when the deBroglie wavelength of a *particle* is reduced to atomic dimensions. (Emin, 1980). Modeling free carriers using the *particle in a box* is well accepted. A model of similar simplicity for polarons does not exist.

### 2.3.3 Observed Properties of Free Carriers and Polarons

While high conductivity is a characteristic of free electron carriers, for instance degenerately doped indium tin oxide (ITO) conducts electricity by free electrons. Free electrons absorb photons at wavelengths greater than  $\sim 1\text{-}2\ \mu\text{m}$ , but do not prevent high transparency in the visible spectrum from 400-800 nm. It is because of this free carrier absorption that *n*-type free carrier materials do not function as IR transmitting electrodes but serve as low emission “low  $\epsilon$ ” glass coatings for insulating windows (Svensson & Granqvist, 1986). Light of energy less than  $\sim 1\ \text{eV}$  is easily absorbed and/or reflected as the free carriers are promoted by the incoming photons to higher energy states that relax and give off phonons or photons. The energy onset of this absorption activity due to

---

\* The Pauli exclusion principle requires that each quantum state can be filled with at most two electrons each with opposite spins (Hummel, 2001).

carrier excitation is referred to as the plasma frequency\*. Polaronons do not exhibit a plasmon resonance near the same region because they are locally bound to the lattice.

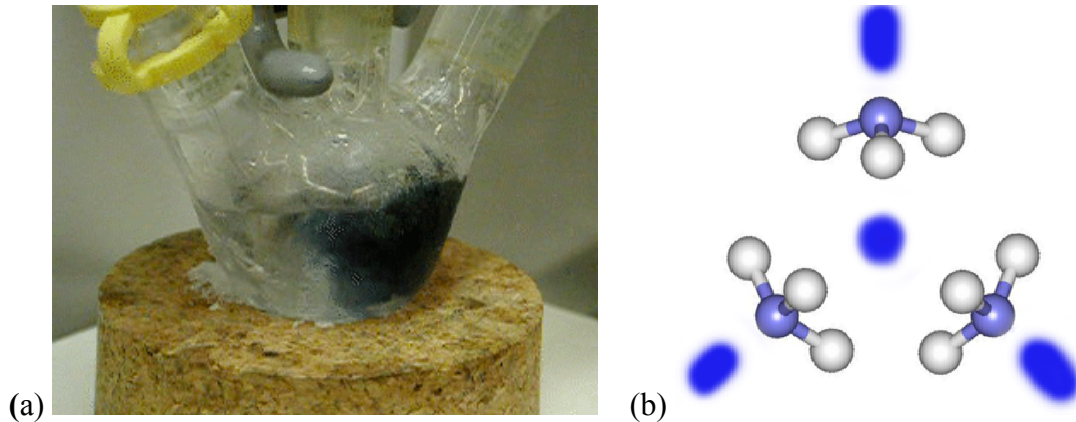


Figure 2-11. A polaron consists of the molecules involved and the local charge region:  
 (a) Liquid ammonia (colorless) forms polarons (dark blue) when sodium metal is added (b) Molecular orientation of polaron in liquid ammonia. Shaded areas are regions of high electron density (donated by sodium).\*\*

As a dramatic demonstration of the effects of polarons on color in white light, the property changes upon formation of polarons in liquid ammonia from electrons injected by sodium metal pellets is illustrated in Figure 2-11. Polarons form as regions of high electron density are created around the sodium ions. The polar ammonia molecules preferentially arrange around the charged regions. This localized charge distorts bonding and coupled with vibrational modes shifts the characteristic optical spectrum of the molecule.

Temperature is a factor to consider when dealing with polarons and free carriers. Free carriers and polarons in semiconductors behave differently as the lattice is heated. Free electrons in metals will decrease in mobility with increasing temperature due to

\* Plasma frequency is a characteristic frequency that separates the optically reflective region from the transparent region. The dielectric constant goes to zero and conditions are right for plasma (fluid-like) oscillation for the entire electron gas.

\*\* Video contained in a separate file ([PolaronClip1.avi](#)).

carrier collisions and scattering with a net result of decreased conductivity.

Semiconductors behave in two different ways depending on their doping regime. The intrinsic semiconductor will decrease in mobility and consequently conductivity until at a high enough temperature thermal energy excites electrons from the valence band to the conduction band. Carrier generation will allow conductivity to increase up to a certain threshold value where carriers begin to collide and scatter causing an overall decrease in conductivity due to the reduction in mobility even as the carrier density increases.

Thermal generation of carriers from extrinsic dopants will also affect the conductivity due to dopant ionization and increased carrier density until the point of saturation. The increased temperature will no longer increase carrier density beyond the saturation concentration, but enhance carrier collision and scattering will reduce mobility and decrease conductivity with increased temperature until the material begins intrinsic carrier generation. Materials in which conduction is limited by hopping experience the opposite effect due to the high population of bound carriers (polarons). As temperature increases, the lattice vibrations increase and the number configurations per second that allow hopping. The time for a carrier to hop is believed to remain constant with increased temperature, but the opportunities for hopping increase. Polarons ideally experience a mobility increase with temperature due to increased hopping. Carrier density remains constant so the net effect is an increased conductivity with increased temperature. When a polaron-conducting material is compared to a free carrier conducting material at higher temperature, the two are distinguished on the basis of mobility and carrier density.

Table 2-6. Observed properties of polarons compared with free carriers.

Observed property	Polaron Observed in transition-metal oxides with ions in multiple oxidation states	Free carrier Metals; <i>n</i> -type or <i>p</i> -type semiconductors
Seebeck coefficient Value	Small $< 20\mu\text{VK}^{-1}$ . <sup>a</sup>	Large $0.1 - 1 \text{ mVK}^{-1}$ Positive for <i>p</i> -type and negative for <i>n</i> -type. <sup>a</sup>
Seebeck coefficient temperature dependence	Nearly <i>independent</i> . <sup>a</sup>	<i>Dependent</i> , decreases with increased temperature.
Conductivity value	Good $\sim 10\text{-}1000 \text{ Scm}^{-1}$ . <sup>a</sup>	Better $1000+ \text{ Scm}^{-1}$ . <sup>e</sup>
Conductivity temp. dependence	Related to $\exp(-E_a)/(kT)$ where $E_a$ is about $0.2 \text{ eV}$ . <sup>b</sup>	Degrades; Plateaus with temperature then decreases. <sup>c</sup>
Carrier density value	High $\sim 10^{21} \text{ cm}^{-3}$ . <sup>b</sup>	Medium to high $10^{18-21+} \text{ cm}^{-3}$ Increases with temperature
Hall mobility	Small $\ll 1 \text{ cm}^2\text{V}^{-1}\text{s}^{-1}$ . <sup>a</sup>	$> 10 \text{ cm}^2\text{V}^{-1}\text{s}^{-1}$
Hall mobility and temperature	Increases with temperature. <sup>c</sup>	Falls as temperature increases. <sup>c</sup>
Carrier density	Promoted by structural disorder. <sup>b</sup>	Increases with temperature.
Hall sign	Anomalous. <sup>a, c</sup>	<i>p</i> -type positive, <i>n</i> -type negative.

<sup>a</sup>(Windisch et al., 2002b)<sup>b</sup>(Windisch et al., 2002a)<sup>c</sup>(Emin, 1982)

The Seebeck coefficient\* changes significantly with temperature for free-carrier conductors but only a negligible amount or not at all for a polaron conductor. This nearly temperature-independent behavior is one of the key indicators of polaron hopping. Table 2-6 summarizes some properties of polaron hopping versus free carrier conducting materials. Hall measurements show an increase in carrier density with temperature and a decrease in mobility. Seebeck measurements give a higher value for carrier density that is not influenced with temperature. In the Hall measurement, carrier count is measured and mobility is calculated.

---

\* A measure of the voltage change with temperature in a material from heat driven diffusion gradient of carriers in the material. If the change is positive it indicates holes are the majority carrier, if negative, then electrons are dominant.

Nickel-cobalt oxide is reported to conduct via a small polaron hopping mechanism (Windisch et al., 2002b). The key considerations for small polaron hopping, shown in Table 2-7, verify that nickel-cobalt oxide is a polaron conductor.

Table 2-7. Key characteristics of small polaron hopping for nickel-cobalt oxide

Characteristic	Observed?
Observed in oxides with ions in more than one oxidation state	Yes (Ni <sup>(+2,+3)</sup> , Co <sup>(+2,+3)</sup> ) <sup>a</sup>
Small Seebeck coefficient	20 $\mu\text{VK}^{-1}$ <sup>b</sup>
Small charge carrier mobility	< (0.1 $\text{cm}^2\text{V}^{-1}\text{s}^{-1}$ ) <sup>b</sup>
Conductivity related to temperature $S = \exp(-E_a)/(kT)$ where $E_a$ is about 0.2 eV	Yes <sup>b</sup>
High carrier density	Yes, approaching $1 \times (10)^{22}$ <sup>b</sup>
Seebeck coefficient is nearly temperature independent	Yes <sup>b</sup>
Correlates with phonon behavior	Yes: XRD & Raman <sup>c</sup>
Promoted by structural disorder	Yes <sup>c</sup>

<sup>a</sup>(Roginskaya et al., 1997; Tareen et al., 1984)

<sup>b</sup>(Windisch et al., 2002b)

<sup>c</sup>(Windisch et al., 2002a)

Temperature dependent measurements of the Hall effect show mobility increasing with temperature while the carrier concentration remains high for polaron conducting films. Conductivity is due to the high density of carriers in spite of low mobility making conduction possible because each carrier hops to contribute to the net current. Activation energy of electrical conductivity is influenced by temperature. Mobility increases as activation energy decreases with increased temperature. Conductivity increases with temperature because mobility increases with temperature. Based on observed properties, a polaron model will be introduced that will relate charge disorder to activation energy for electrical conduction in the nickel-cobalt oxide system.

## 2.4 Nickel-Cobalt Oxide Spinel Structure

Transition metal oxides take on a variety of structures including the delafossite, perovskite, pyrochlore, smectite, sodalite, stibiconite, and spinel structures (Fleischer,

1995). Cations stack in a solid based on a preferred nearest neighbor arrangement. These arrangements created from the stacking orientation determine the nature of the structure and may influence the conduction mechanism. Ternary compounds often arrange in two common structures: perovskite and spinel. (Smyth, 2000) A third more recently studied ternary arrangement is the delafossite structure. (Kawazoe et al., 2000) This section provides a brief background of the spinel structure and its characteristic arrangements in the nickel-cobalt oxide system.

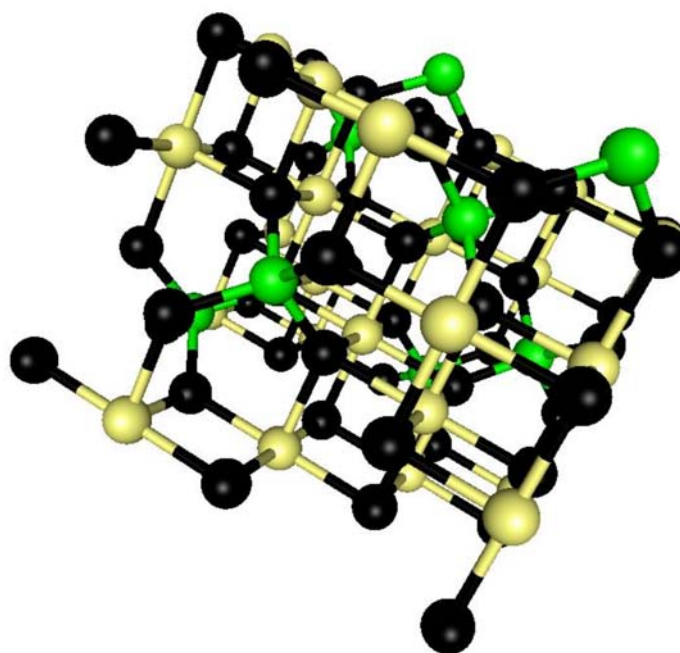


Figure 2-12. Green tetrahedral cations (A), yellow octahedral cations (B), and black oxygen anions (O) form the spinel unit cell with a chemical formula of  $AB_2O_4$  (based on atomic layout (Kingery et al., 1975, p.65).

Spinel, a gem found in nature often mistaken for Ruby, contains magnesium, aluminum and oxygen (*Gem by gem*, 2003; Hughes, 1999; Sickafus, 1999)). The arrangement of cations and oxygen in the gem spinel, shown in Figure 2-12, is the common crystallographic arrangement for a number of other minerals and oxides. Crystallographers refer to other similarly structured systems as having the spinel

structure. The spinel group of natural crystalline materials includes mineral such as spinel ( $\text{MgAl}_2\text{O}_4$ ), chromite ( $\text{FeCr}_2\text{O}_4$ ), coulsonite ( $\text{FeV}_2\text{O}_4$ ), gahnite ( $\text{ZnAl}_2\text{O}_4$ ), hercynite ( $\text{FeAl}_2\text{O}_4$ ), magnesiochromite ( $\text{MgCr}_2\text{O}_4$ ), magnesioferrite ( $\text{MgFe}_2\text{O}_4$ ), magnetite ( $\text{Fe}_3\text{O}_4$ ), trevorite ( $\text{NiFe}_2\text{O}_4$ ), zincochromite ( $\text{ZnCr}_2\text{O}_4$ ). Another isostructural mineral is the linnaeite group with sulfur instead of oxygen occupying the anion sites. (Fleischer, 1995) This sulfide containing linnaeite structure however, is often also referred to as spinel (Ballal & Mande, 1977; Benco et al., 1999; Kishimoto et al., 2000; Ohmuro et al., 1995; Schellenschlager & Lutz, 2000).

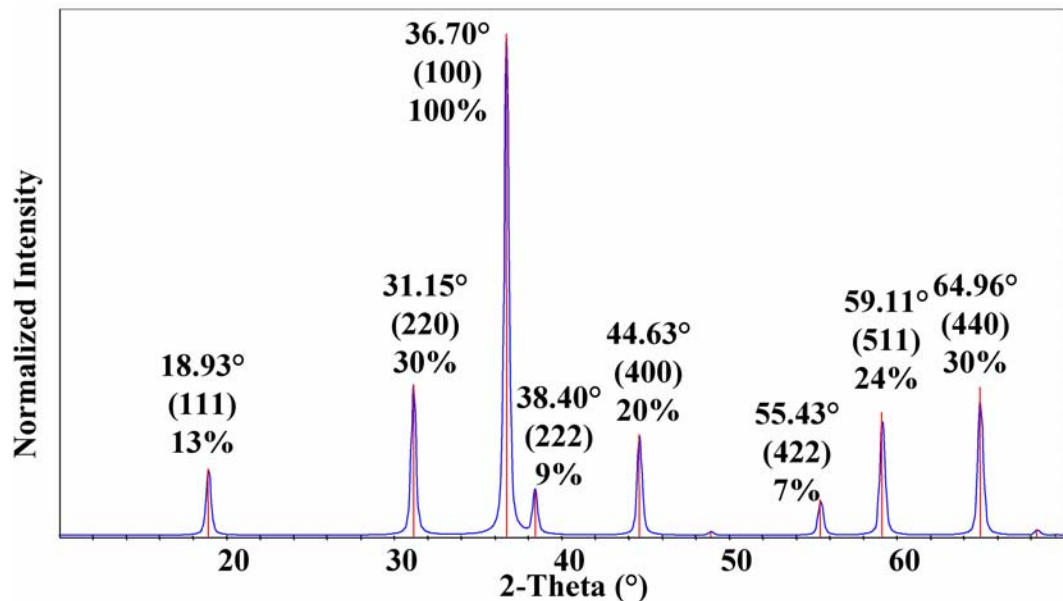


Figure 2-13. A calculated diffraction pattern for  $\text{NiCo}_2\text{O}_4$  annotated with peak positions, planes, and relative intensities from the powder diffraction file database number 73-1702.

As nickel is added to cobalt oxide to make the  $\text{Ni}_x\text{Co}_{3-x}\text{O}_4$  mixture, the spinel structure from the cobalt oxide persists up until cubic nickel oxide precipitates out. The most conductive mixture of nickel-cobalt oxide is spinel structured (Windisch et al., 2002b). Figure 2-13 shows a calculated XRD pattern of the spinel structure.

The atomistic arrangement in the spinel structure accommodates multiple cations in multiple oxidation states and allows hopping conduction (Windisch et al., 2002b). While the literature agrees that the bonding nature between atoms in the spinel structure is mostly ionic, a complete understanding of the bonding is subject to controversy. (Azaroff, 1960).

Grazing incident x-ray diffraction (GIXRD) from both sputtered and solution deposited films exhibit a spinel pattern, similar to the powder diffraction file (PDF) number 73-1702 for nickel-cobalt spinel shown in Figure 2-13. This structure is characterized by a primary peak from the (100) plane at  $36.70^\circ$  (2-theta) and secondary peaks from (220), (400), (511), and (440) at  $31.15^\circ$ ,  $44.63^\circ$ ,  $59.11^\circ$ , and  $64.96^\circ$  (2-theta) respectively.

Nickel addition to cobalt oxide maintains the spinel structure up to its solubility limit when it separates out to form the  $\text{NiCo}_2\text{O}_4$  spinel and a separate cubic NiO phase detectable by XRD. According to Windisch et al. this occurs when nickel concentrations exceed 33% in solution deposited samples and 50% in sputter deposited films. All samples experience nickel oxide precipitation when heated above four hundred degrees (Tareen et al., 1984; Windisch et al., 2001a), however Petrov and Will demonstrated that heating to  $1000^\circ\text{C}$  in oxygen and  $\text{KClO}_3$  at a pressure of 60kbar reversed the phase separation to form spinel structured  $\text{Ni}_{1.71}\text{Co}_{1.29}\text{O}_4$  (Petrov & Will, 1987).

#### **2.4.1 Spinel Sites**

The unit cell from Figure 2-12 is made up of a series of repeating layers illustrated in Figure 2-14. Using the nomenclature  $\text{AB}_2\text{O}_4$  to represent cations and oxygen in the *normal* spinel structure, the A represents the doubly ionized cation found in the

tetrahedral site, the B represents the triply ionized cation found in the octahedral site, and “O” represents the oxygen occupied sites according the space group  $Fd\bar{3}m$  #227.

(Azaroff, 1960)

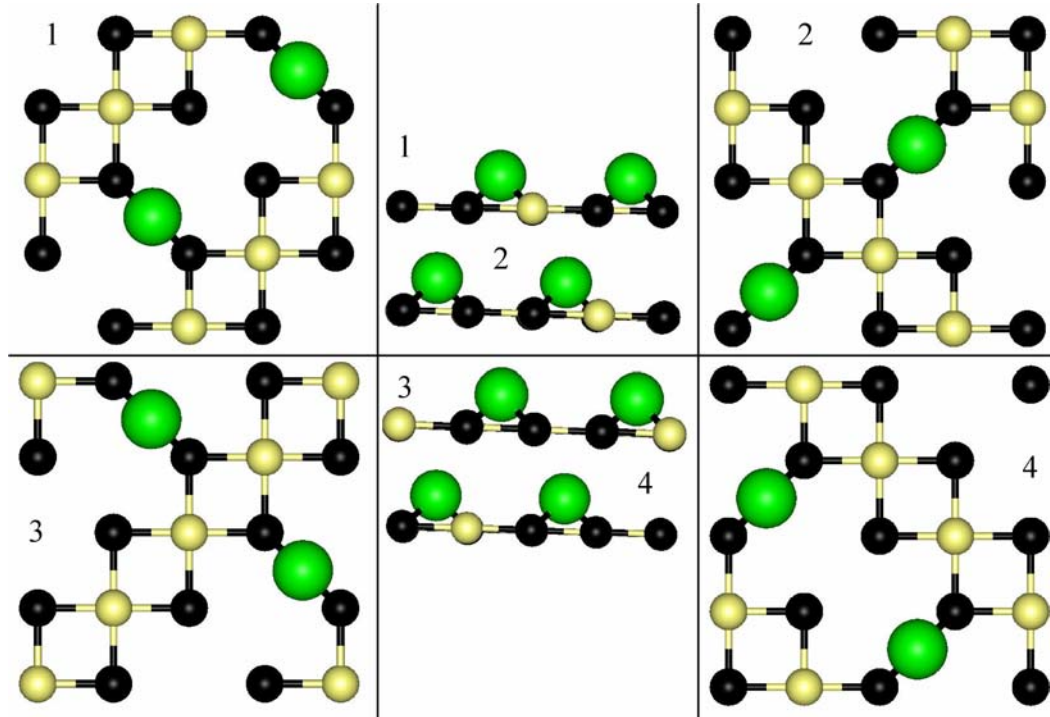


Figure 2-14. Spinel unit cell layers stack with interlocking tetrahedral sites. Oversized green tetrahedral atoms (A) in the numbered layers stick up and connect in the vacancies of the level above. This layered schematic is based on a similar spinel layout detailed by Kingery. (Kingery et al., 1975) p.65.

**Tetrahedral site.** The tetrahedral site (Figure. 2-15), or four-fold coordination site accommodates a cation which bonds with four nearest neighboring oxygen anions. Eight out of 64 possible tetrahedral sites are occupied by a doubly ionized cation. Cobalt is believed to occupy the tetrahedral sites in the nickel-cobalt oxide lattice.

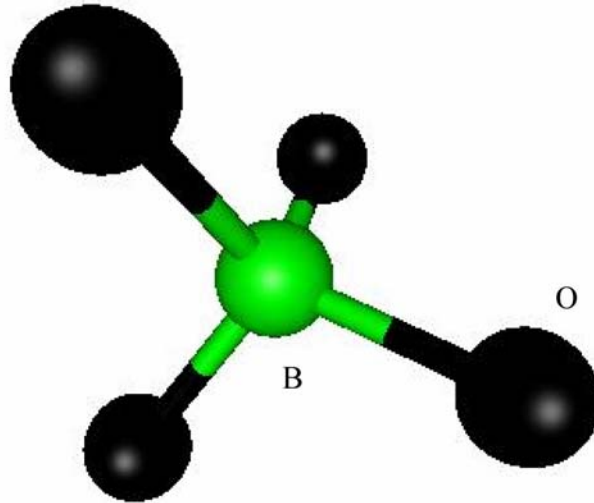


Figure 2-15. Tetrahedral site atom (green) bonded to four surrounding oxygen (black).

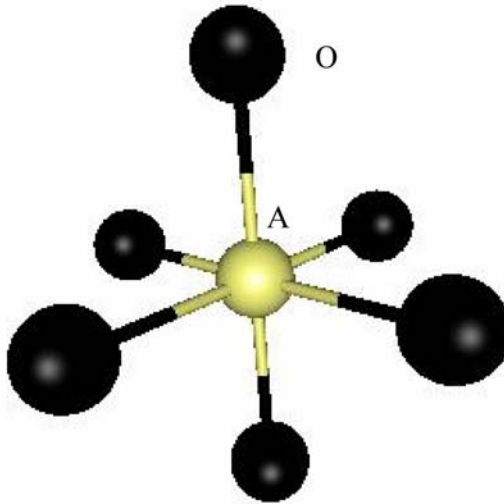


Figure 2-16. The octahedral site atom (yellow) bonds with six surrounding oxygen (black) anions to form a six fold orientation.

**Octahedral site.** The octahedral site (Figure 2-16), or six-fold coordination site, typically is occupied by a cation with a 3+ valence to bond with its 6 nearest oxygen anions. The spinel unit cell contains 32 octahedral sites, of which 16 are occupied. Nickel prefers the octahedral site in the nickel-cobalt oxide (Tareen et al., 1984), and cobalt fills the remaining octahedral sites and then the tetrahedral sites.

The octahedral site plays a role in conductivity. As nickel is added to cobalt oxide, the conductivity increases by up to five orders of magnitude and nickel occupies the octahedral site. However after heat treatment, nickel oxide precipitation causes conductivity to decrease, suggesting that nickel in the octahedral site must have a significant effect.

**Oxygen site.** Oxygen occupies the remaining thirty-two anion sites. Oxygen sites are nearly a close packed cubic lattice (Kingery et al., 1975).

#### 2.4.2 Variations of the Spinel Structure

Not all spinel structures arrange as noted by the  $AB_2O_4$  with the  $A^{2+}$  in the tetrahedral site and the  $B^{3+}$  atoms in the octahedral site. The *inverse* spinel sometimes occurs, where half of the  $B^{3+}$  species occupy the tetrahedral sites. The remaining half of the  $B^{3+}$  cations along with all of the  $A^{2+}$  cations occupy the octahedral sites. Inverse spinel structures are often identified structurally as  $B[AB]O_4$  (Azaroff, 1960). Other distributions of cations between the various lattice sites are possible (Deer, 1962; Kingery et al., 1975).

“The partially inverse spinels can be viewed as partially disordered versions of either end member, the ideal normal spinel or the ideal inverse spinel. The disordered structures contain lattice defects relative to either end member in that cations are located on lattice sites where they do not appear in the ideal reference structure.” (Smyth, 2000, p.20)

Nickel and cobalt compose an oxide spinel where both cations are found in multiple valence states and in multiple sites. This condition of a mixture of multiple valence states in multiple sites is referred to as cation disorder. Verwey et al. postulated a cation charge ordering within iron oxide at a low temperature (Verwey 1939; Verwey & Haayman, 1941; Verwey et al. 1947). Below the Verwey temperature, conductivity decreases dramatically (Monk & Ayub, 1997). Much like Verwey’s postulate, cation

arrangement must have an effect on polaron interaction. Hopping between sites will depend on whether the sites are dissimilar or both tetrahedral or octahedral. Arranging as primarily an inverse spinel (Windisch et al., 2001b), the nickel and cobalt cations may substitute for each other at both the tetrahedral and octahedral lattice sites. If arrangement has an effect, then the opposite must be true as well. Defects and disorder of the cation charge distribution within the spinel structure also has an effect on the conductivity (Windisch et al., 2002a).

### 2.4.3 Spinel and Conductivity

The electrical conductivity for these spinels is generally very limited. In general their bandgaps are large ( $>2.5$  eV) and impurities form deep traps for charge carriers. To understand the limited observed conductivity, the electronic bonding must be considered.

As reported by Smyth et al., for the iron oxide system the following is observed:

“In an octahedral environment, the crystal field splitting gives three equivalent levels of lower energy, the  $t_{2g}$  levels whose orbitals are directed in between the six closest anions, and two equivalent levels of higher energy the  $e_g$  levels whose orbitals point directly at nearest neighbors. The energy separation in this case is sufficient to promote a violation of Hund’s rule (that “equivalent” electron states are singly filled before any of them are doubly occupied), and the six d electrons fill the three lower levels.” (Smyth, 2000, p.18).

Smyth concludes that electrical conductivity is achieved by carrier movement through the bonding orbitals or  $t_{2g}$  orbitals along the octahedral sites. Conduction may be due to movement of holes in anion  $p$ -orbitals. (Ballal & Mande, 1977)

## 2.5 Summary of Literature Review

TCOs are classified by their majority carrier type or conduction mechanism. Both  $n$ -type and  $p$ -type TCOs are needed, but  $n$ -type are more developed and available. The primary reason  $p$ -type TCOs are not as developed is a result of the conductivity being orders of magnitude less than  $n$ -type TCOs. Nickel-cobalt oxide conductivity is order of

magnitudes better than other *p*-type TCOs, yet is still poor in comparison to other well used *n*-type TCOs. *N*-type TCOs block light in the IR while nickel-cobalt oxide transmits it. *N*-type TCOs are free electron conductors with high mobility and nickel-cobalt oxide is a polaron hopping conductor with low mobility. Highly localized charge carriers and the accompanying lattice strain known as small polarons are found in nickel-cobalt oxide and behave distinctly different than the free carrier analog in other oxide semiconductors. Most often polaron hopping is “discovered” as the conduction mechanism by observing material properties. Key differences between free carrier conductors and small polaron conductors are evident from temperature dependent properties such as conductivity and the Seebeck coefficient. Conductivity becomes significant in small polaron conducting material when the carrier concentration becomes extremely large. Polarons conduct through a charge hopping mechanism. Polaron formation does not create a plasma absorption region therefore IR transmission remains high. Properties exhibited by nickel cobalt oxide such as high conductivity and infrared transparency result from the spinel structural arrangement and the high polaron concentrations. Hopping is a low mobility process that requires energy for activation. Achieving conductivity improvements is approached in three ways:

- Increase the cation disorder and lower activation energy by adjusting film deposition conditions and post deposition heat treatment processing.
- Add polarons by doping the system with a monovalent impurity atom such as lithium to further oxidize metallic ions and create more polarons
- Substitute rhodium for cobalt to increase disorder by atomic size distortion.

These methods of enhancing conductivity by are reported in the Chapters 3-5.

## CHAPTER 3 SPUTTERED NICKEL-COBALT OXIDE

### 3.1 Introduction

This chapter discusses the electrical and optical properties of nickel-cobalt oxide and how sputtering conditions and heat treatment conditions affect them. Changing the growth rate or nucleation mode (growth mechanism) by adjusting sputtering conditions may influence the film qualities such as crystallinity, morphology or density (Mattox, 1998). The effects of introducing a third cation such as lithium or rhodium on thin film electrical and optical properties are discussed in Chapters 4 and 5, respectively.

Two primary methods used to deposit nickel-cobalt oxide as infrared transparent conducting oxide (ITCO) thin films include solution deposition and sputtering.\* Conductivity and transparency both vary depending on the method of film deposition. The solubility limit of nickel in cobalt oxide appears to be a function of the deposition method. Nickel solubility in cobalt oxide is enhanced by sputtering and superior film conductivity is observed at increased nickel concentrations. Solution deposition is limited to a maximum concentration of 33% nickel to produce the stoichiometric  $\text{NiCo}_2\text{O}_4$  spinel composition. Sputtered samples allow a nickel concentration of up to 50% to give  $\text{Ni}_{1.5}\text{Co}_{1.5}\text{O}_4$ . Windisch et al. have explained the superior conductivity (order of magnitude improvement) of sputter deposited films in comparison to solution deposited films (Windisch et al., 2001a; Windisch et al., 2001b; Windisch et al., 2002b).

---

\* Refer to Appendix A for additional details of sputtering and solution deposition

A technique of sputter deposition that produces a compositionally varying film (combinatorial sputtering) used in this study produced a finer range of film compositions to find the highest conductivity composition. This combinatorial sputtering deposition technique was repeated to study the effect of select gas compositions on deposited film properties. Traditional sputtering of  $\text{Ni}_{1.5}\text{Co}_{1.5}\text{O}_4$  and  $\text{NiCo}_2\text{O}_4$  from alloy targets show how process conditions of film deposition such as to gas pressure and target-substrate distance affect electrical, optical and structural properties. Heat treatment methods are shown to have a dramatic effect on film properties as well.

### 3.2 Film Preparation and Characterization Procedures

Radio frequency (RF) sputter deposition at 13.56 MHz with a magnetron cathode allows tight control of process variables such as cathode power, substrate temperature, gas flow rate, gas composition, gas pressure, and target-substrate distance inside the vacuum chamber to produce consistent films over large areas. This study analyzes films sputtered with process adjustments such as sputtering gas composition, target-to-substrate distance, and gas pressure. Resulting optical transmission and electrical conductivity will be reported as a function of these sputtering process conditions. Sputtering for this study occurred in one of two configurations: (1) the combinatorial film deposition method used two cathodes simultaneously to generate many compositions in a single run, and (2) the traditional sputtering method used a single cathode and a rotating substrate holder.

The first sputter deposition configuration uses two cathodes simultaneously to produce a film with varying composition. Combinatorial sputtering in Figure 3-1 (also referred to as *combinatoric* sputtering (Freeman et al., 2000)) produced films containing a graded composition between nickel oxide and cobalt oxide in an attempt to find the composition of a nickel-cobalt oxide film with the highest conductivity. The basic setup

included three microscope slides placed end-to-end, divided into nine one-inch sections, and labeled 1-9, as shown in Figure 3-1. All sputtered films were deposited with a base vacuum pressure near  $1 \times 10^{-6}$  Torr. The process gas pressure was held constant at 2 mTorr for the combinatorial experiments.

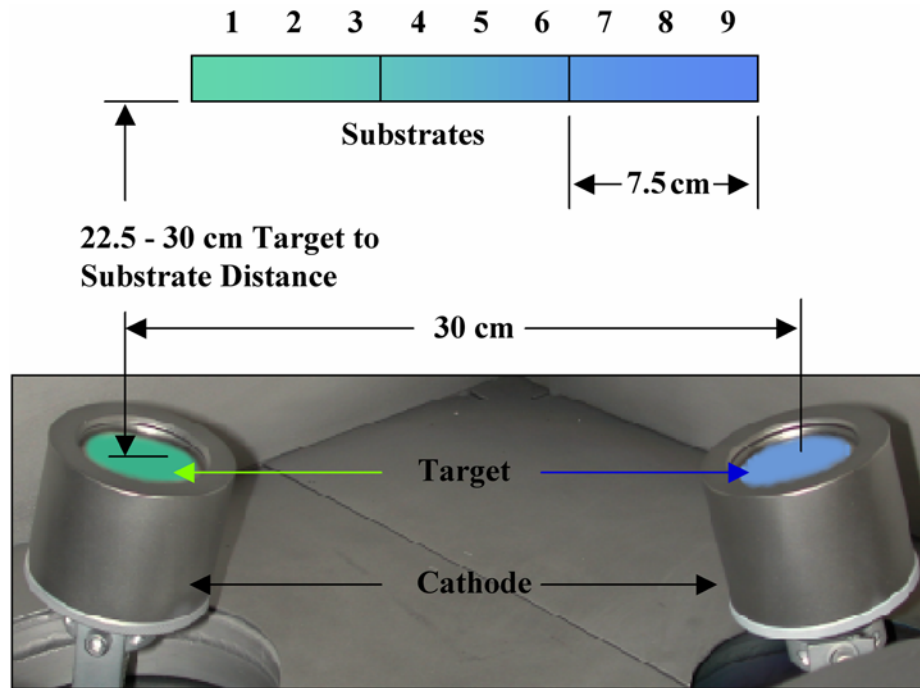


Figure 3-1. Combinatorial sputtering uses a dual cathode setup with targets of different material composition. The resulting compositionally graded film is divided into subsections and numbered 1-9. Sapphire, microscope slides and/or silicon wafer slices served as substrates for combinatorial deposited films.

Factors such as background contamination within the chamber (e.g. pump oil, previously sputtered material, or gas line impurities) may cause slight film variation from one process run to an identical one. By using the combinatorial technique, an array of compositions can be fabricated simultaneously with identical deposition conditions to minimize incidental error from one run to the next. Combinatorial sputter deposition does have its own complexity concerning uniform film thickness attributed to the geometry of the setup and the different materials used as targets. Uneven film thickness

is minimized by adjusting the sputtering rate of the individual cathodes by depositing a film and then changing the cathode power and verifying the effect. During calibration, all other process parameters are held constant.

The second sputtering configuration is called traditional sputtering and includes a single two or three inch cathode powered at 100 or 200 watts, respectively. Process gas pressure and target-substrate distance are also varied. Sputtering time is adjusted to produce films of similar thickness from setups with the varying target-substrate distance. The substrate holder setup for single cathode deposition rotated primarily in an offset rotation setup where the axis of rotation is offset from the center axis of the cathode (see appendix A for clarification on sputtering geometry). Samples of  $\text{Ni}_x\text{Co}_{3-x}\text{O}_4$  were produced on fused silica, *p*-type silicon, sapphire, poly(ethylene-teraphthalate) (PET), and microscope slides with *x* being equal to 1 or 1.5.

Characterization results consist of data from both combinatorial and traditional sputtered films. The matrix for the experiments is shown in Table 3-1.

Table 3-1. Film deposition parameter and sputtering setup matrix for  $\text{Ni}_x\text{Co}_{3-x}\text{O}_4$

Parameter	Setup	Variable range
Film Composition	Combinatorial	$0.8 < x < 1.75$
Gas Composition	Combinatorial	0, 20, 50, 75, 100% $\text{O}_2$
Gas Pressure	Traditional	2, 5, 10 mTorr; $x=1$ , $x=1.5$
Target-Substrate Distance	Traditional	7.5, 10, 15, 30 cm; $x=1.5$

Characterization included x-ray photoelectron spectroscopy (XPS)\* (Brundle et al., 1992), secondary ion mass spectroscopy (SIMS)\* (Brundle et al., 1992) transmission

\* See Appendix B for instrumental setup parameters and operating conditions.

electron microscopy (TEM) \* (Brundle et al., 1992), x-ray diffraction (XRD) \* (Brundle et al., 1992), Fourier transform infrared spectroscopy (FTIR) \* (Brundle et al., 1992), ultra-violet and visible spectroscopy \*, optical and stylus profilometry \*, and room-temperature and temperature-dependent van der Pauw \* measurements. Heat treatment consisted of a ten minute post-deposition heat treatment at 375°C followed by rapid cooling.

XPS was used to determine the chemical composition of select films and then correlate the other characterization information to a specific composition. Electrical van der Pauw measurements were performed with films on all substrates, while FTIR transmission measurements were performed with films on silicon and sapphire substrates. Visible and near-infrared optical spectra were measured from films on fused silica and/or sapphire substrates.

### 3.3 Characterization Results and Discussion

#### 3.3.1 Electrical Properties

Variable composition films from combinatorial sputtering show the effect of process gas composition while traditionally sputtered films from alloy targets show the effects of total chamber sputter gas pressure and target to substrate distance on electrical properties. Substrate material has an effect on the produced film regardless of the film composition and the work function does not appear to vary significantly with composition.

**Gas composition.** The effects of gas composition, with the gas mixtures ranging from 100% oxygen to 100% argon, at a constant pressure of 2 mTorr are shown in Figure

---

\* See Appendix B for instrumental setup parameters and operating conditions.

3-2. Films deposited at constant gas pressure with different gas concentrations of argon and oxygen show that position 7 had the highest conductivity of  $\sim 350 \text{ } \Omega\text{cm}$ .

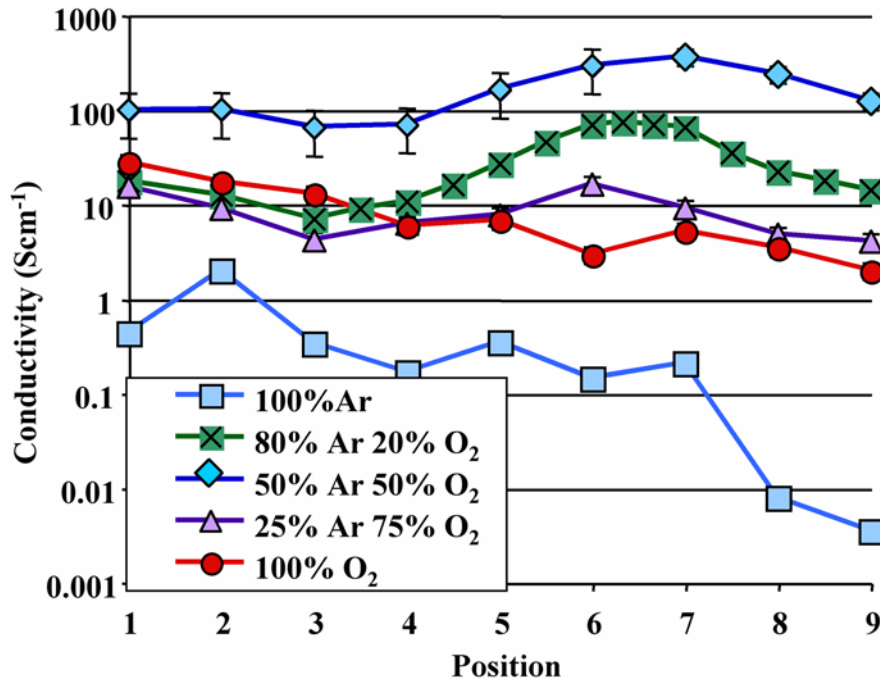


Figure 3-2. Conductivity versus position for combinatorial runs is displayed as a function of oxygen and argon gas composition. The film deposited with the gas concentration of 50% oxygen and 50% argon is the most conductive at position 7.

Combinatorial sputtered films from nickel oxide and cobalt oxide targets deposited with variable gas composition showed marked changes in resistivity as the amount of argon increased up to 50%. The gas with 50% oxygen and 50% argon yielded the highest conductivity across all positions. Resistivity degraded when the argon concentration exceeded 50%. Gas composition appeared to affect the sputter rate and possibly the oxidation state of the cations in the produced film. Argon, with its larger mass, inflicts a greater amount of damage on the target, increasing the sputtering rate compared to oxygen, likely producing a slightly reduced film. Oxygen however promotes complete oxidation of the film. Combining the effects of oxygen and argon produced the highest

conductivity films. Figure 3-3 shows position 7, the highest conductivity position of all the films ( $\sim 350 \Omega\text{cm}$ ), plotted as a function of gas pressure.

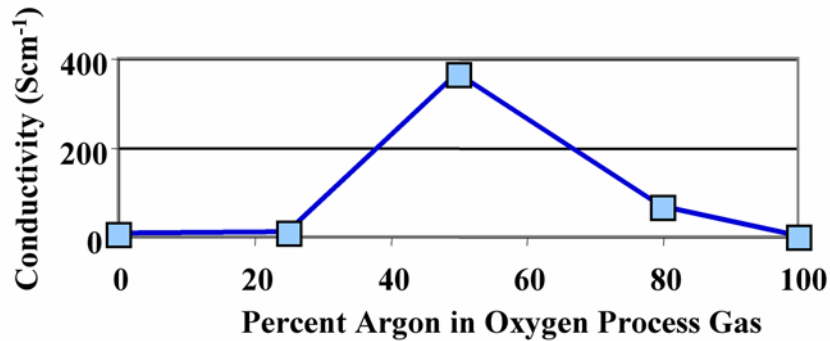


Figure 3-3. Position 7 from Figure 3-2 is the position with the highest conductivity. Conductivity is enhanced at a sputter deposition process gas composition containing 50% oxygen and 50% argon.

This combinatorial study was conducted to fill the gaps between the data points previously reported (Figure 2-8) where the composition with highest conductivity film contains equal parts of nickel and cobalt. Combinatorial sputtering with 5 cm nickel oxide and cobalt oxide targets produced a film with a graded composition as determined by XPS (Figure 3-4).

Possibly due to different magnetic species in the plasma, more cobalt is measured in the sample in Figure 3-4. An ideal deposition would show an equal ratio of nickel to cobalt at position 5. It is interesting that while proportionally more cobalt is in this film, shifting the equal ratio composition  $\text{Ni}_{1.5}\text{Co}_{1.5}\text{O}_4$  to the nickel-rich side, the data show that the nickel-rich side of the film is actually thicker. This suggests that the nickel oxide target and the cobalt oxide target sputtered at different rates. Nickel oxide, being a nonmagnetic target, likely had a higher deposition rate, but being influenced by the magnetic field of the cathode, deposited material in a more confined region. The magnetic nature of the  $\text{Co}_3\text{O}_4$  target may have interacted with the magnetic field from the

cathode to alter its effect on the desired ion trajectory and produce a more diffuse deposition resulting in a lower sputter rate and a higher area of coverage.

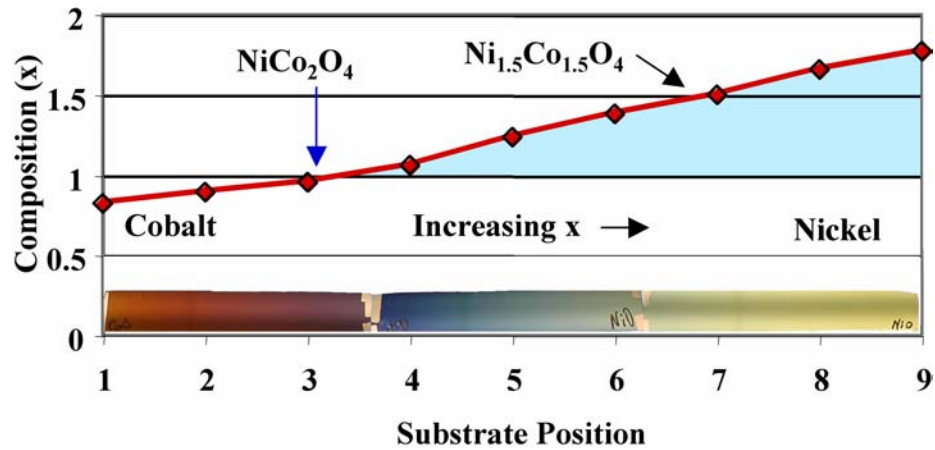


Figure 3-4. Fraction of Ni and Co detected by XPS as a function of position on a combinatorial sputtered  $\text{Ni}_x\text{Co}_{3-x}\text{O}_4$  film. Equal portions of nickel and cobalt were found at position 7 ( $x$  value of 1.5). The blue arrow indicates the solubility limit of nickel from solution deposition. The light blue shaded region shows the increased nickel available from sputtering. Embedded along the abscissa of the graph is a picture of a combinatorial sputtered film on a silicon substrate from this study. The color change is due in part to thickness and in part to compositional variations.

XPS of the film combined with resistivity and thickness data, each as a function of numbered position, yields a relationship between composition and conductivity. XPS of the most conductive combinatorial film is shown in Figure 3-5. Film conductivity is found to be highest at a composition of  $\text{Ni}_{1.5}\text{Co}_{1.5}\text{O}_4$  at  $\sim 350 \text{ Scm}^{-1}$ , agreeing with previously reported results (Windisch et al., 2001a). The composition limit imposed by solution deposition is included for contrast. All compositions to the right of the red vertical line are not possible from solution deposition.

As an indication of the different sputtering rates of nickel and cobalt, a thickness calibration profile shows that the nickel-rich side is thicker than the cobalt-rich side (Figure 3-6). Interference due to the magnetic nature of the cobalt oxide target may contribute to the non-uniform deposition thickness. Sputtering RF power and tilt angle of

the individual cathodes would require fine tuning to flatten the thickness curve. This iterative process of finite adjustment should be addressed in a future study.

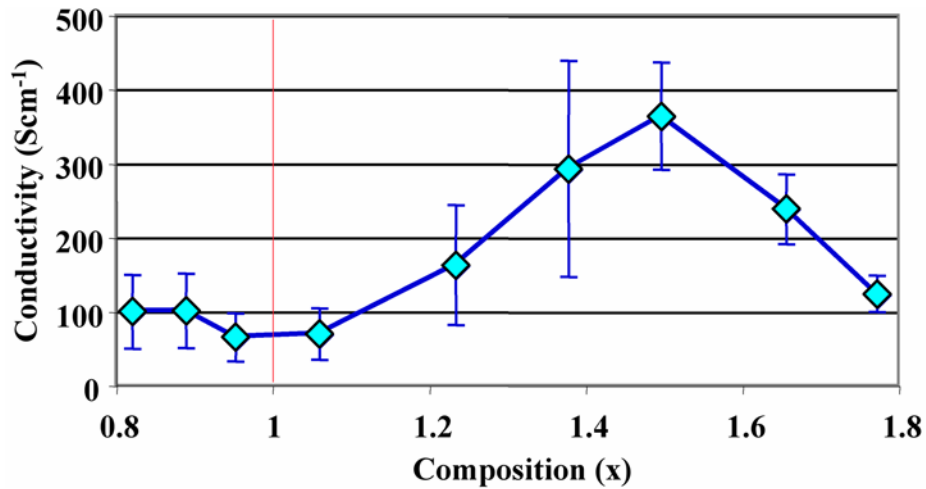


Figure 3-5. Combinatorial sputtered  $\text{Ni}_x\text{Co}_{3-x}\text{O}_4$  film combining conductivity and position with composition with position data to yield conductivity as a function of composition. The highest conductivity film appears at a composition near  $\text{Ni}_{1.5}\text{Co}_{1.5}\text{O}_4$ . The vertical red line at  $x=1$  indicates the solubility limit of nickel when deposited from solution methods.

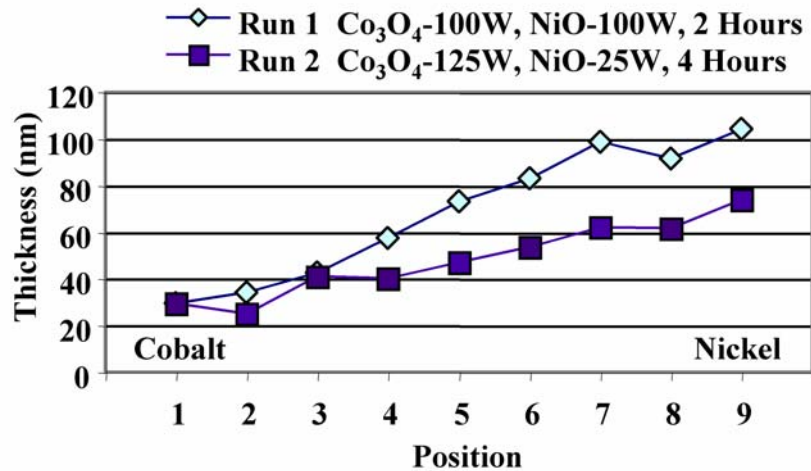


Figure 3-6. A combinatorial substrate thickness profile measured by a stylus profilometer shows that the film thickness is also graded from cobalt rich on the left to nickel rich on the right. Following an initial calibration run, cathode power was adjusted as was deposition time to give a more uniform film. Subsequent combinatorial films were processed using this calibrated power regime.

Figure 3-6 shows the initial calibration run (run 1) with a non-uniform thickness of about 30 nm on the cobalt side and 100 nm on the nickel side. The power was adjusted

and the second deposition ran with a 25% increase in the cobalt cathode power and the nickel cathode power reduced by 75%. Sputter time was doubled to ensure a film of similar thickness. No further increase in the cobalt cathode power was practical because a general rule of thumb for sputtering (specified by one cathode manufacturer) discouraged exceeding a power rating of  $4 \text{ Wcm}^{-3}$  on a 5 cm cathode. Since the thickness difference was now a factor of 2x instead of nearly a factor of 4x, it was deemed acceptable.

**Chamber pressure.** Using the composition from the combinatorial run with the lowest resistivity, an alloy target with equal parts of nickel and cobalt was reactively RF sputtered in 100% oxygen at 10, 5, and 2 mTorr in the traditional setup with an offset rotating substrate holder at a distance of 10 cm. A mixed gas composition was not used for reactive sputtering. Films in Figure 3-7 deposited at 2 mTorr maintained lower resistivity before and after heat treatment. Note that the variance is less than a factor of two and that the best resistivity is near  $2 \text{ m}\Omega\text{cm}$  (a conductivity of  $500 \text{ Scm}^{-1}$ ).

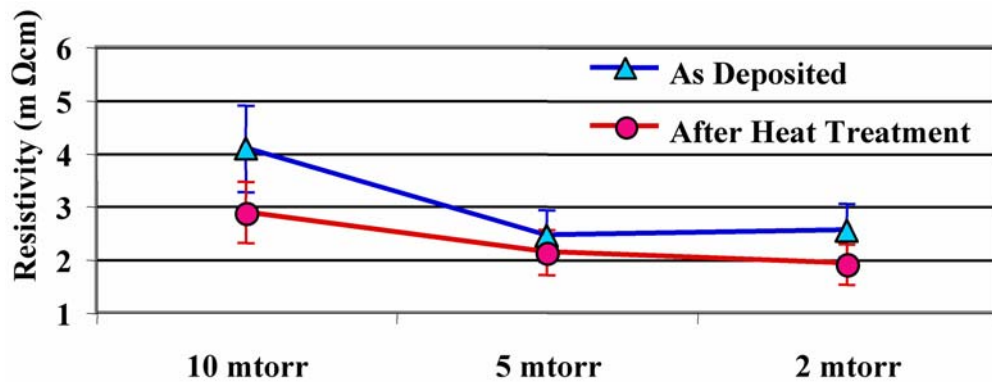


Figure 3-7. The effect of sputtering gas pressure on NiCo alloy sputtered  $\text{Ni}_{1.5}\text{Co}_{1.5}\text{O}_4$  thin film resistivity before and after 10 minutes at  $375^\circ\text{C}$  heat treatment.

While the results for the as-deposited samples are not in complete agreement, the general trend shows that the lower pressure in the range studied is better increase

conductivity. The result of decreased resistivity at a lower pressure this system exhibits is not surprising, but was previously unknown.

Molecules in a vacuum travel an average distance between molecular collisions which changes with pressure. This *molecular mean free path* ( $\lambda$ ) in Equation 3.1 has units of centimeters when pressure (P) is in units of Pascals (O'hanlon, 1989) and is determined by the number of molecules occupying the swept out volume. Higher pressure means more molecules per unit volume and a lower mean free path.

$$\lambda = \frac{6.6}{P} \quad (3.1)$$

In the vacuum chamber this becomes important as the molecules being sputtered from the target surface collide with and lose energy to other molecules before reaching the substrate for film formation. Pressure changes directly influence this mean free path. The experimental parameter of distance between target and substrate may also affect the energy of depositing atoms in a similar fashion.

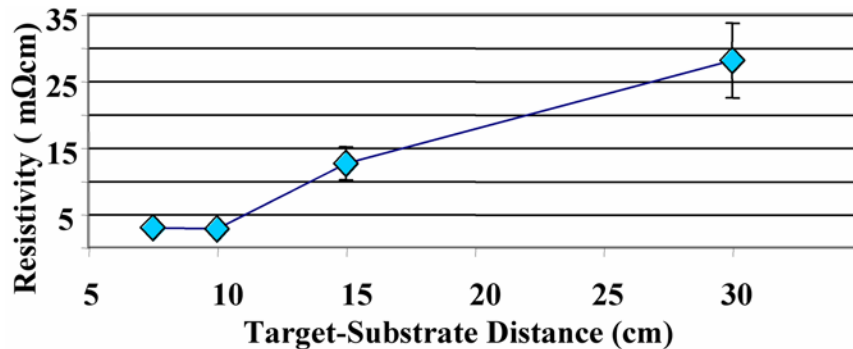


Figure 3-8. Target-substrate distance affects the resistivity of sputtered nickel-cobalt oxide thin films from a NiCo alloy target. Resistivity increases with distance.

**Target-substrate distance.** Increasing target-substrate distance (Figure 3-8) allows a larger area of deposition and enables uniform coating of multiple substrates with the proper substrate motion (see Appendix A for details on planetary rotation). Increased target-substrate sputtering distance results in increased resistivity. Discussion of the

effect evident by these data follows in the Optical Properties Section (3.3.2) and in the Film Structural Properties Section (3.3.3).

**Substrate material.** Substrate material in some cases had an effect on conductivity. Poly(ethylene-terapthalate), a polymer substrate used for OLEDs, had a detrimental effect on film conductivity. It is believed that carbon from the PET substrate reduced the nickel-cobalt oxide film somewhat, which resulted in the observed decrease in conductivity.

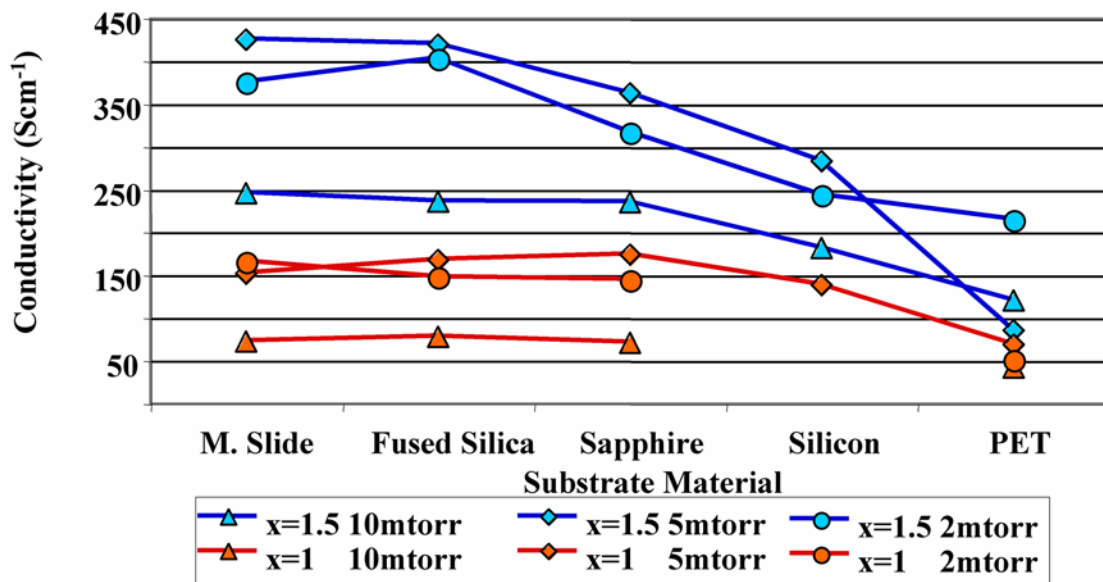


Figure 3-9. Conductivity of  $\text{Ni}_x\text{Co}_{3-x}\text{O}_4$  films on PET substrate is always less than films on other substrates by a factor of 2-4x for as-deposited samples for all pressures and compositions shown.

**Work function.** Sputter condition changes to nickel-cobalt oxide may also affect the work function, a property not reported in the literature. From UPS data, a work function was calculated by with Equation 3.2. An ultraviolet He I source with an energy of 21.218 eV (+ or - 0.001 eV) excites electrons across the band gap. A bias voltage ( $V_B$ ) of two different values was applied and the energy ( $E_{V_B\text{cutoff}}$ ) is extrapolated from Figure 3-10 (energy on the left side of the peak where intensity is zero). The work function is calculated by taking the known photon source energy, subtracting the bias

voltage, and then subtracting the measured valence band cutoff value. The detector work function is important to know also, but is calibrated out of this data and therefore not included in Equation 3.2.

$$\Phi = h\nu - V_B - E_{VBcutoff} \quad (3.2)$$

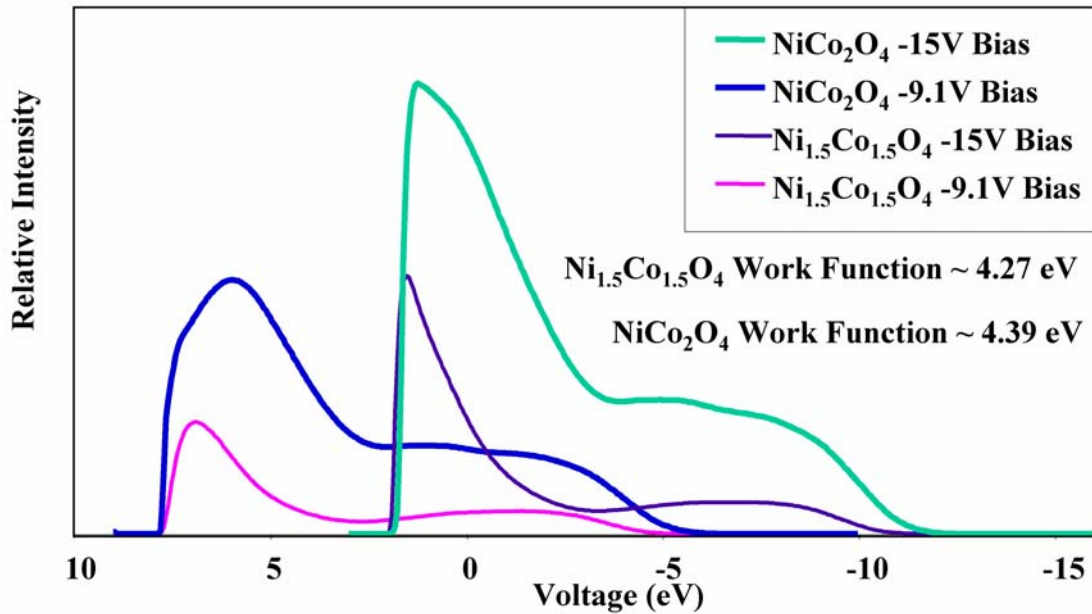


Figure 3-10. UPS work function measurement of NiCo<sub>2</sub>O<sub>4</sub> and Ni<sub>1.5</sub>Co<sub>1.5</sub>O<sub>4</sub> films. Higher nickel content shows a slightly lower work function. Work function values may track inversely with conductivity or increased nickel content.

Compositional differences of oxide films from sputtered NiCo and NiCo<sub>2</sub> alloy targets does not appear to have a dramatic effect on the work function, These results suggest that the work function may vary slightly with composition or conductivity. Assuming the variance is with conductivity, the work function would change with processing conditions. Additional work would be required to quantify this assertion. However, given the small change due to composition in the work function it is doubtful that processing conditions such as sputtering pressure or sputtering distance would have a significant impact on the work function value.

### 3.3.2 Optical Properties

Changes in processing of TCO films affects optical properties though with the opposite general trends of the electrical properties. Variation of optical transmission as a function of film composition has been reported previously (Windisch et al., 2001b).

Incident light impinging on a sample will become a sum of several interactions, including transmission, absorption, reflection, and scattering (Equation 3.3). Often absorption and scattering are assumed to be zero and the calculation simplifies to three terms.

$$I_0 = I_{trans} + I_{abs} + I_{refl} + I_{scatter} \rightarrow I_0 = I_{trans} + I_{refl} \quad (3.3)$$

**Gas composition.** Due to the thickness variation in the combinatorial sputtered films shown in Section 3.2.1, variations in transmission data will not necessarily represent changes with film composition or gas composition, so such data have been excluded from the optical property analysis. The optical transmission measurements would likely yield useful information if the films are of uniform thickness.

**Chamber pressure.** For films of the same composition deposited at different pressures, optical transparency was seen to vary from 5-10%. Transparency decreases with pressure (Figure 3-11) and increased conductivity, agreeing with reported conductivity and transparency relationships (Windisch et al., 2002b). Lower pressures from both compositions (x=1.5 and x=1) exhibit lower transmission. The absence of correction for silicon substrate limits the maximum transparency to 50%, but even with correction, the effect would be similar. Films on silicon substrates, shown in Figure 3-11, show that the transparency of the nickel-cobalt oxide films in the near- to mid-infrared regions (corresponding to light wavelengths of 2.5  $\mu\text{m}$  to 25  $\mu\text{m}$ ) if normalized to 50% would be well above that value.

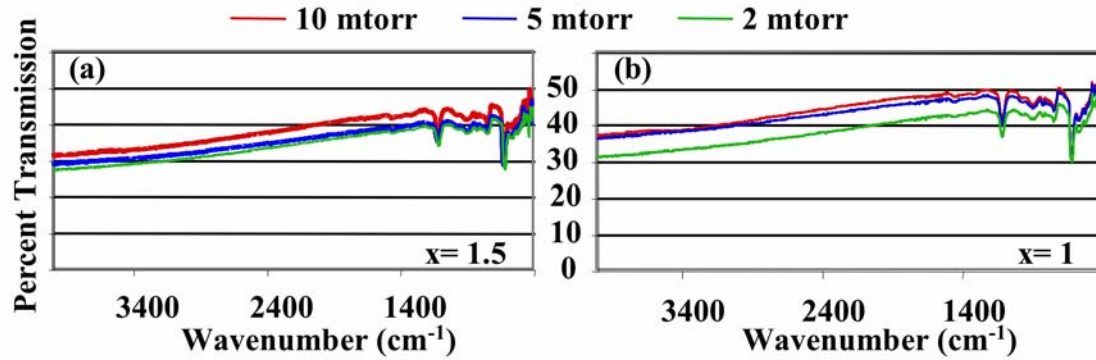


Figure 3-11. FTIR traces from of reactively sputtered  $\text{Ni}_x\text{Co}_{3-x}\text{O}_4$  thin films. (a)  $x = 1.5$  (from NiCo alloy target) and (b)  $x = 1$  (from  $\text{NiCo}_2$  alloy target) show the effect of pressure on transmission. Films nominally 50 nm thick are shown as a function of sputtering gas pressure.

The decrease in transparency seen with decreased sputtering pressure may be due to a change in the index of refraction of the deposited film likely caused by a chemical or structural change induced by the processing conditions. Changes in the index of refraction may result in a 3% change in transmission due to an increased absorption/damping region likely attributable to defects in the lattice.

The index of refraction shown in Equation 3.4 ( $n$ ), is the ratio of the speed of light in a vacuum ( $c$ ) divided by the speed of light in the material ( $v$ ).

$$n = \frac{c}{v} \quad (3.4)$$

A difference in index of refraction of two different materials across an interface results in a loss of transmitted light due to reflection at the interface. The reflected intensity is expressed in Equation 3.5 where  $n_1$  and  $n_2$  are the indices of refraction for the two materials. Percent reflection is the intensity of reflected light ( $I_{\text{refl}}$ ) divided by the incident light ( $I_0$ ) multiplied by 100. This expression is valid for transparent materials and neglects damping. Complex values of  $n$  could be used in the expression to take damping into account.

$$I_{refl} = I_0 \left( \frac{n_1 - n_2}{n_1 + n_2} \right)^2 \quad (3.5)$$

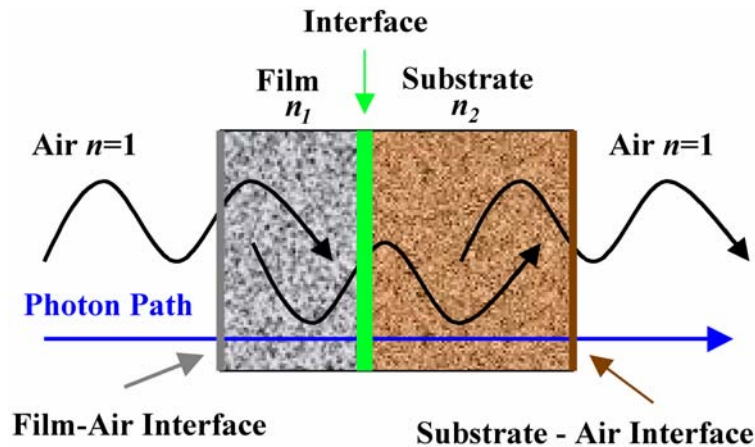


Figure 3-12. Optical transmission through a thin film. On a substrate, it requires a low index of refraction mismatch at all interfaces (to avoid complete reflection) and a low damping coefficient (to avoid extinction) for the particular wavelength of transmitted light (this picture does not show the effects of damping).

The index of refraction is important for TCO films because the light must pass through three interfaces as illustrated in Figure 3-12. A significant difference in index of refraction at any of these interfaces will result in increased optical reflection or damping with an associated loss in transmission. Losses due to reflection from index mismatches of nickel-cobalt oxide ( $n = 2.6-2.8$ ) on a silicon substrate ( $n = 3.5$ ) exceed 50% when damping is assumed to be zero. Absorption or damping mechanisms may include electron excitation with phonon emission (activation of lattice vibrations) and in reality are not zero, but are assumed to be so in Table 3-2.

Assuming that the process pressure causes a shift in the index of refraction from 2.6-2.8, the shift in transparency would be less than 3 percent (see calculation in Table 3-2). A shift greater than 3% could be attributed to a difference in thickness or possibly scattering from process-induced morphology changes, such as increased grain size or grain boundary area.

Table 3-2. Values of index of refraction for films and substrates are shown individually with calculated transmission losses due to interface index mismatch assuming no absorption or extinction.

	<i>n</i> of Film	Substrate	<i>n</i> of Substrate	% Loss in Transmission
NiCo <sub>2</sub> O <sub>4</sub>	2.6	Si	3.5 (1370 nm)	52.8
NiCo <sub>2</sub> O <sub>4</sub>	2.7	Si	3.5	53.6
NiCo <sub>2</sub> O <sub>4</sub>	2.8	Si	3.5	54.5
NiCo <sub>2</sub> O <sub>4</sub>	2.6	SiO <sub>2</sub>	1.46 (300-800 nm)	31.13
NiCo <sub>2</sub> O <sub>4</sub>	2.6	Al <sub>2</sub> O <sub>3</sub>	1.77 (300-5000 nm)	26.85

**Target-substrate distance.** The distance of sputtering between the target and the substrate also had an effect on the optical transmission from which an optical absorption coefficient is calculated. The absorption coefficient ( $\alpha$ ), given in Equations 3.6 and 3.7 multiplied by the film thickness ( $d$ ) is proportional to the intensity of light ( $I_{\text{trans}}$ ) detected after the beam passes through the film:

$$I_{\text{trans}} = I_0 e^{(-\alpha d)} \quad (3.6)$$

Percent transmission is the ratio of measured intensity ( $I_{\text{trans}}$ ) normalized to the background intensity ( $I_0$ ) and then multiplied by 100. When transmission has been measured at a specific wavelength and the film thickness is known, an absorption coefficient can be calculated (Equation 3.7).

$$\alpha = -\frac{1}{d} \ln \left( \frac{I_{\text{trans}} + I_{\text{refl}}}{I_0} \right) \quad (3.7)$$

Care must be taken to account for reflection ( $I_{\text{refl}}$ ) at the air-film, film-substrate, and substrate-atmosphere interfaces in order to obtain an accurate absorption coefficient (interfaces and reflectivity are shown in Figure 3-12).

The optical absorption decreases in Figure 3-13 with increased target to substrate distance. The resistivity trace from Figure 3-8 is included for contrast to show that the electrical properties are affected opposite to the optical properties.

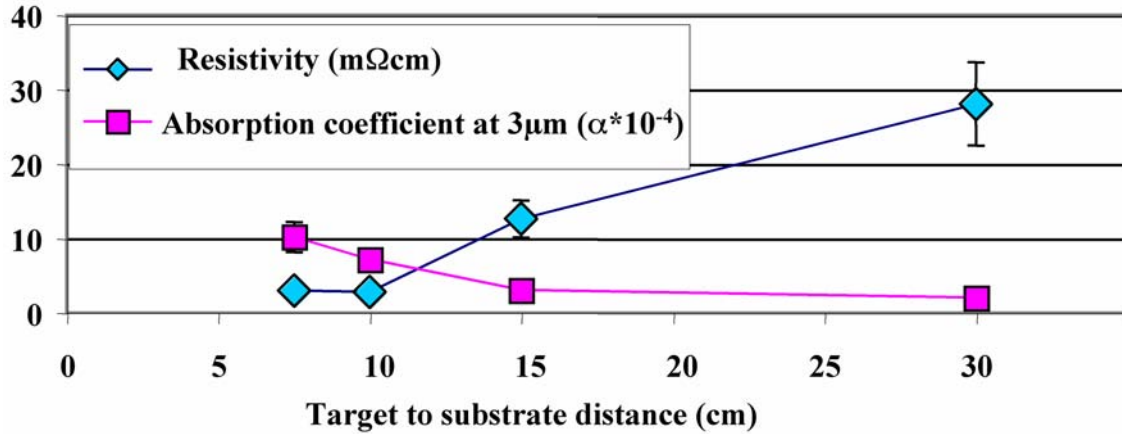


Figure 3-13. Target-substrate distance effects are opposite for the optical absorption coefficient and resistivity from sputtered nickel-cobalt oxide thin films from a NiCo alloy target. As distance increases,  $\alpha$  decreases. The optical absorption coefficient was calculated from a transmission measurement at 3  $\mu\text{m}$  (see Appendix C for absorption coefficient calculation details).

**Electrical band gap.** Sputtering condition changes will likely affect the transmission window of the produced films. Optical transmission spectra are often described by the electrical band gap, or energy of the forbidden region between the valence band and the conduction band. This band gap energy allows photons of a lower energy to pass through the material without exciting electrons from the valence band to the conduction band causing film coloration. Band gap values extrapolated from the Tauc's plot in Figure 3-14 consist of the square of the absorption coefficient multiplied by the photon energy plotted as a function of the photon energy. The plot is extrapolated down to an energy value at the x-axis, which is equal to the optical band gap. Band gap energies are shown in Table 3-3 as a function of nickel concentration. The effect on the

band gap from processing may be affected by process conditions, but that has not yet been determined nor is it available elsewhere in the literature.

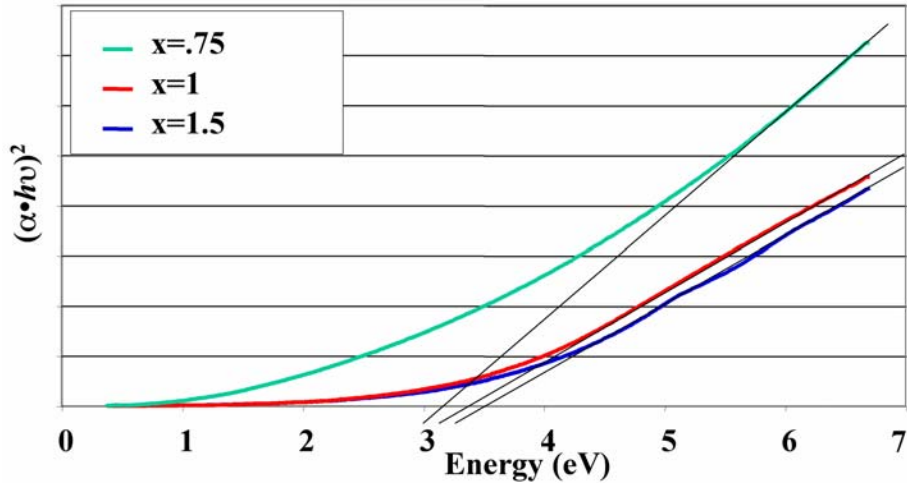


Figure 3-14. Tauc's plot of  $\text{Ni}_x\text{Co}_{1-x}\text{O}_4$  films show a band gap between 3 and 3.75 eV.

Table 3-3. Extrapolated band gap values lines in Figure 3-13.

	$\text{Ni}_{1.5}\text{Co}_{1.5}\text{O}_4$	$\text{NiCo}_2\text{O}_4$	$\text{Ni}_{0.75}\text{Co}_{2.25}\text{O}_4$
Band Gap (eV)	3.2	3.4	3.5

### 3.3.3 Film Structural Properties

The electrical and optical properties are dictated by the atomic structure and grain structure of the films. Structural changes of different target-substrate distances affect the film properties. Basic film properties such as surface and bulk composition are also briefly discussed in this section.

**Target-substrate distance.** Increasing target-to-substrate sputtering distance decreased absorption and increased resistivity for films of similar thickness. Modeling of x-ray diffraction data of  $\text{NiCo}_2\text{O}_4$  films deposited 5 and 15 cm from the target show a decrease in density as sputtering distance increased (see Figure 3-15).

The distance a sputtered metallic ion must travel through the oxygen plasma to get from the target to the substrate will determine its oxidation state and kinetic energy when

it reaches the substrate. The sputter deposition rate, or number of energetic particles incident on the surface, decreases with the square of the difference in distance. The ion flux from the target to the substrate will decrease at longer distances as seen by the fading of the plasma color from the cathode in Figure 3-16.

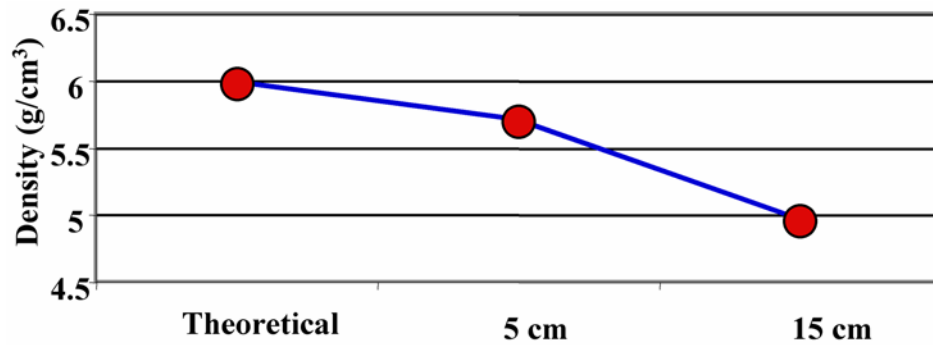


Figure 3-15. Increasing target to substrate sputtering distance decreases film density. Increased porosity is believed to decrease electrical conductivity and increase optical transparency.



Figure 3-16. An oxygen plasma shows a confined plasma region (white plume) near the target and a more dispersed plasma region (yellow-green) at longer distances.

Two factors may influence the film density with distance: (1) temperature of the substrate and (2) the mean free path of the gas. Substrate heating is affected by distance in two ways: (a) a longer distance would allow more time for oxidation reaction in the

plasma with less heating of the substrate from the exothermic oxidation reaction, and (b) a longer distance reduces the energy transfer attributed to the plasma-substrate interaction (the plasma is most energetic near the cathode surface). The two effects combined yield a lower density film at longer distances because a lower substrate temperature will not support surface diffusion required to increase the film density.

Decreased target-substrate distance shows an increase in conductivity likely due to the opposite effect. Oxidation of cobalt metal to cobalt oxide or the nickel metal to the nickel oxide on the surface along with increased surface-plasma interaction could provide heat to the surface allowing greater surface ion mobility to obtain an energetically favorable atomic arrangement. Increased substrate temperature allows diffusion for creating a denser matrix.

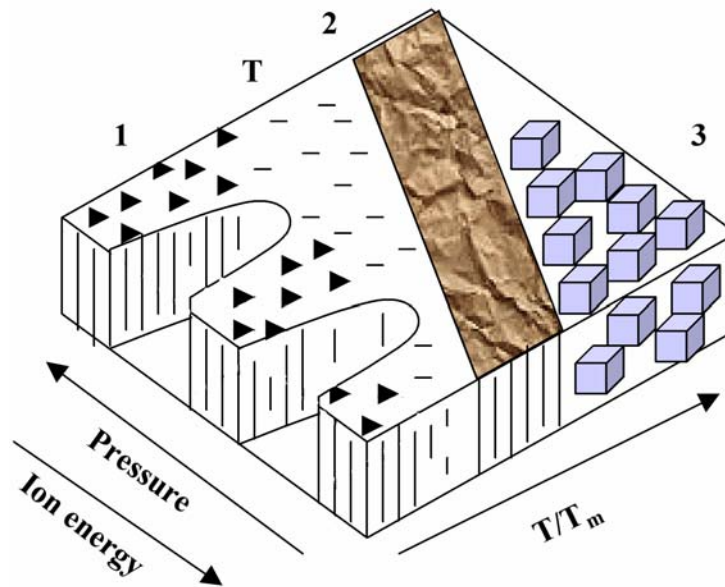


Figure 3-17. The three zone model described by Campbell for film growth in a vacuum (Campbell, 1996).

Campbell elaborates on a three zone model that explains the deposited films.

Figure 3-17 shows a schematic of the regions of film that are affected by the substrate temperature and the incident ion energy described by Campbell.

“At the lowest temperature and ion energy, the film will be an amorphous, highly porous solid with a low mass density. This is the first zone of the diagram. It is caused by the low adatom mobility of the growing film. Metal films deposited in this region can readily oxidize when exposed to air and so may also have high resistivities. If the chamber pressure is lowered or the substrate temperature is raised, the deposition process enters the “T” zone. Films deposited in this region are highly specular and have very small grains. For many microelectronic applications, this is the most desirable region of operation. Increasing the temperature and/or impinging energy further cause the grain size to increase. The second zone has tall narrow columnar grains that grow vertically from the surface. The grains end in facets. Finally, in Zone 3, the film has large 3-D grains. The surfaces of the films in the second and third zones are moderately rough and the films appear milky or hazy,” (Campbell, 1996, p.299)

Films deposited at closer distances are likely shifting to the T region from region 1 with an increase in temperature from the heat transfer of the plasma, and from the ions being more energetic in the plasma. As the pressure decreases, the effect is similar.

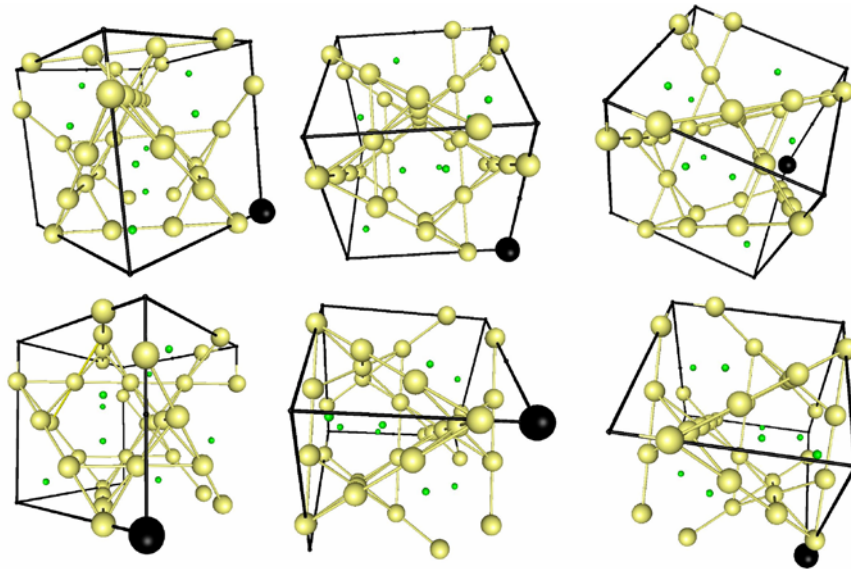


Figure 3-18. A spinel unit cell at different angles of rotation containing octahedral atoms, minimized tetrahedral atoms, and select oxygen atoms for points of reference such as the enlarged black oxygen atom. Lines along octahedral sites are to simply illustrate a crisscrossing three-dimensional network with possible routes for conduction.

Conductivity in the spinel structure may be relatively high due to the multiple pathways for carrier movement to occur. The cation arrangement of the spinel structure allows isotropic electrical conduction that is not restricted to a single dimension,

direction, or a preferred plane. Conductivity likely occurs in all three-dimensions through the octahedral cation network, which forms crisscrossing lines as shown in Figure 3-18. This simplified illustration shows only select reference oxygen ions. The actual network pathways along the octahedral-oxygen ions would be similar, but the path would include an alternating oxygen anions along the path between each cation.

Closer target-substrate distance may produce more of the “cross-linked” conduction lines connections as the film is denser. Greater distance would equate to more broken conduction lines from pores or voids. Varying the distance and angle of incidence may also change the stoichiometry in some cases, which will result in a change in transparency and conductivity. Slight stoichiometry deviations such as increasing oxygen content with longer target-substrate distances may be a possible explanation to the observed property changes.

**Film structure.** The grazing incident x-ray diffraction traces shown in Figure 3-19 appear to be spinel, but do not match the diffraction pattern exactly. X-ray scans of the sputtered nickel-cobalt oxide films are similar to the reference powder diffraction file 73-1702. As such, these films are classified as *spinel-type*. Deviations occur in peaks near 60°. The peak at 55.5° does not exist in the green trace and both of the 59.5° and the 65° peaks appear to be slightly shifted to lower angles.

As suggested earlier, disorder aids in polaron formation with an associated increase in conductivity. An understanding of these deviations and abnormalities may provide insight on carrier generation to further improve film properties such as conductivity. Distortions in the lattice may be due to one or both of the following effects: the Jahn–

Teller effect (Dionne, 1990), or the Verwey transition (charge ordering) effect (Verwey & Haayman, 1941; Verwey et al., 1947; Verwey, 1939).\*

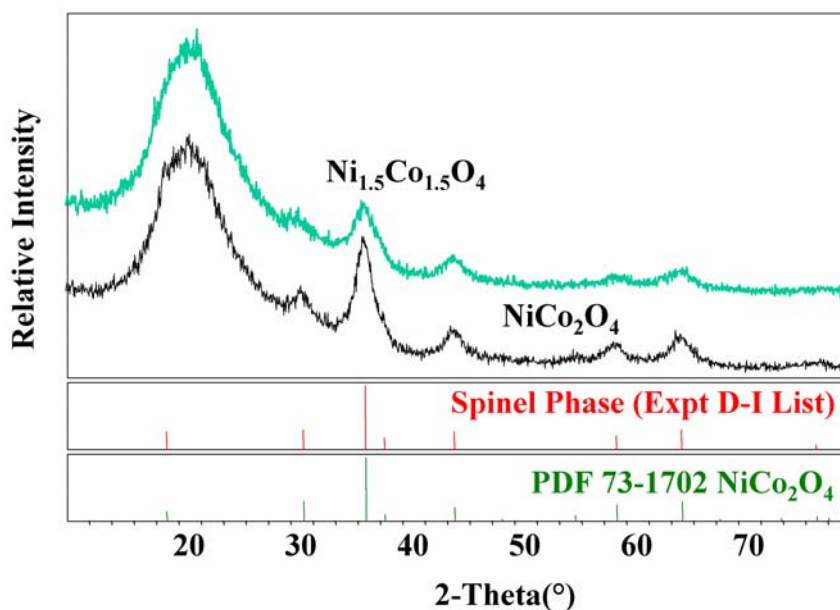


Figure 3-19. Grazing incident x-ray diffraction from sputtered films 50 nm thick appear to be structured as spinel-type, but do not match exactly.

The Jahn-Teller effect is a distortion in bond length that occurs allowing the  $t_{2g}$  or  $e_g$  orbitals to shift energy and lose degeneracy to obtain lower system energy. It is possible that the cubic spinel lattice may slightly distort to contain some tetragonal unit cells and still be spinel-like (Blasse, 1963). Care must be taken in attributing this shift only to the Jahn-Teller effect because it may also be due in part to a Verwey-type transition effect.

Verwey postulated that the cation arrangement and charge distribution with respect to the tetrahedral and octahedral sites being occupied may change at a given temperature. The spinel may shift from normal to inverse. Verwey's system was the  $\text{Fe}_3\text{O}_4$  spinel. Since nickel-cobalt oxide is isostructural with  $\text{Fe}_3\text{O}_4$ , it is possible that the Verwey

\* See Appendix C for more information

transition may occur during heated processing of these thin films which will be discussed in Section 3.3.4 (Verwey & Haayman, 1941; Verwey et al., 1947; Verwey, 1939).

Distortions can affect the film properties although the qualitative knowledge at this point suggests that distortion may have a role, but exactly what that role is has not been determined. Literature data on these nickel-cobalt oxide thin films has concentrated on surface sensitive techniques such as XPS for stoichiometric determination. Bulk film composition may aide in determining the role of distortion or its origin.

**Film surface and bulk composition.** SIMS data in Figure 3-20 shows that the surface composition may be different from the bulk, probably due to the well understood SIMS shift from preferential sputtering making the film surface and interface appear compositionally incorrect. Bulk studies may reveal more information regarding the film composition effects on the optical and electrical properties. The film surface shows nearly equal amounts of nickel and cobalt, while the bulk shows more cobalt.

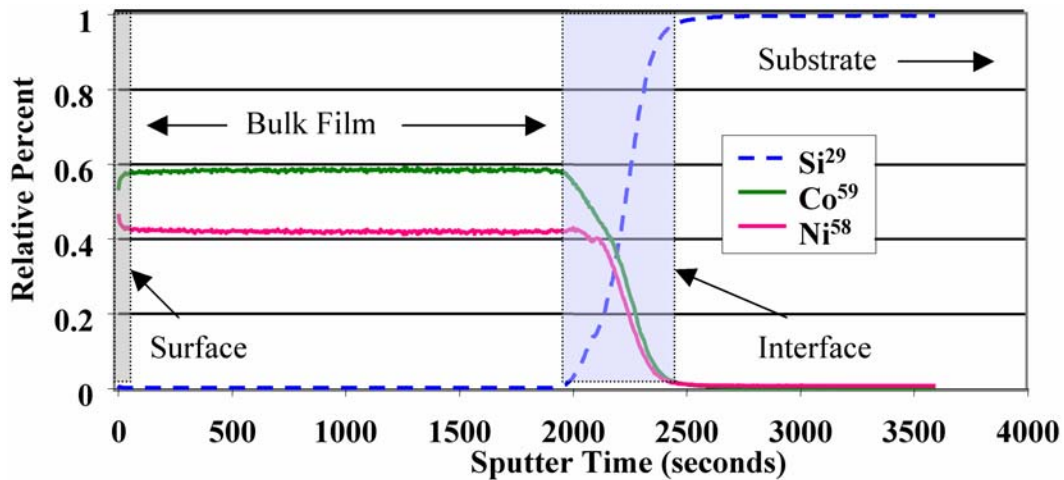


Figure 3-20. Sims profile of nickel-cobalt oxide thin film shows surface composition appears to differ from the bulk composition. XPS analysis for chemical composition on the surface agrees with SIMS data.

Calibration standards were not available for this material. Effects such as preferential sputtering have not been considered, but may take into account phenomena

that occur on the surface during sputter-etching. Sensitivity factors for the nickel-cobalt oxide matrix have been calculated using XPS as a SIMS calibration, however the results may be skewed due to the nature of sputter etching that occurs in the individual systems to remove material and acquire the depth profiles. XPS depth profiling was done with an argon sputtering source to remove surface layers. SIMS was done with an oxygen source and therefore the oxygen is not included with the depth profile in Figure 3-20. The results may not accurately represent the material due to the possible preferential removal of either metal species from the exposed surface during the depth profiling. SIMS did show that in the bulk the film composition is constant.

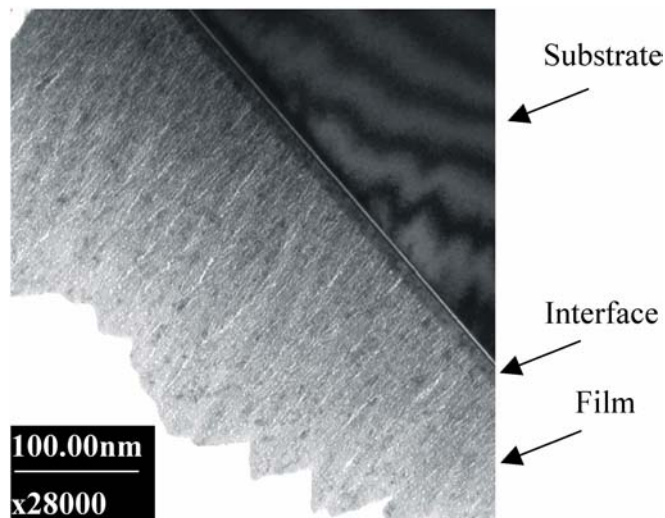


Figure 3-21. Cross-sectional TEM image of sputtered nickel cobalt oxide films on (100) silicon. Nickel-cobalt oxide thin film grows in multi-grained columns.

Micrographs from a transmission electron microscope (TEM) show that the films were homogeneous from the surface down to the interface. The interface is interesting. Notice the dark band that runs diagonally from top center to lower right side at the film-substrate interface in Figure 3-21. The white line is the native silicon dioxide layer found on silicon wafers and is typically 2 nm thick. The dark region at the interface may be a metallic growth layer and the cause of poor transmission and high conductivity. A highly

conductive metal alloy film, thin enough to be transparent and undetectable by XRD could be part of the dark band at the interface surface. It may be a substoichiometric phase that acts as an interface layer on the silicon substrate. Another possibility is that it could include a metal-silicide layer of reacted metal with the surface of the substrate. Nickel silicide is used in silicon wafer fabrication processing as an interconnect because of its high conductivity, but nickel or cobalt silicide optical properties have not been reported. Both are thermodynamically stable and could form as cations migrate through the silicon dioxide barrier layer into the bulk wafer. The SIMS profile in Figure 3-20 does not agree with the data in Figure 3-22 where increased concentrations of cobalt is detected at the interface and substrate regions which would substantiate this claim.

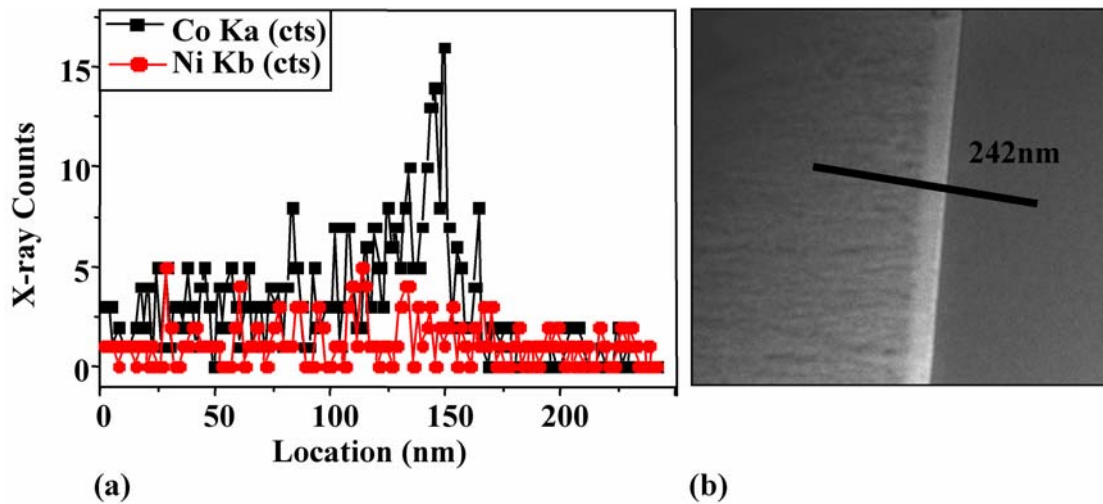


Figure 3-22. Nickel-cobalt oxide-silicon wafer interface. (a) Energy dispersion spectroscopy (EDS) of area the shown in (b), the STEM micrograph of film-substrate interface scan region used for EDS analysis in (a).

The interface layer is cobalt rich according to the EDS data from the STEM shown in Figure 3-22. The cobalt rich region may be part of a substoichiometric spinel film at the interface between the nickel-cobalt oxide and the silicon dioxide native layer on the surface of the silicon wafer. Closer inspection of the SIMS data in Figure 3-20 shows the

cobalt content falls off and the nickel content remains steady before tailing off. It is possible that this is merely evidence of the preferential sputtering artifact. EDS does not rely on film layer removal for characterization as SIMS and is therefore not subject to preferential sputtering effects. The cobalt rich region detected by EDS is probably not indicative of silicide formation, otherwise the silicon trace in the SIMS depth profile would have a spike in it representing the metal-silicide layer was present. A closer examination reveals a change in slope of the silicon trace about mid way through the interface region. This slope change could indicate a metal-silicide formation, but it could also result from the native silicon dioxide layer, which would have a different sputtering rate than unoxidized silicon. The data are best interpreted to mean that the film-substrate interface consists of a cobalt rich nickel-cobalt oxide layer on the native silicon dioxide surface of the silicon wafer.

### **3.3.4 Post Deposition Heat Treatment**

Heat treatment of the nickel-cobalt oxide films result in increases in conductivity with concomitant decreases in transparency depending on the method used for heat treatment and the temperature involved . As mentioned in Chapter 2, temperatures above 400°C cause phase separation of nickel oxide within the spinel film. Film properties degradation occurs over periods of days for as deposited and annealed samples left exposed to air at room temperature. Typical degradation of conductivity is a factor of two after one week. Successive heat treatments can return the film conductivity to nearly the same value as before the degradation if the cooling rate is on the order of ~150°C/min. When the cooling rate is less than 15°C/min, the film conductivity can be artificially *aged* to the degradation value had the sample had been left exposed to air for

several days. Transparency responds the opposite to conductivity after heat treatment activity.

**Heat and conductivity.** Figure 3-23 shows a plot of the natural log of conductivity plotted against the reciprocal of temperature multiplied by 1000. As temperature increases from 300 K to 625 K, shown by the blue traces for the two different composition films, the conductivity measured at temperature increases. These particular films were first heat treated at 375°C (a  $1000/T$  value of 1.54) for ten minutes and then rapidly quenched to room temperature before commencing the heated conductivity measurement. The conductivity increases with increasing temperature.

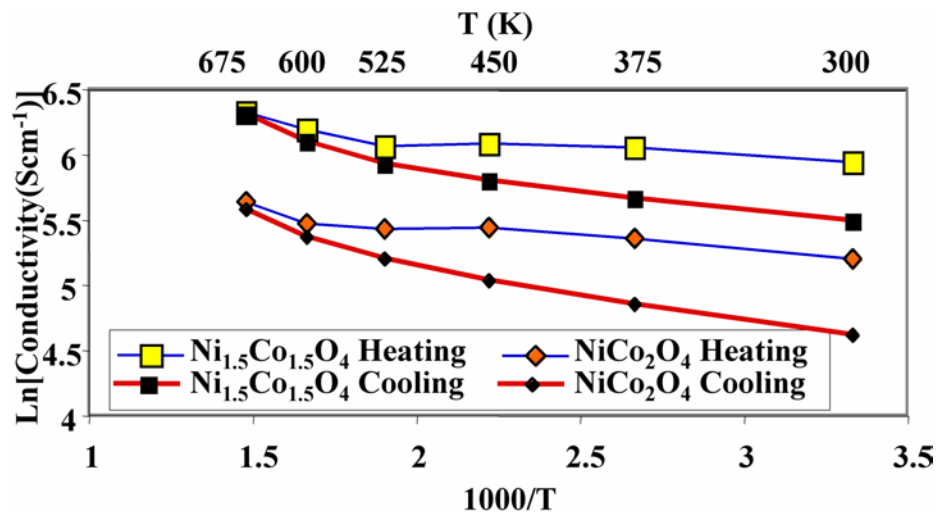


Figure 3-23. An Arrhenius plot of conductivity and the reciprocal of temperature (K) shows that at high temperatures, the film conductivity is high. A temperature of 525 K graphed near 1.5 on the abscissa divides the low temperature region on the right from the high temperature region on the left. The two regions have different activation energies for electrical conduction. The heating and cooling rate is limited to a maximum of 15°/min to avoid instrument damage.

Notice the difference in conductivity at the same temperature upon cooling from the highest temperature shown by the red curves. The room temperature conductivity upon cooling is always below its original value. There is a temperature where the heating and cooling data are nearly superimposed above, but depart below. Windisch et al.

reported this anomaly of conductivity being different for two regions of slope associated with each of the heating and cooling curves, and have different slopes versus temperature at high versus low values (Windisch et al., 2002b).

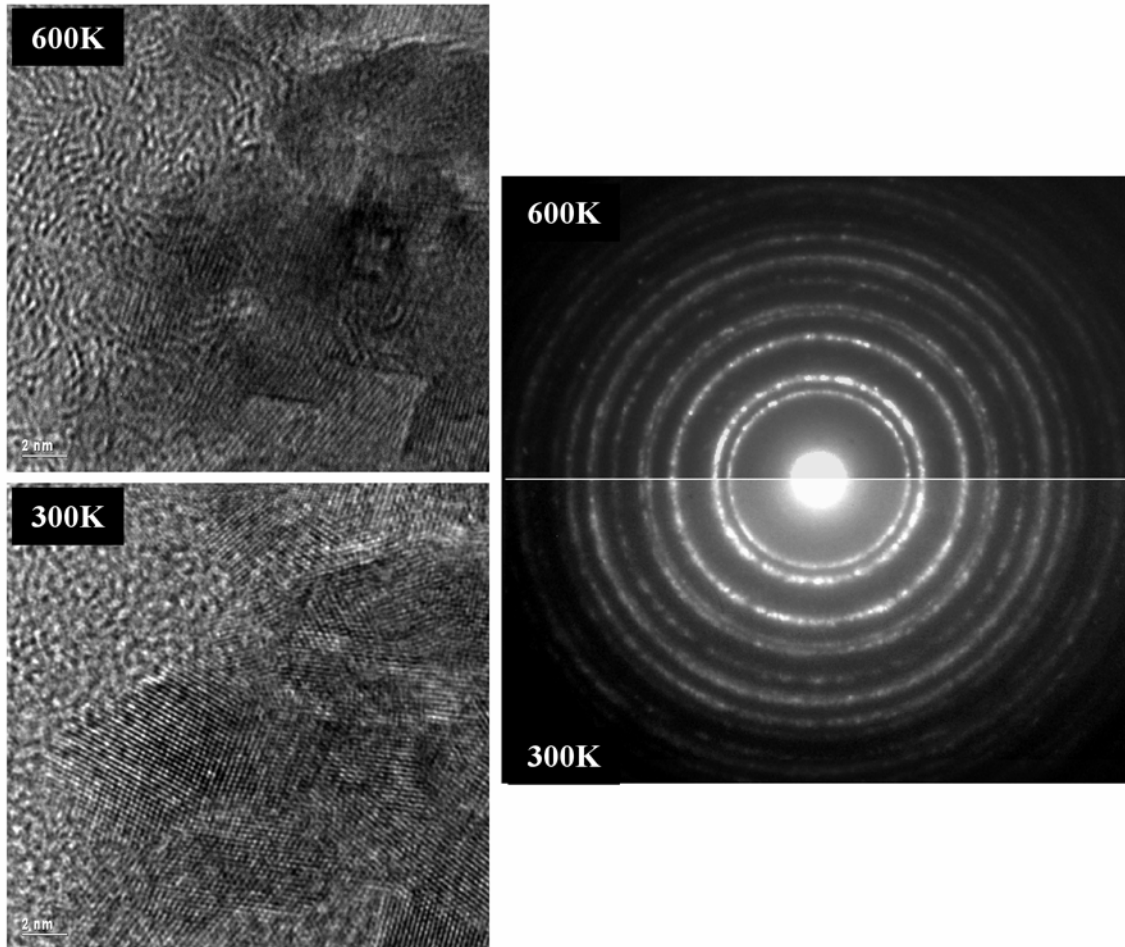


Figure 3-24. TEM image and diffraction patterns at 300 K and 600 K showing no detectable structural changes for the two temperatures.

Their speculation was that the transition could be the result of a Verwey transition near 525K that accounts for the change in slope of both the heating and cooling curves. Verwey et al. described the a temperature transition in  $\text{Fe}_3\text{O}_4$  in terms of an order/disorder transition resulting from the preferential ordering of the cations which changed the activation energy for electrical conduction (Verwey & Haayman, 1941; Verwey et al., 1947; Verwey, 1939). Rather than being a Verwey transition, it could be a

structural transition, a magnetic transition or possibly a mobile species within the lattice that has a different hopping activation energy triggered at a higher temperature.

The explanation for the effects of heat treatment is open to speculation. One such speculation invalidated by Figure 3-24 is that of a structural transformation. If a structural transformation occurred, the TEM diffraction pattern generated at 300 K would be different from the pattern at 600 K. No change is indicated, suggesting that no structural changes occurred and therefore rules out the Jahn-Teller effect as a significant contributor. It is, however, possible that the metastable state quenched in relaxed out before the STEM was performed or was processed out as the sample was prepared or during the analysis from localized electron beam heating. If the 600 K temperature experiment was conducted first then the structure is expected to be similar at 300K.

Magnetic measurements would be required to invalidate the suggestion of a magnetic transition. Samples were run on a vibrating sample magnetometer (VSM), but no significant hysteresis could be detected either due to lack of a transition or more probably due to a lack of sensitivity because the film was too thin. A magnetic transition such as a spin state realignment triggered at a specific temperature may correlate with a Verwey transition in that the arrangement of the cations and ordering/disordering of their charges may contribute or detract from a magnetic domain arrangement of the crystal. This is still unknown and could be the subject of a future study.

The last suggestion was that a mobile species could be the cause of the change in electrical conductivity slope upon heating. The only mobile species in the lattice is oxygen. Oxygen is typically present as  $O^{2-}$  anions occupying the 32 available anion sites. Oxidizing conditions during sputtering and heat treatment may allow excess atomic

oxygen to adsorb on the surface from dissociated carbon dioxide, water molecules, or molecular oxygen. Oxygen in the spinel cell would not necessarily be restricted to one site only and at elevated temperatures may have enough energy to site hop or form Frenkel defects involving oxygen ions (Callister 1997). In addition, a superstoichiometric film could result in the lattice in the presence of  $O^{1-}$ . These oxygen defects could add additional electrical carriers to increase conductivity and will be further discussed below.

**Effect of heat treatment cooling parameters.** Film cooling rate also has an effect on the observed properties. Figure 3-25 shows the effect of cooling rate on transmission in the visible and near infrared regions. Optical transmission measurements were collected after quenching from the heat treatment described earlier, and after the temperature dependent conductivity measurements shown in Figure 3-23.  $Ni_xCo_{3-x}O_4$  films where  $x = 1$  are lower in conductivity overall than the films where  $x = 1.5$ .

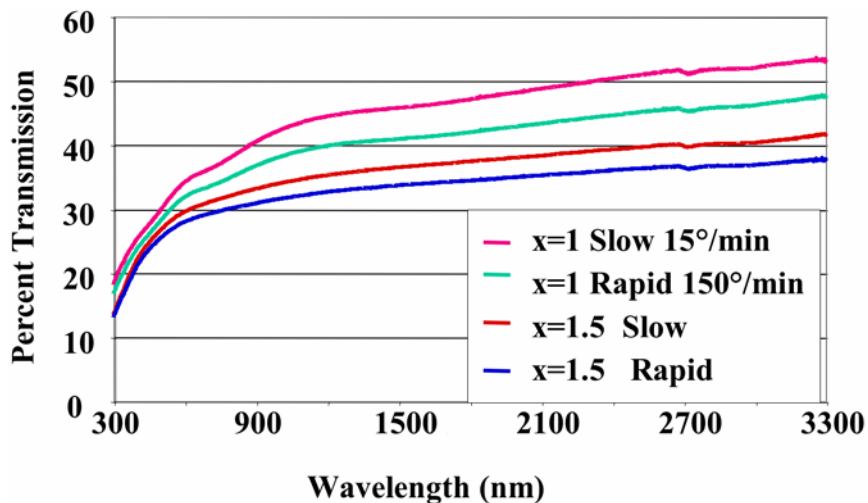


Figure 3-25. Effects of heat treatment cooling rate after heat treatment on optical properties of  $Ni_xCo_{3-x}O_4$  samples from Figure 3-23.

Heating alone does not ensure high conductivity. When cooled slowly, the conductivity degrades rather than improves. Conductivity can be increased by up to an

order of magnitude by quenching rapidly from 375°C to room temperature by using a large heat sink versus slowly cooling the sample at a controlled 10-15°C per minute.

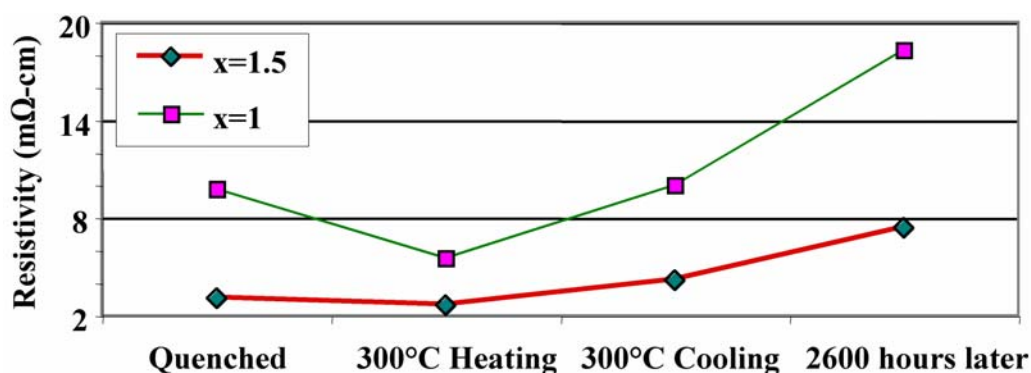


Figure 3-26. Resistivity of  $\text{Ni}_x\text{Co}_{3-x}\text{O}_4$ . (1) quenched to room temperature after heat treatment at 375°C for 10 minutes in air, (2) at 300°C, the first point of the temperature dependent conductivity measurement on the heating cycle, (3) at 300°C, the last point of the temperature dependent conductivity measurement on the cooling cycle, and (4) ~16 weeks after the cooling heat treatment.

**Effect of time after heat treatment.** Samples exposed to ambient atmosphere for days to months after quenching exhibited resistivities that slowly increase by a factor of two or more. Figure 3-26 shows a  $\text{Ni}_{1.5}\text{Co}_{1.5}\text{O}_4$  sample after a heat treatment cycle.

**Discussion of heat treatment effects.** Heat treatment of nickel-cobalt oxide thin films has an appreciable effect on both optical transmission and electrical conductivity. Electrical conductivity improvements are a factor of cooling rate with the optical properties degrading with increased conductivity. Heat treatment may either repair or induce defects depending on the cooling procedure. Since the phase transition does not appear to be probable, it is possible that localized defects form from atomic disorder or cation disorder, or Frenkel defect oxygen and carriers get trapped in these locally deformed regions becoming polarons. Disorder increases the number of polarons in the lattice and therefore increases the conductivity. Quenched samples have lower activation

energies for conductivity in both low and high temperature regions compared to slowly cooled films (summarized in Figure 3-27).

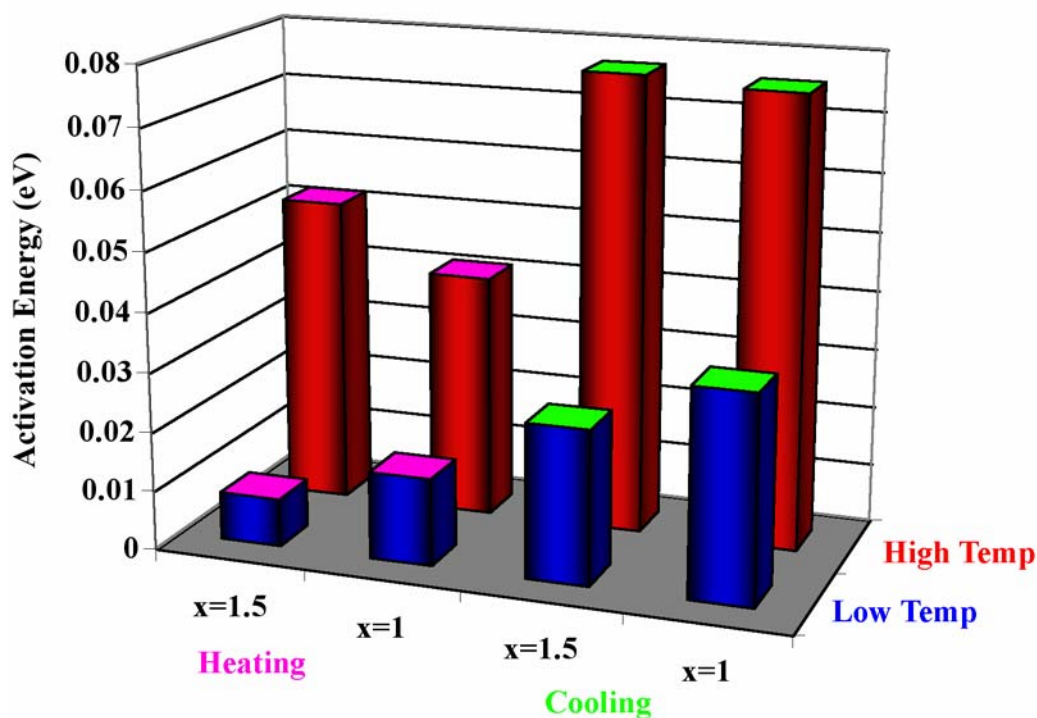


Figure 3-27. Rapidly quenched sample activation energies of  $\text{Ni}_x\text{Co}_{3-x}\text{O}_4$  change after heating when they are slowly cooled.

Activation energies calculated from Figure 3-23 and included in Table 3-4 show that the values calculated from heating a quenched sample are all lower than those activation energies calculated from slowly cooling the same samples. Rapid quenching must therefore lock in some degree of disorder or defect structure.

Table 3-4. Increase in activation energies of  $\text{Ni}_x\text{Co}_{3-x}\text{O}_4$  from the temperature regions in Figure 3-23 graphed in Figure 3-27.

	Heating to cooling low temp	Heating to cooling high temp
x=1	0.020	0.035
x=1.5	0.018	0.025

The possibility that a magnetic or physical phase transition could be the cause of the two different transition regions can be ruled out by the same arguments advanced in

the heat and conductivity subsection above. Transport of surface adsorbed species such as oxygen into the lattice to increase the oxidation state of nickel or cobalt to form more polarons and increase conductivity would be a thermally activated process. STEM data does not show a significant structural change with heat treatment, which indicates that the bulk of the grains do not experience the increased oxygen effect, but the grain boundaries may accommodate extra oxygen. These highly defective regions with excess oxygen would be *frozen* in the film when it is rapidly cooled. The steady state preferred structure would not be achieved due to kinetic limitations upon cooling. The thin film would relax to this condition perhaps by the excess oxygen escaping. These extra defects may distort the unit cell via the Jahn-Teller effect or a Verwey charge ordering effect just enough to allow a lower ensemble average of activation energy by increasing the distribution of activation energies for individual sites. A model that approximates this disorder idea is presented in Chapter 6.

Another possible explanation for the increased conductivity at higher temperatures would be densification due to heat treatment. Heat would result in increased density from the increased solid state diffusion and the increase in film conductivity could result from elimination of voids. However, it is unlikely that porosity would increase at low sample cooling rates making this explanation less likely. XPS data showed high surface concentrations of carbonyl on the nickel-cobalt oxide films (Windisch et al., 2001a; Windisch et al., 2001b; Windisch et al., 2002b). If carbon was to permeate the lattice and take oxygen to form carbonates upon cooling, this could increase the disorder during heating. If this mechanism is operative, the data suggest that carbonates would decompose and reoxygenate the lattice or even form bubbles of carbon dioxide molecules

thereby increasing porosity. While this idea cannot be entirely discounted, it is considered unlikely that the carbonate will decompose upon cooling.

### 3.4 Summary and Conclusions

The combinatorial approach is effective for depositing a film with a continuously variable composition over a large area in one run. The effects of gas composition during combinatorial sputtering and the effects of total chamber gas pressure and different target to substrate distances using single target sputtering in the offset rotation setup made up this study.

Optimum conductivity is achieved from combinatorial films containing equal parts of nickel and cobalt when sputtered in a gas mixture of 50% argon and 50% oxygen. The best film conductivity of  $375 \text{ Scm}^{-1}$  may be a result of ideal growth conditions with the gas mixture promoting complete oxidation and a higher deposition rate.

The gas pressure study shows that a chamber pressure of 2 mTorr yields the highest reported film conductivity to date at  $500 \text{ Scm}^{-1}$  compared to the 5 mTorr ( $400 \text{ Scm}^{-1}$ ) and 10 mTorr ( $333 \text{ Scm}^{-1}$ ) following rapidly quenched after heat treatment. This enhanced conductivity is attributed to a higher growth rate and increased adatom mobility during growth due to the lower molecular mean free path.

Increased distance of target to substrate decreased the film density increased film porosity and decreased conductivity, but increased transparency. Target-substrate distance effects on the film density are believed to be controlled by phenomena similar to those from lower pressures i.e. higher surface mobility from depositing species due to less gas phase scattering. Less plasma-film interaction at longer distances may also be a factor. Closer target-substrate distances result in denser more electrically conductive films with lower optical transmission, opposite of the films deposited at longer distances.

Heat treatment showed improvement in conductivity when films were rapidly quenched and degradation when slowly cooled. Transparency once again behaved opposite to the electrical conductivity. Temperature dependent conductivity showed that after a rapid quenching heat treatment, the activation energy of conduction is lower than from a film that was slowly cooled. This heat treatment cooling rate effect is a new discovery for this system and is believed to be due to excess oxygen in the lattice. Rapid cooling from heat treatment at 375°C to room temperature may lock in defects that increase the concentration of polarons. Slow cooling allows them to *anneal* out, resulting in improved transparency across the infrared region and lower conductivity.

Band gaps of 3.2 and 3.5 eV and work functions of 4.39 and 4.27 eV are reported for  $\text{Ni}_x\text{Co}_{3-x}\text{O}_4$  at  $x = 1$  and  $x = 1.5$ , respectively. These band gap and work function values have not previously been reported to date.

## CHAPTER 4 THE ROLE OF LITHIUM

### 4.1 Introduction

Adding lithium to the nickel oxide, cobalt oxide, and nickel-cobalt oxide systems is a currently acceptable practice in lithium battery electrodes (Appandairajan et al., 1981; Banov et al., 1995; Benqlilou-Moudden et al., 1998; Carewska et al., 1997; El-Farh et al., 1999; Fransson et al., 2002; Ganguly et al., 1997; Gendron et al., 2003; Gover et al., 1999; Han et al., 1999; Julien, 2000; Julien et al., 1999; Kim et al., 2002; Koumoto & Yanagida, 1981; Moshtev et al., 2002; Moshtev et al., 1996; Moshtev et al., 1999; Robertson et al., 1999; Seguin et al., 1999; Shirakami et al., 1998; Stoyanova et al., 1997; Yoshimura et al., 1998; Zhecheva et al., 1996). The same is true for molten carbonate fuel cell electrodes (Fukui et al., 2000; Kuk et al., 1999; Kuk et al., 2001). Improvement in some properties resulted as lithium was added in specific quantities, however the material requirements for battery electrode and fuel cell electrode technology is fundamentally different than those for optoelectronics. Optoelectronics is primarily concerned with photon-solid interactions and electrical conduction. Batteries and fuel cells deal with electrochemical properties such as ionic conduction and intercalation (Koumoto & Yanagida, 1981; Wolverton & Zunger, 1999; Zhecheva et al., 1996). Many studies have been done with lithium in nickel-cobalt oxide (Puspharajah et al., 1997; Urbano et al., 2001), but none have attempted to probe nickel-cobalt oxide with added lithium for use as an infrared-transparent thin-film electrode.

Initial studies suggested that the addition of lithium to the nickel-cobalt oxide system would favorably improve conductivity and transparency based the fact that lithium could be incorporated into the spinel unit cell at a tetrahedral site (Appandairajan et al., 1981; Windisch et al., 2001a; Windisch et al., 2002a; Windisch et al., 2001b; Windisch et al., 2002b). Lithium, a monovalent ion (for general spinel structure information see (Azaroff, 1960; Kingery et al., 1975; Smyth, 2000)), could substitute for divalent or trivalent cobalt resulting in a net negative charge in the lattice. An adjacent cation in a tetrahedral site should then increase its oxidation state to maintain charge neutrality in the crystal. It is also possible, though not as likely, that a neighboring octahedral cation could increase its oxidation state by donating an electron to balance the charge offset from the lithium substitution on the tetrahedral site (Appandairajan et al., 1981). Such an increase in oxidation state will change the bonding nature at that site (create a polaron) resulting in increased conductivity.

This prediction assumes that the lithium will substitute for a cation on a tetrahedral site, however it is possible that lithium, being a small atom, may prefer to enter the lattice as an interstitial and produce an opposite effect. Interstitial lithium would add a positive charge, likely requiring a neighboring cation to reduce its oxidation state. The result would be a net decrease in conductivity from polaron annihilation. Assuming the first case, XPS binding energies might be expected to scale or shift with lithium addition, as would the lattice parameter. Changes in transparency and electrical conductivity may occur as well.

Preliminary proof of principle data are shown in Figure 4-1 for contrast and comparison to experimental results of this study. A favorable improvement in resistivity

for solution deposited nickel cobalt oxide with 10% addition of lithium was recorded. The improvement from lithium in the solution nickel-cobalt oxide films combined with an order of magnitude increased conductivity reported in the literature for sputter deposited versus solution deposited films (Figure 2-8) provided motivation to determine the effects of lithium in sputtered samples. Experimental results will show that lithium behaved in a manner unexpected and yielded new and interesting details of the nickel-cobalt oxide system with and without lithium doping.

This chapter focuses on the electrical, optical, structural, and chemical changes produced by the presence of lithium in the nickel-cobalt oxide system. Electrical properties were largely of interest with respect to heat treatment parameters and activation energies of conductivity to explore disorder in the system. Optical properties provided insight to understand the electrical results that were confirmed by both the structural and chemical analysis.

## **4.2 Experimental Procedure**

### **4.2.1 Deposition**

A solution deposition method produced some of the films for this study<sup>\*</sup>. Solutions of metal nitrates and a combustion agent are mixed in aqueous solution and eye-dropped onto the substrate just before spinning at 3500 rpm for ~30 seconds. Placing the wet film substrate on a hot plate at ~375°C ignites the glycine combustion agent included in the solution to decompose the nitrates and produce a uniform film ~50 nm thick.

Both traditional and combinatorial films were sputter deposited<sup>\*</sup> in a vacuum chamber evacuated to near  $1 \times 10^{-6}$  Torr and backfilled to 10 mTorr for all depositions. Reactive RF sputtering was performed in 100% oxygen using alloy target while

---

<sup>\*</sup> Additional details of solution and sputter deposition are included in Appendix A.

sputtering of oxide targets was performed with 50% oxygen and 50% argon. Oxide targets of  $\text{Ni}_{1.5}\text{Co}_{1.5}\text{O}_4$  and  $\text{Ni}_{1.35}\text{Co}_{1.35}\text{Li}_{0.3}\text{O}_4$  were used in the combinatorial setup to deposit a film with a graded lithium concentration (schematic in Figure 3-1).

#### 4.2.2 Characterization

Film thickness was measured with an optical or stylus profilometer. X-ray reflectivity (XRR) measurements of select films provided confirmation of the profilometry data (See Appendix B for more information on characterization techniques and data). Electrical measurements conducted in a van der Pauw apparatus provided resistivity values when combined with measured film thickness. Temperature dependent van der Pauw data were collected from room temperature up to 675 K.

Fourier transform infrared (FTIR)\* (Brundle et al., 1992) was used to measure film transparency with respect to air and with respect to the silicon or sapphire substrate over the range of  $4000\text{ cm}^{-1}$  to  $400\text{ cm}^{-1}$  after 2 minutes of a nitrogen purge. A dual beam ultraviolet-visible spectrometer was used to measure transparency from the ultra violet region to the near infrared region (200 nm-3300 nm). The deposited film composition was determined using x-ray photoelectron spectroscopy (XPS)\* (Brundle et al., 1992) and secondary ion mass spectrometry (SIMS)\* (Brundle et al., 1992). Depth profiled dynamic SIMS data was calibrated with high resolution XPS depth profile scans. Grazing incident x-ray diffraction (GIXRD)\* (Brundle et al., 1992) provided information on the crystal structure, crystallite size and orientation, and lattice parameter.

---

\* For details on characterization techniques, please refer to Appendix B.

### 4.2.3 Sample Heat Treatment

Films were heat treated to  $\sim 375^\circ\text{C}$  for 10 minutes in air. Films on fused silica, sapphire, or silicon substrates were cooled by removal to a heat sink for rapid quenching to room temperature, followed by characterization. Cooling rates were monitored and controlled at rates  $< 15^\circ\text{C}/\text{min}$  on the van der Pauw stage. Rapid cooling rates on the aluminum heat sink were calculated to be well over  $150^\circ\text{C}/\text{min}$ , but did not exceed  $15^\circ\text{C}/\text{s}$  according to a model where ideal conduction conditions were assumed.

## 4.3 Characterization Results

### 4.3.1 Electrical Properties

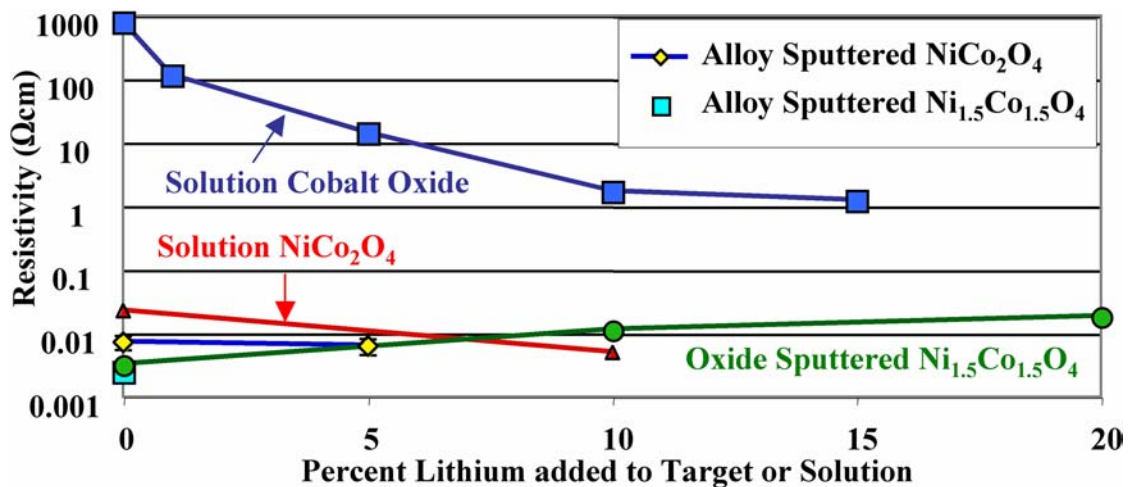


Figure 4-1. Thin films with added lithium deposited from solution precursors or sputtering.

Thin films from several deposition methods, including solution deposition, reactive RF sputtering from alloy targets, and RF sputtering from metal-oxide targets, were compared with respect to the concentration of lithium added to the starting material target or solution (Figure 4-1). Cobalt oxide films deposited from solution with 1, 5, 10, and 15% lithium showed a favorable decrease in resistivity with lithium addition, (blue squares Figure 4-1). The optimum amount of nickel for conductivity was added to the

cobalt oxide solution, along with 10% lithium, and these films also showed a favorable decrease in resistivity. The data from the cobalt oxide system (Figure 4-1), show little change in resistivity for lithium content between 10 and 20% suggesting the effect has saturated.

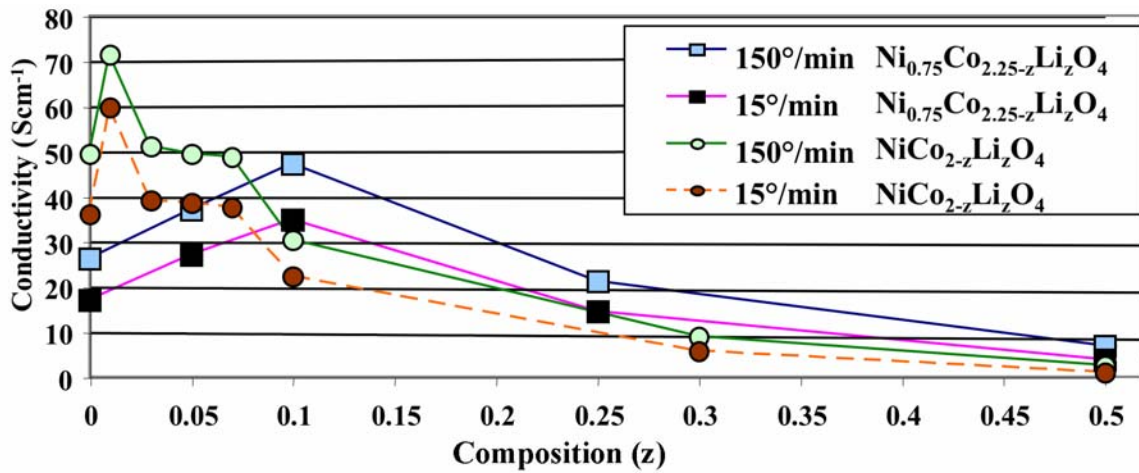


Figure 4-2. Conductivity changes based on the cooling rate following heat treatment for all compositions of lithium in nickel-cobalt oxide films.

As mentioned earlier, the design of this experiment was to increase the conductivity of the best nickel-cobalt film by adding lithium. Sputtering had shown lower resistivity values for nickel-cobalt oxide thin films. Samples of NiCo<sub>2</sub>O<sub>4</sub> were reactively RF sputtered in 100% oxygen using the composition of the solution samples as a guide. A small decrease in resistivity with the NiCo<sub>2</sub>O<sub>4</sub> spinel composition was seen (Figure 4-1 yellow squares). This effect was very small, and the conductivity from sputtering deposited films could be increased much more by adding more nickel. The Ni<sub>1.5</sub>Co<sub>1.5</sub>O<sub>4</sub> films sputtered from oxide targets fabricated in the laboratory\* and found (Chapter 3) to exhibit the lowest resistivity, increased in resistivity upon addition of lithium (green circles). The effects of lithium on electrical resistivity of sputter deposited films

\* Recipes and procedure of oxide target production included in Appendix A.

prompted a reinvestigation of the solution deposition method. High lithium concentrations in the presence of high nickel concentrations appear to degrade conductivity, so very small amounts of lithium were added to the solutions used for film deposition. Figure 4-2 shows the result of starting with the ideal composition of  $\text{NiCo}_2\text{O}_4$  and adding lithium and decreasing cobalt by equal concentrations, i.e.  $\text{NiCo}_{2-z}\text{Li}_z\text{O}_4$ .

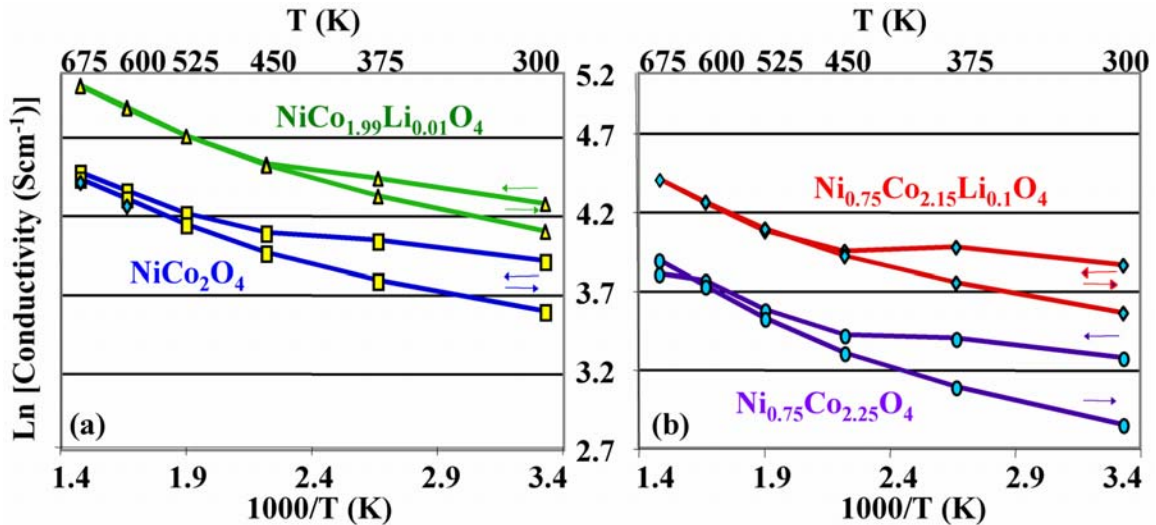


Figure 4-3. Conductivity as a function of temperature for 50 nm thick solution deposited thin films. Films of (a)  $\text{NiCo}_{2-z}\text{Li}_z\text{O}_4$  and (b)  $\text{Ni}_{0.75}\text{Co}_{2.25-z}\text{Li}_z\text{O}_4$  show that small amounts of lithium increase conductivity. All films exhibited a decrease in room temperature conductivity after the heating cycle. Each film was heat treated and rapidly cooled prior to the temperature dependent conductivity measurement.

Small amounts of lithium increase conductivity in the substituted solution deposited samples. In fact, a  $z$  value of 0.01 in  $\text{NiCo}_{2-z}\text{Li}_z\text{O}_4$ , ( $\text{NiCo}_{1.99}\text{Li}_{0.01}\text{O}_4$ ) yields the highest conductivity for that series. The same concentration of lithium does not have the same effect when the nickel content in the film is reduced (cobalt to nickel ratio of 3-to-1 or  $\text{Ni}_{0.75}\text{Co}_{2.25-z}\text{Li}_z\text{O}_4$ ). Substituting lithium in this system shows that a  $z$  value of 0.1 ( $\text{Ni}_{0.75}\text{Ni}_{2.15}\text{Li}_{0.1}\text{O}_4$ ) was required for optimization. When small doses of lithium substitute for cobalt, increased conductivity is observed. The changes are  $\sim 2x - 3x$  rather

than near 10x as expected. Conductivity after rapid and slow cooling is shown in Figure 4-2 and 4-3. The faster cooling rate always yields a better conductivity.

Figure 4-3 shows temperature dependent conductivity values for solution deposited films. Four samples from Figure 4-2 (the two samples without any lithium and the two highest conductivity samples) are shown. For clarity, lower conductivity compositions are omitted from the plot, but are tabulated in Appendix C. Conductivity as a function of temperature for high conductivity films increases with temperature, but upon cooling the samples exhibit lower room temperature conductivities. The conductivity after sequential heat treatments with different cooling rates (10-15°C/min versus quenching on an aluminum, brass or water chilled brass plate (~150°C/min)) for one sample are shown in Figure 4-4.

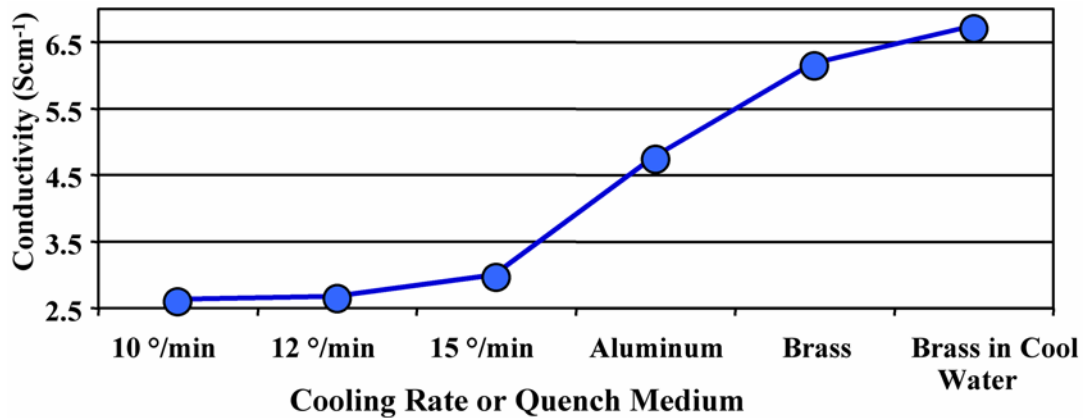


Figure 4-4. Rate of sample cooling after heat treatment had a dramatic effect on conductivity. Aluminum and Brass heat sinks have effective cooling rates greater than at least 150°C per minute, possibly as high as 15°C per second. The faster the cooling rate, the higher the conductivity.

A maximum cooling rate of 15°/min was allowed by the van der Pauw measurement instrument. The quenching medium for most samples in this study was an aluminum block. While the exact cooling rate for the aluminum and brass heat sinks are unknown, a calculation was done using the thermal mass of the fused silica substrate with

a heat flux through the surface in contact with the cooling block. The cooling block heat capacity is assumed to be infinite and the conduction contact is assumed to be perfect to yield a maximum theoretical cooling rate of  $\sim 15^\circ\text{C/s}$ . The heat sinks used were of sufficient thermal mass that no significant temperature rise was expected.

The break between a larger slope and a smaller slope for the conductivity data in Figure 4-3 near 450K ( $1000/T = 2.22$ ) has previously been reported (Windisch et al., 2002b). Note that above this temperature, the conductivity is independent of temperature, while below it conductivity depends upon quenching rate. The origin of this break will be discussed further below.

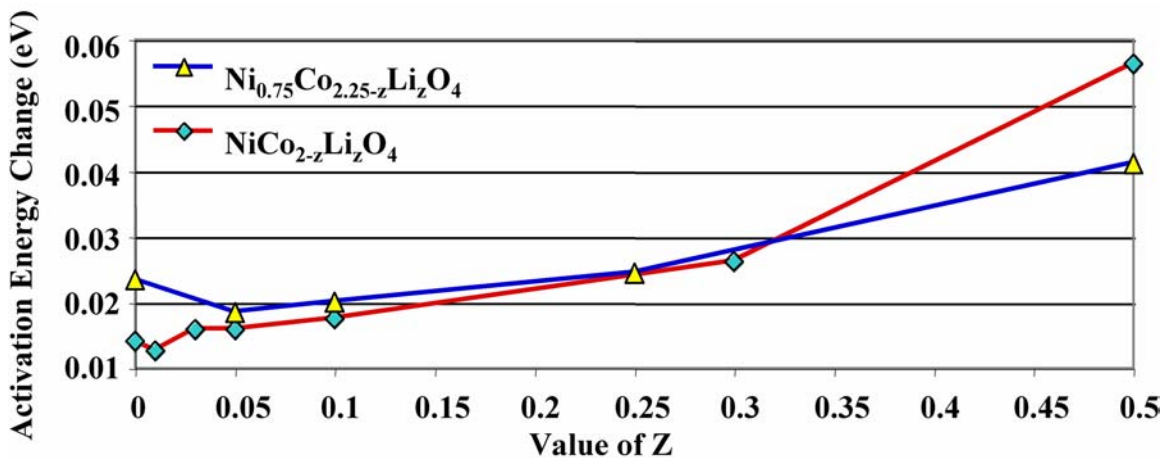


Figure 4-5. Activation energy dependence for  $\text{Ni}_{0.75}\text{Co}_{2.25-z}\text{Li}_z\text{O}_4$  and  $\text{NiCo}_{2-z}\text{Li}_z\text{O}_4$  from solution on lithium content. Lithium substitutes in increasing amounts for cobalt and as conductivity decreases, the activation energy increases. All samples were heated and cooled at  $15^\circ\text{C/min}$ .

Hopping of polarons in the nickel-cobalt oxide spinel is the primary mechanism of electrical conductivity. The slopes of the Arrhenius plots in Figure 4-3 (additional plots found in Appendix C) are proportional to the activation energy required to induce charge carrier motion. Of interest are the activation energies for the low temperature slopes of the quenched state and the slowly cooled state. These differences in activation energy for the two series ( $\text{NiCo}_{2-z}\text{Li}_z\text{O}_4$  and  $\text{Ni}_{0.75}\text{Co}_{2.25-z}\text{Li}_z\text{O}_4$ ) are shown in Figure 4-5. The most

conductive film has the lowest activation energy and the most resistive film has the highest activation energy, consistent with expectation. Note that more lithium in the film results in a larger difference between the activation energies of the quenched film state and the slowly cooled state. Also, the larger variance is observed in samples with lower overall conductivity.

Conductivity degrades when too much lithium is added to the target or precursor solution. At low concentrations, and depending on the nickel content in the film, lithium had either a positive or negative effect on conductivity. The next section will discuss the role of lithium in the nickel-cobalt oxide system and its effect on optical properties.

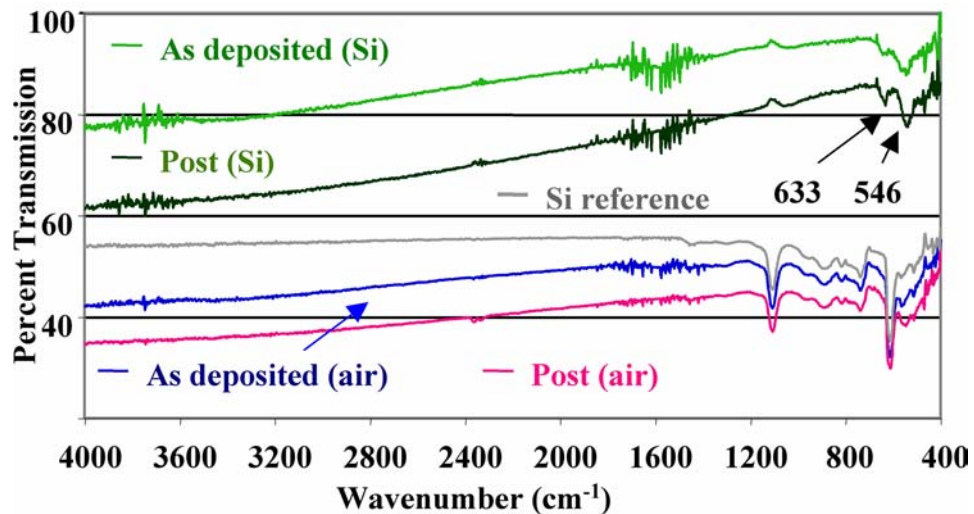


Figure 4-6. FTIR mid IR transmission spectra of alloy-target reactive sputter-deposited  $\text{Ni}_{0.95}\text{Co}_{1.95}\text{Li}_{0.15}\text{O}_4$ . Transmission spectra measured before and after heat treatment with rapid cooling, referenced to air and to a bare silicon substrate. Absorption regions at  $633\text{ cm}^{-1}$  and  $546\text{ cm}^{-1}$  are characteristic of spinel lattice vibrations.

#### 4.3.2 Optical Properties

Optical properties are also affected by the different lithium film concentrations. Thin film transparency from FTIR between  $400\text{ cm}^{-1}$  and  $4000\text{ cm}^{-1}$  of a reactive sputter deposited 50 nm thick  $\text{Ni}_{0.95}\text{Co}_{1.95}\text{Li}_{0.15}\text{O}_4$  film is shown in Figure 4-6 (*Post* means after

quench). The transmission spectrum of a film (as deposited) is compared to the transmission spectrum after heat treatment followed by rapid quenching (with an aluminum block). The IR transparency decreases after the quenching treatment, consistent with an increased conductivity. Similar results are observed for all samples after quenching. When the transparency of the films is corrected to remove the silicon absorption spectra, the characteristic spinel absorption peaks at  $633\text{ cm}^{-1}$  and  $546\text{ cm}^{-1}$  are observed.

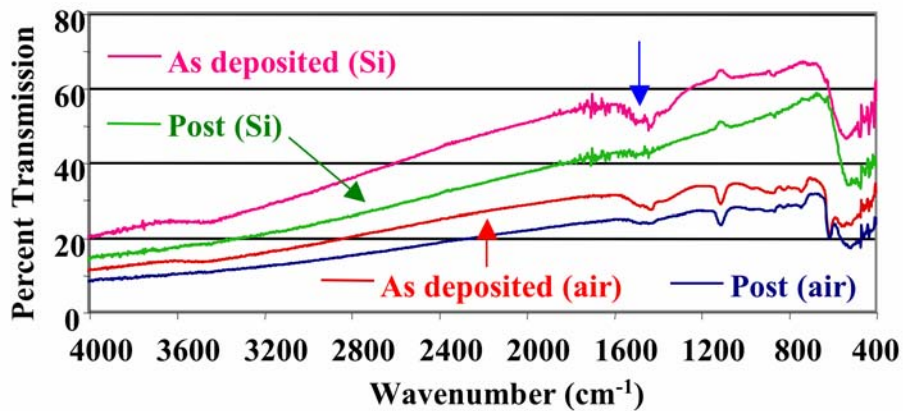


Figure 4-7. FTIR mid IR transmission spectra of oxide-target sputter-deposited  $\text{Ni}_{1.2}\text{Co}_{1.2}\text{Li}_{0.6}\text{O}_4$ . Transmission spectra measured before and after heat treatment with rapid cooling. The spectra marked post is after quenching on an Al block. Those marked air are spectra taken of the film and substrate uncorrected for the silicon substrate referenced to air. Those marked Si have been corrected for absorption of the silicon substrate. A region of interest near  $1400\text{ cm}^{-1}$  was found (blue arrow) in samples prior to heat treatment.

Thin film transparency from FTIR of a sputtered 250 nm thick  $\text{Ni}_{1.3}\text{Co}_{1.3}\text{Li}_{0.6}\text{O}_4$  film is shown in Figure 4-7. The transmission spectrum of the film as deposited is compared to its transmission spectrum after heat treatment and rapid quenching just as in Figure 4-6. A decrease in optical transparency is seen after the quenching treatment. When the film spectra are corrected for silicon absorption spectra, an absorption band near  $1400\text{ cm}^{-1}$  (blue arrow) is obvious and the characteristic spinel absorptions were not

observed. Traces labeled *Post* are the transmission data taken after quenching the sample from heat treatment of ten minutes at 375°C. The absorption feature at 1400 cm<sup>-1</sup> is significantly reduced immediately after quenching. The surface of the Ni<sub>1.3</sub>Co<sub>1.3</sub>Li<sub>0.6</sub>O<sub>4</sub> sample exhibits a milky white haze after prolonged exposure to atmosphere.

The effect of lithium on films sputter deposited using the combinatorial technique (discussed earlier) from a Ni<sub>1.5</sub>Co<sub>1.5</sub>O<sub>4</sub> target and a Ni<sub>1.35</sub>Co<sub>1.35</sub>Li<sub>0.3</sub>O<sub>4</sub> target revealed a chemical reaction at the film surface. Figure 4-8 shows the FTIR spectra from various substrate positions. Positions 7 and 9 (closer to the lithium target) showed the same substantial absorption near 1400 cm<sup>-1</sup> compared to film positions 1 and 3 (closer to the target with no lithium). More lithium appears to lead to this absorption peak. The spectra were not all uniform films with the same thickness, therefore they were normalized to a common value of 45% at 1200 cm<sup>-1</sup> to the intensity of the feature near 1400 cm<sup>-1</sup>. Based on the interpretation below, the feature near 1400 cm<sup>-1</sup> is not a function of thickness of the films.

The absorption at 1400 cm<sup>-1</sup> is attributed to carbonate formation, as seen from the grey carbonate reference spectrum shown in Figure 4-8 from lithium carbonate in potassium bromide that also shows a strong absorption near 1400 cm<sup>-1</sup>. The broad absorption band near 1600 cm<sup>-1</sup> is from water and accounts for the remaining deviation of the reference spectra. Formation of the surface carbonate is discussed in Section 4.3.4.

The combinatorial film provided interesting information with respect to the absorption region near 1400 cm<sup>-1</sup> and its correlation with lithium, but it was not structurally identical with other lithium-containing nickel-cobalt oxide films. The film conductivity across all positions was an order of magnitude less than optimized sputter

deposited nickel-cobalt oxide thin films, probably due to the large target-to-substrate distances required to get adequate coverage for the combinatorial film.

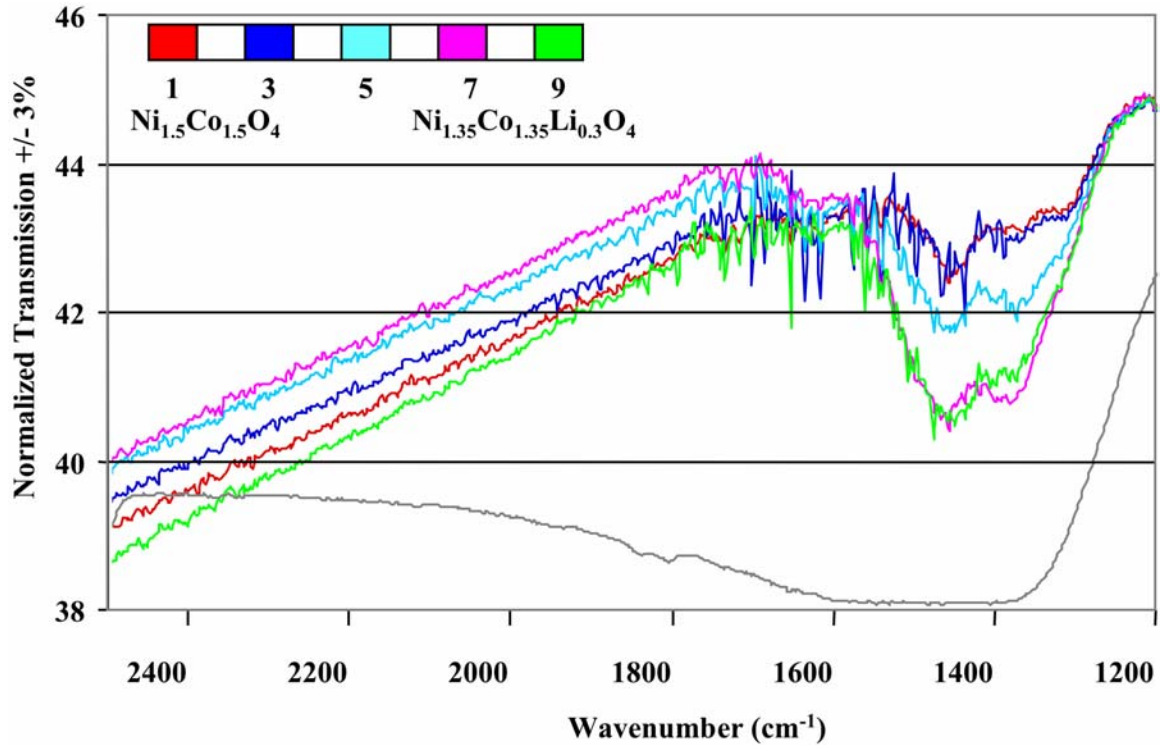


Figure 4-8. Normalized FTIR spectra at 1200 cm<sup>-1</sup> show the absorption region near 1400 cm<sup>-1</sup> assigned to carbonate on the surface when compared with a carbonate reference spectrum shown in grey. Film position in relation to the lithium target appears to determine the strength of the absorption.

### 4.3.3 Structural Properties and Composition

For corrected FTIR data, near 610 cm<sup>-1</sup> and 540 cm<sup>-1</sup> indicate that the films are not amorphous. The spinel structure is confirmed by grazing incident x-ray diffraction (GIXRD referred to hereafter as XRD). The combinatorial film shown in Figure 4-9 appears to be weakly crystalline with only low intensity spinel peaks. The film is most probably highly disordered with a low density, similar to those reported in Chapter 3 with a large target-substrate distance. A peak near 43° appears to shift to a lower angle from areas of the film positioned closer to the lithium-containing target

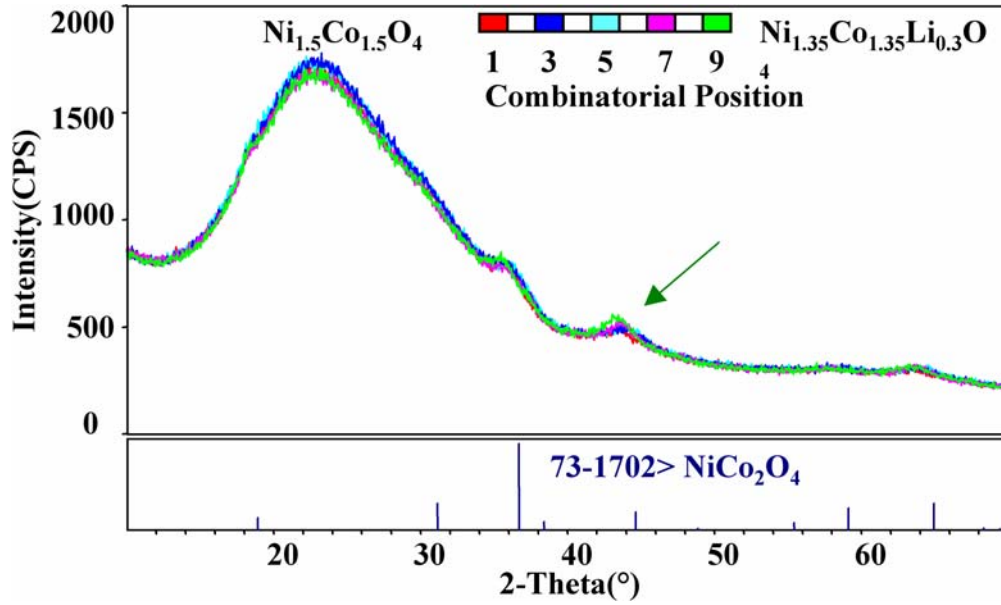


Figure 4-9. Grazing incidence XRD from combinatorial sputter deposited films deposited from oxide targets. Note the weak crystalline diffraction peaks from the film.

Other films deposited by sputtering and solution were analyzed with XRD. The lattice parameters calculated from fitted XRD patterns are shown in Figure 4-10. The method of deposition determines the lattice parameter. The oxide target sputtered films all had a much larger lattice parameter that increases with the addition of lithium (blue). Films deposited from reactive sputtering with alloy targets all had a smaller lattice parameter. It is reported that nickel addition to cobalt oxide increases the lattice parameter (Windisch et al., 2001a; Windisch et al., 2001b; Windisch et al., 2002b). The same trend is evident from films deposited from an alloy target (magenta and green). The addition of lithium to nickel cobalt oxide (green data) also increased the lattice parameter. The theoretical lattice parameter calculated from the powder diffraction data is included as a reference point. All measured lattice parameters were larger than the theoretical value. An explanation of this observation is discussed below.

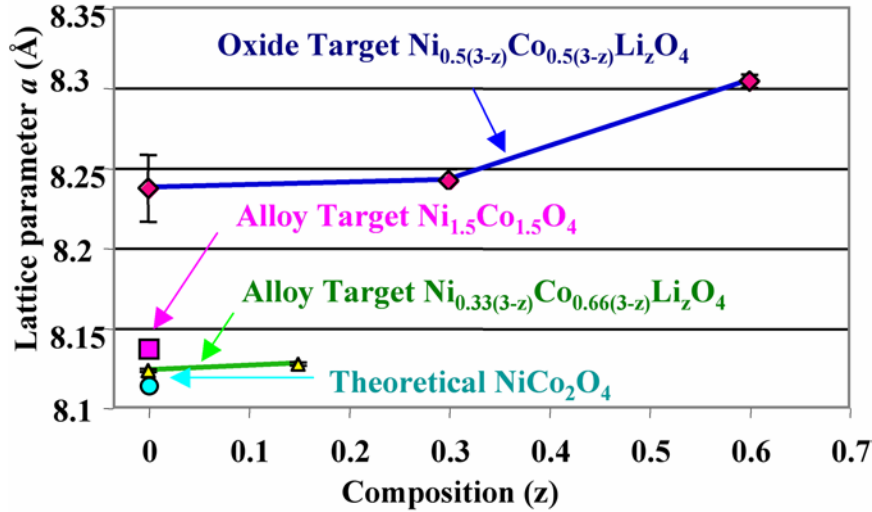


Figure 4-10. Films sputter deposited from an alloy target have a smaller lattice expansion than films deposited from oxide targets. The theoretical lattice parameter from powder diffraction files is also shown.

The increase of the lattice parameters appears to be proportional to the amount of lithium. Data from Windisch et al. show that as nickel is added to into cobalt oxide, the lattice parameter expands (Windisch et al., 2001b; Windisch et al., 2002b). As more impurities are added in the spinel system, the unit cell expands to accommodate the different cations. Table 4-3 shows the data plotted in Figure 4-10 with the error margin determined from XRD data.

Table 4-1. Numerical data from Figure 4-10 are listed in columns. The calculated lattice parameter from the powder diffraction file is less than the experimentally measured values. The experimental values increase with lithium addition and depend on the method of production of the film.

Source	Formula	Lattice Parameter (Å)	Error
Theoretical	NiCo <sub>2</sub> O <sub>4</sub>	8.114	-
Alloy Target	NiCo <sub>2</sub> O <sub>4</sub>	8.123	0.001
Alloy Target	Ni <sub>0.95</sub> Co <sub>1.85</sub> Li <sub>0.15</sub> O <sub>4</sub>	8.127	0.001
Alloy Target	Ni <sub>1.5</sub> Co <sub>1.5</sub> O <sub>4</sub>	8.137	0.001
Oxide Target	Ni <sub>1.5</sub> Co <sub>1.5</sub> O <sub>4</sub>	8.237	0.021
Oxide Target	Ni <sub>1.35</sub> Co <sub>1.35</sub> Li <sub>0.3</sub> O <sub>4</sub>	8.242	0.007
Oxide Target	Ni <sub>1.2</sub> Co <sub>1.2</sub> Li <sub>0.6</sub> O <sub>4</sub>	8.304	0.004

A lattice parameter increase from 8.23 Å to 8.30 Å in films sputter deposited from oxide targets indicates that lithium may not have substituted for cobalt, but occupy interstitial sites. XRD scans of the same films showed the spinel structure as is evident in Figure 4-11. Changes in the texture of the film with increased lithium are reasonable.

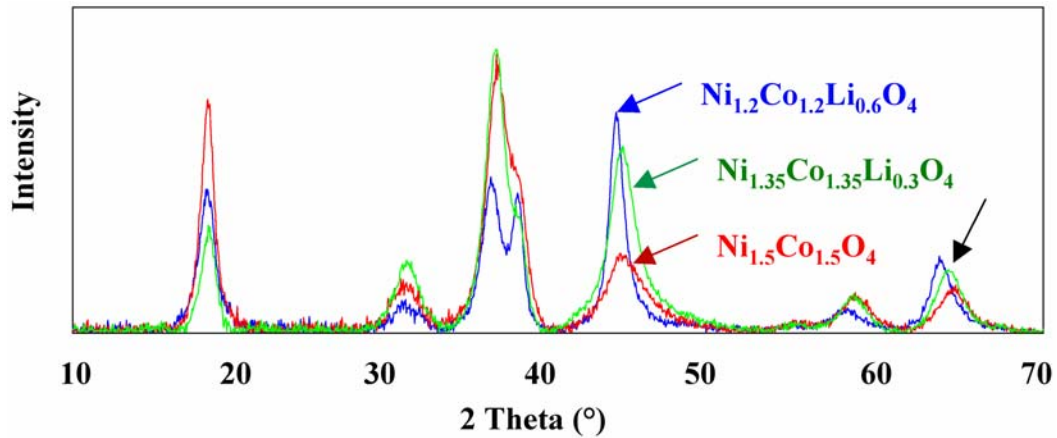


Figure 4-11. XRD of sputtered films with incremental amounts of lithium (not normalized for intensity). The peak near 65° (below the black arrow) shifts to a lower angle and the peak near 18° decreases in intensity with increased lithium concentration.

XRD data collected after heat treatment of solution deposited samples to observe any structural changes that may occur from changes in cooling rates as a function of lithium concentration. The XRD scans from solution deposited samples are shown in Figure 4-12, collected after heat treatment followed by rapid quenching and again after heat treatment followed by slow cooling. The spectra are identical to the unaided eye, but some peak narrowing after rapid quenching can be demonstrated. This narrowing of peaks reflects a larger calculated crystallite size in these samples.

A change in the lattice parameter between the two cooling rates could be detected by fitting the XRD pattern, with a smaller lattice parameter at a faster cooling rate as shown in Table 4-2. While crystallite size varied, it did not appear to scale with cooling rate.

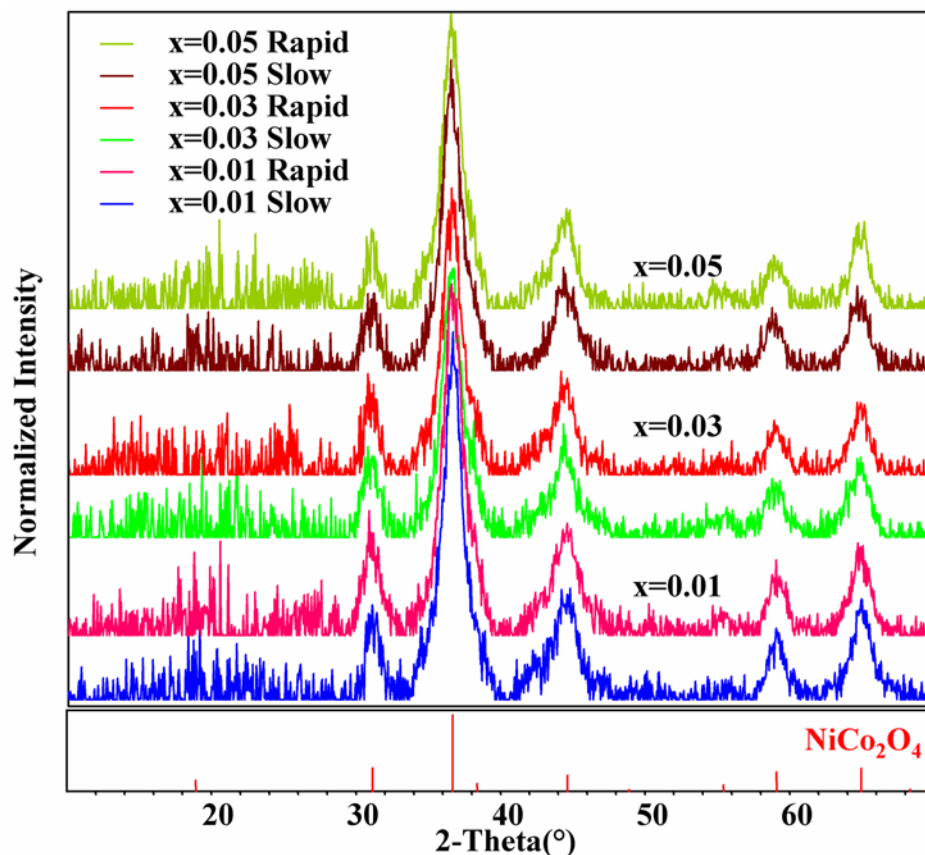


Figure 4-12. XRD spectra show no obvious changes for fast versus slow cooling for  $\text{Ni}_{0.75}\text{Co}_{2.25-z}\text{Li}_2\text{O}_4$ . Fitting the curves reveals changes shown in Table 4-4.

Table 4-2. Lattice parameter of  $\text{Ni}_{0.75}\text{Co}_{2.25-z}\text{Li}_2\text{O}_4$  as a function of lithium fraction ( $z$ ) before and after rapid cooling from a 10 minute  $375^\circ\text{C}$  heat treatment.

$\text{Ni}_{0.75}\text{Co}_{2.25-z}\text{Li}_2\text{O}_4$	Z=0.00	Z=0.01	Z=0.03	Z=0.05	Z=0.1	Z=0.3	Z=0.5
Lattice Parameter	8.1313	8.14497	8.1414	8.1548	8.1419	8.1332	8.1279
After Quench	-	8.1327	8.1360	8.1327	-	-	-
Crystallite Size	80	50	55	50	90	63	-
After Quench	-	55	55	50	-	-	-

#### 4.3.4 Chemical Properties

Film composition was measured by XPS and SIMS. XPS analysis of the combinatorial film from the oxide targets (discussed in Section 4.3.2) with the absorption band at  $1400\text{ cm}^{-1}$ , as well as the variable lattice parameter films from the previous structural section were of particular interest. SIMS was collected from films

sputter deposited from the oxide target with varying lithium concentrations including the highest concentration. From both XPS and SIMS analyses, depth profiling data were collected, but the sensitivity to Li was low and high, respectively.

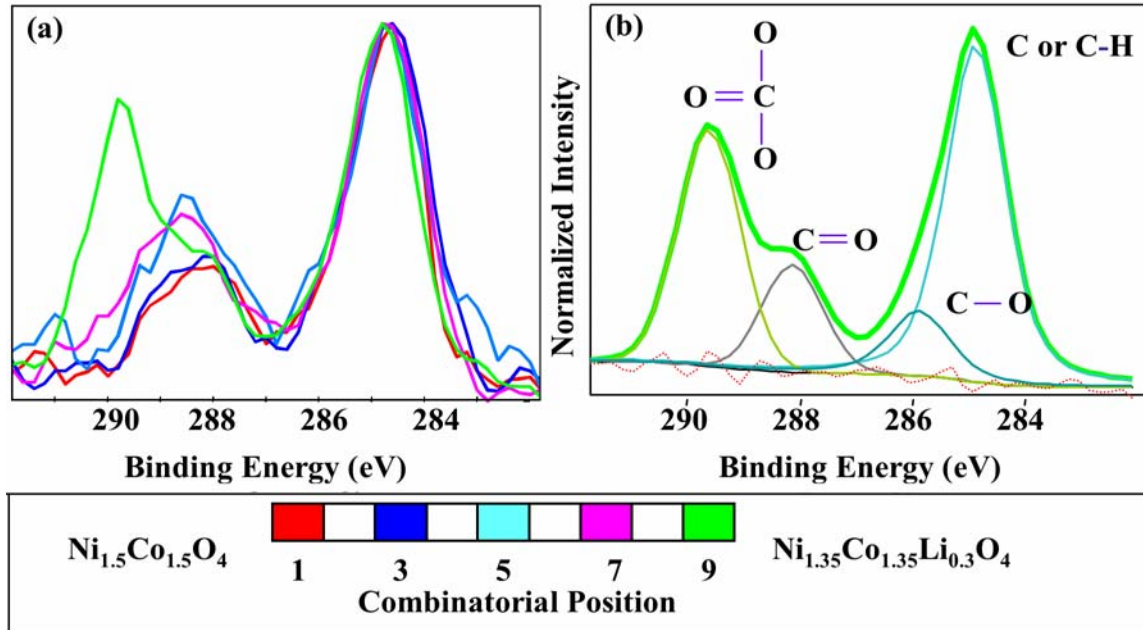


Figure 4-13. XPS of the Carbon 1s region from the combinatorial sputtered film (a) at positions identified by the color code, and (b) curve fit to show composition of position 9. Carbonate at a binding energy of 290 eV appears with lithium only at position 9. All curves show the presence of carbonyl near 288 eV.

The combinatorial film sputtered from oxide targets of  $\text{Ni}_{1.5}\text{Co}_{1.5}\text{O}_4$  and  $\text{Ni}_{1.35}\text{Co}_{1.35}\text{Li}_{0.3}\text{O}_4$  was analyzed with XPS to observe surface compositional changes with position and lithium concentration. Changes in the carbon 1s peak are shown in Figure 4-13. Carbon bound as carbonyl, whose 1s peak shifted from 284.6 to 288.2 eV, was detected all across the film. The area of the film closest to the  $\text{Ni}_{1.35}\text{Co}_{1.35}\text{Li}_{0.3}\text{O}_4$  target (green trace, position 9) shows a large peak at 290 eV, a binding energy associated with carbon bonded with three oxygen atoms in a carbonate. This carbonate binding energy region is not prominent at other positions of the film.

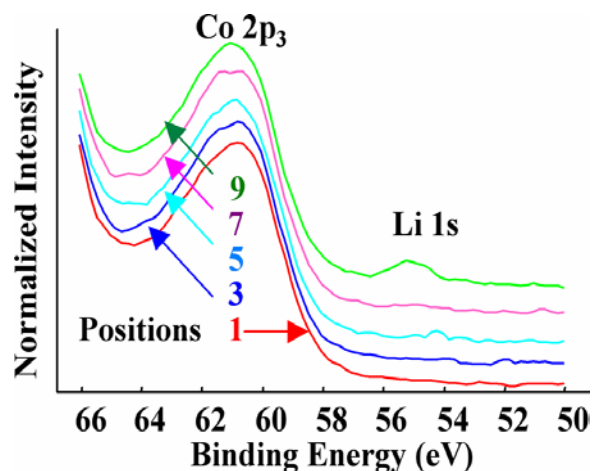


Figure 4-14. XPS of combinatorial deposited nickel-cobalt oxide film with variable lithium concentration. Lithium is only detected at position 9, the position closest to the  $\text{Ni}_{1.35}\text{Co}_{1.35}\text{Li}_{0.3}\text{O}_4$  target. See Figure 4-13 for trace numbering position key.

Figure 4-14 shows XPS data from the combinatorial film over an energy range which includes the Co2p and the Li 1s photoelectron peaks. Lithium is only detected at position 9, which indicates a high lithium concentration based on the low sensitivity of XPS for lithium. Position 7 may show trace amounts of lithium, while any lithium signal from the remainder of the films is below the noise level. Carbonate and lithium are both in the film at position 9.

SIMS depth profile data were collected from the film showing the FTIR carbonate absorption peak near  $1400\text{ cm}^{-1}$ . The SIMS data shows predominantly lithium at the surface, which decreases after sputtering for a few hundred seconds to a low, constant level at which time the nickel and cobalt signal increased and remained constant throughout the film. As shown in Figure 4-15, the film is composed of nearly equal parts of nickel and cobalt and a nearly-constant concentration of lithium in the bulk of the film. Based on quantitative XPS calibration, the solubility limit of lithium in nickel-cobalt oxide is  $\sim 15\%$ . Another interesting feature shown by the SIMS is the interface layer

where the film meets the substrate. The concentration of lithium drops before the other cations with nickel concentration slightly increasing at the interface.

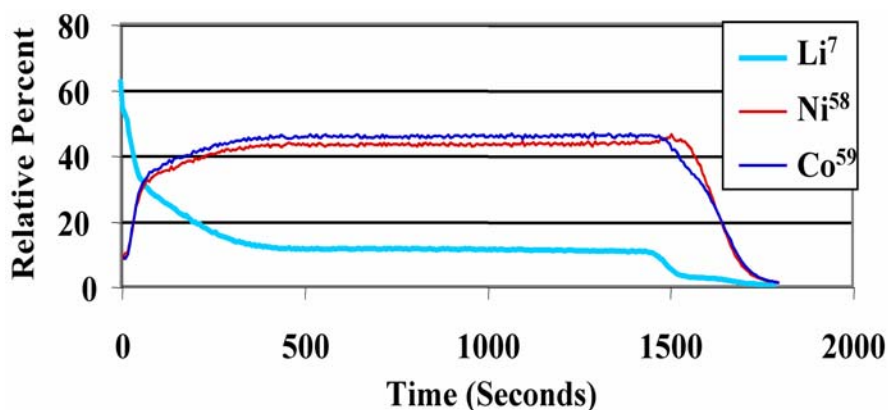


Figure 4-15. SIMS depth profile of a thin film sputtered from a Ni<sub>1.5</sub>Co<sub>1.5</sub>Li<sub>0.6</sub>O<sub>4</sub> target.

XPS analysis is correlated with heat treatment of solution deposited lithium-containing films is shown in Figure 4-16. The Li 1s peak was undetectable and is therefore omitted. Rapid quenching of Ni<sub>0.75</sub>Co<sub>2.24</sub>Li<sub>0.01</sub>O<sub>4</sub>, Ni<sub>0.75</sub>Co<sub>2.22</sub>Li<sub>0.03</sub>O<sub>4</sub>, and Ni<sub>0.75</sub>Co<sub>2.2</sub>Li<sub>0.05</sub>O<sub>4</sub> produced no significant changes in the Ni 2p and Co 2p binding energy regions. Minor changes may appear to be visible but may be in intensity only. A case might be made to differentiate the peak shapes at 858 eV in the Ni 2p region, but a calibrated quantitative measure will be required to make such an assertion. Significant changes are seen comparing the slow cooling versus rapid cooling O 1s and C 1s peaks at 531.2 eV and 285 eV, respectively. After quenching, the O 1s shoulder at 531.2 eV appears to decrease. Also the carbon content, likely due to adventitious carbon on the surface, decreases after the rapid cooling heat treatment. The lithium film concentrations do not appear to influence the order or arrangements in any of the plots suggesting that the effects seen here with heat treatment are not a function of the lithium concentration. For example, the O 1s peak at 531.2 eV shows the purple curve at the top with blue and then red beneath. The C 1s region shows the order as red, purple, and then blue. If

lithium concentration is a factor ordering of red, purple, and then blue or blue, purple, and then red is expected in both cases, but they are different.

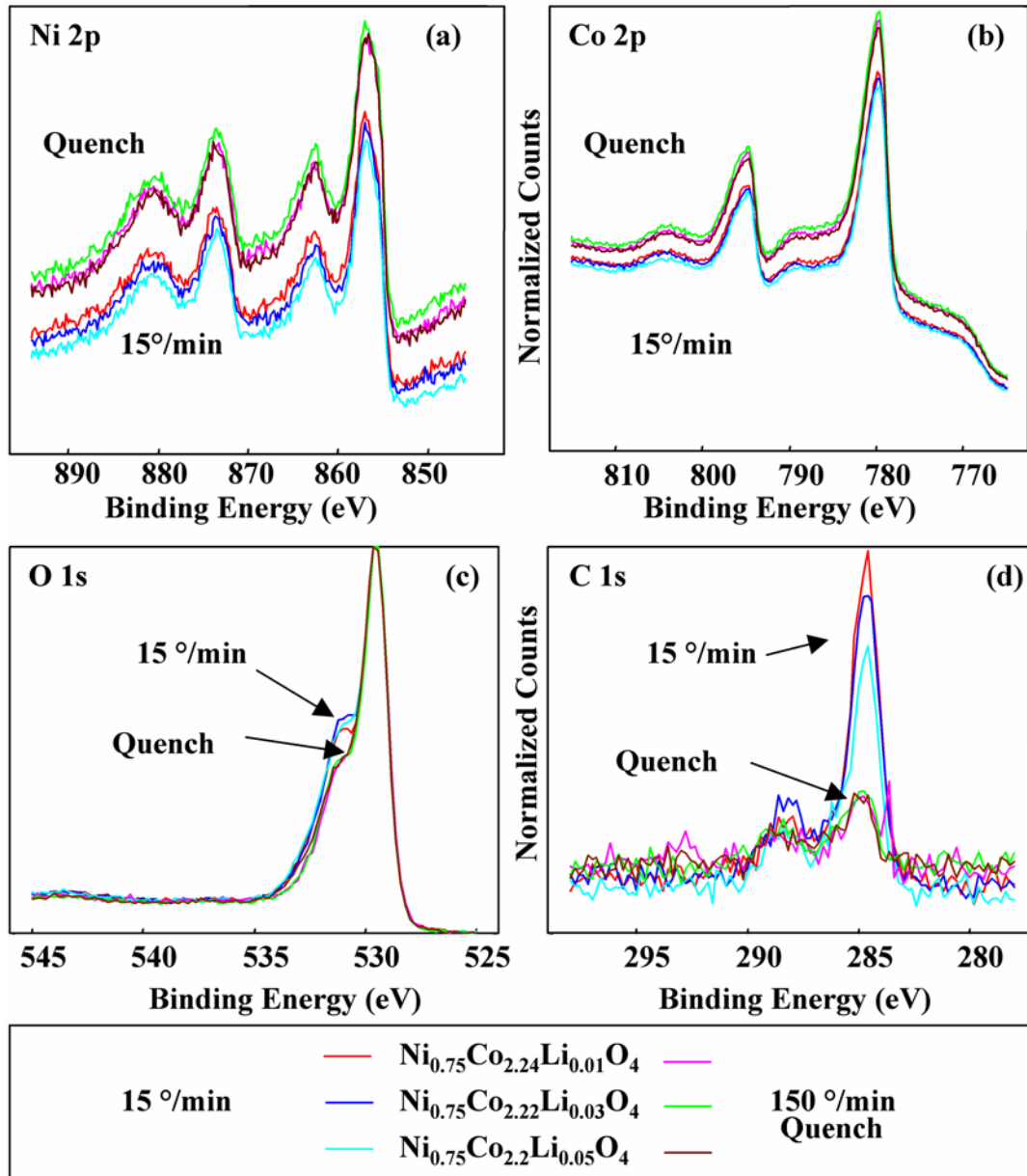


Figure 4-16. XPS of (a) Ni 2p, (b) Co 2p, (c) O 1s, and (d) C 1s binding energy regions from solution deposited films of nickel-cobalt oxide containing lithium following slow and fast cooling after heat treatment.

## 4.4 Discussion

### 4.4.1 Lithium Effects

The resistivity of nickel-cobalt oxide did not decrease with additions of lithium as was expected based in the effects of adding more nickel to cobalt oxide. Lithium substitution did not decrease the resistivity of cobalt oxide to the same extent as just adding nickel. This may be a result of lithium being in a different oxidation state, or energetically preferring a different site than nickel. Only specific lithium concentrations in specific nickel-cobalt oxide samples were beneficial i.e. led to increased conductivity. For example, electrical conductivity of solution deposited  $\text{NiCo}_{1.99}\text{Li}_{0.01}\text{O}_4$ , and  $\text{Ni}_{0.75}\text{Co}_{2.15}\text{Li}_{0.1}\text{O}_4$ , both increased, however the sample with more nickel requires less lithium to increase the conductivity. The samples with less nickel require more lithium to produce a positive effect, yet the absolute conductivity is not as high as the sample with a higher nickel concentration. Compositions with higher and lower concentrations of lithium for these amounts of nickel and cobalt do not enhance electrical conductivity. This leads to the conclusion that there may be an optimum number of carriers within the lattice that can be activated. Once this number is exceeded, reduced conductivity will be observed. Lithium may perturb the localized states required for polarons formation and reduce the carrier concentration and the conductivity. Note that lithium-enhanced conductivity exhibited improvements less than 2x, not the order-of-magnitude changes between the conductivities of sputter deposited (high conductivities) versus solution deposited nickel-cobalt oxide films. In all cases, the resistivity values for nickel-cobalt oxide films with or without lithium are much higher than those from *n*-type TCOs.

The improved conductivity by lithium addition to solution deposited films is not realized in the sputter deposited films. One nickel-cobalt oxide film deposited by

reactive RF sputtering from an alloy target (making  $\text{Ni}_{0.95}\text{Co}_{1.9}\text{Li}_{0.15}\text{O}_4$ ) shows a small decrease in resistivity. The reason for this single improvement is unknown and is considered to be insignificant due to the small change.

Films sputter deposited from oxide targets with added lithium showed lower conductivities upon lithium addition. According to XRD data, the unit cell expanded even though a similar or somewhat smaller lattice parameter was predicted upon lithium substitutional addition. Lattice expansion suggests that lithium incorporated as an interstitial rather than occupying a tetrahedral site occupied by cobalt. Interstitial lithium would add a positive charge balanced in the matrix by the reduction of a neighboring cation. The net result would be a decrease in conductivity from the reduction in the number of polarons charge carriers, just as was observed.

Reduced conductivity may also result from insulating layers of carbon and oxygen species found on the surface. XPS and SIMS analysis indicate that lithium is concentrated on the surface and XPS data show it is bound as a carbonate. A logical sequence leading to surface carbonate would be for lithium to segregate to the surface where it forms a hydroxide. Adsorbed carbon dioxide reacts with the lithium hydroxide to form surface layers of lithium carbonate. The SIMS data suggest that lithium has a solubility limit of  $\sim 15\%$  in the sputter deposited nickel-cobalt oxide. Observation of a concentrated lithium surface layer and lower concentration in the film may be due to two possible scenarios: (1) lithium diffuses to the surface at room temperature, or (2) the SIMS sputtering process greatly enhances the lithium sputter yield due to lithium's low mass and high ionization probability. Both are likely to be true, but the XPS data support the presence of a true lithium surface layer bound as carbonate. In addition to artifacts

from SIMS analysis, preferential sputtering of lithium during deposition may create an initial lithium-rich layer on the substrate which remains on the surface as a “floating layer” while the film grows underneath. This lithium “floating or surfactant layer” may then react with wet air forming lithium hydroxide when the chamber is vented. Lithium hydroxide on the surface then reacts with adsorbed carbon dioxide on the surface to form lithium carbonate. No matter the formation mechanism, this hazy carbonate layer could block electrical contact without significantly reducing optical transparency. Lithium is therefore detrimental to film conductivity from sputtering due to its high surface concentration and subsequent carbonate formation on the surface.

It is also possible that conductivity reduces when too much lithium is added because metastable nickel forms nickel oxide similar to the effect observed when nickel-cobalt is overheated and nickel oxide precipitates. Heat treatment procedures exceeding 400°C cause decreased conductivity due to this phase segregation. Lithium may change the decomposition temperature or act as a nucleation agent or inhibitor at sufficiently high concentrations. If the heat treatment and quenching lead to nickel oxide precipitation, the change in conductivity will not be recoverable, contrary to the data. It is therefore concluded that nickel oxide precipitation did not cause the changes in conductivity.

#### **4.4.2 Effects of Heat Treatment**

Activation energies show that quenching has a greater effect when the conductivity is lower, as seen in Figure 4-3. Quenching may freeze in cation distribution disorder among the available spinel octahedral and tetrahedral sites (discussed more in chapter 6) with increased activation seen as resistivity increases.

The rate of cooling after heat treatment has an effect on conductivity that is dependent upon the rate of cooling. Faster cooling leads to higher conductivity, presumably by creating more polarons from the freezing of a disordered structure. This conductivity improvement relaxes with time at room temperature because it is a metastable state as seen in Figure 4-4.

Quenching of the films decreased optical transparency. More polarons, believed to result from the nickel and oxygen electron exchange in the octahedral site, presumably introduce more *d-d* transitions and increase the optical absorption as seen in Figure 4-6. Heat treatment also reduced the carbonate feature in Figure 4-7. This is most easily explained by carbonate evaporating during the heat treatment.

Heat treatment affects nickel-cobalt-lithium oxide films by increasing the conductivity and reducing the carbon and an oxygen species when the film is cooled quickly following heat treatment. XPS data shows that heat treatment has no significant effect on the nickel or cobalt 2p regions. The effect of heat treatment is shown in the C 1s and the O 1s regions with a decrease in the adventitious carbon, carbonyl and a decrease in the higher binding energy oxygen region, consistent with volatilization of carbonate. A decrease in the higher binding energy O 1s peak, shown in Figure 4-16c, does not scale proportionally with conductivity that increased after the quenching heat treatment. Improved conductivity with the decreased O 1s peak may contradict the reported data shown in Figure 2-6 that suggests the peak intensity scales proportionally with conductivity. The oxygen peak shown in the data for nickel-cobalt-lithium oxide may originate from both lattice defect oxygen as well as the surface carbonate layer which is not a factor in films with no lithium. For films with lithium, is not an absolute

indicator of defect oxygen. It may be a combination of several effects. The interference of the higher binding energy O 1s peak may be explained as (1) the increased oxidation of the surface when heat treated in the presence of air, or (2) surface adsorbed species in pores of the film may be thermally desorbed during the heat treatment. According to the FTIR spectra, the original spectra (Figure 4-7 and Figure 4-8) show that the absorption regions at  $1400\text{ cm}^{-1}$  will disappear after the heat treatment. A combination of both effects may be possible and result in a shift in the electron density of the nickel atoms near the surface to provide a conducting path on the surface and into the bulk film below, which would also explain the decrease in transparency. A third less probable explanation may be possible, but would be more a function the experimental setup. If the carbonate layers simply desorbed during heat treatment, then the surface would be in better contact with the probe. Contact probe pressure could greatly influence the conductivity measurement in this instance and would introduce additional uncertainty. Data as a function of probe pressure may answer this question, but was not pursued.

Table 4-4 shows that the lattice parameter of the quenched nickel-cobalt oxide with small amounts of lithium is reduced. It seems counter-intuitive to suggest that the lattice shrinks as a result of more cation disorder and lattice distortion, but it would be consistent with lithium changing from an interstitial to substitutional ion in a tetrahedral or an octahedral site, and upon quenching, the disordered arrangement of these cations in the lattice could produce more polarons. By definition, the polaron induces a localized lattice strain and therefore may exhibit lattice shrinkage when the majority carriers are holes. In addition, cations in a higher oxidation state will be smaller and therefore the lattice parameter will decrease. This shift to a smaller lattice parameter is therefore

plausible and indicative of an increased polaron concentration from cation disorder in the crystalline spinel solid. A maximum amount of disorder in the lattice may be induced by nickel when it is present. The addition of lithium may have merely ordered the lattice in a different way and therefore had the effect of increasing the activation energy of conduction, resulting in a lower conductivity.

#### **4.5 Conclusions**

Lithium improves electrical properties only in three sets of conditions: two compositions deposited from solution and one deposited by sputtering. The improvements in electrical conductivity from lithium in these three compositions is by less than a factor of two and were less than the improvement made in conductivity in films containing no lithium and deposited by sputtering rather than from solution. Other compositions of nickel-cobalt oxide with lithium, whether sputtered or solution deposited, produces films with increased resistivity and expanded lattice parameters. The behavior of films containing lithium is similar to those not containing lithium with respect to optical and electrical properties following heat treatment. Heat treatment followed by quenching increases conductivity and decreases transparency. In contrast to high concentrations of added lithium, which causes a lattice expansion, heat treating and quenching films with small lithium doses causes a lattice shrinkage and an increase in conductivity. Increased lithium causes a rapid increase in the activation energy for film conductivity for both quenched and slowly cooled films, but the magnitude depends upon whether the temperature is cooled fast (quenched-high conductivity) or slow (slow cooling-low conductivity). Heat treatment effects upon conductivity and transparency are reversible for films with and without lithium. It is concluded that the film is in a

metastable state following a rapid quench from after heat treatment, and that cation disorder is responsible for this change.

Lithium in films deposited from solution tends to increase conductivity when added in the correct amount, which is a function of the nickel-to-cobalt ratio. Higher nickel-to-cobalt ratios require less lithium for increased conductivity. The improved conductivity value is still small in comparison to the high conductivity sputtered films without lithium. Up to 15% of lithium incorporates in the lattice. Lattice expansion suggests this high lithium concentration results in occupation of interstitial sites rather than substitutional site replacement for cobalt or nickel. Polaron annihilation instead of polaron creation results from the interstitial lithium. Excess lithium beyond the solubility limit segregates to the surface, forms carbonate and results in reduced conductivity. The formation of the carbonate surface layer was detected FTIR and XPS.

## CHAPTER 5 RHODIUM SUBSTITUTION FOR COBALT

### 5.1 Introduction

Nickel-cobalt oxide conducts via a polaron hopping mechanism. Polaron hopping is a relatively slow process because a polaron is made up of a charge carrier and a lattice strain, both of which move during electrical conduction. Conductivity is the product of polaron density, mobility, and an electron's charge. In a polaron hopping system, conductivity is regulated by the polaron density because the hopping mobility is low. Improvement to conductivity in a hopping conduction system is achieved by increasing the number of carriers. Substitution of rhodium for cobalt in the nickel-cobalt oxide system is expected to increase conductivity and transparency. Conductivity will increase with increased polaron density from structural distortion introduced as the larger rhodium ion occupies the octahedral site (Windisch et al., 2002b). Substitution of rhodium for cobalt should improve optical transparency because moving deeper in the periodic table to a larger mass will shift the absorption frequencies to lower values and increase the forbidden band gap of transition metal oxides.

Rhodium may also play a role in cation charge disorder as discussed in Chapters 3 and 4 where Verwey-type transitions affect the cation charge disorder following quenching heat treatment that does not significantly reduce crystallinity. Disorder of cation charges may change the charge distribution from the normal to inverse spinel cation arrangement.

Nickel-cobalt-rhodium oxide spinel has been reported (Blasse, 1963). Rhodium may cause a structural shift in stability from the spinel structure to forming separate phases and reducing the crystallinity of the films as structural disorder in the lattice increases (Da Silva Pereira et al., 1994; Tavares et al., 1996). Structural disorder would increase the polaron density, but may present complications if the conduction pathways are disrupted to the extent that carrier hopping is obstructed by the disorganization. An increase in the carrier density amounts to little or no increase in conductivity if their formation creates potential barriers or discontinuities in the hopping paths. Emin, Stoneham, and Tauc have all commented on the role of structural disorder and the increased polaron formation in such an arrangement (Emin, 1994; Emin & Bussac, 1994;; Stoneham, 1980; Tauc, 1976). In these cases, structural disorder increases the polaron density and the conductivity increases.

A calculation done by Windisch, Ferris, et al. shows that rhodium substitution in the nickel-cobalt oxide system may shift the density of states of the *d* orbitals and result in a decreased optical absorption due to an increase in the disorder in the system, shown in Figure 5-1 (Windisch et al., 2002a; Windisch et al., 2002b). The calculation assumes that rhodium will be substituted completely for cobalt. The density of electron quantum states in the quantum levels at energies between 0 and 2 eV shifts down with rhodium and appear to combine and shift left at energies of 0 to -4 eV to a more negative energy. The energy spectrum between 0 and -2 eV showed a shift to the left with substituted rhodium. Shifts to a decreased density of states in the 0 to 2 eV region indicate that the addition of rhodium may reduce optical absorption in that region from decreased *d-d* transitions and result in improved optical and infrared transparency.

Other studies on bulk powder samples show that rhodium spinel forms as rhodium is added to the nickel-cobalt oxide system and the degree of crystallinity of the spinel structure decreases with rhodium (Da Silva Pereira et al., 1994). When the powder samples are heated to 500°C, NiO precipitates, however processing at 350°C produces a spinel phase for  $\text{NiCo}_{2-x}\text{Rh}_x\text{O}_4$  at a value of  $x$  up to 0.5 (Da Silva Pereira et al., 1994; Tavares et al., 1996).

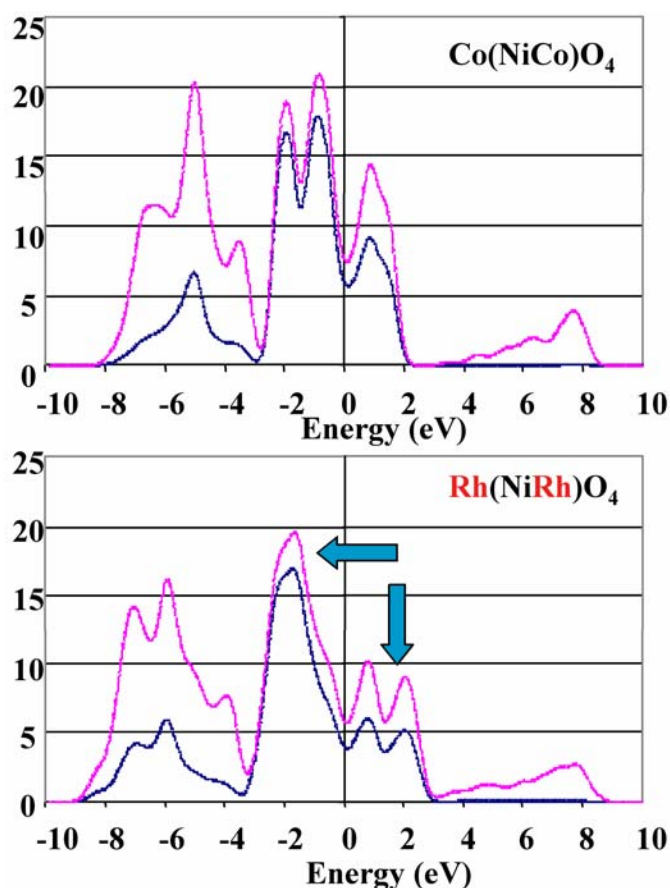


Figure 5-1. First principles d-band density of states calculation of rhodium substituted for cobalt. Energy of 0 eV is the Fermi energy.

Blasse produced a set of powder samples of nickel-cobalt-rhodium oxide by heating at 1100°C for several days. With complete substitution of Rh for Co in the spinel crystal cell, the normally cubic spinel system is reported as a tetragonal variant, being elongated with  $c/a > 1$ . The cubic to tetragonal structural shift is attributed to the Jahn-

Teller\* effect. Spin states of the tetrahedrally located ions are not quenched if the lattice is cubic. In other words, the magnetic moments of the divalent metal ions are considerably larger in the cubic phase than in the tetragonal phase because they are three-fold degenerate in the tetrahedral site. With distortion from the Jahn-Teller effect, the degeneracy is removed and the angular orbital momentum is for the greater part quenched. The structure returned to a cubic spinel above 400 K, reversing the Jahn-Teller effect (Blasse, 1963). Nickel rhodium conductivity results were not given but due to the change in structure from cubic to tetragonal, a more disordered structure allowing more polarons should be beneficial to conductivity.

This chapter discusses results from electrical, optical, structural, and chemical characterization of solution and sputter deposited nickel-cobalt-rhodium thin films.

## 5.2 Experimental Procedure

### 5.2.1 Film Deposition

**Solution deposition.** Solution precursors containing specific molar quantities of nickel nitrate, cobalt nitrate, aqueous rhodium nitrate, and malonic acid were dissolved in ethanol to total 20 mL followed by filtering with a 5  $\mu\text{m}$  filter. Films produced by solution deposition were composed of the amounts shown in Table 5-1.

Precursor solutions were dropped on silicon substrates and spun at  $\sim 3500$  rpm and for 5-10 seconds until the substrate came to full rotation speed and a constant green color showed. Spinning was stopped and the substrate removed from the spin coater and baked at  $\sim 375^\circ\text{C}$  for 10 minutes. Film thickness was on the order of 25-50 nm per layer

---

\* The Jahn-Teller effect is where degeneracy of orbitals is lost as they shift and distort to obtain a lower symmetry and lower more energetically favorable state.

deposited. Multiple spin cast film layers were successively deposited on individual substrates to obtain films of greater thickness for greater ease in characterization.

Table 5-1. Composition recipe of  $\text{NiCo}_{2-v}\text{Rh}_v\text{O}_4$  used for solution deposited samples.

h value	$\text{Ni}(\text{NO}_3)_2$	$\text{Co}(\text{NO}_3)_2$	$\text{RhNO}_3$ (aq)	Malonic Acid	Ethanol (mL)
moles					
0	0.0022	0.0044	-	0.009798	20
0.25	0.0022	0.00385	0.00055	0.009798	20
0.5	0.0022	0.0033	0.0011	0.009798	20
1	0.0022	0.0022	0.0022	0.009798	20
grams					
0	0.63879	1.280576	-	1.02	20
0.25	0.63879	1.120504	0.4051397	1.02	19
0.5	0.63879	0.960432	0.8102795	1.02	18
1	0.63879	0.640288	1.620559	1.02	18

**Sputtering.** Sputtering conditions similar to those found in Chapter 3 and 4 were used to deposit various film compositions with the exception of a DC power supply was used instead of an RF power supply. Chamber base pressure was  $\sim 1 \times 10^{-6}$  Torr backfilled to a pressure of 10 mTorr with 100% oxygen (See Appendix A for sputtering systems and other deposition details). Two-inch alloy targets of Rh,  $\text{NiRh}_2$ , and  $\text{NiRh}_4$  were reactively sputtered with the DC power supply operating in controlled amperage mode set at 0.25 A resulting in 408 V and a power of about 90 W for 5-10 minutes. Target to substrate distances varied from 10 cm to 30 cm with substrate fixtures in double planetary and single rotation setups. Two-inch alloy targets were powered by a 1 kW MDX DC power supply. Deposition distances of 12.5 cm or less were used in the offset rotation setup. Samples were placed on the substrate holder platen along the radius of rotation directly over the cathode axis. Rotation speeds were  $\sim 60$  rpm. Films deposited at distances between 15 and 30 cm were done by either the offset rotation sample setup or the double planetary rotation. Double planetary rotation provides uniform films and is most often used for commercial production where film homogeneity is of utmost

importance. Single rotation requires less target material and less time to produce a film. Substrates were cleaned in an ionized air stream prior to introduction in the vacuum chamber to remove any particles that may cause pinholes in the produced films.

### **5.2.2 Post Deposition Heat Treatment**

Annealing heat treatment occurred at temperatures at 375°C in air for 10 minutes. Films of fused silica, sapphire, or silicon substrates were cooled on a heat sink followed by immediate electrical and optical measurements.

### **5.2.3 Characterization**

Film thickness was measured with an optical or stylus profilometer. X-ray reflectivity (XRR) measurements of select films provided confirmation of the profilometry measurements. Van der Pauw measurements and Hall effect measurements were conducted at room temperature and incrementally up to 675 K with measurements taken both before and after heat treatment.

Fourier transform infrared (FTIR) (Brundle et al., 1992) measured film transparency with respect to air and with respect to the silicon or sapphire substrate. A dual beam ultra violet visible (UVVIS) spectrometer measured transparency from the ultra violet region to the near infrared region (~200 nm-3300 nm). Deposited film composition was determined using x-ray photoelectron spectroscopy (XPS) (Brundle et al., 1992) and secondary ion mass spectrometry (SIMS) (Brundle et al., 1992).

## **5.3 Results**

### **5.3.1 Electrical Properties**

**Solution deposited films.** Samples with rhodium substituted for cobalt have reasonably high conductivity with values between 110 Scm<sup>-1</sup> and 290 Scm<sup>-1</sup> (Figure 5-2)

compared to other solution deposited samples with conductivity values up to  $70 \text{ Scm}^{-1}$  from aqueous solution deposition methods reported in Chapter 4.

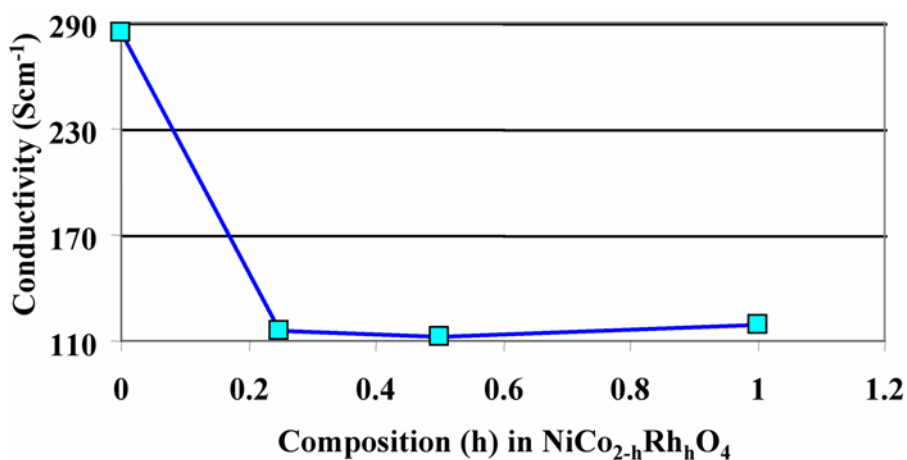


Figure 5-2. Effect of rhodium fraction (h) on conductivity for four-layer films on silicon substrates deposited from solution.

The addition of rhodium to nickel-cobalt oxide was predicted to increase conductivity. As seen in Figure 5-2, the rhodium concentration doubles between each point on the plot and the conductivity staying nearly the same, except where  $h = 0$ . Nickel-cobalt oxide films were originally reported to have conductivity values of  $\sim 10\text{-}90 \text{ Scm}^{-1}$ . It is possible that using a combustion agent such as malonic acid in an ethanol solvent, instead of glycine as a combustion agent in a water solvent, may have changed the film so the bake-off procedure creates more voids. Malonic acid as a combustion agent, if added in too high of a concentration, causes the film to appear to boil as microscopic bubbles emerging from the bulk of the film shatter the surface. The visible pock marks could easily be a source of reduced conductivity from the discontinuous conduction lines through the craters.

**Sputtered films.** As in the nickel cobalt oxide system, the sputtered films show increased conductivity over solution deposited films by only a factor of 2x or 3x. It appears that there is a slight decrease in conductivity when replacing cobalt with rhodium

(Figure 5-3). It reduces conductivity, but only slightly for the alloy sputtered  $\text{NiRh}_4\text{O}_x$  film in Figure 5-3.

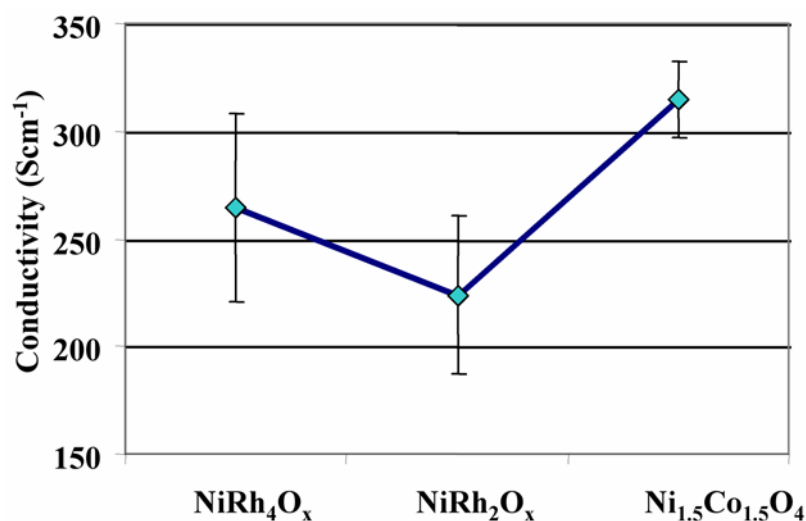


Figure 5-3. Sputtered nickel-rhodium oxide and nickel-cobalt oxide films deposited at 7.5 cm in 10 mTorr of 100% oxygen.

Sputtered films of  $\text{NiRh}_4\text{O}_x$  show the effect of changing target to substrate distance on resistivity in Figure 5-4. Similar to the nickel cobalt oxide system (Figure 3-8), the electrical resistivity increases with increased target-substrate distance.

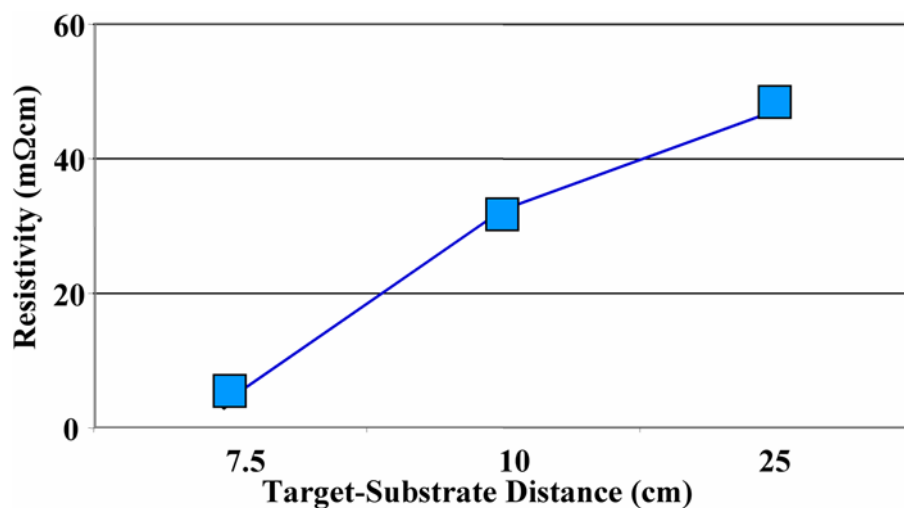


Figure 5-4. Resistivity of  $\text{NiRh}_4\text{O}_x$  as a function of target-substrate distance. Increased distance increases resistivity

It is probable that the growth mechanism is governed by the molecular mean free path and plasma-substrate interaction which will produce a lower density film at the longer distance.

### 5.3.2 Optical Properties

**Solution deposited films.** Transmission spectra of  $\text{NiCo}_{2-h}\text{Rh}_h\text{O}_4$  films 4 layers thick are shown in Figure 5-5 after correction for the silicon substrate absorption peaks. The most conductive film is the least transparent in the IR spectrum and contains no rhodium. Spinel absorption lines appear in all spectra near 550 and 650  $\text{cm}^{-1}$ . The spinel absorption peaks for  $\text{NiCo}_{2-h}\text{Rh}_h\text{O}_4$  are sharpest in the films where  $h = 0$  most probably due to the highly crystalline spinel film structure (Windisch et al., 2002a). As discussed in Chapter 3, increased conductivity accompanies a concomitant decrease in transparency.

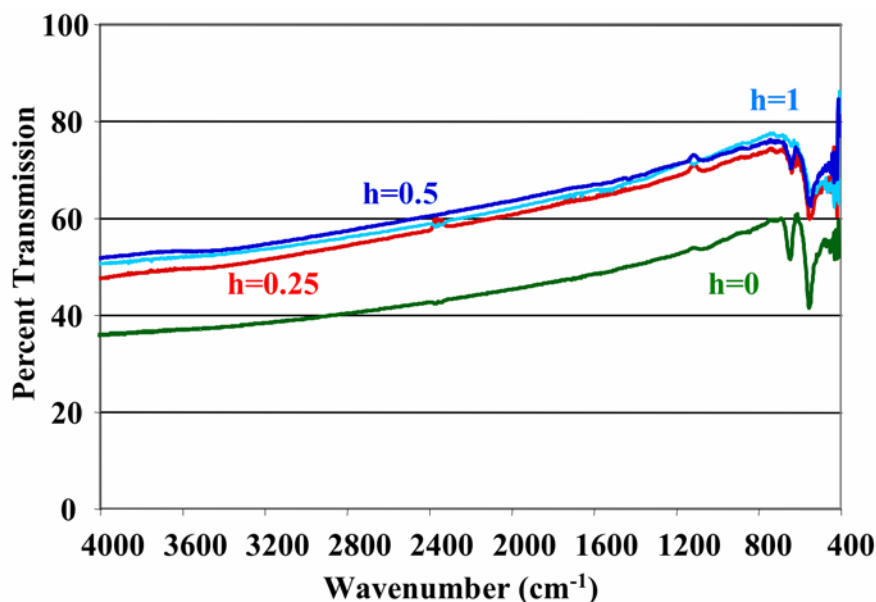


Figure 5-5. Solution deposited  $\text{NiCo}_{2-h}\text{Rh}_h\text{O}_4$  FTIR transmission spectra were all corrected for the silicon substrate absorption peaks.

**Sputter deposited films.** A comparison of calculated absorption coefficients described in Equation 3.6 is shown in Figure 5-6. As substrate distance increases, the

calculated absorption coefficient decreases indicating that increased target-substrate distance leads to a lower density. Decreased density is responsible for the increased electrical resistivity for films deposited at different distances described in Chapter 3.

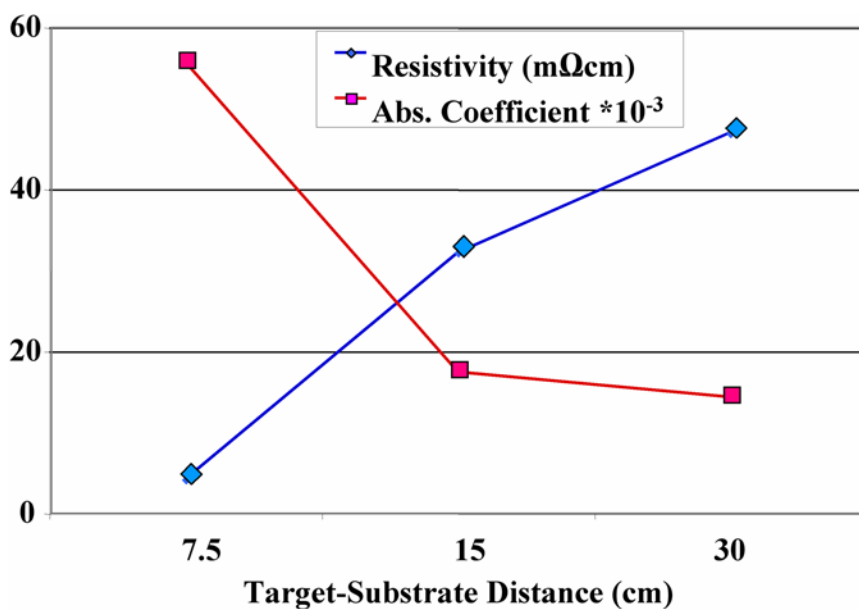


Figure 5-6. Resistivity and optical absorption coefficient at 3  $\mu\text{m}$  as a function of sputtering target-substrate deposition distance.

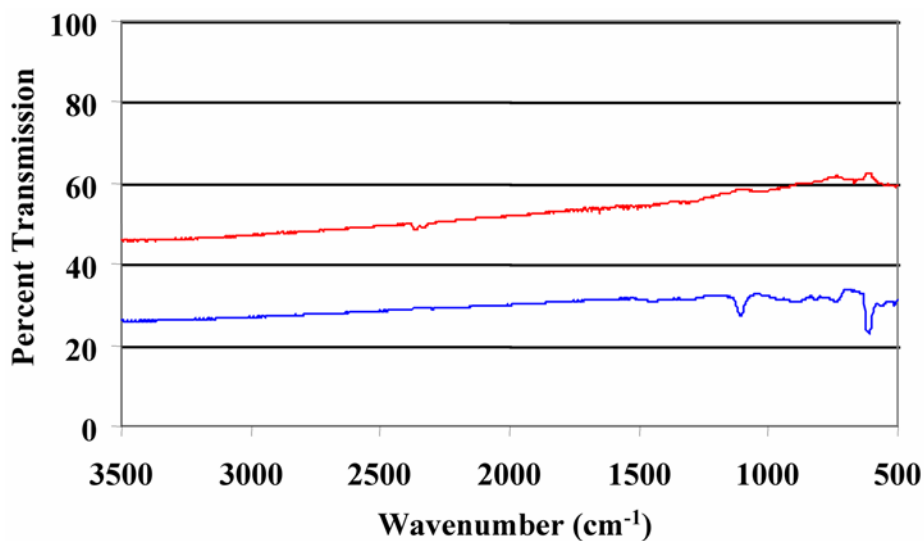


Figure 5-7.  $\text{NiRh}_2\text{O}_x$  FTIR data referenced to air (lower blue trace) and corrected for the silicon substrate (upper red trace).

FTIR data of a  $\text{NiRh}_2\text{O}_x$  film with a transmission near 70% at 700  $\text{cm}^{-1}$  is shown in Figure 5-7. Optical correction removes the absorption bands normally seen from the

silicon substrate (blue) in addition to the film features. The red data plot is essentially featureless suggesting that the sputtered films are amorphous because the typical spinel absorption peaks are not observed.

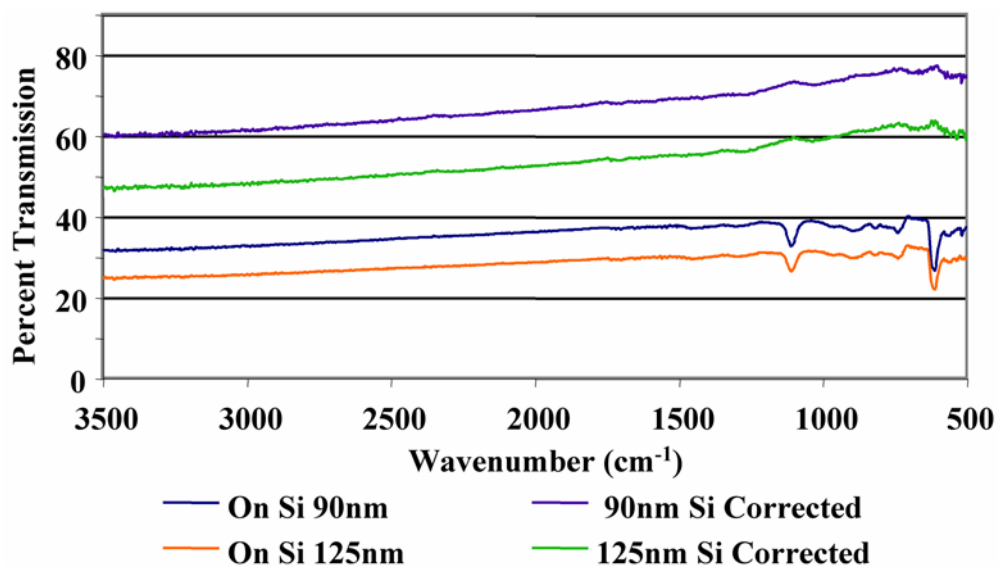


Figure 5-8. FTIR spectra of two  $\text{NiRh}_4\text{O}_x$  samples of different thicknesses deposited from  $\text{NiRh}_4$  alloy target by DC sputtering. Both films are shown with and without substrate correction. Notice that there are no sharp absorption bands at either  $540\text{ cm}^{-1}$  or  $630\text{ cm}^{-1}$  from spine absorption.

Figure 5-8 shows FTIR data of a  $\text{NiRh}_4\text{O}_x$  film with a transmission near 80% at  $700\text{ cm}^{-1}$ . Thin films (90 nm) of nickel-rhodium oxide reactively DC sputtered on silicon substrates show transparency of  $\sim 75\%$  for films nearly twice as thick as nickel-cobalt oxide (50 nm). Nickel-rhodium oxide optical transmission compared to nickel cobalt oxide optical transmission shows improved transparency at similar thickness with similar electrical conductivity.

### 5.3.3 Structural Properties

Structurally the solution and sputtered films are not identical. Sputtered films do not exhibit the spinel absorption peaks at  $546\text{ cm}^{-1}$  and  $\sim 640\text{ cm}^{-1}$ , while the solution films all exhibit the spinel absorption peaks.  $\text{NiCo}_{2-h}\text{Rh}_h\text{O}_4$  films in Figure 5-9 show that

as  $h$  increases, the spinel peak intensities appear to decrease, and the structure is more amorphous. Apparently the addition of rhodium does introduce disorder into the lattice as seen in the IR spectra for  $\text{NiRh}_s\text{O}_4$  where  $s = 2$  and  $s = 4$ . Both are nearly flat lines in Figure 5-9.

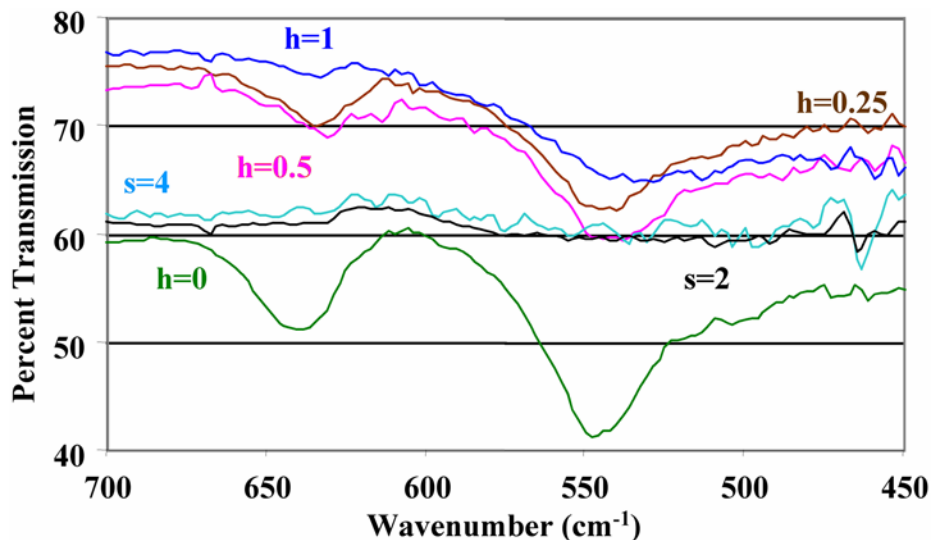


Figure 5-9. FTIR of solution deposited  $\text{NiCo}_{2-h}\text{Rh}_h\text{O}_4$  and sputtered  $\text{NiRh}_s\text{O}_4$  thin films corrected for silicon substrate absorption. All of the solution compositions show the spinel absorption bands near  $640\text{ cm}^{-1}$  and  $540\text{ cm}^{-1}$ . None of the sputtered films show the spinel absorption lines.

The higher frequency mode at  $\sim 640\text{ cm}^{-1}$  is correlated with the octahedral site while the mode at  $\sim 540\text{ cm}^{-1}$  is a function of both the octahedral and the tetrahedral site vibrations.

The differences between sputtered and solution deposited films, which are amorphous and crystalline spinel, respectively, probably arise from the growth mechanism being limited by the growth speed.

Far infrared spectra of the 4-layer solution deposited films show the spinel absorption at  $546\text{ cm}^{-1}$ , which appears to shift to lower frequency as rhodium concentration increases. The film with a composition of  $h = 1$  does not appear to have a significant spinel peak despite the stoichiometry of equal parts nickel, cobalt and

rhodium. This stoichiometry should allow rhodium and nickel to occupy all of the octahedral sites and cobalt should occupy the tetrahedral sites. Also evident from these data is the broad peak near  $400\text{ cm}^{-1}$  attributed to the  $\text{Ni}^{3+}$  cation state when no rhodium is present.

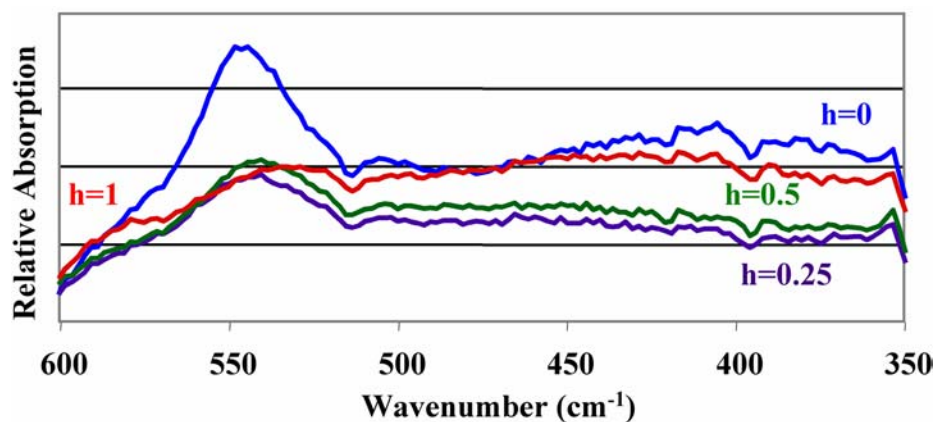


Figure 5-10. Far IR spectra of solution deposited  $\text{NiCo}_{2-h}\text{Rh}_h\text{O}_4$  from FTIR show the structure of the films.

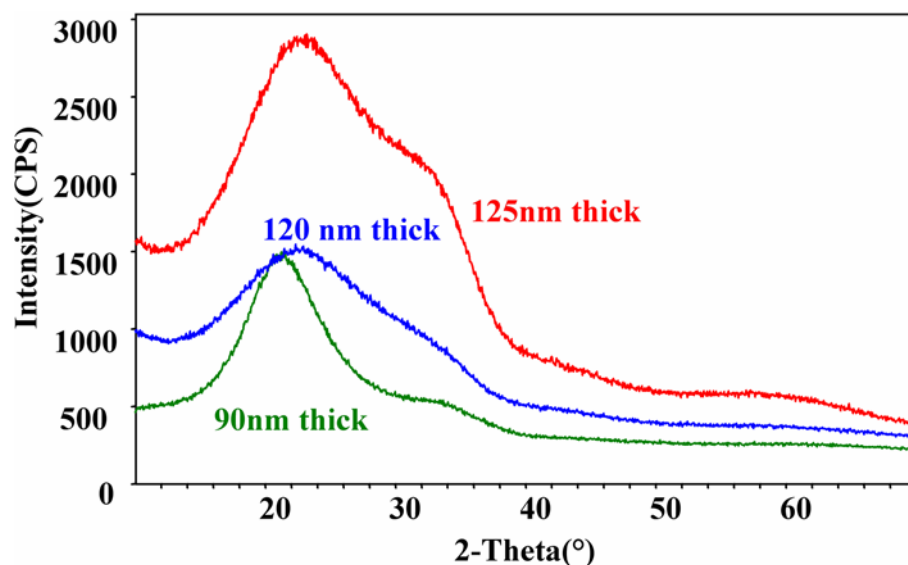


Figure 5-11. XRD of  $\text{NiRh}_4\text{O}_x$  film from DC alloy sputter deposition.

Sputtered films did not exhibit XRD peaks (Figure 5-11 and Figure 5-12). As suggested above, the addition of rhodium adds distortions to the lattice. Beyond what was predicted, the rhodium actually distorts the lattice beyond the Jahn-Teller effect to an

amorphous state. Both  $\text{NiRh}_4\text{O}_x$  and  $\text{NiRh}_2\text{O}_x$  compositions of sputtered nickel-rhodium were amorphous. Film heat treatment up to  $600^\circ\text{C}$  followed by rapid quenching did not improve the film crystallinity from the amorphous state.

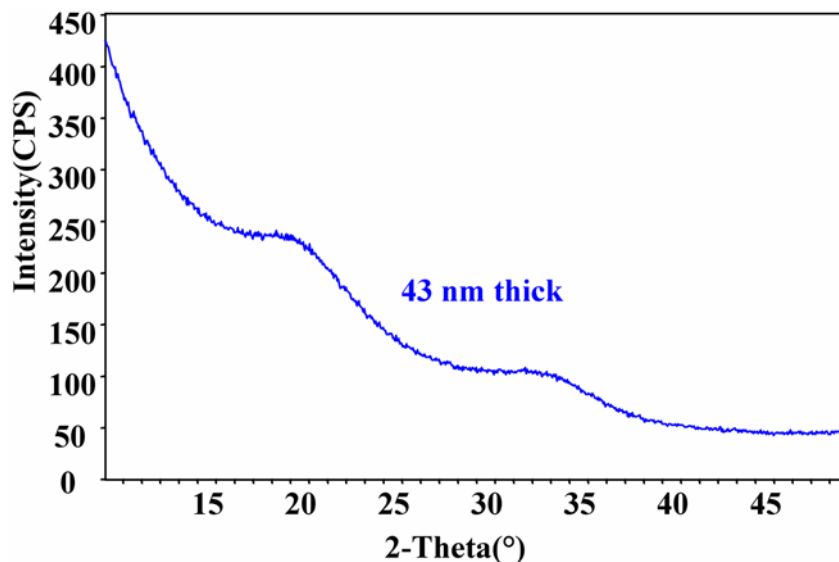


Figure 5-12. XRD of amorphous  $\text{NiRh}_2\text{O}_x$  thin film from DC alloy sputter deposition.

#### 5.3.4 Chemical Properties

Nickel rhodium appears to be stoichiometric on the surface as expected, however depth profiling shows, the films lack oxygen. It has not been determined whether this lack of oxygen in the bulk of the film is intrinsic to the material or an artifact of its preferential removal. Interaction of oxygen with the argon sputtering beam used to perform the depth profile (Smentkowski, 2000). If this oxygen depletion is intrinsic to the film, dangling bonds would be a source of blocked polaron hopping and may cause a reduction in conductivity.

The oxygen depletion may be a result of the argon bombardment that takes place during the XPS depth profiling. Surface stoichiometry, while not always indicative of the bulk, may actually be more representative of the bulk of the film. XPS depth profiles show rhodium in the silicon substrate deeper than would be expected. Another

possibility is that the rhodium-oxide octahedral bonding, being less covalent because it is a 5d bond with a 2p orbital as opposed to a cobalt 3d bond with a 2p orbital may more easily releases the oxygen in the lattice. The result would be a diffusion of oxygen through the native silicon dioxide layer to form a deeper SiO<sub>2</sub> layer. As rhodium is reduced, which is thermodynamically favorable, the formerly bound oxygen is free to diffuse through the lattice and possibly into the substrate as seen in Figure 5-13 with the extended tail of the red trace.

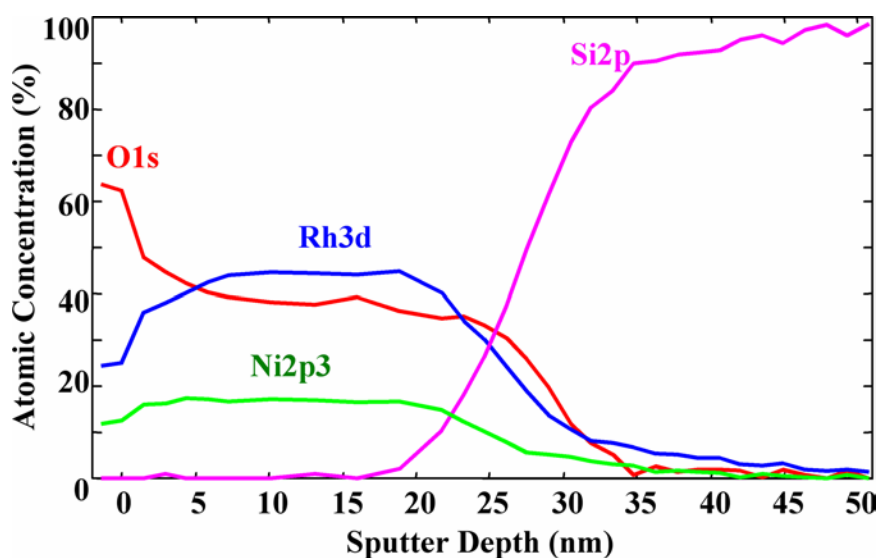


Figure 5-13. XPS depth profile showing the surface of sputter deposited NiRh<sub>2</sub>O<sub>x</sub> is different than the bulk concentration. Concentrations of Ni and Rh at 35 nm indicate diffusion into the substrate. Depth was calibrated by sputtering a standard and confirmed with optical and stylus profilometry.

Data in Figure 5-14 are similar to Figure 5-13 except that the ratio of nickel to rhodium is 1:4 instead of 1:2. Films in Figure 5-14 were deposited under the same conditions as the film in Figure 5-13, but for a longer period of time giving a thickness of ~200 nm compared with ~35 nm. The film surface in Figure 5-14 also appears oxygen depleted prior to sputtering. In both cases, the oxygen always decreases with the onset of sputtering indicating that the surface is oxidized, but the sputtered bulk of the film is

reduced. The concentrations of rhodium, nickel, and oxygen appear to be constant through the film to the substrate interface.

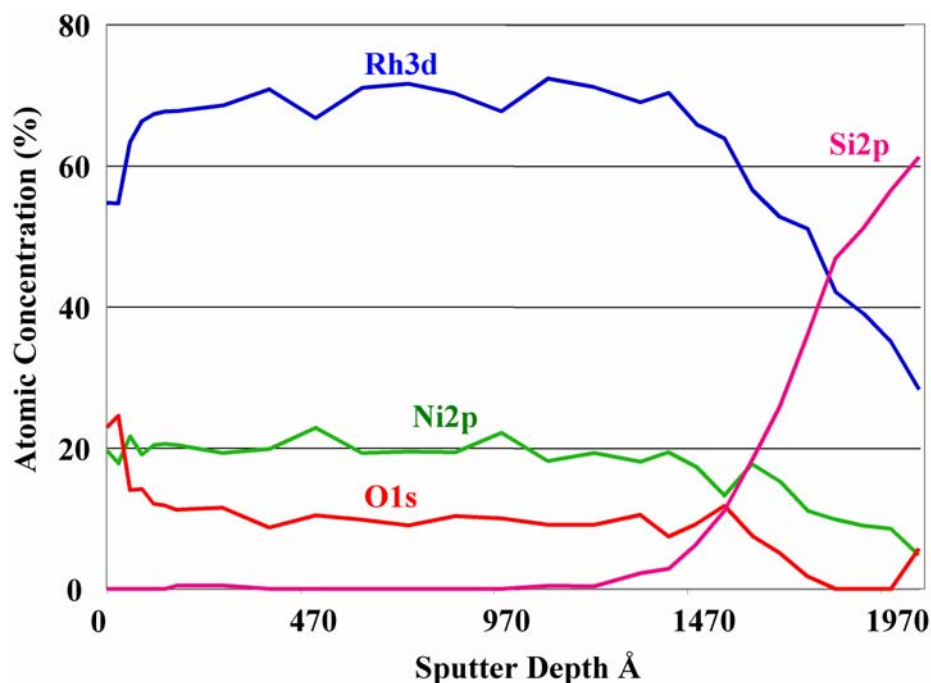


Figure 5-14. XPS depth profile of a film sputtered from a NiRh<sub>4</sub> target shows an oxygen depleted surface.

The multiplexed data from the XPS depth profiles, shown in Figures 5-15 indicate that the chemical state of the nickel and rhodium species changes with depth. At the interface, the O 1s peaks shift to higher energy indicating a region of silicon dioxide (black data plot in Figure 5-15c and Figure 5-15d). The Ni 2p<sub>3/2</sub> doublet peak located at ~855 eV and ~861 eV in Figure 5-15a and Figure 5-15b appears to change immediately upon sputtering with the peak near 861 eV decreasing in intensity with increasing sputtering time. Rhodium also appears to shift chemical state at the onset of sputtering as the Rh 3d line (shown in Figure 5-16e and Figure 5-16f) at 309 eV shifts to lower binding energy near 308 eV.

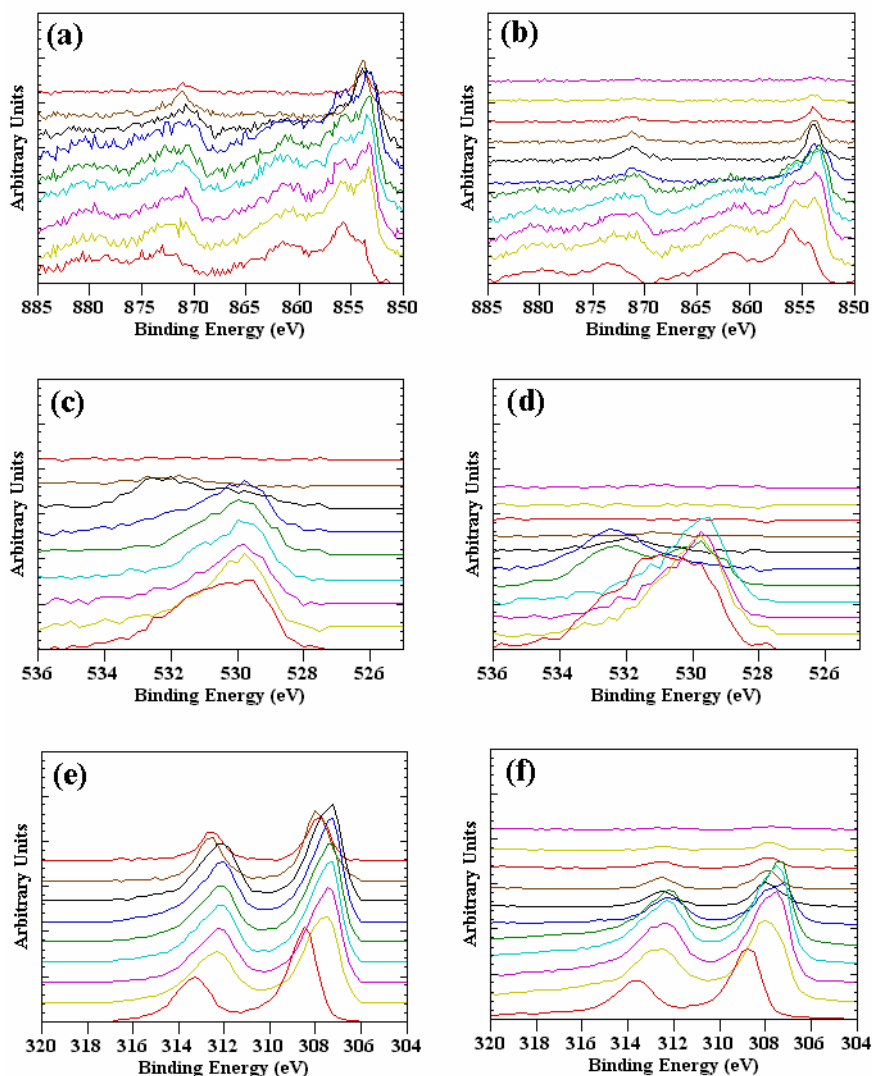


Figure 5-15. Multiplex binding energy data from XPS depth profiles. Nickel 2p binding energy region of films deposited from (a) NiRh<sub>4</sub> and (b) NiRh<sub>2</sub> alloy targets. Oxygen 1s binding energy region of films deposited from (c) NiRh<sub>4</sub> and (d) NiRh<sub>2</sub> alloy targets. Rhodium 3d binding energy region of films deposited from (e) NiRh<sub>4</sub> and (f) NiRh<sub>2</sub> alloy targets. Data plotted near the base of each plot is the surface. Successive stacked data plots are deeper in the sample towards the film-substrate interface.

#### 5.4 Discussion

More polarons may form with the increased lattice distortion brought about by the substitution of rhodium for cobalt, however, an overall increase in conductivity is not observed. An increase in polaron density may not make up for discontinuous conduction paths from the increased structural disorder that allows the formation of the extra carriers.

This results in a decreased mobility due to obstructed hopping. More polarons cannot lead to higher conductivity if they cannot hop to contribute to the current.

Evident from solution deposition parameters, the films may have micro craters as a result of the burning of the malonic acid and ethanol that occurs during the deposition process heat treatment. Craters could also obstruct hopping along the octahedral sites (illustrated in Figure 3-18 as crisscrossing lines of conduction), but were not considered critical because all films were deposited under identical conditions and multiple film coatings were essentially continuous.

Similar to the process study in Chapter 3, increasing the distance of the target to the substrate for sputtered samples increases resistivity while the absorption coefficient decreases. This effect is attributed to the combination of lost energy due to increased collisions as distance increases and a reduced plasma interaction at the longer distance so less energy is transferred to the substrate. Lower energy transfer at the substrate equates to a lower substrate temperature and lower surface mobility. An energetically preferred structural arrangement may not occur with lower surface mobility from the lower energy at the surface and may result in discontinuous conductivity paths along octahedral sites. Longer sputter distance results in lower film density, increased resistivity, and increased transparency, similar to the nickel-cobalt oxide system.

Optical transmission data show some degree of spinel structure in solution deposited films exhibited by characteristic spinel peaks at  $\sim 540\text{ cm}^{-1}$  and  $\sim 640\text{ cm}^{-1}$ . Far infrared spectra show a shift to a lower frequency of the  $546\text{ cm}^{-1}$  spinel peak with increasing rhodium concentration accompanied by a broadening of the band. This shift is expected because the higher mass of rhodium will cause a shift to a lower vibrational

frequency in the octahedral mode. Far infrared data also indicate a characteristic  $\text{Ni}^{3+}$  band near  $380\text{ cm}^{-1}$  for the  $\text{NiCo}_2\text{O}_4$  sample that appears to weaken with increased rhodium concentration. These results agree with the proposed incorporation of rhodium in the octahedral site. Weakening of the specified absorption peaks agrees with the addition of structural disorder to the system with increased rhodium concentrations. The amorphous sputter deposited films of  $\text{NiRh}_2\text{O}_x$  and  $\text{NiRh}_4\text{O}_x$  are surprising, but not unexpected. The flat-lined infrared data at  $640\text{ cm}^{-1}$  and  $540\text{ cm}^{-1}$  were confirmed with featureless XRD scans indicating an amorphous structure. The amorphous structure may occur because both nickel and rhodium are octahedral site occupants. When rhodium is partially substituted for cobalt, it is probable that the cobalt remains in the tetrahedral sites affording a measure of spinel phase stability. With no tetrahedral site resident, the spinel structure is not supported. As seen in the IR spectra in Figure 5-9, the decrease in spinel vibrational modes with the decrease in cobalt concentration supports this assertion.

Previous data indicate that powder spinel nickel-rhodium oxide was produced via several days of high temperature processing exceeding  $1100^\circ\text{C}$  (Blasse, 1963). XRD data was not shown to be pure spinel. Da Silva Perieira et al. indicate that nickel oxide separates from electrodes produced at temperatures of  $500^\circ\text{C}$ , a finding that is commensurate with the results shown by Windisch et al. showing nickel oxide precipitation at  $400^\circ\text{C}$  in the nickel-cobalt oxide thin films (Da Silva Pereira et al., 1994; Windisch et al., 2001b). The amorphous sputtered films of  $\text{NiRh}_2\text{O}_x$  and  $\text{NiRh}_4\text{O}$  in this study indicate possible film-substrate reactions. Blasse's claims a tetragonal to cubic Jahn-Teller shift may occur and refers to XRD in his text and lets the reader assume all the materials were crystalline spinel. The temperatures used to process those nickel-

rhodium powders would have likely contaminated the samples with traces of precipitated nickel oxide. Further high temperature treatment tests of nickel-rhodium oxide films on infrared transparent, other than silicon, is required to address this disparity of information.

It is probable that this disordered structural arrangement gives the nickel rhodium its high conductivity, though its conductivity is not better than crystalline  $\text{NiCo}_2\text{O}_4$  suggesting that there may be a maximum density of polarons in a given volume that limits the maximum conductivity for a polaron conducting film. A discussion of maximum conductivity will follow in Chapter 6.

XPS depth profiles of sputtered nickel rhodium films indicate that the film surface may be more oxidized than the bulk film seen by shifts of metallic peaks to lower binding energies at the onset of sputtering. This does not necessarily indicate that the film is substoichiometric in the bulk. The disparity between bulk and surface may, however, be due a preferential sputtering artifact articulated by Smentkowski, who explored the sputtering of various metal oxide systems addressing the problem of the preferential removal of oxygen over the metal cation during sputtering. He addresses many systems that show a depletion of oxygen on the surface after the process of sputtering used in depth profiling (Smentkowski, 2000, Holloway & Nelson, 1979). The results from this study are inconclusive as to whether the bulk of the film is partially reduced in the bulk or completely the result of an artifact from sputtering, a point to be further investigated.

Depth profiles also indicate that rhodium and nickel diffuse into the silicon wafer beyond the native oxide layer. Formation of metal silicides has not been confirmed. Nickel silicide is highly conductive and used extensively as an interconnect material in

the microelectronics industry (Xu et al., 1998). Thermodynamically the formation of rhodium silicide or rhodium silicate is more favorable than nickel silicide based on a free energy calculation, but kinetics of formation of one phase versus the other has not been studied. Nickel oxide has been shown to form nickel silicide under the influence of argon bombardment (Gonzalez-Elipse et al., 1991). It is possible that a base layer of nickel silicide forms during the initial nickel-rhodium oxide film deposition or during the sputter depth profile of the XPS analysis; however, a silicide phase formation as shown by Gonzales-Elipse et al. exhibits a single strong binding energy peak near 853 eV from XPS, which is not observed in this analysis. Binding energy peaks at 854.5 eV and 862 eV merely broadened and appear to converge, indicative of reduction.

It may be that the heat from the depth profiling argon beam induces localized diffusion of nickel and rhodium into the substrate during sputtering. The idea of rhodium diffusion into the substrate may be plausible, but once again, the results are not definitive to support this assertion. Future studies will need to further elaborate on the interaction of the argon plasma with the nickel-cobalt-rhodium oxide system.

## 5.5 Conclusions

Conductivity decreases with increased rhodium concentration dropping from 290  $\text{Scm}^{-1}$  to about 110  $\text{Scm}^{-1}$  for solution deposited samples. Sputtered oxide films from alloy targets of  $\text{NiRh}_4$  and  $\text{NiRh}_2$  with conductivities of 260  $\text{Scm}^{-1}$  and 225  $\text{Scm}^{-1}$ , respectively, show comparable conductivity with nickel-cobalt oxide at 310  $\text{Scm}^{-1}$ . Sputtered film resistivity increased from 3.8  $\text{m}\Omega\text{cm}$  to 48  $\text{m}\Omega\text{cm}$  with increased target-substrate distance similar to observations in other nickel cobalt oxide films that increase in resistivity with increased target-substrate sputtering distance (Chapter 3).

Infrared transparency for solution deposited  $\text{NiCo}_{2-h}\text{Rh}_h\text{O}_4$  films compositions with  $h = 0, 0.25, 0.5$  and  $1$  show improvements of 10-15% and a decrease in conductivity of nearly 50%. Sputtered films exhibit an increase in the optical absorption coefficient at  $3 \mu\text{m}$  as target-substrate distance decreases from 30 cm to 7 cm. This change in absorption typifies increased density with shorter target-substrate distance, common in sputtered films. FTIR data of sputtered films shows that oxide films deposited from the  $\text{NiRh}_4$  alloy target were similar in transparency and more conductive than the oxide films of similar thickness deposited from the  $\text{NiRh}_2$  target.

Structurally, the sputtered films are amorphous. The solution deposited films exhibit spinel absorption peaks at  $546 \text{ cm}^{-1}$  and  $\sim 640 \text{ cm}^{-1}$  in the infrared spectrum that broaden and shift to lower frequency with increased rhodium concentration. Low frequency shifts are expected from the larger mass of the rhodium ion compared to the cobalt ion being replaced.

XPS results show that the film composition was homogeneous through the bulk of the film. The disparity of oxygen concentration at the surface and the bulk of the film may be real or an indication of preferential removal of oxygen that occurs during the XPS sputter depth profiling. Silicide formation at the surface of the silicon wafer and the nickel-rhodium film most probably does not occur; however the presence of a silicide film is not completely ruled out.

Amorphous nickel-rhodium oxide structures from sputtering are unexpected, but not surprising because the addition of rhodium, by design, is to induce structural disorder and allow increased polaron formation. Structural disorder is believed to be due to the octahedral occupation of both nickel and rhodium with neither occupying the tetrahedral

position. While more polarons may form, a competing degradation of the conduction pathways due to the disordered structure impedes the hopping motion for increased electrical conductivity.

## CHAPTER 6 DISORDER AND POLARON CONDUCTIVITY

### 6.1 Introduction

While it is customary to think of electrons and holes as conducting elements in a solid state lattice, when the lattice is distorted by these charges, special properties result and the charge carrier under these conditions is called a polaron. Since polarons are electrons or holes trapped in bandgap quantum states associated with lattice distortions, their motion is thermally activated resulting in low mobility at room temperature ( $< 0.1 \text{ cm}^2\text{V}^{-1}\text{s}^{-1}$ ). Polarons form as the lattice distorts to accommodate the extra charge state, creating the potential well, and effectively trapping the carrier in the self-induced strain region. Similar to electrons and holes, conductivity is proportional to the product of the polaron density times its mobility. When the lattice is disordered, an electronic carrier is more easily trapped. In the case of polarons, disorder increases the polaron density and increases the conductivity of the film.

Two types of disorder are discussed in this chapter (see Figure 6-1). First is a structural disorder of the cations and anions that constitute the crystal lattice (Section 6.2). The films produced were expected to be a pure phase of crystalline spinel rather than amorphous. Typical amorphous structures exhibit little if any long-range structural order. The second disorder type deals with the disordered distribution of the cation charges in spinel film (Section 6.3). Cation charge disorder, attributed to a Verwey-like order/disorder transition (Chapters 3 and 4), affects the activation energy of nickel-cobalt oxide films as a function of the rate of cooling that follows heat treatment. A model for

the cation charge disorder based on localized carrier interactions that detail a similar effect on activation energy is described in this chapter. Section 6.4 discusses an estimate for maximum conductivity in the spinel nickel-cobalt oxide system considering realistic boundaries of disorder.

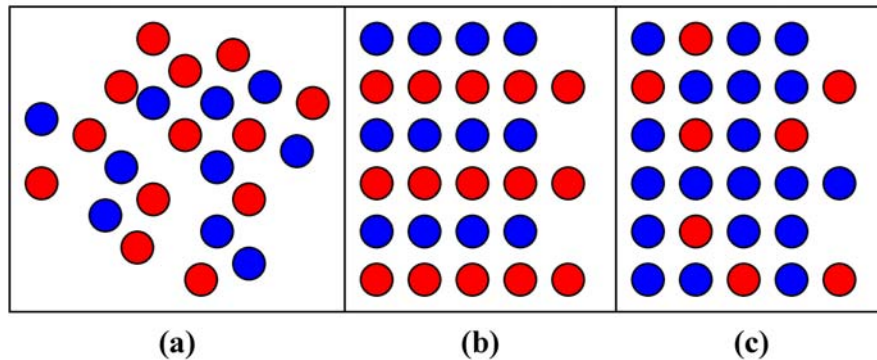


Figure 6-1. Schematic of disorder. (a) Amorphous structural disorder, (b) an ordered structure, and (c) a crystalline structure with disordered charge distribution. Red corresponds to one oxidation state of a cation, while blue is a second oxidation state.

## 6.2 Structural Disorder

Structural disorder is the random arrangement of ions in a solid. In many cases, lattice disorder can be correlated with a decrease in crystallinity. Due to the random atomistic arrangement, structural disorder produces a variety of trapped states (polarons) with a distribution of activation energies that enable conduction. Work by Emin and Tauc has shown that disorder in amorphous  $\text{SiO}_2$  can produce polarons by trapping holes in the oxygen p orbitals (Emin & Bussac, 1994; Tauc, 1976).

Figure 6-2 shows the effects of nickel concentration on activation energy. With lower nickel concentration, the film conductivity decreases and activation energy increases. The addition of nickel was shown to induce disorder. The activation energy shifts in nickel-cobalt oxide thin films as a function of composition as shown from temperature dependent conductivity data (Windisch et al., 2002b). Data in Figure 6-2a

were gathered during the heating cycle from samples previously quenched after being subjected to heat treatment of  $\sim 375^\circ\text{C}$  for 10 minutes in air.

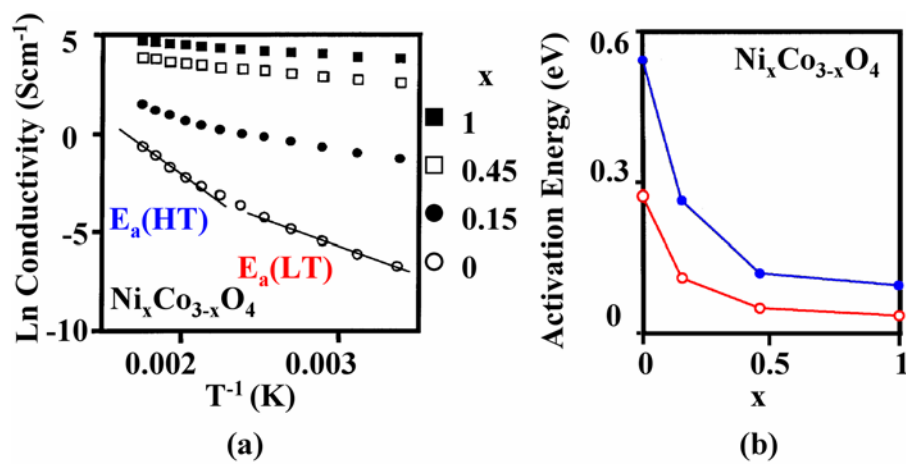


Figure 6-2. The effect of composition on temperature dependant conductivity and activation energy. Plots of (a) Arrhenius conductivity plot and (b) activation energies calculated from the two different energy regions in plot (a). (Based on data presented by Windisch et al., 2002b, Figure 5, p. 93, slightly modified and color added).

Optical techniques such as laser Raman and Fourier transform far infrared absorption spectroscopy were also used to show the effects of nickel in the cobalt oxide lattice. Raman peaks for cobalt oxide were seen to rapidly broaden to amorphous features with small additions of nickel (Windisch et al., 2002a; Windisch et al., 2002b). An additional study by Windisch et al. showed that a mode near  $373\text{ cm}^{-1}$  increased in intensity with an increased concentration of  $\text{Ni}^{3+}$  as activation energy decreased indicating polaron formation (Windisch, 2003a). These films structures were reported as spinel despite the change in nickel concentration suggesting this system may have been affected by disorder.

A shift of  $\text{NaPO}_3$  from a crystalline to amorphous structure induced by processing is shown in Figure 6-3. The amorphous  $\text{NaPO}_3$  structure is made by rapid cooling the melt on a metal plate. It exhibits a broad, relatively featureless Raman band in the far IR,

whereas the crystalline state (made by heat treating the amorphous material at 300°C for 2 hours) shows distinct peaks correlating with specific molecular vibrational modes.

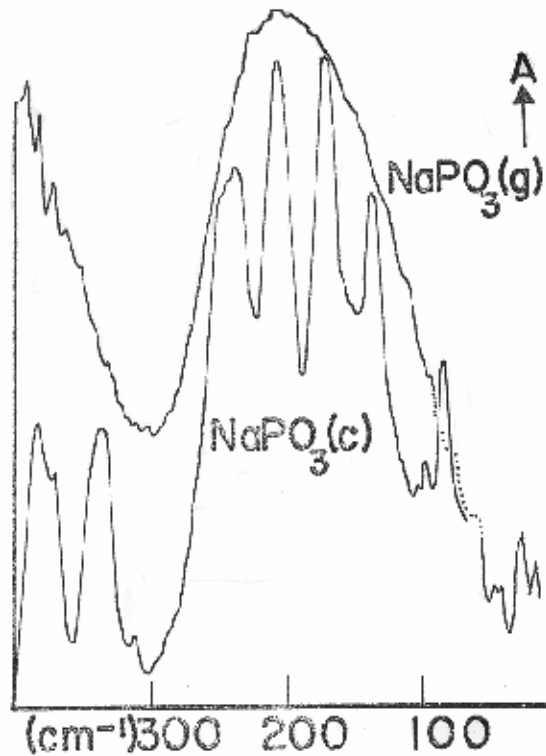


Figure 6-3. NaPO<sub>3</sub> glass phase (amorphous) with a broad band covering the bond vibrational modes. Crystalline NaPO<sub>3</sub> phase shows distinct individual active vibrational modes easily distinguished due to the ordered structure of the film. Reprinted with permission from Exarhos, G.J. (1974) Spectroscopic investigations of glasses and polymers. Ph.D., Brown University.

XRD data for the nickel-cobalt oxide data in Figure 6-2 did not show a decrease in crystallinity with the increase in nickel concentration. Windisch et al. also reported that the lattice parameter increased with increased nickel concentration in cobalt oxide (Roginskaya et al., 1997; Windisch et al., 2002b). This shift in lattice parameter suggests that spinel remains as the major phase, nickel incorporates into the lattice (Windisch et al., 2002b), and that structural lattice disorder may be part of, but is not the entire cause of increased conductivity.

Data from the nickel-cobalt-rhodium oxide system prepared by solution deposition (presented in Figure 5-9) show that with increased rhodium, the structure shifts to an amorphous state. More structural disorder in that case did not cause improved conductivity, an unexpected result based on Emin's predictions. The shift to an amorphous state does not necessarily increase the conductivity (presented in Chapter 5 and illustrated in Figures 5-2 and 5-3). Stoneham describes transition metal oxides from a modeling standpoint and addresses the effects of impurity additions. His modeling results indicate that the addition of lithium impurities to nickel oxide cause a trapped hole to localize on a cation adjacent to the substitutional impurity (Stoneham, 1980). Trapped holes localize on the rhodium impurity in the  $\text{NiCo}_{2-h}\text{Rh}_h\text{O}_4$  system and require more energy to hop because of the rhodium interaction with the cobalt in the lattice (as  $h$  increases from 0 to 1).

When the rhodium completely replaces the cobalt, conductivity values are nearly recovered, suggesting that the carrier gets trapped at the impurity site. Structural disorder introduced by the substituted cation does not produce the desired result of increased conductivity. This may be caused by the coupling of the disorder with some type of bonding anomaly such as a change in trapped-carrier activation energy from the interaction of rhodium with its neighbors. Tauc reasons that carriers are much less mobile in glasses than in crystals (Tauc, 1976). It is probable that mobility decreases due to disrupted carrier paths within the irregular lattice as the increased rhodium concentration shifts the spinel to an amorphous state.

Raman data of nickel-cobalt oxide show some degree of disorder may occur as indicated by the broadening of the spinel bands. This disorder is probably a decoupling of the active modes from the Jahn-Teller effect rather than a shift to an amorphous state.

### **6.3 Cation Charge Disorder**

#### **6.3.1 Introduction**

Verwey et al. postulated that the charge distribution within a structured solid may affect the activation energy of electrical conductivity in spinel  $\text{Fe}_3\text{O}_4$  (Verwey & Haayman, 1941; Verwey et al., 1947; Verwey, 1939). Cation charge order/disorder is suggested to decrease/increase conductivity, respectively. A transition that occurred during conductivity experiments was attributed to a disorder/order charge distribution within the crystalline lattice. This reported transition for the iron oxide spinel system occurs below room temperature near the Neel temperature of 200K for  $\text{Fe}_3\text{O}_4$  (Verwey & Haayman, 1941; Verwey et al., 1947; Verwey, 1939).

Nickel-cobalt oxide films quenched after heat treatment are more conductive than the slowly cooled films (shown in Figure 3-23) and exhibit a decreased slope (activation energy) in the Arrhenius conductivity curve. This change in slope is attributed to a Verwey-type transition caused by an increase cation charge disorder induced by the kinetics of cooling. Film conductivity after quenching decreases with exposure to atmosphere. Equilibration requires time for kinetics to reduce the film to a more favorable energy state of an ordered charge distribution. Slow cooling of the films after heat treatment shows effects similar to prolonged exposure to atmosphere. Quenched-in cation charge disorder and its effects on the activation energy for carrier conduction are modeled in the next section by a site-to-site interaction model.

Charge disorder may be affected by addition of impurities. The addition of impurities may affect the populations of defects (polarons form at defect sites), in addition to the types of defects and the mechanism allowing more to form (Stoneham, 1980). Cation charge disorder affects carriers hopping between two neighboring ions. This interchange requires two ions of different oxidation states. If the cation order is random, then the probability of an adjacent site where the carrier can hop will be high.

Bringing the concept of a bound carrier together with the influence of disorder, there are several classical models for a bound carrier in a potential well. In the following, a model for polaron conductivity of the nickel-cobalt oxide spinel system is outlined based on the *particle in a box* model for lattice dynamics and a spin model for carrier disorder effects.

### 6.3.2 Disorder and the Polaron Hopping Activation Energy Model

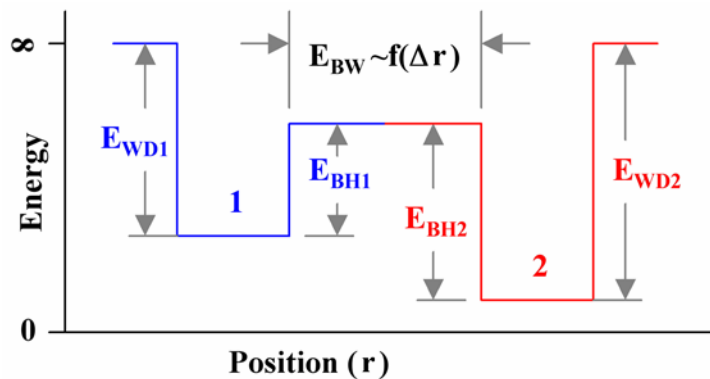


Figure 6-4. A double well potential with the associated energies that influence carrier motion between the wells.  $E_{BW}$  labels a positional distance whose value depends upon the distance the carrier must hop between the two wells ( $r$ ). The carrier is found in position 1 (blue) or position 2 (red).

The *particle in a box* model approximates a carrier in a one dimensional well with infinite potential energy surface barriers (described in Chapter 2). The particle is bound to the regions inside the 1-D box (energy well). Two wells placed side by side share an adjoining potential barrier with a finite value. Two mechanisms are possible that allow a

trapped carrier in state 1 to move to state 2 (Figure 6-4). The first is to tunnel through the barrier, and the second is to hop over it. Assuming tunneling is negligible at room temperature, there are three energies that combine to equal the activation energy required for the barrier hopping process:

1. Barrier height,  $E_{BH}$ . Energy of the barrier height is influenced by the polaron nature i.e. the atomic species involved with the self-trapped state or the cation-anion interaction at the occupied site.
2. Barrier width,  $E_{BW}$ . Energy of the barrier width is directly proportional to the distance between two hopping sites. Hopping distance is also described as the polaron size. The extent of the local distortion in the lattice is what classifies a polaron as large or small. A large polaron displaces atoms beyond its near neighbors, while a small polaron is highly localized to the site and its nearest neighbors. As more disorder is introduced, barrier widths may become distributed in sizes.
3. Well depth,  $E_{WD}$ . Energy of the well depth on either side of the barrier is not necessarily the same in a disordered system. In a perfectly ordered system, the well depth would be the same. This base energy value of organizational energy is affected by the interaction between polarons based on the polaron distribution throughout the lattice. Disordered cation charge arrangement, grain structure defects, or an amorphous arrangement affect this energy.

The well width is not considered because the lattice is assumed to be a distribution of well sizes within the range of being classified as small polarons. The extent of a small polaron wave function is not greater than the lattice parameter.

As temperature increases, the probability of a hop occurring increases from well depth ( $E_{WD}$ ) or barrier height ( $E_{BH}$ ) reduction. Physically this correlates to increased lattice vibrational motion that will increase the probability of the polaron being in a position energetically favorable to move. Availability of neighboring sites and neighboring carrier interactions also affect the activation energy required for hopping. The interactions of the carriers and their effect on the activation energy have important implications on the conductivity. Conductivity has been related to cation disorder in previous sections. The relationships between disorder and activation energy needs closer examination. Conductivity is the product of the carrier density ( $n$ ) multiplied by the mobility of the carrier ( $\mu$ ) and the charge of an electron ( $q$ ) as shown in Equation 6.1:

$$\sigma = n\mu q \quad (6.1)$$

Since the carrier charge is constant at  $1.602 \times 10^{-19}$  C, the only ways to affect conductivity is to create more carriers by producing distortions in the lattice where carriers will be trapped, or arranging the charges in the lattice such that the activation energy for movement is minimal. Rapid cooling from heat treatment must affect the mobility in order to change the conductivity because it changes the activation energy. Activation energy decreases will increase carrier mobility. As will be shown by the disorder model, a disordered state decreases the activation energy.

While the particle in the box model for polaronic materials is illustrative for the hopping nature of conduction, the heterogeneity of the trap energies and the effect of

disorder need to be examined in closer detail. For the particle in the box model, polaronic sites are represented without interactions with the remaining material.

If we were to picture electronic conduction between adjacent sites, the question remains: how do the neighboring sites affect the conduction process? Using a spin model for site-site interactions, this question is examined. Both one and two dimensional spin lattices are illustrated in Figure 6-5a and b, respectively, with the charge carrier (electron or hole) residing at the center (darker colored) site. To represent the interaction between neighboring sites, the dipole-dipole interaction energy is used as a first approximation of the interaction between sites for both a 1-D and 2-D solid (Figure 6-5, a and b).

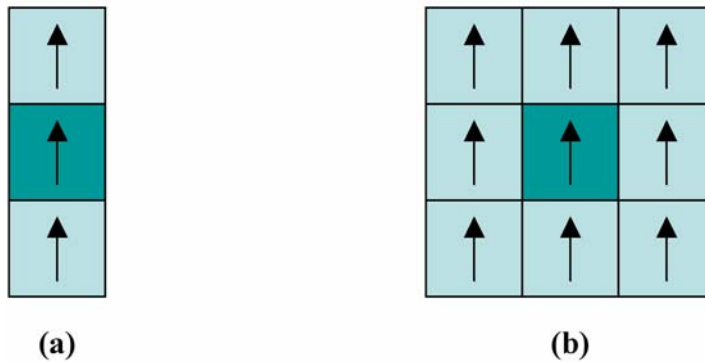


Figure 6-5. Schematic illustration of one (a) and two-dimensional (b) spin models for polarons defined by adjacent site interactions. Darker colored site is coordinate origin.

Equation 6.2 shows the relation of the dipole stabilization energy between two dipoles at neighboring sites. The dipoles ( $\mu_1$  and  $\mu_2$ ) are located on adjacent sites (1 and 2) spaced at a distance ( $r$ ). The dipoles are oriented at  $\theta_1$  and  $\theta_2$ .

$$E(r) = \frac{-u_1 u_2 (2 \cos \theta_1 \cos \theta_2 - \sin \theta_1 \sin \theta_2)}{4\pi\epsilon_0 r^3} \quad (6.2)$$

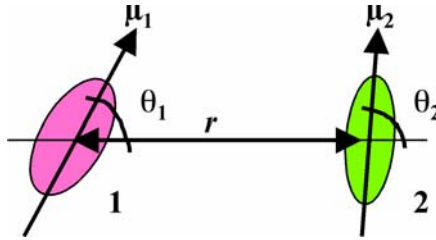


Figure 6-6. Illustration of dipole-dipole interactions between adjacent sites for polaronic spin model variables in Equation 6.2.

Figure 6-6 schematically illustrates the dipole magnitude and orientation. Position 1 in pink is canted slightly towards dipole 2 that is nearly normal to the distance vector  $r$ . For this model, the orientation angle ( $\theta$ ) of each dipoles is constrained between 0 and 90 degrees. Imposing a unit dipole moment ( $\mu = 1$ ) on all sites, and replacing the numerical constants with 'k', Equation (6.2) for the one-dimensional case reduces to Equation 6.3.

$$E(r) = -k(2 \cos \theta_1 \cos \theta_2 - \sin \theta_1 \sin \theta_2) \quad (6.3)$$

The interaction energy for an individual site becomes Equation 6.4.

$$E(\text{site}) = E(\text{dipole} - \text{dipole}_{\text{above}}) + E(\text{dipole} - \text{dipole}_{\text{below}}) \quad (6.4)$$

When the spins of the adjacent sites are all perfectly aligned (maximum alignment), the largest dipole-dipole stabilization energy is found (highest activation energy). Using this relationship and an analogous form for the two dimensional case, heterogeneity is introduced into this system by generation of a random distribution of orientations of the dipole vectors with respect to each other.

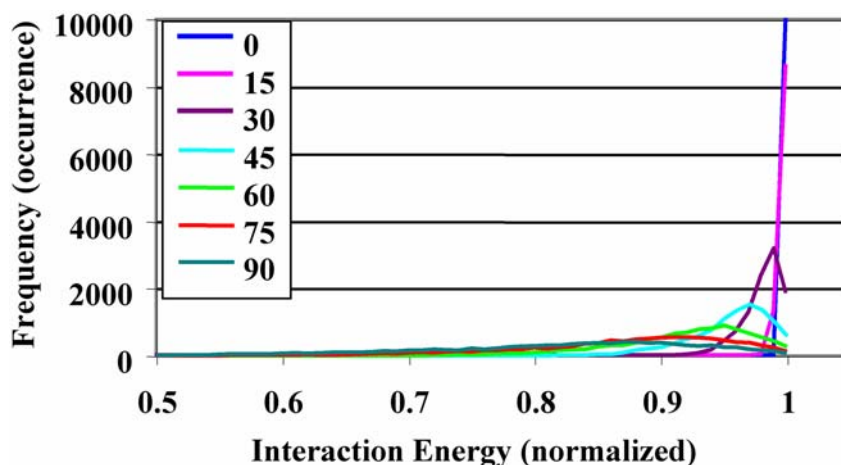


Figure 6-7. Energy distribution functions for one-dimensional polaron disorder model. The distribution is taken as an ensemble average containing 10,000 sites with interaction energies normalized to an ideal ordering case where  $\theta$  equals 0.

Using a 10,000 element lattice, the following histograms (Figure 6-7 and Figure 6-8) of interaction energies were generated for one and two-dimensional lattices for random distributions of dipole orientations constrained within a specified angular amplitude. Interaction energies were normalized to the maximum value as determined by the ideal alignment ( $\theta = 0$ ) case.

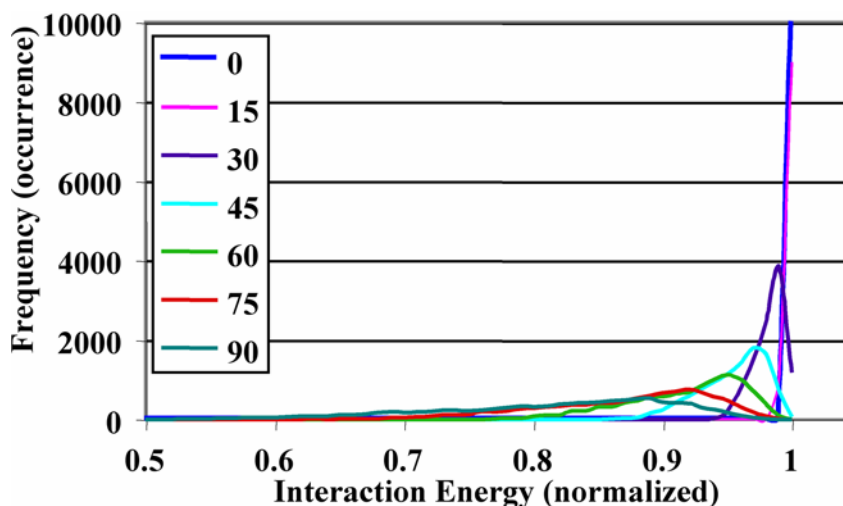


Figure 6-8. Energy distribution functions for two-dimensional polaron disorder model. Distributions were taken from an ensemble of 10,000 sites, with interaction energies normalized to ideal ordering case where  $\theta$  equals 0.

By introducing this heterogeneity, the effect of disorder is shown to create distribution of site energies, with the maximum value varying as a function of the extent of angular variation. As the experimental system will exhibit a degree of disorder, the ensemble-average value is constituted from an energetically defined distribution of sites, with site energies both higher and lower than the measured value. In terms of the particle in the box model described earlier, the energy level of the polaronic site is better described as a distribution of energy states, with an accompanying range of activation energies for site hopping.

#### 6.4 Resistivity Limit

When nickel is added to cobalt oxide, improvements in conductivity were on the order of  $10^2 - 10^4$  from a lower value of  $0.001 \text{ Scm}^{-1}$  up to  $\sim 333 \text{ Scm}^{-1}$  (Windisch et al., 2001a; Windisch et al., 2001b; Windisch et al., 2002b). Conductivity reported in this work is up to  $500 \text{ Scm}^{-1}$  with the enhancement from processing. Both lithium and rhodium dopants in addition to several different process optimizations designed to increase conductivity\* showed some small measure of enhancement. The conductivity in these materials remains high due to the high carrier density despite the low mobility characteristic of the hopping mechanism of polaron motion. The rationale behind dopant additions or cation charge disorder was to create more carriers for conductivity. More carriers, created by dopant addition, cation charge disorder, or induced by processing were designed to increase conductivity. There is a realistic saturation limit of polarons in the lattice. It is possible that a saturation limit of polarons exists in the lattice. Once the saturation limit is reached, additional carriers will only increase the lattice distortion and

---

\* See Figures 3-7, 3-9, 3-13, 4-1, 4-2, 4-3, 4-4, 5-2, 5-3, 5-4, 5-6)

impede the hopping motion of available carriers. Polaron saturation will impose a lower limit to resistivity. Hopping distance (barrier width) could change, or the localization of the carrier (well depth) could increase due to the increased strain. Additional interaction among carriers may also degrade the hopping process.

Based on a unit cell with a theoretical lattice parameter of 8.114 Å and assuming the crystal is 100% dense, an estimation of the number of allowed polarons in one spinel unit cell is made. This estimation of the saturation limit of polarons in the material will allow a projection of the maximum conductivity in these materials. It should be noted that these estimates are based on a number of idealized conditions and that this limit is a maximum achievable goal for these conditions. A number of processing and compositional factors will affect the validity of this model and its agreement with experimental measurements.

A maximum of one polaron per lattice cation (each polaron is a bound carrier) would yield a total of 24 cation sites in a spinel cell made up of 16 octahedral and 8 tetrahedral coordinated locations. It is unrealistic to assume that every site will be distorted to create a polaron, so the number of polaron sites per unit cell is an arbitrary value chosen that is less than the total number of sites available. Table 6-1 shows the available sites and which cations occupy them.

Table 6-1. Spinel sites and occupation for polaron density calculation.

	Octahedral	Tetrahedral	Oxygen (anion)
Total Sites Available	16	8	32
Ni	8 or 12*	-	-
Co	8 or 4*	8	-
Li**	-	YES	-
Rh**	YES	-	-

\*Depends on the metallic ratio of nickel and cobalt—if equal parts, nickel will occupy the octahedral site. If the concentration of nickel is greater than the concentration of

cobalt then nickel oxide precipitation may reduce the accuracy of the site density calculation.

\*\*Li and Rh are included to indicate which sites are affected as they are added.

Since the increase in conductivity is attributed to the increase in nickel concentration, polarons must form around the nickel ions, providing a starting point for calculating the theoretical conductivity. The spinel composition of NiCo<sub>2</sub>O<sub>4</sub> has 8 nickel ions per unit cell. The theoretical polaron density, in units of cm<sup>-3</sup> (Equation 6.5), is the product of the number of cells per cubic centimeter (Equation C.2, Appendix C) multiplied by the number of sites per cell.

$$8 \frac{Ni}{cell} \cdot 1 \frac{(Polaron)}{Ni} 1.87195 \cdot (10)^{21} \frac{cell}{cm^3} = 1.49756 \cdot (10)^{22} \frac{(Polaron)}{cm^3} \quad (6.5)$$

If the number of polarons per cell increases to 12, then the polaron density will increase to 2.246x10<sup>22</sup> cm<sup>-3</sup>. Table 6-2 shows the calculated conductivity with the mobility at 0.1 and 1 cm<sup>2</sup>V<sup>-1</sup>s<sup>-1</sup> when equation 6.1 is used with q as the constant charge of an electron equal to 1.602x10<sup>-19</sup> C. Values of mobility shown were chosen based on Emin's statement that small polaron hopping was indicated by a mobility less than 1 cm<sup>2</sup>V<sup>-1</sup>s<sup>-1</sup> (Emin, 1982).

Table 6-2. Theoretical value of conductivity assuming a polaron density given by the number of hopping polarons in a unit cell with a constant mobility.

Polarons / Cell	Polaron Density, cm <sup>-3</sup>	Mobility, cm <sup>2</sup> V <sup>-1</sup> s <sup>-1</sup>	Conductivity, S cm <sup>-1</sup>
0.8	1.498x10 <sup>21</sup>	0.10	24
1.2	2.246x10 <sup>21</sup>	0.10	36
2.4	4.492x10 <sup>21</sup>	0.10	72
8.0	1.498x10 <sup>22</sup>	0.10	240
<b>12.0</b>	<b>2.246x10<sup>22</sup></b>	<b>0.10</b>	<b>360</b>
24.0	4.492x10 <sup>22</sup>	0.10	720
0.8	1.498x10 <sup>21</sup>	1.0	240
<b>1.2</b>	<b>2.246x10<sup>21</sup></b>	<b>1.0</b>	<b>360</b>
<b>8.0</b>	<b>1.498x10<sup>22</sup></b>	<b>1.0</b>	<b>2400</b>
12.0	2.246x10 <sup>22</sup>	1.0	3600
24.0	4.492x10 <sup>22</sup>	1.0	7200

Windisch et al. stated that 10% of all nickel is in the 3+ oxidation state. The  $\text{Ni}^{3+}$  is the polaron entity (Windisch et al., 2002b). The maximum would be 0.8 per unit cell for a theoretical density of  $1.498 \times 10^{21} \text{ cm}^{-3}$ . If mobility was  $1 \text{ cm}^2 \text{ V}^{-1} \text{ s}^{-1}$  then the conductivity would increase by an order of magnitude to  $2400 \text{ Scm}^{-1}$ . High conductivity ITO films are reported with conductivities near  $4,000 \text{ Scm}^{-1}$  (Minami et al., 2000). Nickel cobalt oxide films will likely not reach those values unless the carrier mobility increases. Increased mobility will, however cause scattering collisions due to such high carrier concentrations and may not necessarily result in a higher conductivity. It is unrealistic to assume that all octahedral sites will host polarons, so the projected maximum conductivity of  $7200 \text{ Scm}^{-1}$  should be considered too high. This high concentration of polarons would also distort the spinel lattice resulting in the lower mobility corresponding to the lower conductivity that was reported earlier. Thus the maximum realistic conductivity of the nickel-cobalt oxide system should be much less than  $2400 \text{ Scm}^{-1}$  in agreement with the experimental data where the highest reported value is  $\sim 500 \text{ Scm}^{-1}$ .

The Hall effect data mentioned in Chapter 2 is anomalous with carrier densities as high as  $5 \times 10^{23} \text{ cm}^{-3}$ . This value suggests the physically unrealistic interpretation that every cation in the lattice is a polaron host simultaneously. A potential explanation of the carrier density exceeding the theoretical maximum is the thermal generation of carriers, resulting in a change of conductivity mechanism, or a mixed carrier population of both quasi-free electrons and *p*-type polarons. Thermal energy translated into lattice distortions would reduce the well depth and shift the conduction regime to a more quasi-free type of carrier population. This argument is not a verifiable option as the Hall measurement is anomalous for this material. Seebeck data on the material should support

this mechanism. Further information on the anomalous Hall effect can be explored by reading the works of Emin (Emin, 1977, 1980; Emin & Emin, 1977)

### **6.5 Conclusions**

This chapter discussed the effects of disorder in the nickel-cobalt oxide system with respect to structural disorder and cation charge disorder with a model that illustrates the change in activation energy of electrical conductivity with a disordered arrangement of cations. The attempts to increase the polaron density in Chapters 4 and 5, suggest that a polaron saturation effect occurs when the polaron density reaches  $2.25 \times 10^{22} \text{ cm}^{-3}$  limiting the conductivity to a range between  $\sim 360 \text{ Scm}^{-1}$  and  $\sim 2400 \text{ Scm}^{-1}$  from polaron hopping when the mobility is between  $\sim 0.1 \text{ cm}^2 \text{V}^{-1} \text{s}^{-1}$  and  $1.0 \text{ cm}^2 \text{V}^{-1} \text{s}^{-1}$ . Attempts to increase the polaron concentration to achieve a higher conductivity may perturb the lattice and reduce mobility or carrier population resulting in a net decrease in conductivity.

## CHAPTER 7 CONCLUSIONS, FUTURE WORK, AND APPLICATIONS

### 7.1 Conclusions

Nickel-cobalt oxide is the *p*-type material system of interest to function as an infrared transparent conducting oxide (ITCO) because of its infrared transparency (up to 90% at 16  $\mu\text{m}$ ), and relatively high conductivity ( $\sim 500 \text{ Scm}^{-1}$ ). Nickel-cobalt oxide exhibits these characteristics due in part to the intrinsic carrier type and the conduction mechanism attributed to the spinel crystal structure.

This study investigated three methods of increasing conductivity. First was the optimization of sputter deposition process conditions. Adjusting sputter process parameters was designed to adjust the growth conditions affecting film properties such as density, morphology or crystallinity and increase the film conductivity. The second method for increased conductivity was substituting lithium for cobalt. Replacing a divalent cobalt ion on a tetrahedral site with a monovalent lithium ion was anticipated to shift a neighboring cobalt cation to a higher oxidation state and form a polaron. The increased polaron (carrier) density would result in a net increase in conductivity. The third method for increased conductivity in the nickel-cobalt oxide system was to substitute rhodium for cobalt. Rhodium is similar in electronic structure to cobalt, and is located in the row beneath on the periodic table. Rhodium size was expected to induce structural distortions and provide sites for polaron formation, resulting in an increased conductivity. Due to the shifted energy of the d orbital electrons in the rhodium ion, transparency at wavelengths closer to the optical spectrum was expected to increase.

Films from each study were subjected to heat treatment to ensure complete oxidation and to see the effects of thermal treatment. Heat treatment cooling studies suggest that cation disorder is a dominant factor in polaron formation and a significant factor affecting the activation energy of electrical conduction. A model relating activation energy to cation site disorder showed that activation energy decreased as disorder increased.

### **7.1.1 Summary of Sputter Processing of Nickel-Cobalt Oxide**

For sputtered films, the conductivity was larger with a 50% O<sub>2</sub>-50% Ar composition, a lower sputter gas pressure (2 mTorr vs. 10 mTorr), and a smaller target-to-substrate distance (best at 5 cm). The effects of composition are due to the resulting cation oxidation states, while the effects of pressure and substrate distance were attributed to more energetic sputtered particles causing increased mobility of surface adatoms on the substrate and film surfaces. The 5 cm target-to-substrate distance results in a 20% increase in film density, compared to a 15 cm distance with both producing a crystalline spinel structure. The best film conductivity of the gas mixture series of ~350 Scm<sup>-1</sup> may be a result of ideal growth conditions promoted by complete oxidation and a higher deposition rate. The gas pressure study showed that a chamber pressure of 2 mTorr yielded a higher conductivity film (~500 Scm<sup>-1</sup>) compared to the 5 mTorr (~400 Scm<sup>-1</sup>) and 10 mTorr (~333 Scm<sup>-1</sup>) for films rapidly quenched after heat treatment. This enhanced conductivity is attributed to a higher growth rate and increased adatom mobility during growth due to the shorter molecular transport path and more energy transfer from the plasma heating the substrate.

Increased target to substrate distance decreased the film density from 5.7 g/cm to 5 g/cm, increased film porosity, decreased conductivity from ~250 Scm<sup>-1</sup> to ~35 Scm<sup>-1</sup>, and

decreased the optical absorption coefficient at 3  $\mu\text{m}$  from  $\sim 10^5$  to  $\sim 2 \times 10^4$ . Target-substrate distance effects on the film density are believed to be controlled by phenomena similar to those from lower pressures of 2 mTorr instead of 10 mTorr i.e. higher surface mobility from depositing species due to less gas phase scattering. Less plasma-film interaction at longer distances may also be a factor.

Band gaps of 3.5 eV, 3.4 eV, and 3.2 eV were reported from  $x$  equal to 0.75, 1, and 1.5 in  $\text{Ni}_x\text{Co}_{3-x}\text{O}_4$ , respectively. Work functions of 4.39 and 4.27 were also reported for composition ( $x$ ) values of 1 and 1.5, respectively.

In summary, lower gas pressures of 2 mTorr and short target-substrate distances of 5 cm resulted in conductivities of up to  $500 \text{ Scm}^{-1}$  and transmission of up to 40% (if corrected for the silicon substrate absorption and index mismatch, the transmission would be  $\sim 80\%$ ) at 7.15  $\mu\text{m}$  ( $1400 \text{ cm}^{-1}$ ).

### 7.1.2 Summary of the Role of Lithium

Lithium additions to sputter and solution deposited films of  $\text{Ni}_x\text{Co}_{3-x-y}\text{Li}_y\text{O}_4$  were found to decrease and increase the electrical conductivity by less than a factor of two. Lithium in solution films tends to increase conductivity when added in specific amounts, depending on the nickel concentration. Lithium improved electrical properties only in three sets of conditions: two compositions deposited from solution and one deposited by sputtering. The two solution deposited conditions were in  $\text{Ni}_x\text{Co}_{3-x-y}\text{Li}_y\text{O}_4$  at  $y = 0.01$  when  $x = 1$  and  $y = 0.1$  when  $x = 0.75$ . Higher nickel-to-cobalt ratios required less lithium for increased conductivity. The improved conductivity value of  $72 \text{ Scm}^{-1}$ , up from  $37 \text{ Scm}^{-1}$  was still small in comparison to the high conductivity sputtered films without lithium ( $500 \text{ Scm}^{-1}$ ).

When sputtered, lithium concentrations up to 15% incorporate in the lattice according to SIMS and XPS analysis. Lattice expansion suggests this high lithium concentration resulted in occupation of lithium interstitials causing polaron annihilation. Excess lithium beyond the solubility limit segregated to the surface, formed carbonate and resulted in reduced conductivity. The formation of the carbonate surface layer was detected FTIR and XPS.

In summary, lithium substitution in solution deposited  $\text{NiCo}_{2-z}\text{Li}_z\text{O}_4$  films with a  $z$  value of up to 0.1 results in conductivity increases of 35% and up to 84% transmission at  $7.15 \mu\text{m}$ .

### 7.1.3 Rhodium Substitution for Cobalt

Sputtered oxide films from alloy targets of  $\text{NiRh}_4$  and  $\text{NiRh}_2$  with conductivities of  $260 \text{ Scm}^{-1}$  and  $225 \text{ Scm}^{-1}$ , respectively, showed comparable conductivity with nickel-cobalt oxide at  $310 \text{ Scm}^{-1}$ . Sputtered film resistivity increased from  $3.8 \text{ m}\Omega\text{cm}$  to  $48 \text{ m}\Omega\text{cm}$  with increased target-substrate distance similar to observations in other nickel cobalt oxide films that increased in resistivity with increased target-substrate sputtering distance. An increase in conductivity was not observed with increased rhodium concentration in solution deposited samples as conductivity dropped from  $290 \text{ Scm}^{-1}$  to about  $110 \text{ Scm}^{-1}$ .

Sputtered nickel-rhodium oxide films are more transparent into the visible and near infrared regions with a transparency of 60% at  $600 \text{ nm}$  with similar conductivity compared to nickel-cobalt oxide films. Transparency from  $2 \mu\text{m}$  to  $10 \mu\text{m}$  was improved by  $\sim 10\%$  with the rhodium present. Data show that nickel-rhodium oxide is just as conductive at  $200 \text{ S/cm}^{-1}$  with nickel-cobalt oxide at similar thicknesses, but optically

nickel-rhodium oxide is more transparent; however, nickel-rhodium oxide film properties change after heat treatment and do not show the reversible heat treatment properties possibly due to rhodium reduction in oxidation state. Sputtered films exhibit an increase in the optical absorption coefficient from  $1.5 \times 10^4$  to  $5 \times 10^5$  at  $3 \mu\text{m}$  as the target-substrate distance decreased from 25 cm to 7.5 cm. FTIR data of sputtered films shows that oxide films deposited from the  $\text{NiRh}_4$  alloy target were similar in transparency and more conductive than the oxide films of similar thickness deposited from the  $\text{NiRh}_2$  target.

Infrared transparency for solution deposited  $\text{NiCo}_{2-h}\text{Rh}_h\text{O}_4$  films of  $h$  equal 0, 0.25, 0.5 and 1 showed improvements of 10-15% and a decrease in conductivity of up to ~50%. The solution deposited films exhibited spinel infrared absorption peaks at  $\sim 546 \text{ cm}^{-1}$  and  $\sim 640 \text{ cm}^{-1}$  that broadened and shifted to lower frequency with increased rhodium concentration. Low frequency shifts were expected from the larger mass of the rhodium ion compared to the cobalt ion being replaced.

Solution and sputter deposition of  $\text{Ni}_x\text{Co}_{3-x-y}\text{Rh}_y\text{O}_4$  films were crystalline (spinel) and amorphous, respectively, and remained so with heat treatments up to  $550^\circ\text{C}$ . Attempts to crystallize the sputtered films were unsuccessful. Amorphous nickel-rhodium oxide structures from sputtering were unexpected, but not surprising because the addition of rhodium, by design, was to induce structural distortion and allow additional polaron formation. Structural disorder is due to the octahedral site occupation of both nickel and rhodium. With no tetrahedral site occupants, the spinel structure collapses unless cobalt remains to occupy it. While more polarons may have formed, a competing degradation of the conduction pathways due to the disordered structure impeded their hopping motion.

In summary, sputter deposited  $\text{NiRh}_5\text{O}_4$  films with an s value of up to 4 results in conductivity decreases of up to 22% and up to 70% transmission at  $7.15 \mu\text{m}$ . Solution deposited  $\text{NiCo}_{2-h}\text{Rh}_h\text{O}_4$  films with an h value of up to 0.5 results in conductivity decreases of up to 60% and up to 70% transmission at  $7.15 \mu\text{m}$  because the rhodium created an amorphous structure impeding carrier motion, but did not greatly affect the optical transmission.

#### **7.1.4 Heat Treatment**

Heat treatment showed improvement in conductivity by up to 2x when films were rapidly quenched and of up to 2x degradation when slowly cooled. Transparency behaved opposite to the electrical conductivity. After a rapid quenching heat treatment, the activation energy ( $\sim 0.01 \text{ eV} - 0.08 \text{ eV}$ ) of conduction is about  $0.01 \text{ eV}$  lower compared to a slow cooled sample. The change was attributed to a larger concentration of polarons upon quenching due to a greater degree of disorder. This heat treatment cooling rate effect is a new discovery for this system.

The behavior of films containing lithium was similar to those not containing lithium with respect to optical and electrical properties following heat treatment. Quenching ( $\sim 150^\circ\text{C}/\text{min}$ ) produced higher conductivities (2x), while slow cooling ( $10^\circ\text{C}/\text{min}$ ) results in lower conductivities after heat treatment at  $375^\circ\text{C}$  for 10 minutes in air. Heat treatment increases conductivity by up to 2x and decreases transparency by up to 15%. In contrast to sputtered films with large lithium concentrations ( $> 5\%$  added) which caused a lattice expansion, heat treatment and quenching of lithium films from solution with small lithium concentrations caused slight lattice shrinkage according to XRD data fits. This anomaly of lattice shrinkage is not fully explained with an

accompanying increase in conductivity. Increased lithium caused a rapid increase in the activation energy for film conductivity for both quenched and slowly cooled films, but the magnitude depends on the rate of cooling. Heat treatment effects upon conductivity and transparency were reversible for films with and without lithium. It was concluded that the film was in a metastable state following a rapid quench from after heat treatment, and that cation disorder was responsible for the 100% increase in conductivity.

#### **7.1.5 Disorder and Polaron Conductivity**

Having attempted with dopants to increase the polaron density through processing and impurity addition, it is concluded that a polaron saturation effect probably occurs when the polaron density reaches  $2.25 \times (10)^{22} \text{ cm}^{-3}$  limiting the conductivity to a projected range between  $\sim 360 \text{ Scm}^{-1}$  and  $\sim 2400 \text{ Scm}^{-1}$  from polaron hopping when the mobility is between  $\sim 0.1$  and  $1.0 \text{ cm}^2\text{V}^{-1}\text{s}^{-1}$ . Attempts to increase the conductivity beyond this value will perturb the lattice such that either mobility decreases or the carrier population decreases resulting in lower conductivity. The effects of cation charge disorder and structural disorder in the nickel-cobalt oxide system were modeled and mathematically related to activation energy of electrical conductivity. The model shows that as disorder increases, activation energy decreases, consistent with the experimental data.

#### **7.2 Future Work**

Due to the non-existence of IR transmitting conductors, there is a pressing need to further develop the nickel-cobalt oxide system and expound on its limitations and provide a baseline of comparison for other material systems that may be developed in the future. Future work may include:

- Additional processing studies of nickel-cobalt oxide to find a deposition technique or geometry to produce a further optimized ITCO film. Maximizing both conductivity and transparency while providing a figure of merit at various wavelengths in the infrared would be useful.
- Investigation on the effects of doping such as lithium and rhodium on the carrier population and whether they only affect the number of carriers or the mobility. This will require improved methods of characterizing mobility. Increases in conductivity were not conclusively due to one or the other.
- A method to determine experimentally the disorder in the system and whether or not super ion exchange or the neighboring environment surrounding the polaron influences its mobility.
- A detailed investigation into the model used to approximate the effect of disorder on activation energy of electrical conductivity might yield a more empirical fit to the system that would take into consideration the two activation energy regions.
- Beam line studies of films could be used to determine the site occupied by the substituting lithium ions and whether it is substituting for nickel or cobalt preferentially. Lithium is predicted to occupy the tetrahedral site, but further evidence could substantiate this claim.
- Additional studies to determine the structural differences between solution and sputter deposited films may provide further insight as to why the sputtered films are more conductive, but less transparent.

- Magnetic property studies of nickel-cobalt oxide would reveal the effects of heat treatment and doping on the magnetic nature of the thin films.
- Quantitative calibrated XPS depth profiles could be used to explain the bulk and surface film compositional differences and if there is indeed an effect from preferential sputtering of oxygen from the argon sputtering beam.
- Transparency studies of combinatorial sputtered films at various gas compositions would produce data to better relate composition and growth conditions with optical properties.
- High temperature studies of the stability of nickel-rhodium oxide on substrates other than silicon would show if a reaction at the film-substrate interface is affecting film conductivity and oxygen concentration.

Learning more about the film structural properties and how they relate to the electrical and optical properties will allow incremental improvements in film conductivity and transparency enabling it for use in future applications in IR devices.

### **7.3 Applications**

A wealth of applications including IR sensors and actuators such as night vision displays, friend-foe identification, and local area networking, are in production, but would be greatly enhanced by the development of an IR transparent conducting material such as nickel-cobalt oxide. Additional devices such as organic IR emitting devices (OLEDs), longer wavelength fiber optics, higher power IR lasers, or solid-state optical temperature sensors could also be developed. The future is bright and with further development the world of the IR could be put to use.

## APPENDIX A DEPOSITION DETAILS

### A.1 Sputtering

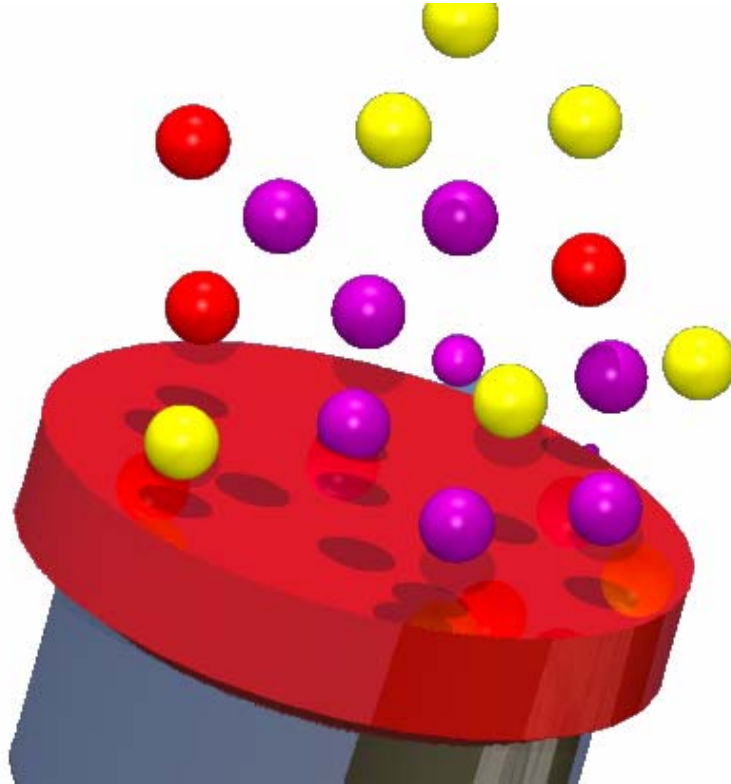


Figure A-1. A sputtering target (red) mounted on a cathode (silver) with impinging gas ions (purple) and target particles being removed (red).

#### A.1.1 Definition

Sputtering is a process of using high voltage to create a plasma (ionized gas) and bombard a surface (target) and cause it to “sputtering” off particles (Mahajan & Harsha, 1999). This flux of target particles coming off is collected as a thin film on a substrate of the user’s choosing such as a microscope slide, fused-silica, sapphire, silicon wafers, or poly(ethelene terephthalate). Sputter coating is a well developed method used for thin film deposition and is widely used in the microelectronics and data storage manufacturing

processes as well as food processing for metallization of such item as food storage bags deposition although the process conditions vary greatly from one application to the next. For a more technical description, see (textbook on sputter deposition.

### A.1.2 Equipment

Sputtering is done in a vacuum chamber. These chambers can be made of glass, aluminum or stainless steel as long as they can be evacuated to a sufficient background pressure to preclude the sputtering process from being contaminated by water vapor or carbon species normally found in the air. The equipment used in this study consisted of two chambers (Figure A-2) each of stainless steel construction pumped by Varian diffusion pumps backed by oil rotary vane pumps.

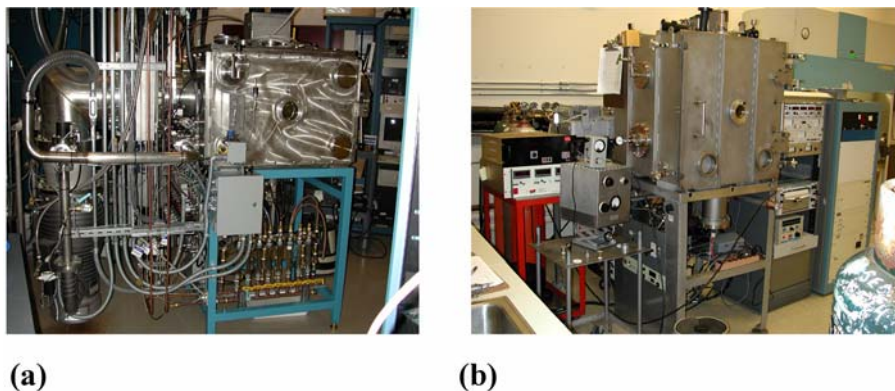


Figure A-2. Vacuum chambers used for sputtering deposition. (a) E-beam deposition chamber located in room 1317 at the EMSL at PNNL (b) the M chamber located in RTL room 120 at PNNL. Both systems were used for sputter deposition for the films in this study.

**Cathode.** A cathode is a fixture used to feed voltage and a cooling medium (usually water) into the chamber and it holds the target material. While they vary in size from one inch to several inches, the ones used for this study were two inches and three inches.

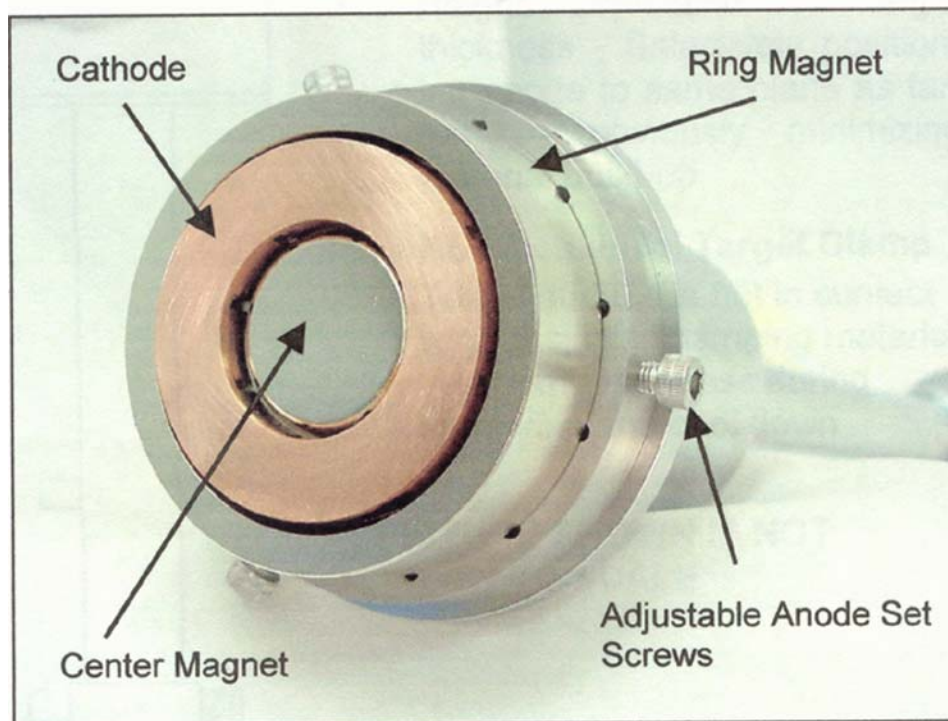


Figure A-3. Three-inch sputter cathode used to deposit thin films. Reprinted from US Inc. (2003) *Mak™ Owner's operation and maintenance manual of the mak sputtering sources*. San Jose: US Inc. (Figure on p.7) with permission.

**Target.** A target is a piece of material fabricated for sputtering that is placed on the cathode. Targets used in this study were both alloy and oxide targets of two different sizes:

- 5 cm (Rh, Pd, NiRh<sub>4</sub>, NiRh<sub>2</sub>, NiO, Co<sub>3</sub>O<sub>4</sub>, Ni<sub>1.5</sub>Co<sub>1.5</sub>O<sub>4</sub>, Ni<sub>1.35</sub>Co<sub>1.35</sub>Li<sub>0.3</sub>O<sub>4</sub>, Ni<sub>1.2</sub>Co<sub>1.2</sub>Li<sub>0.6</sub>O<sub>4</sub>)
- 7.5 cm (Ni, Co, NiCo, NiCo<sub>2</sub>, NiCo<sub>3</sub>, Ni<sub>0.95</sub>Co<sub>1.95</sub>Li<sub>0.15</sub>O<sub>4</sub>)

### A.1.3 Configuration/Setup

**Combinatorial sputtering.** Benefits of the combinatorial sputtering technique include adequate process control, fewer necessary targets, and generation of multiple compositions in a single run. Combinatorial films provide ample data to compare and contrast compositionally variant properties such as conductivity and transparency from a

single deposition run. Numbered Positions (9 divisions-one per inch on a 3 inch microscope slide)

- Cathodes may be tilted for more uniform coverage
- Less time to produce a range of films
- More data is produced per run
- Compositional variation requires fewer targets
- Easier to relate properties only to composition
- Fixed substrate geometry may limit film uniformity
- Mismatched cathodes require calibration

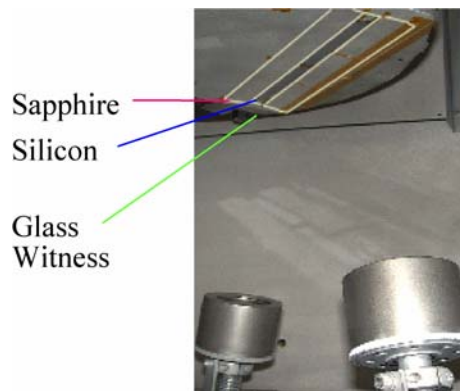


Figure A-4. Combinatorial sputtering setup inside of chamber with mounted substrates prior to pump-down for sputtering.

**Single rotation.** Single rotation is where the substrate holder spins on axis with the longitudinal axis of the cathode (Figure A-5). This setup was used for a few select films.

**Offset rotation.** Offset rotation (Figure A-6) is like single rotation, but the axis of substrate holder is parallel, but not in line with the longitudinal axis of the cathode. This setup was used for a majority of film depositions.

**Double planetary rotation.** Double planetary rotation is like the earth orbiting the sun shown in Figure A-7. Double planetary rotation is used in many cases to obtain

uniform thickness and morphology over larger areas not possible with single or offset rotation. Often the planetary setup requires a longer target to substrate distance to work effectively. Double planetary rotation was available in both chambers and was used in some cases.

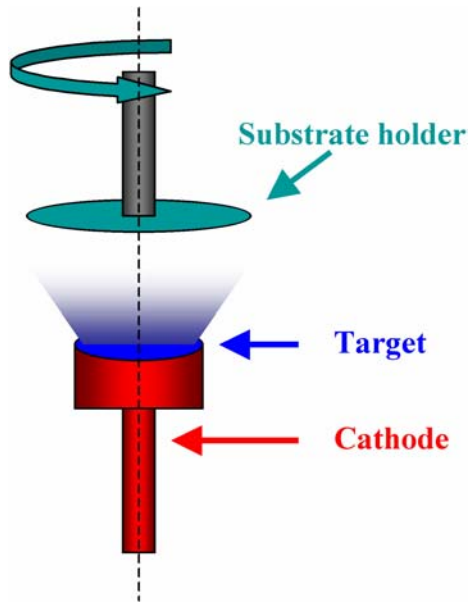


Figure A-5. Single rotation setup.

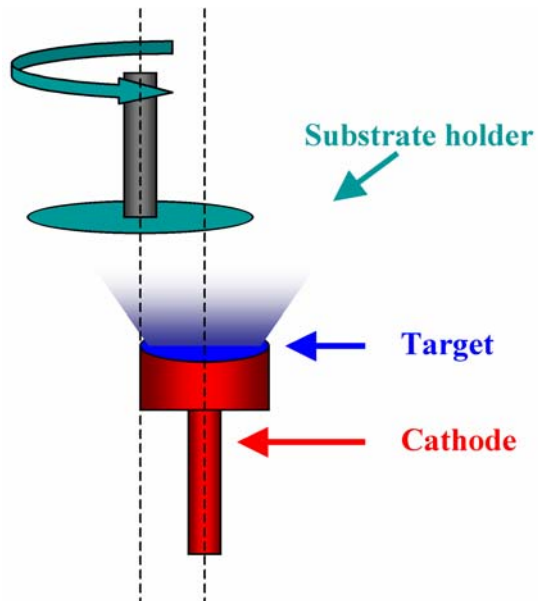


Figure A-6. Offset rotation setup.

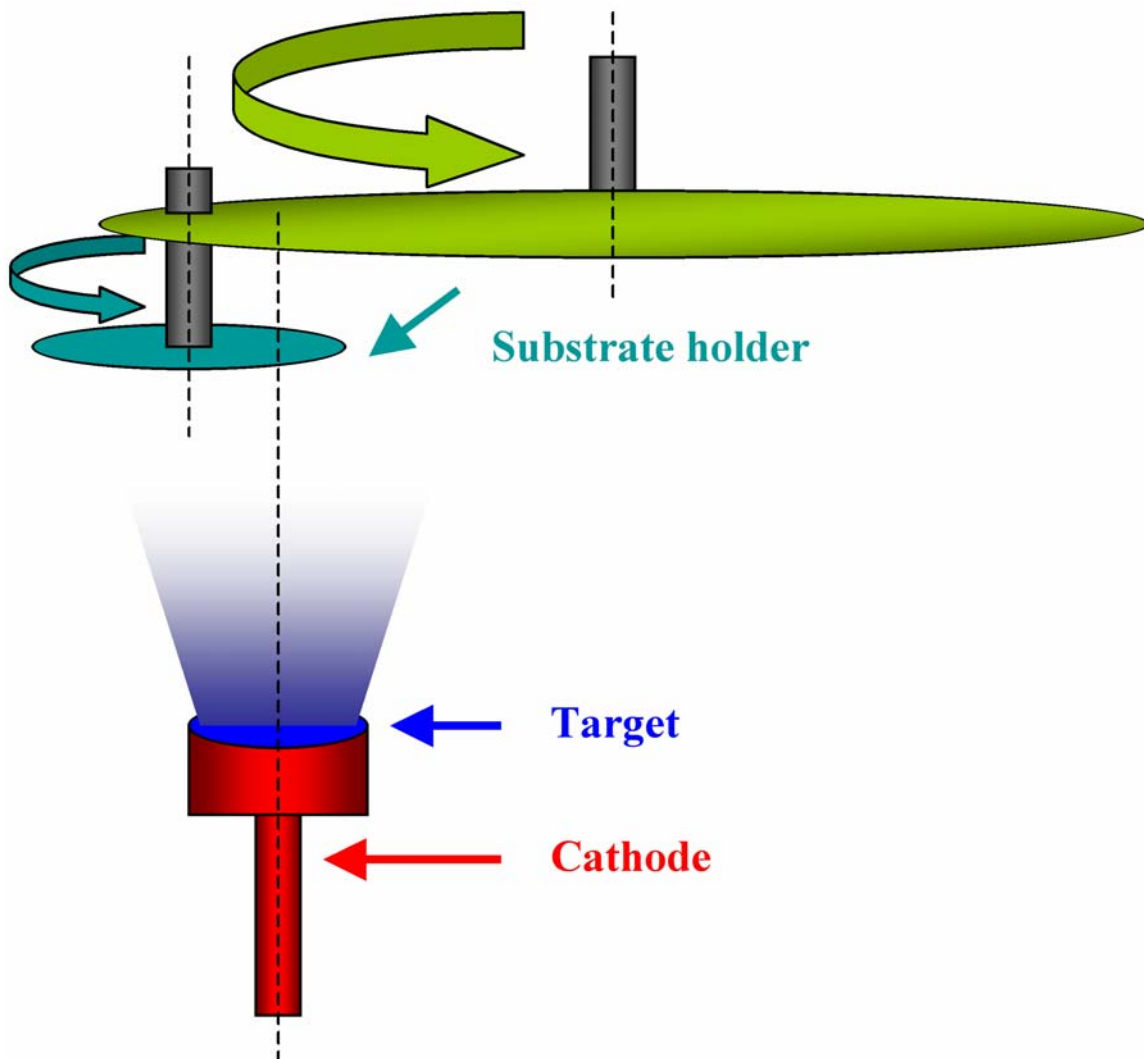


Figure A-7. Double planetary rotation setup. The target is blue, the substrate is green-blue, and the cathode is red.

#### A.1.4 Target Production

Custom target manufacturing incorporated techniques of solution preparation where metal nitrates in aqueous solution were boiled down and then heated to facilitate nitrate decomposition without the organic additive. The produced cake was then ground and again heated to 350°C to ensure complete dissociation of the nitrates resulting in finely divided powder. Pressing a green disk required a 6 cm die and a uniaxial press at

15 ksi. Using a heating and cooling rate of  $5^{\circ}\text{C}/\text{min}$  the green target was sintering at  $900^{\circ}\text{C}$  for two hours yielding a  $\sim 5$  cm sputtering target.



Figure A-8. Pressed target produced from nitrate solutions used for sputtering.

### A.2 Solution Deposition

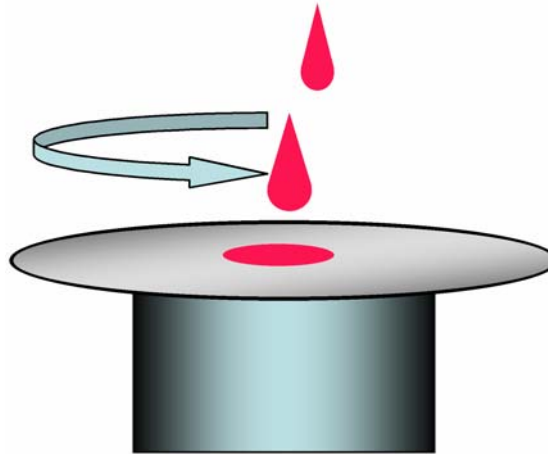


Figure A-9. The solution deposition method involves dropping a precursor solution on a spinning substrate prior to baking to form a film. Nitrate solutions require a combustion agent such as glycine or malonic acid, in aqueous based or alcohol based solutions, respectively, to ensure complete decomposition of the nitrates leaving an oxide film. Films are baked at  $400^{\circ}\text{C}$  for 10-15 minutes after spinning.

Solution deposition comprises of dropping an aqueous or alcohol based metal nitrate solution containing an organic combustion agent on a spinning substrate. After spinning, the substrate is immediately transferred to a hotplate and cooked at approximately  $400^{\circ}\text{C}$  for 10 minutes. The organic additive ignites and the nitrates

dissociate leaving behind a thin metal oxide film on the order of 50 nm thick.

Combustion agents such as glycine is used in aqueous solution for deposition on  $\text{SiO}_2$ .

Malonic acid is the combustion agent used in ethanol based solutions for deposition on

Si. Solution deposition is simple because the solutions are simple to prepare, one

solution can make many samples, and solutions are easily mixed in various compositions.

Substrate preparation includes baking substrates at  $>400^\circ\text{C}$  for up to 1 hour prior to

deposition. The ability to reproduce high quality films proves very difficult however

when attempting to maintain film consistency. Also, creating thick films requires

multiple coating spins and uniformity degrades with each successive deposition.

## APPENDIX B CHARACTERIZATION METHODS AND DETAILS

Electrical characterization included Hall and van der Pauw measurements, and temperature dependent van der Pauw measurements. Optical spectral characterization included infrared transmission measurements with Fourier transform infrared spectroscopy (FTIR) and ultra-violet and visible spectroscopy (UVVIS). Structural analysis included optical and stylus profilometry to measure film thickness, transmission electron microscopy (TEM), and x-ray diffraction (XRD). Secondary ion mass spectrometry (SIMS) and x-ray photoelectron spectroscopy (XPS) were used to determine the chemical composition and bonding states in the film.

### B.1 Electrical Characterization

#### B.2.1 Hall Effect

The Hall effect system used had a 1 T magnet with a four-pin probe in the van der Pauw setup. The gold contacting pins were spaced at 0.5 cm to the sample with a spring. The apparatus is enclosed in aluminum, isolated from light during the measurement.



Figure B-1. Hall effect apparatus made by MMR technologies. It consists of sample dewar, magnet, measurement equipment and control computer.

### B.2.2 van der Pauw

The van der Pauw setup uses the same equipment as the Hall measurement, but does not require the magnet. Care was taken to ensure proper seating of the contacts with the film (see Figure B-1 and Figure B-2).

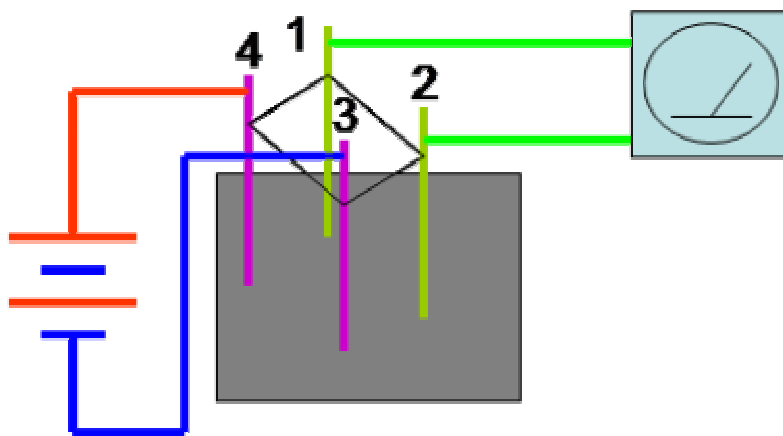


Figure B-2. A van der Pauw resistivity probe setup and measurement schematic. Four probes are used to apply a current and measure an applied voltage. Eight measurements are collected using both a positive and negative current between each pin e.g. source: 3-4, measure: 1-2; source 4-1, measure 2-3; source 1-2, measure 3-4; etc.

## B.2 Optical Characterization

### B.3.1 FTIR



Figure B-3. Nexus 570 FTIR with 3 detectors was used for high sensitivity mid IR ( $4000\text{ cm}^{-1}$  to  $650\text{ cm}^{-1}$ ), mid IR ( $4000\text{ cm}^{-1}$  to  $400\text{ cm}^{-1}$ ), and far IR ( $500\text{ cm}^{-1}$  to  $100\text{ cm}^{-1}$ ) measurements.

A Nicolet 210, a NEXUS 570 (Figure B-3), and a Nicolet 560 were all used to measure transmission of samples in the wave number regions between  $4000\text{ cm}^{-1}$  -  $400\text{ cm}^{-1}$ . The NEXUS 570 also has the capability to measure the far IR from  $500\text{ cm}^{-1}$  down to  $150\text{ cm}^{-1}$ . In each case, the chamber was allowed to equilibrate with a flowing nitrogen purge after admitting the sample into the holder. Purge times were typically at least one minute, but most often two minutes before both the background scan and the sample measurement.

### **B.3.2 UVVIS.**

Visible and near IR was performed using the Carey 5 UVVis, shown in Figure B-3. The UVVis has a wavelength range of 190 nm-3300 nm with the capability of measuring reflectance, and absorption/transmission in these ranges. The dual beam spectrometer offers the option of a zero and 100% transmission spectra corrections to ensure an absolute zero reference and a maximum that will not exceed 100%.



Figure B-4. Varian CAREY 5 dual beam ultra violet-visible spectrophotometer.

## **B.4 Structural Characterization**

### **B.4.1 Profilometry**

A Tencor Alphastep 200 (Figure B-5) was used to determine film thickness of sputtered samples from a taped witness substrate. The tape was removed and the stylus

dragged across the film-substrate interface to give a film thickness. Optical profilometry using a white light interferometer was used to verify results of the stylus profilometer. Results from both of these methods were compared with the average values provided by x-ray reflectivity measurements.



Figure B-5. Stylus profilometer used to measure step height of the deposited film.

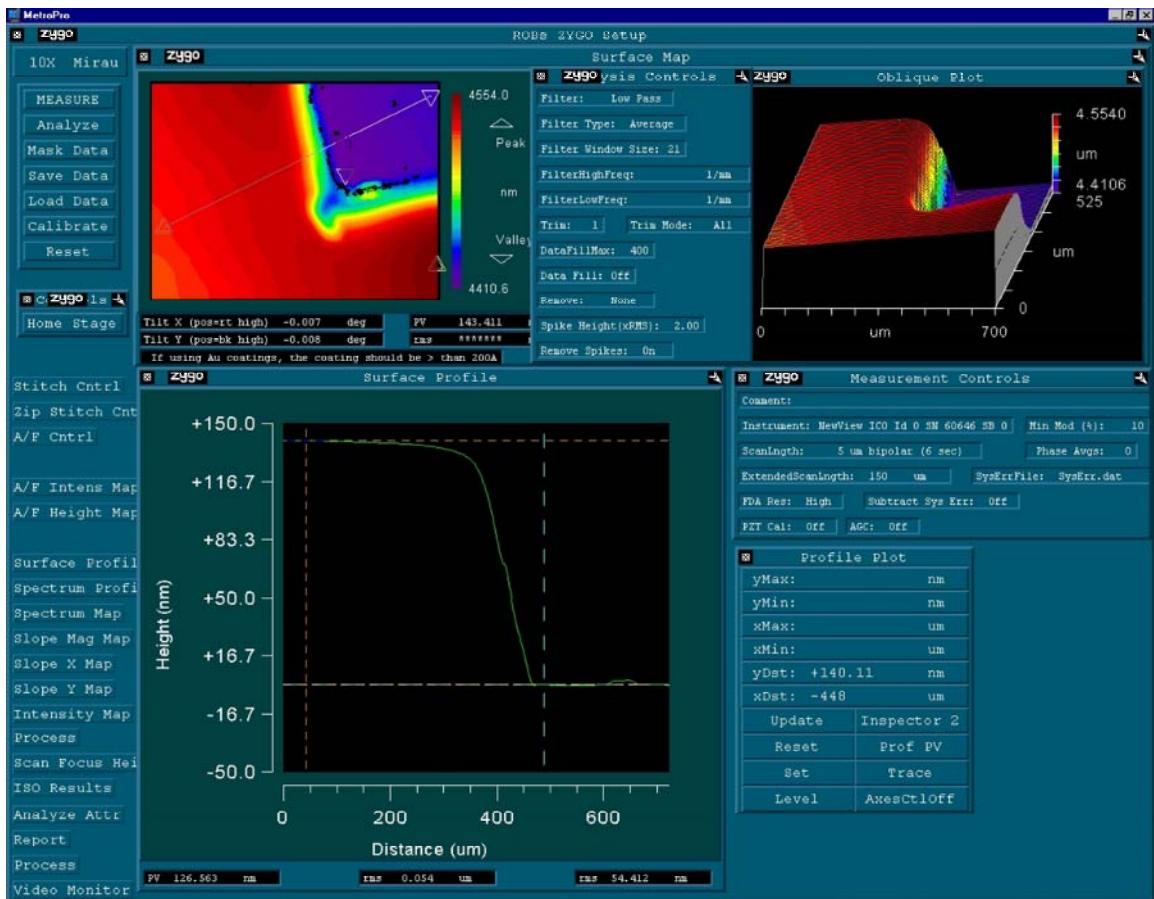


Figure B-6. Optical profilometer software screen capture. Instrument made by Zygo.

### B.4.2 XRD

The powder diffraction file is a database resource of both measured and calculated x-ray diffraction patterns for known substances used to compare with generated XRD.

Table B-1 shows the relevant information included in the database entry.

Table B-1. Powder diffraction file number 73-1702 used as the standard of comparison for nickel cobalt oxide thin films and powders. Taken from the JCPDS-International Center for Diffraction data. PCPDFWIN v. 2.2.

73-1702	Wavelength = 1.54060				
NiCo <sub>2</sub> O <sub>4</sub> Nickel Cobalt Oxide	d(A)	Int	h	k	l
Rad: CuK $\alpha$ 1 $\lambda$ : 1.54060 d-sp: Calculated	4.6846	132	1	1	1
	2.867	298	2	2	0
Cut off: 17.7 Int.: Calculated I/Cor.: 4.51	2.4464	999*	3	1	1
Ref: Calculated fro ICSD using POWD-12++, (1997)	2.3423	87	2	2	2
Ref: Knop, O., Reid, KIG., Sutarno, Nakagawa, Y., Can. J. Chem., 46, 3463 (1968)	2.0285	200	4	0	0
	1.8614	7	3	3	1
Sys.: Cubic S.G.: Fd3m (227) a: 8.114(14) Z: 8	1.6562	71	4	2	2
Ref: Ibid.	1.5615	244	5	1	1
Dx: 5.982 ICSD#: 024211	1.4343	295	4	4	0
Peak height intensity. R-factor: 0.054. PSC: cF56.	1.3715	11	5	3	1
Structural reference: Knop, O., Reid, K.I.G., Sutarno, Nakagawa, Y., Can. J. Chem., 46, 3463 (1968). Mwt: 240.56.	1.3523	1	4	4	2
Volume[CD]: 534.20	1.2829	19	6	2	0
	1.2373	52	5	3	3
	1.2232	28	6	2	2
	1.1711	18	4	4	4
	1.1361	5	5	5	1

The following tables display the configuration data for the XRD system used in collecting the data for this study. The two setups used included x-ray reflectivity (XRR) (Table B-2), grazing incident x-ray diffraction (GIXRD) (Table B-3). XRR was used to gather information on the thickness of the produced thin films. GIXRD was used instead of the powder diffraction setup because the thickness of the films did not provide a suitable signal to noise ratio for peak analysis to provide lattice analysis such as the crystallite size or the lattice parameter.

Table B-2. X-ray reflectivity (XRR) experimental system setup parameters.

Apparatus	
Diffractionmeter	Philips X'Pert MPD System (PW3040/00 type)
X-ray Source	Sealed Ceramic Tube
Anode	Fixed, Long-Fine-Focus, Cu
Wavelength, $\lambda$	$K\alpha_1$ , 1.5406 Å
Voltage	45 kV
Current	40 mA
Power	1.8 kW
Goniometer	$\theta$ - $\theta$ (Vertical, 220 mm radius)
Sample Platform	Philips Multi-Purpose Sample Stage (PW1821 type)
Sample Support	Glass Optical Flat
Scan Geometry	Symmetric
Incident Optics	
Beam Conditioner	Göbel Mirror (Parallel Beam, Equatorial Divergence $<0.04^\circ$ )
Slit	$1/32^\circ$ (Fixed)
Soller Slit	None
Axial Beam Mask	10 mm
Receiving Optics	
Anti-scatter Slit	0.1 mm (Fixed)
Receiving Slit	0.1 mm (Fixed)
Soller Slit	0.04 radians
Monochromator	Curved Graphite
Detector	Xe-filled Proportional Counter

Table B-3. Grazing-incidence x-ray diffraction (GIXRD) experimental summary system setup parameters.

Apparatus	
Diffractionmeter	Philips X'Pert MPD System (PW3040/00 type)
X-ray Source	Sealed Ceramic Tube
Anode	Fixed, Long-Fine-Focus, Cu
Wavelength, $\lambda$	$K\alpha_1$ , 1.5406 Å
Voltage	45 kV
Current	40 mA
Power	1.8 kW
Goniometer	$\theta$ - $\theta$ (Vertical, 220 mm radius)
Sample Platform	Philips Multi-Purpose Sample Stage (PW1821 type)
Sample Support	Glass Optical Flat
Scan Geometry	Asymmetric

continued	continued
<b>Incident Optics</b>	
Beam Conditioner	Göbel Mirror (Parallel Beam, Equatorial Divergence <0.04°)
Slit	1/2° (Fixed)
Soller Slit	None
Axial Beam Mask	20 mm
<b>Receiving Optics</b>	
Collimator	Parallel Plate, 0.27 radians
Receiving Slit	None
Soller Slit	None
Monochromator	Flat Graphite
Detector	Xe-filled Proportional Counter

### B.4.3 TEM / STEM

Cross sectional high resolution scanning transmission electron microscopy was done on selected ~0.5  $\mu\text{m}$  thick films deposited from alloy target reactive RF sputtering. Cross-sectional specimens were prepared by gluing two samples film-to-film and then cutting vertical sections which were first mechanically thinned from the both side to a thickness of ~ 20  $\mu\text{m}$ . Final thinning to electron transparency was accomplished by ion milling using a 5 keV  $\text{Ar}^+$  ion beam incident at  $12^\circ$ . XTEM analyses was carried out in a JEOL 2010F instrument operated at 200 keV using selected area electron diffraction (SAED) and bright-field (BF), dark-field (DF), high-angle annular dark field (HAADF), EDS analysis, and lattice resolution imaging techniques.

## B.5 Chemical Characterization

### B.5.1 SIMS

SIMS mass surveys and depth profiles were acquired with a Perkin-Elmer PHI 660 SIMS system using a 6keV oxygen primary ion beam with positive secondary acquisition. The current intensity was set at 108nA. During mass survey and depth profile acquisition, the raster size was varied between 200x200  $\mu\text{m}^2$ , 300x300  $\mu\text{m}^2$ ,

350x350  $\mu\text{m}^2$  and 400x400  $\mu\text{m}^2$  with 65% gating. The neutralizer was used during the analysis for charge compensation. Quantitative XPS was used to calculate a SIMS sensitivity factor assuming ionization probabilities for the elements being analyzed. Once the sensitivity values were determined, the raw data was adjusted accordingly and reported.

### **B.5.2 UPS**

Using the He I line of a helium lamp with a photon energy of 21.218 eV, an XPS analysis system was used to acquire the UPS spectrum at a vacuum level of  $\sim 1 \times 10^{-9}$  Torr

### **B.5.3 XPS**

A  $K\alpha$  x-ray beam was used with a pass energy of 45 eV in multiplex mode with a 5 KeV argon sputtering source energy.

**Wide and narrow scan data collection.** The XPS measurements were made using a Physical Electronics Quantum 2000 Scanning ESCA Microprobe. This system uses a focused monochromatic Al K $\alpha$  x-rays (1486.7 eV) source for excitation and a spherical section analyzer. The instrument has a 16 element multichannel detection system. The X-ray beam used was a 100 W, 107  $\mu\text{m}$  beam rastered over a 1.4 mm x 0.2 mm area. The x-ray beam is incident normal to the sample and the x-ray detector is at 45° away from the normal. The survey scans were collected using a pass energy of 117.4 eV. For the Ag 3d<sub>5/2</sub> these conditions produce a FWHM of better than 1.6 eV. The high energy resolution data was collected using a pass energy of 23.5 eV. For the Ag 3d<sub>5/2</sub> these conditions produce a FWHM of better than 0.74 eV. The collected data were referenced to an energy scale with binding energies for Cu 2p 3/2 at  $932.62 \pm 0.05$  eV and Au 4f at  $83.96.0 \pm 0.05$  eV.

Analyzer type: Spherical Section Analyzer

Analyzer mode: Constant Pass Energy or FAT  
Detector: Multichannel resistive plate  
Emission angle: 45 degrees  
Incident angle: 0 degrees  
Source to analyzer angle: 45 degrees  
Analyzer angular acceptance width: 20 degrees

**Depth profile data collection.** The XPS measurements were made using a Physical Electronics Quantum 2000 Scanning ESCA Microprobe. This system uses a focused monochromatic Al K $\alpha$  x-rays (1486.7 eV) source for excitation and a spherical section analyzer. The instrument has a 16 element multichannel detection system. The X-ray beam used was a 40, 200  $\mu\text{m}$  beam spot. The x-ray beam is incident normal to the sample and the x-ray detector is at 45° away from the normal. The profile data was collected using a pass energy of 58.7 eV. For the Ag 3d $_{5/2}$  these conditions produce a FWHM of better than 0.87 eV. The collected data were referenced to an energy scale with binding energies for Cu 2p 3/2 at  $932.62 \pm 0.05$  eV and Au 4f at  $83.96.0 \pm 0.05$  eV.

Ion gun:

- 2kV Ar $^+$  ions
- Ion beam raster area 5 mm x 3 mm
- Spot size: 150  $\mu\text{m}$  minimum beam diameter
- Sputter source incident angle: 45 degrees
- Sputter source polar angle 60 degrees
- Sputter source azimuthal angle: 90 degrees

APPENDIX C  
CALCULATIONS, EQUATIONS, AND EFFECTS

**C.1 Unit Cell Specifics**

Taking 8.114Å as the theoretical lattice parameter, the unit cell consists of 24 cations (8 tetrahedral, 16 octahedral) and 32 oxygen anions for a total of 56.

Table C-1. Unit cell sites and weights for density calculation.

	Ni	Co	O
Octahedral site	8	8	
Tetrahedral site		8	
Oxygen site			32
Atomic wt.	59.8	58.9	15.9997
Wt. per cell	478.4	3534	7680
Valence state	3+, 2+	3+, 2+	2-, 1-
Ionic rad (2+, tet)	69 pm	73 pm	124 pm
Ionic rad (2+, oct)	83 pm	79 pm	
Ionic rad (2+, oct, h.spin)		88.5 pm	
Ionic rad (3+)	70 pm	68.5 pm	
Ionic rad (3+, h.spin)	74 pm	75 pm	

Using the total number of sites in the cell and multiplying the weight of each atom give the grams per mol per cell. Dividing by Avogadro's number gives the weight of one cell (Equation C.1).

$$59.8 \frac{gm}{Ni} \cdot 8 \frac{Ni}{Cell} + 58.9 \frac{gm}{Co} \cdot 16 \frac{Co}{Cell} + 16 \frac{gm}{O} \cdot 32 \frac{O}{cell} = 3.1957489(10)^{-21} \frac{gm}{cell} \quad (C.1)$$

Taking the lattice parameter of the unit cell, cubing it and converting from angstroms to centimeters gives the volume occupied per cell, the reciprocal of which is the number of cells per cubic centimeter, shown in Equation C.2.

$$\left( \frac{8.114 \text{ \AA}}{cell} \right) \cdot \left( \frac{10^{-8} cm}{1 \text{ \AA}} \right)^3 = 5.34201 \cdot (10)^{-22} \frac{cm^3}{cell} = 1.87195 \cdot (10)^{21} \frac{cell}{cm^3} \quad (C.2)$$

## C.2 Theoretical Film Density

Multiplying the number of cells per volume and the grams per cell gives a theoretical density in grams per cubic centimeter (Equation C.3).

$$1.87195(10)^{21} \cdot 3.196(10)^{-21} = 5.98 \frac{gm}{cm^3} \quad (C.3)$$

If cells were stacked in cylindrical columns and packed hexagonally (Figure C-1), then the maximum percent density would be ~90.6%.

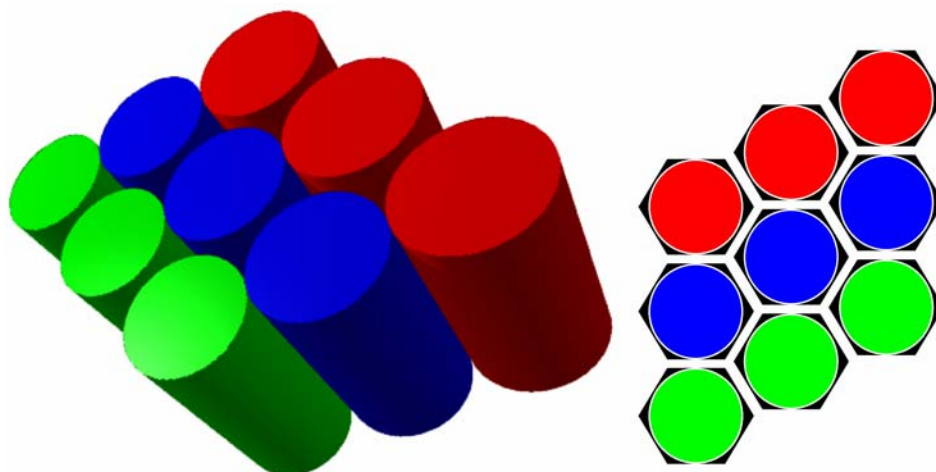


Figure C-1. Hexagonally packed cylinders in 3-D on film and top view.

If the packing of the cylindrical columns changed to a cubic arrangement (Figure C-2) then the density drops to 78.5% of the theoretical 100% dense matrix.

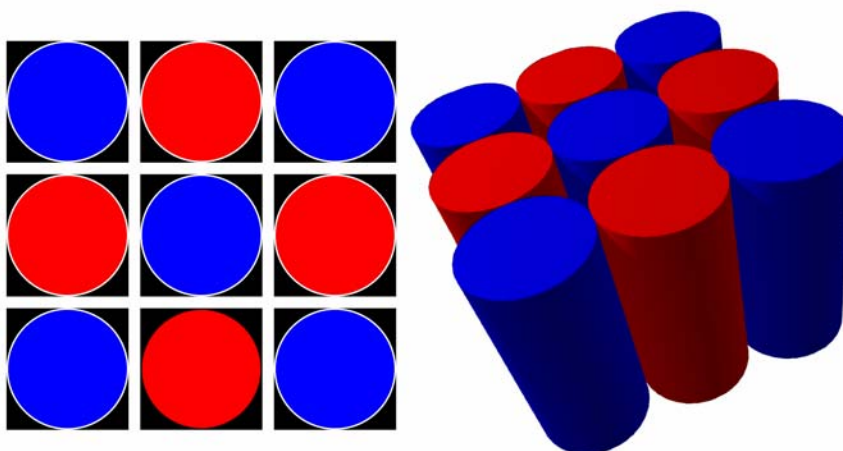


Figure C-2. Cubic packed cylinders top view and in 3-D as would be seen in the film.

### C.3 Heike's Rule

The formula used for determining the carrier concentration from the Seebeck measurement is called Heike's Rule. Alpha is the Seebeck coefficient ( $\alpha$ ) is the slope of the change in voltage ( $\Delta V$ ) measured with the change in temperature ( $\Delta T$  in Equation C.4).

$$\alpha = \frac{\Delta V}{\Delta T} \quad (C.4)$$

Heike's rule is the proportional relationship of the Seebeck coefficient to the density of carriers in the material (Rao & Raveau, 1998, Tareen et al., 1984).

$$\alpha = \frac{k}{e} \ln\left(\frac{1-c}{c}\right) \quad (C.5)$$

The letter  $c$  represents the carrier concentration ratio of the number of active carriers over the number of carriers available.

### C.4 Absorption Coefficient Calculation.

The procedure for calculating absorption coefficient involves using a transparency measurement system similar to the UVVis system mentioned in Appendix B. The first step is to measure the percent transmission as a function of wavelength. Using Equation C.6, and assuming that absorption is 0 and scattering is zero, the only other effect that needs to be considered is the reflection. The index of refraction of each material present that creates and interface the light must pass through is required to accurately calculate the percent of light reflected at the interfaces and added to the transmission.

$$I_{transmission} = I_0 - I_{absorption} - I_{reflection} \quad (C.6)$$

Percent transmission is the ratio of transmitted light and incident light so divide equation C.6 by  $I_0$ .

$$\frac{I_{transmission}}{I_0} = 1 - \frac{I_{absorption}}{I_0} + \frac{I_{reflection}}{I_0} \quad (C.7)$$

Assume Reflection can be calculated from the refractive indices of both materials

$$\frac{I_{reflection}}{I_0} \cdot 100 = \%R = 100 \cdot \left( \frac{n_1 - n_2}{n_1 + n_2} \right)^2 \quad (C.8)$$

The index of refraction for air is 1 and the spinel is 2.6, ~25% is lost at the film-air interface. The index of refraction of the fused silica is 1.46 resulting in ~ 4% loss from the film-substrate interface, and so add 29% to all measured values and the %T lost to absorption

Convert the reflection corrected transmission value to absorbance by subtracting sum of %R value and %T value from 100. Dividing by 100 you get absorbance which is found in Equation C.10.

$$I_{absorption} = I_0 \cdot e^{(-\alpha \cdot d)} \quad (C.9)$$

Solving for  $\alpha$ , the absorption coefficient, yields get Equation C.10. Plug in the absorption figure calculated above for  $I_{absorption}/I_0$  and the film thickness to yield the absorption coefficient.

$$\alpha = -\frac{1}{d} \ln \left( \frac{I_{absorption}}{I_0} \right) \quad (C.10)$$

### C.5 Jahn-Teller Effect

The Jahn-Teller effect is a term used to describe a system going to a lower energy state from a state of degeneracy by shifting the degenerate orbitals slightly due to an atomistic distortion. For example a cubic system may become slightly tetragonal to allow a stepped energy level of the  $t_{2g}$  orbitals rather than a triple degeneracy (Dionne, 1990).

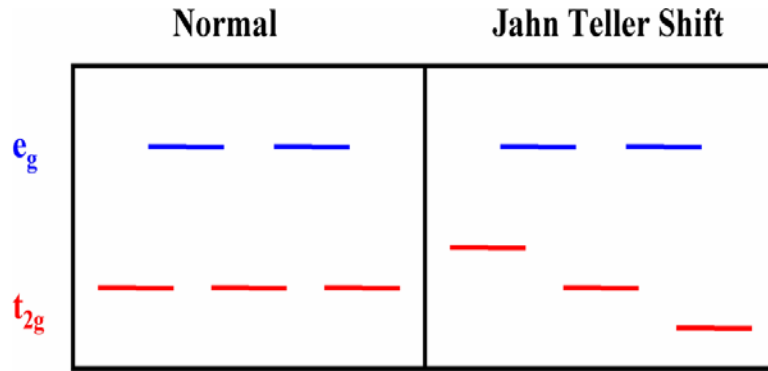


Figure C-3. Degenerate energy level orbitals in the normal spinel state and schematic of orbital energy shift due to the Jahn-Teller effect.

### C.6 Verway Transition

Charge ordering of cations was postulated by C.J. Verway in 1939 and has been used as an argument to describe the behavior of  $\text{Fe}_3\text{O}_4$  and its multiple cation states. At a temperature of X (400K for  $\text{Fe}_3\text{O}_4$ ) the Verway or *order-disorder* transition occurs and is believed to be an ordering of the cation charges. This charge ordering alters the activation energy of electrical conductivity.

### C.7 Nickel-Cobalt Oxide Activation Energy Curves

Using Equation C.11, when rearranged as C.12 will match the form given in Equation C.13 that is easily graphed. The ordinate axis (y) corresponds with  $\ln(\sigma)$ , the abscissa (x) corresponds with  $1/T$ , m is the slope and is the value from the graph ( $E_a/k$ ). When multiplied by the Boltzman constant of  $8.6175 \text{ eVK}^{-1}$  gives  $E_a$ . The remaining value is the y intercept (b) corresponding to the preexponential term of the conductivity equation.

$$\sigma = \sigma_0 \exp\left(-\frac{E_a}{kT}\right) \quad \text{or} \quad \frac{\sigma_{act}}{\sigma_{norm}} = \frac{\sigma_{\infty}}{\sigma_{norm}} \exp\left(-\frac{E_a}{kT}\right) \quad (\text{C.11})$$

$$\ln(\sigma) = -\frac{E_a}{kT} + \ln(\sigma_0) \quad (\text{C.12})$$

$$y = mx + b \quad (\text{C.13})$$

The slopes from Figure C-4 were used as  $m$  in this case to find the value of the activation energy ( $E_a$ ) using Equation C.14 rearranged to give Equation C.15. The Boltzman constant in  $eVK^{-1}$  is shown with  $1/T$  being the variable  $x$  in Equation C.14 and Equation C.15.

$$-\frac{E_a}{kT} = \frac{E_a (eV)}{8.6175(10)^{-5} \left(\frac{eV}{K}\right)} \cdot \frac{1}{T(K)} \quad (C.14)$$

$$E_a = -\frac{m \cdot 8.6175(10)^{-5} \left(\frac{eV}{K}\right)}{1000} \quad (C.15)$$

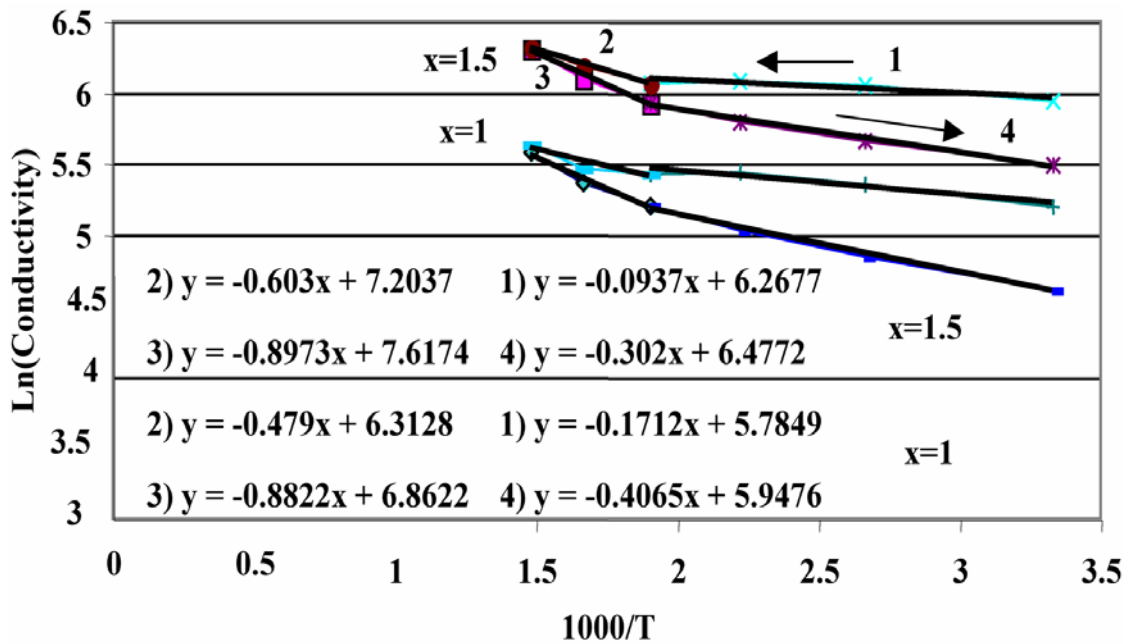


Figure C-4. Activation energies are the slope taken from the curve fits to the heating traces

Table C-2. Activation energies of  $Ni_xCo_{3-x}O_4$  films from Figure C-4. All values are in millivolts taken from slopes of curves in Figure C-4.

$Ni_xCo_{3-x}O_4$	Low Up	High Up	High Down	Low Down
x=1	14.75	41.27	76.02	35.03
x=1.5	8.07	41.2	76.02	35.03

### C.8 Lithium in Nickel-Cobalt Oxide Activation Energy Curves

Table C-3. Activation energies of  $\text{NiCo}_{2-z}\text{Li}_z\text{O}_4$  films from solution deposition. All values are in millivolts taken from slopes of curves in Figure C-5.

$\text{NiCo}_{2-z}\text{Li}_z\text{O}_4$	$z=0.00$	$z=0.01$	$z=0.03$	$z=0.05$	$z=0.1$	$z=0.3$	$z=0.5$
$E_a$ Low Up	11.7	19.6	19.4	19.4	13.2	15.2	6.17
$E_a$ Low Down	35.2	32.2	35.3	35.3	30.7	41.4	62.5
$E_a$ High Up	47.5	58.5	59.3	66.9	56.2	80.6	130
$E_a$ High Down	58.9	58.9	59.3	66.9	63.9	88.2	140

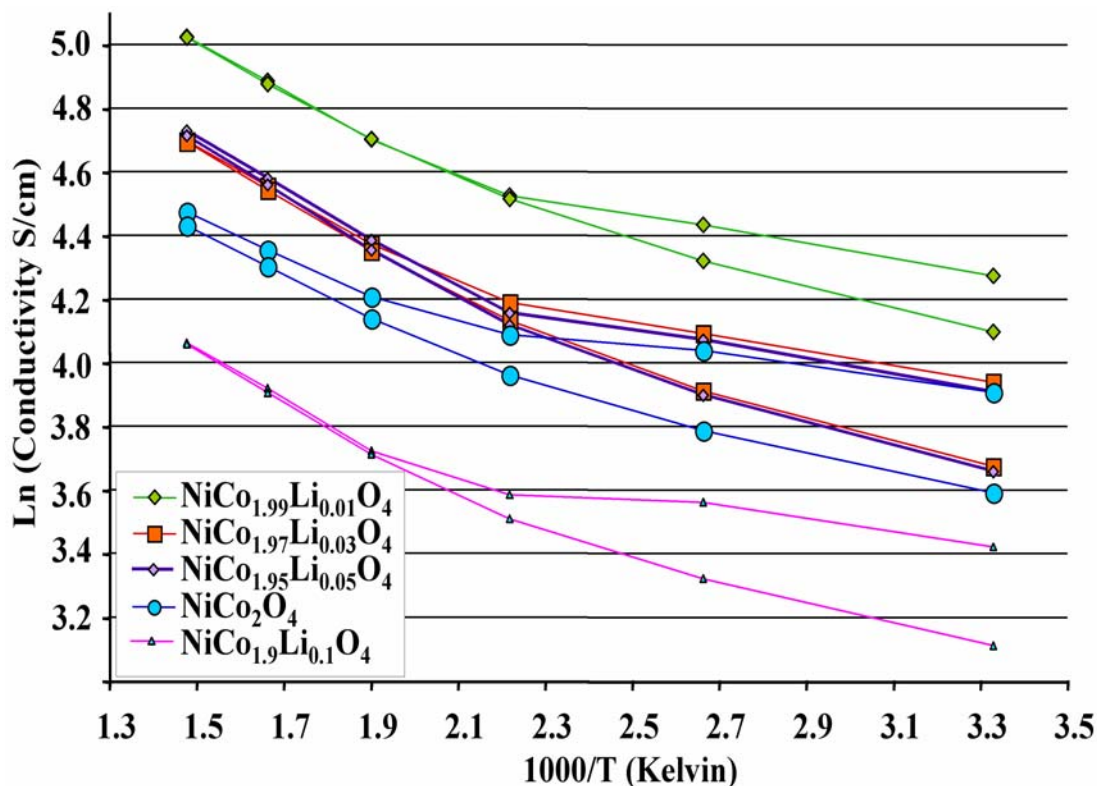


Figure C-5. Measured conductivity as a function of temperature for  $\text{NiCo}_{2-z}\text{Li}_z\text{O}_4$  films from solution. The highest conductivity is from the sample with the lowest concentration of lithium.

Table C-4. Activation energies of  $\text{Ni}_{0.75}\text{Co}_{2.25-z}\text{Li}_z\text{O}_4$  films from solution deposition. All values are in millivolts taken from slopes of curves in Figure C-6.

	$Z=0.00$	$Z=0.05$	$Z=0.1$	$Z=0.25$	$Z=0.5$
$E_a$ Low Up	11.71	9.91	7.505	35.20	13.08
$E_a$ High Up	47.50	52.11	53.67	70.41	115.65
$E_a$ High Down	68.59	56.88	56.76	76.12	114.22
$E_a$ Low Down	12.38	28.43	27.52	36.87	54.20

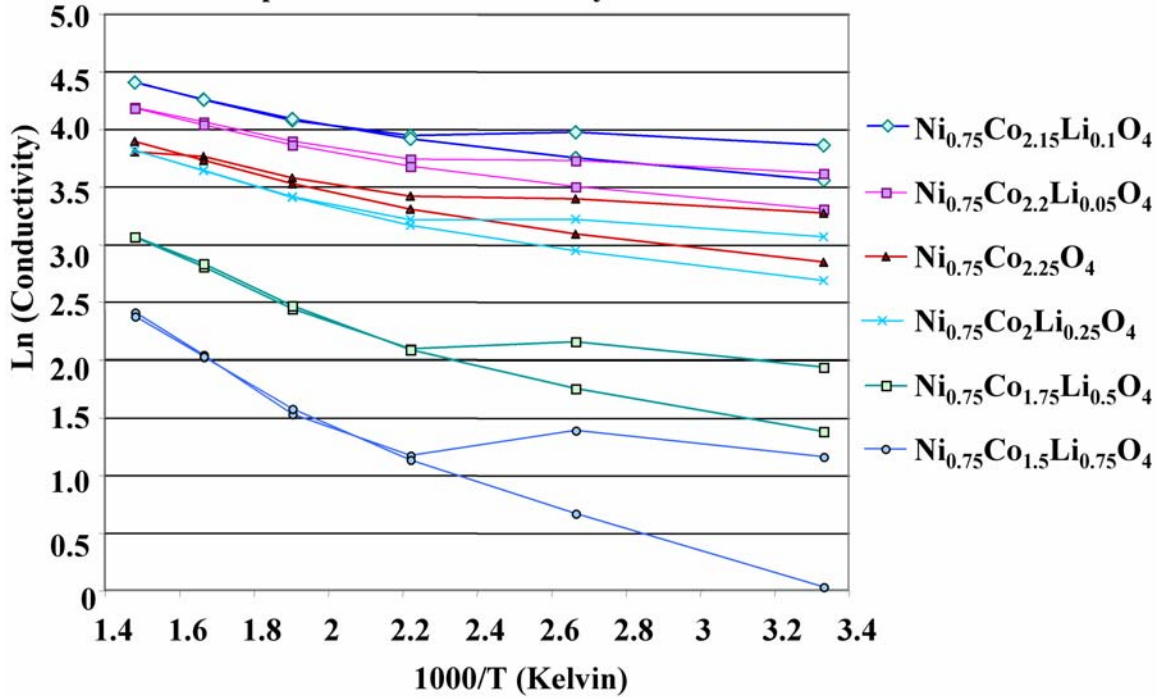


Figure C-6. Conductivity is temperature dependent for  $\text{Ni}_{0.75}\text{Co}_{2.25-z}\text{Li}_z\text{O}_4$  from solution. Lithium in increasing amounts substitutes for cobalt. All samples were heated and cooled at  $15^\circ/\text{minute}$ .

### C.9 Heat Treatment Quench Model

If the sample substrate of fused silica is 3 mm thick and 2.54 cm in diameter, the effective thermal mass is low. Thermal contact quality between the substrate surface and the cooling block surface were subject to uncertainty and believed to be the reason for the differences in cooling between the aluminum and brass. Brass in cool water was a faster quench because the brass sink was below room temperature when the quench began increasing the cooling rate. Using the thermal conductivity of fused silica, the time required to remove the amount of thermal energy stored in the substrate by its heat capacity times its thermal mass was  $\sim 20$  s. Cooling from  $\sim 400^\circ\text{C}$  to room temperature at  $25^\circ\text{C}$  was  $375^\circ\text{C}$  in 20 s. The effective maximum cooling rate is  $\sim 15^\circ\text{C/s}$  or  $\sim 1200^\circ\text{C}$  per minute.

## LIST OF REFERENCES

- Appandairajan, N.K., Viswanathan, B., & Gopalakrishnan, J. (1981). Lithium-substituted cobalt oxide spinels  $\text{Li}_x\text{M}_{1-x}\text{Co}_2\text{O}_4$  ( $\text{M} = \text{Co}^{2+}, \text{Zn}^{2+}$ ,  $0 < \text{or} = x < \text{or} = 0.4$ ). *Journal of Solid State Chemistry*, 40(1), 117-121.
- Austin, I.G., Mott, N.F. (1969). Polarons in crystalline and non-crystalline materials. *Advances in Physics*, 18, 41-102.
- Azaroff, L.V. (1960). *Introduction to solids*. New York: McGraw-Hill.
- Ballal, M.M., & Mande, C. (1977). Chemical shifts of copper and cobalt k absorption discontinuities in the spinels  $\text{CuCr}_2\text{X}_4$  ( $\text{X} = \text{O}, \text{S}, \text{Se}, \text{Te}$ ),  $\text{CoCr}_2\text{X}_4$  ( $\text{X} = \text{O}, \text{S}$ ) and  $\text{Cu}_{0.5}\text{Co}_{0.5}\text{Cr}_{2-x}\text{Rh}_x\text{S}_4$  ( $x=0, 1, 2$ ). *Journal of the Physics and Chemistry of Solids*, 38(8), 843-848.
- Banov, B., Bourilkov, J., & Mladenov, M. (1995). Cobalt stabilized layered lithium-nickel oxides, cathodes in lithium rechargeable cells. *Journal of Power Sources*, 54(2), 268-270.
- Belova, I.D., Roginskaya, Y.E., Shifrina, R.R., Gagarin, S.G., Plekhanov, Y.V., & Venetsev, Y.N. (1983). Co (III) ions high-spin configuration in nonstoichiometric  $\text{Co}_3\text{O}_4$  films. *Solid State Communications*, 47(8), 577-584.
- Benco, L., Barras, J.-L., Atanasov, M., Daul, C., & Deiss, E. (1999). First principles calculation of electrode material for lithium intercalation batteries:  $\text{TiS}_2$  and  $\text{LiTi}_2\text{S}_4$  cubic spinel structures. *Journal of Solid State Chemistry*, 145(2), 503-510.
- Benqlilou-Moudden, H., Blondiaux, G., Vinatier, P., & Levasseur, A. (1998). Amorphous lithium cobalt and nickel oxides thin films: Preparation and characterization by RBS and PIGE. *Thin Solid Films*, 333(1-2), 16-19.
- Bergh, A., Craford, G., Duggal, A., & Haitz, R. (2001). The promise and challenge of solid-state lighting. *Physics Today*, 54(12), 42-47.
- Biju, V., & Khadar, M.A. (2001). DC conductivity of consolidated nanoparticles of NiO. *Materials Research Bulletin*, 36(1-2), 21-33.

- Blasse, G. (1963). New type of superexchange in the spinel structure some magnetic properties of oxides  $\text{Me}^{2+}\text{Co}_2\text{O}_4$  and  $\text{Me}^{2+}\text{Rh}_2\text{O}_4$  with spinel structure. *Philips Research Reports*, 18, 383-392.
- Brundle, C.R., Evans, C.A.J., & Wilson, S. (1992). *Encyclopedia of materials characterization: Surfaces, interfaces, thin films*. Boston: Butterworth-Heinemann.
- Callister, W.D. (1997). *Materials science and engineering: An introduction* (Fourth ed.). New York: Wiley.
- Campbell, S.A. (1996). *The science and engineering of microelectronic fabrication*. New York: Oxford University Press.
- Carewska, M., Scaccia, S., Croce, F., Arumugam, S., Wang, Y., & Greenbaum, S. (1997). Electrical conductivity and  $^{6,7}\text{Li}$  NMR studies of  $\text{Li}_{1+y}\text{CoO}_2$ . *Solid State Ionics, Diffusion & Reactions*, 93(3-4), 227-237.
- Carey, M.J., Spada, F.E., Berkowitz, A.E., Cao, W., & Thomas, G. (1991). Preparation and structural characterization of sputtered  $\text{CoO}$ ,  $\text{NiO}$ , and  $\text{Ni}_{0.5}\text{Co}_{0.5}\text{O}$  thin epitaxial-films. *Journal of Materials Research*, 6(12), 2680-2687.
- Cheng, C.-S., Serizawa, M., Sakata, H., & Hirayama, T. (1998). Electrical conductivity of  $\text{Co}_3\text{O}_4$  films prepared by chemical vapour deposition. *Materials Chemistry and Physics*, 53(3), 225-230.
- Chopra, K.L., Major, S., & Pandya, K. (1983). Transparent conductors - a status review. *Thin Solid Films*, 102, 1-46.
- Cox, P.A. (1987). *The electronic structure and chemistry of solids*. Oxford [Oxfordshire]; New York: Oxford University Press.
- da Silva Pereira, M.I., da Costa, F.M.A., & Tavares, A.C. (1994). Electrochemical behaviour of  $\text{NiCo}_{2-x}\text{Rh}_x\text{O}_4$  spinel system. *Electrochimica Acta*, 39(11-12), 1571-1578.
- Deer, W.A. (1962). *Rock-forming minerals*. London: Longmans.
- Dionne, G.F. (1990). Spin states and electronic conduction in Ni oxides. *Journal of Applied Physics*
- Duan, N., Sleight, A.W., Jayaraj, M.K., & Tate, J. (2000). Transparent p-type conducting  $\text{CuSCo}_{2+x}$  films. *Applied Physics Letters*, 77(9), 1325-1326.
- El-Farh, L., Massot, M., Lemal, M., Julien, C., Chitra, S., Kalyani, P., Mohan, T., & Gangadharan, R. (1999). Physical properties and electrochemical features of lithium nickel-cobalt oxide cathode materials prepared at moderate temperature. *Journal of Electroceramics*, 3(4), 425-432.

- Emin, D. (1977). The sign of the hall effect in hopping conduction. *Philosophical Magazine*, 35, 1189-1198.
- Emin, D. (1980). The hall effect in hopping conduction. In C.L. Chien & C.R. Westgate (Eds.), *Hall effect and its applications. Proceedings of the commemorative symposium, 13 Nov. 1979* (pp. 281-298). Baltimore, MD, USA: Plenum.
- Emin, D. (1982). Small polarons. *Physics Today*, 35(6), 34-40.
- Emin, D. (1994). Disorder effects on small-polaron formation and hopping. *International Journal of Modern Physics B*, 8(7), 819-827.
- Emin, D., & Bussac, M.-N. (1994). Disorder-induced small-polaron formation. *Physical Review B (Condensed Matter)*, 49(20), 14290-14300.
- Fleischer, M. (1995). *Glossary of mineral species 1995* (7th ed.). Tucson, AZ: Mineralogical Record.
- Forrest, S., Burrows, P., & Thompson, M. (2000). The dawn of organic electronics. *IEEE Spectrum*, 37(8), 29-34.
- Fransson, L., Nordstrom, E., Edstrom, K., Haggstrom, L., Vaughey, J.T., & Thackeray, M.M. (2002). Structural transformations in lithiated  $\eta'$ - $\text{Cu}_6\text{Sn}_5$  electrodes probed by in situ Mossbauer spectroscopy and x-ray diffraction. *Journal of the Electrochemical Society*, 149(6), 736-742.
- Freeman, A.J., Poepelmeier, K.R., Mason, T.O., Chang, R.P.H., & Marks, T.J. (2000). Chemical and thin-film strategies for new transparent conducting oxides. *MRS Bulletin*, 25(8), 45-51.
- Fujii, E., Tomozawa, A., Torii, H., & Takayama, R. (1996). Preferred orientations of NiO films prepared by plasma-enhanced metalorganic chemical vapor deposition. *Japanese Journal of Applied Physics Part 2*, 35(3A), L328-L330.
- Fukui, T., Ohara, S., Okawa, H., Hotta, T., & Naito, M. (2000). Properties of NiO cathode coated with lithiated Co and Ni solid solution oxide for MCFS. *Journal of Power Sources*, 86(1-2), 340-346.
- Galtayries, A., & Grimblot, J. (1999). Formation and electronic properties of oxide and sulphide films of Co, Ni and Mo studied by XPS. *Journal of Electron Spectroscopy and Related Phenomena*, 99, 267-275.
- Ganguly, P., Venkatraman, T.N., Rajamohanam, P.R., & Ganapathy, S. (1997). Evidence for multiple M sites in  $\text{AMO}_2$  compounds:  $^{59}\text{Co}$  solid state NMR studies on  $\text{LiCoO}_2$ . *Journal of Physical Chemistry B*, 101(51), 11099-11105.
- Gem by gem.* (2003). Retrieved June 10, 2003, from <http://www.gemstone.org/gem-by-gem/english/spinel.html>

- Gendron, F., Castro-Garcia, S., Popova, E., Ziolkiewicz, S., Soulette, F., & Julien, C. (2003). Magnetic and electronic properties of lithium cobalt oxide substituted by nickel. *Solid State Ionics, Diffusion & Reactions*, 157, 125-132.
- Giesbers, J.B., Prins, M.W.J., Cillessen, J.F.M., & vanEsch, H.A. (1997). Dry etching of all-oxide transparent thin film memory transistors. *Microelectronic Engineering*, 35(1-4), 71-74.
- Gonzalez-Elipe, A.R., Alvarez, R., Holgado, J.P., Espinos, J.P., Munuera, G., & Sanz, J.M. (1991). XPS study of the Ar<sup>+</sup>-induced reduction of Ni<sup>2+</sup> in NiO and Ni-Si oxide systems. *Applied Surface Science (1985)*, 51(1-2), 19-26.
- Goodwin-Johansson, S., Holloway, P.H., McGuire, G., Buckley, L., Cozzens, R., Schwartz, R., & Exarhos, G. (2000). Artificial eyelid for protection of optical sensors. *Smart Structures and Materials 2000: Electroactive Polymer Actuators and Devices (EAPAD)*, (3987), 225-231.
- Gordon, R.G. (2000). Criteria for choosing transparent conductors. *MRS Bulletin*, 25(8), 52-57.
- Gover, R.K.B., Yonemura, M., Hirano, A., Kanno, R., Kawamoto, Y., Murphy, C., Mitchell, B.J., & Richardson, J.W., Jr. (1999). The control of nonstoichiometry in lithium nickel-cobalt oxides. *Journal of Power Sources*, 81-82, 535-541.
- Haenen, J., Visscher, W., & Barendrecht, E. (1986). Characterization of NiCo<sub>2</sub>O<sub>4</sub> electrodes for O<sup>-2</sup> evolution .2. Nonelectrochemical characterization of NiCo<sub>2</sub>O<sub>4</sub> electrodes. *Journal of Electroanalytical Chemistry*, 208(2), 297-321.
- Han, K.-S., Tsurimoto, S., & Yoshimura, M. (1999). Fabrication temperature and applied current density effects on the direct fabrication of lithium nickel oxide thin-film electrodes in LiOH solution by the electrochemical-hydrothermal method. *Solid State Ionics, Diffusion & Reactions*, 121(1-4), 229-233.
- He, J., Lindstrom, H., Hagfeldt, A., & Lindquist, S.-E. (1999). Dye-sensitized nanostructured p-type nickel oxide film as a photocathode for a solar cell. *Journal of Physical Chemistry B*, 103(42), 8940-8943.
- Holloway, P.H., & Nelson, G.C. (1979). Preferential sputtering of Ta<sub>2</sub>O<sub>5</sub> by argon ions. *Journal of Vacuum Science & Technology A-Vacuum Surfaces and Films*, 16(2), 793-796.
- Hosono, H., Yasukawa, M., & Kawazoe, H. (1996). Novel oxide amorphous semiconductors: Transparent conducting amorphous oxides. *Journal of Non-Crystalline Solids*, 203, 334-344.

- Hotovy, I., Buc, D., Hascik, S., & Nennewitz, O. (1998a). Characterization of NiO thin films deposited by reactive sputtering. *Vacuum Electronic Properties of Metal/Non-Metal Microsystems.*, 50(1-2), 41-44.
- Hotovy, I., Huran, J., Janik, J., & Kobzev, A.P. (1998b). Deposition and properties of nickel oxide films produced by DC reactive magnetron sputtering. *Vacuum*, 51(2), 157-160.
- Hu, C.-C., & Cheng, C.-Y. (2002). Ideally pseudocapacitive behavior of amorphous hydrous cobalt-nickel oxide prepared by anodic deposition. *Electrochemical and Solid-State Letters*, 5(3), 43-46.
- Hughes, R.A.S., K.E. (1999). Spinel compounds: structure and property relations. *Journal of the American Ceramic Society*, 82(12), 3277-3278.
- Hummel, R.E. (2001). *Electronic properties of materials* (3rd ed.). New York: Springer.
- Iida, A., & Nishikawa, R. (1994). A thin-film of an Ni-NiO heterogeneous system for an optical-recording medium. *Japanese Journal of Applied Physics Part I*, 33(7A), 3952-3959.
- Julien, C. (2000). Local cationic environment in lithium nickel-cobalt oxides used as cathode materials for lithium batteries. *Solid State Ionics*, 136-137, 887-896.
- Julien, C., El-Farh, L., Rangan, S., & Massot, M. (1999). Studies of  $\text{LiNi}_{10.6}\text{Co}_{0.4}\text{O}_2$  cathode material prepared by the citric acid-assisted sol-gel method for lithium batteries. *Journal of Sol-Gel Science and Technology*, 15(1), 63-72.
- Kawazoe, H., Yanagi, H., Ueda, K., & Hosono, H. (2000). Transparent p-type conducting oxides: design and fabrication of p-n heterojunctions. *MRS Bulletin*, 25(8), 28-36.
- Kawazoe, H., Yasukawa, M., Hyodo, H., Kurita, M., Yanagi, H., & Hosono, H. (1997). P-type electrical conduction in transparent thin films of  $\text{CuAlO}_2$ . *Nature*, 389(6654), 939-942.
- Kennedy, R.J. (1996). The growth of iron oxide, nickel oxide and cobalt oxide thin films by laser ablation from metal targets. *IEEE transactions on magnetics* 31(6), 3829-3831.
- Kim, D., Kim, M.-K., Son, J.-T., & Kim, H.-G. (2002). Effect of target properties on deposition of lithium nickel cobalt oxide thin-films using RF magnetron sputtering. *Journal of Power Sources*, 108(1-2), 239-244.
- Kim, J.-G., Pugmire, D.L., Battaglia, D., & Langell, M.A. (2000). Analysis of the  $\text{NiCo}_2\text{O}_4$  spinel surface with auger and x-ray photoelectron spectroscopy. *Applied Surface Science*, 165(1), 70-84.

- King, W.J., & Tseung, A.C.C. (1974). Reduction of oxygen on nickel-cobalt oxides .2. Correlation between crystal-structure and activity of  $\text{Co}_2\text{NiO}_4$  and related oxides. *Electrochimica Acta*, 19(8), 493-498.
- Kingery, W.D., Bowin, H.K., & Uhlmann, D.R. (1975). *Introduction to ceramics* (2<sup>nd</sup> Ed.). New York: John Wiley & Sons.
- Kishimoto, Y., Ohno, T., Nagata, S., Matsumoto, N., Kanashiro, T., Michihiro, Y., & Nakamura, K. (2000). NMR study of  $\text{Cu}(\text{Ir}_{0.95}\text{Rh}_{0.05})_2\text{S}_4$ . *Physica B*, 281-282, 634-635.
- Kitao, M., Izawa, K., Urabe, K., Komatsu, T., Kuwano, S., & Yamada, S. (1994). Preparation and electrochromic properties of RF-sputtered  $\text{NiO}_x$  films prepared in  $\text{Ar}/\text{O}_2/\text{H}_2$  atmosphere. *Japanese Journal of Applied Physics Part 1*, 33(12A), 6656-6662.
- Koumoto, K., & Yanagida, H. (1981). Electrical conduction in pure and Li-substituted  $\text{Co}_3\text{O}_4$ . *Communications of the American Society*, C-156 - C-157.
- Kuk, S.T., Song, Y.S., & Kim, K. (1999). Properties of a new type of cathode for molten carbonate fuel cells. *Journal of Power Sources*, 83(1-2), 50-56.
- Kuk, S.T., Song, Y.S., Suh, S., Kim, J.Y., & Kim, K. (2001). The formation of  $\text{LiCoO}_2$  on a  $\text{NiO}$  cathode for a molten carbonate fuel cell using electroplating. *Journal of Materials Chemistry*, 11(2), 630-635.
- Kumagai, H., Matsumoto, M., Toyoda, K., & Obara, M. (1996). Preparation and characteristics of nickel oxide thin film by controlled growth with sequential surface chemical reactions. *Journal of Materials Science Letters*, 15(12), 1081-1083.
- Lewis, B.G., & Paine, D.C. (2000). Applications and processing of transparent conducting oxides. *MRS Bulletin*, 25(8), 22-27.
- Liu, Z.L., Yu, A.S., & Lee, J.Y. (1999). Synthesis and characterization of  $\text{LiNi}_{1-x-y}\text{Co}_x\text{Mn}_y\text{O}_2$  as the cathode materials of secondary lithium batteries. *Journal of Power Sources*, 81-82, 416-419.
- Lunkenheimer, P., Loidl, A., Ottermann, C.R., & Bange, K. (15). Correlated barrier hopping in  $\text{NiO}$  films. *Physical Review B (Condensed Matter)*, 44(11), 5927-5930.
- Mahajan, S., & Harsha, K.S.S. (1998). *Principles of growth and processing of semiconductors*. New York: WCB/McGraw-Hill.

- Marco, J.F., Gancedo, J.R., Gracia, M., Gautier, J.L., Rios, E., & Berry, F.J. (2000). Characterization of the nickel cobaltite,  $\text{NiCo}_2\text{O}_4$ , prepared by several methods: an XRD, XANES, EXAFS, and XPS study. *Journal of Solid State Chemistry*, 153(1), 74-81.
- Mattox, D.M. (1998). *Handbook of physical vapor deposition (PVD) processing : film formation, adhesion, surface preparation and contamination control*. Westwood, N.J.: Noyes Publications.
- Minami, T. (2000). New n-type transparent conducting oxides. *MRS Bulletin*, 25(8), 38-44.
- Minami, T., Sonohara, H., Kakumu, T., & Takata, S. (1995). Physics of very thin ITO conducting films with high transparency prepared by DC magnetron sputtering. *Thin Solid Films*, 270(1-2), 37-42.
- Minami, T., Yamamoto, T., Toda, Y., & Miyata, T. (2000). Transparent conducting zinc-co-doped ITO films prepared by magnetron sputtering. *Thin Solid Films*, 373(1-2), 189-194.
- Monk, P.M.S., & Ayub, S. (1997). Solid-state properties of thin film electrochromic cobalt-nickel oxide. *Solid State Ionics, Diffusion & Reactions*, 99(1-2), 115-124.
- Morin, F.J. (1954). Electrical properties of NiO. *Physical Review*, 93(6), 1199-1204.
- Moshtev, R., Zhatilova, P., Bakalova, I., & Vassilev, S. (2002). Synthesis, XRD characterization, and cycling performance of cobalt doped lithium nickelates. *Journal of Power Sources*, 112(1), 30-35.
- Moshtev, R., Zlatilova, P., Manev, V., & Tagawa, K. (1996). Synthesis of  $\text{LiNiO}_2$  in air atmosphere: x-ray diffraction characterization and electrochemical investigation. *Journal of Power Sources*, 62(1), 59-66.
- Moshtev, R., Zlatilova, P., Vasilev, S., Bakalova, I., & Kozawa, A. (1999). Synthesis, XRD characterization and electrochemical performance of overlithiated  $\text{LiNiO}_2$ . *Journal of Power Sources*, 81-82, 434-441.
- O'Hanlon, J.F. (1989). *A user's guide to vacuum technology* (2nd ed.). New York: Wiley.
- Ohmuro, Y., Ohachi, T., & Taniguchi, I. (1995). Ionic conduction of  $\text{Ag}^+$  and  $\text{Cu}^+$  ions in vacancy defect spinel compounds  $(\text{MIn}_5\text{S}_8)_{1-x}(\text{In}_2\text{S}_3)_x$  (M=Cu or Ag,  $x < 1$ ) in microwave regime. *Solid State Ionics, Diffusion & Reactions*, 79, 53-59.
- Ohya, Y., Koyama, H., Ban, T., & Takahashi, Y. (1998). Electrical properties of p-n contact with oxide semiconductor thin films fabricated by liquid phase method. *Materials Science and Engineering B-Solid State Materials For Advanced Technology*, 54(1-2), 55-59.

- Park, S., Keszler, D.A., Valencia, M.M., Hoffman, R.L., Bender, J.P., & Wager, J.F. (2002). Transparent p-type conducting bacu/sub 2/s/sub 2/ films. *Applied Physics Letters*, 80(23), 4393-4394.
- Parravano, G. (1955). Thermoelectric behavior of nickel oxide. *The Journal of Chemical Physics*, 23(1), 5-10.
- Patil, P.S., Kadam, L.D., & Lokhande, C.D. (1996). Preparation and characterization of spray pyrolysed cobalt oxide thin films. *Thin Solid Films*, 272(1), 29-32.
- Pejova, B., Isahi, A., Najdoski, M., & Grozdanov, I. (2001). Fabrication and characterization of nanocrystalline cobalt oxide thin films. *Materials Research Bulletin*, 36(1-2), 161-170.
- Petrov, K., & Will, G. (1987). A new cobalt-nickel oxide spinel prepared under high pressure in an oxygen atmosphere. *Journal of Materials Science Letters*, 6(10), 1153-1155.
- Polo da Fonseca, C.N., Davalos, J., Kleinke, M., Fantini, M.C.A., & Gorenstein, A. (1999). Studies of LiCoO<sub>x</sub> thin film cathodes produced by rf Sputtering. *Journal of Power Sources*, 81-82, 575-580.
- Puspharajah, P., Radhakrishna, S., & Arof, A.K. (1997). Transparent conducting lithium-doped nickel oxide thin films by spray pyrolysis technique. *Journal of Materials Science*, 32(11), 3001-3006.
- Rao, C.N.R., & Raveau, B. (1998). *Transition metal oxides : structure, properties, and synthesis of ceramic oxides* (2nd ed.). New York: Wiley-VCH.
- Robertson, A.D., Trevino, L., Tukamoto, H., & Irvine, J.T.S. (1999). New inorganic spinel oxides for use as negative electrode materials in future lithium-ion batteries. *Journal of Power Sources*, 81-82, 352-357.
- Roginskaya, Y.E., Morozova, O.V., Lubnin, E.N., Ulitina, Y.E., Lopukhova, G.V., & Trasatti, S. (1997). Characterization of bulk and surface composition of Co<sub>x</sub>Ni<sub>1-x</sub>O<sub>y</sub> mixed oxides for electrocatalysis. *Langmuir*, 13(17), 4621-4627.
- Sanz, J.M., Soriano, L., Prieto, P., Tyuliev, G., Morant, C., & Elizalde, E. (1998). Electronic structure and chemical characterization of ultrathin insulating films. *Thin Solid Films*, 332(1-2), 209-214.
- Sato, H., Minami, T., Takata, S., & Yamada, T. (1993). Transparent conducting p-type NiO thin-films prepared by magnetron sputtering. *Thin Solid Films*, 236(1-2), 27-31.
- Schellenschlager, V., & Lutz, H.D. (2000). Raman spectroscopic studies on decomposition of spinel-type cobalt chromium indium sulfide solid solutions. *Materials Research Bulletin*, 35(4), 567-574.

- Schumacher, L.C., Holzhueter, I.B., Hill, I.R., & Dignam, M.J. (1990). Semiconducting and electrocatalytic properties of sputtered cobalt oxide films. *Electrochimica Acta*, 35(6), 975-984.
- Seguin, L., Amatucci, G., Anne, M., Chabre, Y., Strobel, P., Tarascon, J.M., & Vaughan, G. (1999). Structural study of NiO<sub>2</sub> and CoO<sub>2</sub> as end members of the lithiated compounds by in situ high resolution X-ray powder diffraction. *Journal of Power Sources*, 81-82, 604-606.
- Shirakami, T., Takematsu, M., Hirano, A., Kanno, R., Yamaura, K., Takano, M., & Atake, T. (1998). Spin glass-like magnetic properties of LiNiO<sub>2</sub>. *Materials Science & Engineering B* 54(1-2), 70-72.
- Sickafus, K.E., Hughes, Richard. (1999, March 6, 2000). *Spinel compounds: Background & historical perspective*. Retrieved June 10, 2003, from <http://www.ruby-sapphire.com/spinel.htm>
- Smentkowski, V.S. (2000). Trends in sputtering. *Progress in Surface Science*, 64(1-2), 1-58.
- Smyth, D.M. (2000). *The defect chemistry of metal oxides*. New York: Oxford University Press.
- Snowden, D.P.S., H. (1965). Hopping conduction in NiO. *Physical Review Letters*, 14(13), 497-499.
- Stoneham, A.M. (1980). Theory of defect processes. *Physics Today*, 33(1), 34-42.
- Stoyanova, R., Zhecheva, E., Alcantara, R., Lavela, P., & Tirado, J.L. (1997). EPR studies of Li<sub>1-x</sub>(Ni<sub>y</sub>Co<sub>1-y</sub>)<sub>1+x</sub>O<sub>2</sub> solid solutions. *Solid State Communications*, 102(6), 457-462.
- Svensson, J., & Granqvist, C.G. (1986). Electrochromic hydrated nickel-oxide coatings for energy efficient windows: optical-properties and coloration mechanism. *Applied Physics Letters*, 49(23), 1566-1568.
- Tareen, J.A.K., Malecki, A., Doumerc, J.P., Launay, J.C., Dordor, P., Pouchard, M., & Hagenmuller, P. (1984). Growth and electrical-properties of pure and Ni-doped Co<sub>3</sub>O<sub>4</sub> single-crystals. *Materials Research Bulletin*, 19(8), 989-997.
- Tauc, J. (1976). Amorphous semiconductors. *Physics Today*, 29(10), 23-24.
- Tavares, A.C., Bochatay, L., Da Silva Pereira, M.I., & Da Costa, F.M.A. (1996). Oxygen evolution on NiCo<sub>2-x</sub>Rh<sub>x</sub>O<sub>4</sub> spinel system. *Electrochimica Acta*, 41(13), 1953-1959.
- Taylor, A.K., & Kagle, J.B. (1963). *Crystallographic data on metal and alloy structures*. New York: Dover Publications, Inc.

- Tipler, P.A. (1999). *Physics for scientists and engineers* (4 ed. Vol. I, II, III). New York: W. H. Freeman.
- Ueda, K., Hase, T., Yanagi, H., Kawazoe, H., Hosono, H., Ohta, H., Orita, M., & Hirano, M. (2001). Epitaxial growth of transparent p-type conducting CuGaO<sub>2</sub> thin films on sapphire (001) substrates by pulsed laser deposition. *Journal of Applied Physics*, 89(3), 1790-1793.
- Ueda, K., Inoue, S., Hirose, S., Kawazoe, H., & Hosono, H. (2000). Transparent p-type semiconductor: Layered oxysulfide. *Applied Physics Letters*, 77(17), 2701-2703.
- Urbano, A., Ferreira, F.F., DeCastro, S.C., Landers, R., Fantini, M.C.A., & Gorenstein, A. (2001). Electrochromism in lithiated nickel oxide films deposited by rf sputtering. *Electrochimica Acta*, 46(13-14), 2269-2273.
- Varkey, A.J., & Fort, A.F. (1993). Solution growth technique for deposition of nickel-oxide thin-films. *Thin Solid Films*, 235(1-2), 47-50.
- Verwey, E.J., Haayman, P.W., & Romeijn, F.C. (1947). Physical properties and cation arrangement of oxides with spinel structures .2. Electronic conductivity. *Journal of Chemical Physics*, 15(4), 181-187.
- Verwey, E.J.W. (1939). Electronic conduction of magnetite (Fe<sub>3</sub>O<sub>4</sub>) and its transition point at low temperatures. *Nature*, 144(3642), 327-328.
- Verwey, E.J.W., & Haayman, P.W. (1941). Electronic conductivity and transition point of magnetite ("Fe<sub>3</sub>O<sub>4</sub>"). *Physica*, 8(9), 979-987.
- Windisch, C.F., Exarhos, G.J., Ferris, K.F., Engelhard, M.H., & Stewart, D.C. (2001a). Infrared transparent spinel films with p-type conductivity. *Thin Solid Films*, 398, 45-52.
- Windisch, C.F., Exarhos, G.J., & Sharma, S.K. (2002a). Influence of temperature and electronic disorder on the Raman spectra of nickel cobalt oxides. *Journal of Applied Physics*, 92(9), 5572-5574.
- Windisch, C.F., Exarhos, G.J., Owings, R.O. (2003a). Site occupancy distribution of cations in nickel cobalt oxides. *Journal of Applied Physics*, Submitted.
- Windisch, C.F., Ferris, K.F., & Exarhos, G.J. (2001b). Synthesis and characterization of transparent conducting oxide cobalt-nickel spinel films. *Journal of Vacuum Science & Technology A-Vacuum Surfaces and Films*, 19(4), 1647-1651.
- Windisch, C.F., Ferris, K.F., Exarhos, G.J., & Sharma, S.K. (2002b). Conducting spinel oxide films with infrared transparency. *Thin Solid Films*, 420, 89-99.

- Windisch, C.F.J., Exarhos, G. J., Engelhard, M. H., Stewart, D. C. (2003b). Influence of heat treatment on properties of spinel ITCO films. *Unpublished Manuscript*.
- Wolverton, C., & Zunger, A. (1999). First-principles theory of cation and intercalation ordering in  $\text{Li}_x\text{CoO}_2$ . *Journal of Power Sources*, 81-82, 680-684.
- Xu, D.-X., Das, S.R., Peters, C.J., & Erickson, L.E. (1998). Material aspects of nickel silicide for ULSI applications. *Thin Solid Films*, 326(1-2), 143-150.
- Yamamoto, H., Tanaka, S., & Hirao, K. (2003). Effects of substrate temperature on nanostructure and band structure of sputtered  $\text{Co}_3\text{O}_4$  thin films. *Journal of Applied Physics*, 93(7), 4158-4162.
- Yoshimura, M., Han, K.S., & Tsurimoto, S. (1998). Direct fabrication of thin-film  $\text{LiNiO}_2$  electrodes in  $\text{LiOH}$  solution by electrochemical-hydrothermal method. *Solid State Ionics*, 106(1-2), 39-44.
- Zhecheva, E., Stoyanova, R., & Zarkova, L. (1996). Lithium doping of cobalt-nickel spinel oxides at low temperatures. *Materials Research Bulletin*, 31(6), 593-602.

## BIOGRAPHICAL SKETCH

Robert Reed Owings graduated from Greeley West High School in Greeley, Colorado. After one semester at Ricks College (now renamed Brigham Young University – Idaho) he served two years of volunteer missionary service for The Church of Jesus Christ of Latter Day Saints. He returned to study at Ricks College, where he married and graduated with an associate's degree in mechanical engineering. Transferring to the University of Idaho, he graduated cum laude in metallurgical engineering and received the outstanding senior award from the college of mines and earth resources. His master's work was completed in materials science and engineering at the University of Florida. Robert is the father of two children.